MUrine Tools to Catch High-Affinity Plasma cells (MUTCHAP)

MICHAEL JOHN PRICE

A thesis submitted to the University of Birmingham
for the degree of Doctor of Philosophy

INSTITUTE OF IMMUNOLOGY AND IMMUNOTHERAPY
COLLEGE OF MEDICAL AND DENTAL SCIENCE
UNIVERSITY OF BIRMINGHAM
MARCH 2021

Abstract

The generation of high-affinity antibodies is critical for natural and induced protective immune responses and production of efficacious therapeutic monoclonal antibodies. Germinal centre matured plasma cells (GCmat PCs) produce these long-term high-quality responses. The signals and mechanisms by which GCmat PCs are induced are not fully elucidated. We developed parallel strategies to generate novel gene manipulated mice where GCmat PCs are easily identifiable by fluorescent markers controlled by GC-specific *S1pr2* and PC-specific *Prdm1* expression.

Combination of validated transgenic alleles generated the High-Affinity LOw-affinity (HALO) PC mouse, able to distinguish between GCmat PCs and extrafollicular PCs. Kinetic assessment of early GC output confirmed previous results from our lab that GCmat PC output peaks early then declines. Furthermore, we detected transient re-expression of CD38 in GCmat PC precursors and GCmat transitioning PCs, an intriguing result with a yet undetermined function.

In tandem, we developed and characterised a novel split fluorescent reporter, diSplit670. CRISPR/Cas9 enhanced targeted insertion placed each part of diSplit670 under control of endogenous *Prdm1* and *S1pr2* in separate mouse embryonic stem cell (ESC) lines. To-date, germline transmission has been achieved for one targeted ESC line.

These novel tools would be uniquely suited to interrogate the biology of GCmat PCs.

Acknowledgements

Firstly, I would like to extend my sincerest thanks and gratitude to both Professor Kai-Michael Toellner and to Dr Mike Snaith. Their combined supervision, guidance and tutelage over the past four years has been invaluable. Thank you to Kai for sharing your significant experience and expertise in plasma cell biology and for helping to develop my critical thinking as an immunologist. Likewise, thank you to Mike for sharing your expertise in gene targeting and emerging technologies, and for your valuable advice on how to develop as an early career scientist.

Davide, Ted, Juan Carlos, and Yang, I am especially grateful for all of the training and advice you all have given, and for all the patience you have shown to deal with all of my technical questions. Thank you.

To all members of the Toellner Group and Transgenic Team, thank you for the support, conversation and laughs throughout. You all have helped to transform the daunting prospect of PhD life into a positive experience that I am sure will stand me in good stead for the future.

Thank you to my wonderful parents, Gill and Phil, and sister, Sarah. You have always believed in and supported me, given nothing but encouragement, and been willing ears when I have needed to vent. Thank you to Naomi – having someone embark on the same journey and truly understand what the other is feeling has been invaluable. Looking forward to the fun and free times post-thesis!

Table of Contents

List of Figures and Tables

Abbreviations

Ab	antibody
Ad SA	adenoviral major late transcript splice acceptor
Ag	Antigen
AID	activation induced cytidine deanimase
APRIL	a proliferation-inducing ligand
BAC	bacterial artificial chromosome
BAFF	B-cell activating factor
Bcl6	B-cell lymphoma 6
BCMA	B-cell maturation antigen
BCR	B-cell receptor
BiFC	bimolecular fluorescence complementation
Blimp1	B lymphocyte-induced maturation protein 1
BM	bone marrow
BMSU	Biomedical Services Unit
bp	base pair
BphP	bacteriophytochromes
BV	biliverdin IXa
CB	centroblast
CC	centrocyte
CDS	coding sequence
CHX	cycloheximide
CLL	chronic lymphocytic leukaemia
CRISPR	clustered regularly interspaced short palindromic repeats
CSR	class-switch recombination
DC	dendritic cell
diRFP670	dimeric iRFP670
DSB	double-stranded breaks
DZ	dark zone
EF	extrafollicular
ELISA	enzyme-linked immunosorbent assays
Em_{max}	Emission maximum
ESC	embryonic stem cells
Ex_{max}	Excitation maximum
EZH2	Enhancer Of Zeste 2 Polycomb Repressive Complex 2 Subunit
FACS	fluorescence associated cell sorting
FDC	follicular dendritic cells
Fo	follicular
FP	fluorescent protein
GAF	cGMP phosphodiesterase/adenyl cyclase/FhlA
GAP-43	Growth associated protein 43
GC	germinal centre
GCmat	germinal centre matured
gDNA	genomic DNA
GGS	glycine-glycine-serine
GLT	germline transcript
gMFI	geometric mean fluorescence intensity
GTI	GC:T-zone interface
GTIRC	GC:T-zone interface reticular cell

H3K27me3	trimethylated histone 3 lysine 27
HA	homology arm
HALO PC	High-Affinity LOw-affinity Plasma Cell
HAPi670	High-Affinity Plasma cell near infrared FP670
HAT	hypoxanthine-aminopterin-thymidine
HPRT	hypoxanthine-guanine phosphoribosyltransferase
HSV-tk	Herpes Simplex Virus thymidine kinase
ICAM-1	intercellular adhesion molecule-1
ICOSL	inducible T-cell co-stimulator ligand
Ig	immunoglobulin
iLP	intestinal lamina propria
IRES	internal ribosome entry site
iRFP	near-infrared fluorescent protein
IVF	in vitro fertilisation
IVIS	In Vivo Imaging System
Kb	kilobase
kDA	kiloDalton
KLH	Key Limpet Hemocyanin
LLPCs	long-lived plasma cells
LN	lymph node
LSL	LoxP-STOP codon-LoxP
LZ	light zone
mAb	monoclonal antibody
MBC	memory B-cell
MEF	mouse embryonic fibroblast
mem	plasma membrane
MGI	Mouse Genome Informatics
miRFP	monomeric iRFP
mTmG	membrane-Tomato membrane-GFP
MW	molecular weight
MZ	marginal zone
NADPH	Nicotinamide adenine dinucleotide phosphate
neo^R	neomycin resistance cassette
NK-κB	nuclear factor kappa-light-chain-enhancer of activated B cells
NIR	near infrared
NK	natural killer
NP	4-hydroxy-3-nitrophenyl acetyl
NTC	no template control
OVA	ovalbumin
PAM	protospacer adjacent motif
PAS	Per/Arndt/Sim
PB	plasmablast
PC	plasma cell
Pen/Strep	penicillin / streptomycin
PGK	phosphoglycerate kinase
PHY	phytochrome-specific
PI3K	phosphatidylinositol-3-OH kinase
PIP3	phosphatidylinositol-(3,4,5)-trisphosphate
PNI	pronuclear injection
PTEN	Phosphatase and tensin homolog

Puro	puromycin	TACI	transmembrane activator and calcium-modulator and cyclophilin ligand interactor
$puro^R$	puromycin resistance cassette	TALENs	transcription activator-like effector nucleases
RIPA	Radio-Immunoprecipitation Assay	T-D	T-dependent
ROI	region of interest	Tfh	T follicular help
S1P	sphingosine 1-phosphate	Th	T helper
S1PR2	sphingosine 1-phosphate receptor 2	T-I	T-independent
scFv	single chain Fv	Tr	transitioning
SD	standard deviation	TV	targeting vector
sgRNA	single guide RNA	UoB	University of Birmingham
SHM	somatic hypermutation	UPR	unfolded protein response
SLAM	signalling lymphocytic activation molecule	UTR	untranslated region
SRBC	sheep red blood cell	WT	wild-type
Syk	Spleen tyrosine kinase		

Chapter 1. Introduction

1.1 B cell development, activation, and the onset of the antibody response

One arm of the mammalian adaptive immune response is mediated by B lymphocytes. These immune cells can differentiate into antibody secreting or plasma cells (PCs) which are factories for the secreted form of immunoglobulin (Ig); called antibody (Ab). Human and murine studies show that PCs are able to secrete over 10,000 Ab molecules per second (Hibi and Dosch, 1986; Manz, Thiel and Radbruch, 1997). The membrane-anchored splice variant of Ig is the B-cell receptor (BCR). There are five different isotypes of antibodies; IgD, IgM, IgA, IgE and IgG which differ structurally in their constant (Fc) region. IgA and IgG antibodies both possess sub-classes; IgA1 and IgA2 for IgA, and IgG1, IgG2, IgG3 and IgG4 (in humans) and IgG1, IgG2b, IgG2a or IgG2c (haplotype dependent) and IgG3 (in mice). The Fc region of the different Ab isotypes confer distinct properties and effector functions. IgG and IgE are monomeric, IgA can be dimeric (the mucosal secreted form) and serum IgM is pentameric to enhance avidity to antigen. IgG antibodies are typically neutralising and efficiently promote opsonisation, IgM is a potent activator of the classical complement pathway and upon antigen:IgE complex formation by IgE bound to Fcε receptor on mast cells / basophils / eosinophils an array of chemical mediators are released. Further, the Fc region can enable Ab access into otherwise restricted locations; IgG1 can efficiently bind neonatal Fc receptors for active transport across the placenta into foetal blood and from mammary glands into colostrum, whereas IgA can bind polymeric Ig receptor for transport across lung or gut mucosal epithelium (Gould *et al.*, 2003; Woof and Ken, 2006; Schroeder and Cavacini, 2010; Vidarsson, Dekkers and Rispens, 2014; Collins, 2016). The function of IgD, which is predominantly co-expressed on mature naïve B-cells with IgM of the same antigen specificity, has been an enigma to B-cell

biologists. However, reports of IgD secreting PCs at mucosal surfaces and recent studies into the maintenance of autoreactive anergic peripheral B-cells have shed light on the roles played by IgD (reviewed (Gutzeit, Chen and Cerutti, 2018)). Amongst mammalian cells, B-cells are unique being the only cell type to undergo somatic hypermutation (SHM) following cognate antigen (Ag) recognition. SHM of the Ig VDJ genes results in cellular scale Darwinian evolution of the BCR and ultimately in high-affinity antibody production.

There are two pathways for B-cell development; foetal-derived B-1 cells and bone marrow (BM) derived conventional B-2 cells. B-1 cells represent a minority population of total B-cell numbers in adult mice, reside within body cavities and lymphoid tissues and are "innate-like" (Baumgarth, 2017), whereas conventional B-2 cells are the majority population and are responsible for traditional adaptive immune responses.

During BM B-cell development, each B-cell produces a single mature BCR generated by somatic recombination, rearrangement, and random mutation of immunoglobulin (Ig) V, D, and J gene segments. This produces an initial diverse repertoire of BCR specificities, estimated at 10^{11}, from which autoreactive B-cells which bind strongly to self-Ag and cannot edit specificity are disposed of within BM central tolerance (Brink and Phan, 2018). Self-reactive B-cells with weak to medium self-binding survive central tolerance but are induced to a state of limited or non-responsiveness; termed anergic B-cells (Brink and Phan, 2018). Some strongly autoreactive B-cells do not encounter their self-Ag in the BM and are not removed by central tolerance. After emergence from the BM those strongly autoreactive transitional B cells undergo peripheral tolerance, are removed and do not enter the naïve B-cell compartment (Russell *et al.*, 1991; Yau *et al.*, 2013). The remaining naïve immature $IgD^{+}IgM^{+}$ B-cell

repertoire, which possess a BCR with random, typically low, affinity for cognate Ag, exit the BM and migrate to B-cell follicles within the spleen to continue differentiation (Rolink *et al.*, 1999; Pillai and Cariappa, 2009). In an immunocompetent adult mouse this is estimated at 1-2x10^7 immature B-cells per day (Carsetti, Köhler and Lamers, 1995).

Within the spleen, recently BM emigrant immature B-cells termed transitional 1 (T1) B-cells develop into transitional 2 (T2) B-cells (Loder *et al.*, 1999; Allman *et al.*, 2001), and can be distinguished by reciprocal expression of surface CD23 and CD21 with T2 B-cells expressing both markers (Rolink, Andersson and Melchers, 1998; Loder *et al.*, 1999). Through differential tonic BCR signal strength and B-cell activating factor (BAFF) mediated signalling, T2 B-cells can further differentiate into mature marginal zone (MZ) or follicular (Fo) B-cells (Pillai and Cariappa, 2009; Rowland *et al.*, 2010). However, T2 B-cells can also give rise to T3 B-cells, which are believed to represent a pool of anergic B-cells (Merrell *et al.*, 2006; Teague *et al.*, 2007) which display typical Fo B-cell markers, but which downregulate cell-surface IgM (Allman *et al.*, 2001; Merrell *et al.*, 2006).

In mice, most MZ B-cells are located in the marginal zone area surrounding the splenic B-cell follicle and do not migrate, however in humans MZ B-cells are also found in the lymph node (LN) subcapsular sinus, tonsillar crypt epithelium and in subepithelial areas of mucosal associated tissue (Cerutti, Cols and Puga, 2013). Mature naïve Fo B-cells can reside within the B-cell follicle adjacent to the T-cell zone but are free to circulate through lymph, blood, BM, and secondary lymphoid tissues.

Even low-affinity cognate BCR:Ag interactions are sufficient to activate mature naïve $IgD^{+}IgM^{+}$ B-cells (Shih *et al.*, 2002) and this Ag-activated population express CCR7 (Reif *et al.*, 2002) and migrate in a CCR7-dependent manner toward chemokines CCL19 and CCL21 at the B-cell follicle:T-zone interface, for their first interaction with primed cognate T lymphocyte (MacLennan *et al.*, 1997). Cognate B:T lymphocyte interactions, including CD40L stimulation of B-cells (Casamayor-Palleja, Khan and MacLennan, 1995), induce extrafollicular Ig class switch recombination (CSR) shown by strong expression of germline Ig heavy chain transcripts after cognate B-T cell interactions (Toellner *et al.*, 1998; Marshall *et al.*, 2011; Roco *et al.*, 2019). CCR7 sensitivity is reduced following cognate interaction and dominant EBI2 signalling leads to Ag-activated B-cell migration to, and accumulation in, interfollicular areas (Haynes *et al.*, 2007; Kelly *et al.*, 2011), located at the T-zone:red pulp bridging channel in the spleen and edges of the T-zone by the subcapsular sinus in LNs. Exchange of critical signals which occurs in these interfollicular locations determine the divergence of Ag-activated B-cells form an early extrafollicular plasmablast (EF PB) fate or transition to a germinal centre (GC) B-cell phenotype (Kerfoot *et al.*, 2011).

1.2 The extrafollicular plasmablast response.

Low-affinity Ag-activated B-cells may lineage commit, without re-entry into B-cell follicles, to EF PBs as early as 18 h after primary immunisation with the T-independent (T-I) antigen, 4-hydroxy-3-nitrophenyl acetyl (NP)-Ficoll (Vinuesa *et al.*, 2001) or within 24 h of a T-dependent (T-D) secondary response for Ag-specific MBCs (Toellner *et al.*, 1996). The growth phase and expansion of EF PBs occurs at the extrafollicular foci in the spleen and at the medullary cords in LNs (MacLennan *et al.*, 2003). Studies of early EF PBs indicated very low numbers of mutations in the V region, examined by microdissection and sequencing (Sze *et al.*, 2000; Toellner *et al.*, 2002), indicative of little/no SHM but that some undergo CSR (Marshall *et al.*, 2011; Roco *et al.*, 2019). It was also reported that EF PBs transition into low-affinity terminally differentiated EF PCs after only five to six cycles of mitosis, and typically most of these will possess a short lifespan before death by apoptosis and/or replacement by either nascent EF PCs or GC-derived PC (Sze *et al.*, 2000). This rapid initial low-affinity extrafollicular antibody response could be critical for limiting infection whilst high-affinity responses with enhanced effector functions are being generated, and MZ and B-1 cells are uniquely spatially positioned to perform this (Martin, Oliver and Kearney, 2001).

1.3 The formation and maturation of the GC reaction.

The conventional GC is a transient anatomical structure that forms during T-D immune responses in secondary lymphoid tissues that typically last for 3 weeks (MacLennan, 1994) and is supported by specialised stromal cells that are natively organised into networks (Victora and Nussenzweig, 2012; De Silva and Klein, 2015; Silva-Cayetano and Linterman, 2020). However, inducible formation of ectopic tertiary GCs in non-lymphoid tissues, for example in influenza infected lung, can be driven by type I interferon induced CXCL13 expression

combined with other cues, such as persistent antigenic or inflammatory stimulus (Denton *et al.*, 2019; Tan *et al.*, 2019). Further, the transcriptomes of specialised GC T follicular helper (Tfh) cells, follicular dendritic cells (FDC) and GC-like B-cells found in ectopic GCs were conserved to their counterparts from conventional GCs in secondary lymphoid tissues (Denton *et al.*, 2019; Tan *et al.*, 2019).

GC formation is initiated at a molecular level by Ag-activated B-cells which, after interactions at the interfollicular areas, lose EBI2 expression (Gatto *et al.*, 2009; Kelly *et al.*, 2011) which is mediated by the upregulation and repressive action of B-cell lymphoma 6 (Bcl6) (Basso *et al.*, 2010), and which inversely regulate two G-protein coupled receptors; inducing sphingosine 1-phosphate receptor 2 (S1PR2) and losing S1PR1 expression (Green *et al.*, 2011; Shinnakasu *et al.*, 2016). This leads to GC seeding by assembly of initial proliferating blasts within follicle centres. The transcriptional repressor Bcl6 is necessary for GC initiation, as $Bcl6^{-/-}$ GC B-cell precursors or those with an inactivating mutation could not inhibit EBI2 expression and did not re-enter the follicle (Kitano *et al.*, 2011; Huang *et al.*, 2014). S1PR2 is reported to have a dual role in; spatial localisation and segregation of GC B-cells in the follicle centre, and GC B-cell homeostasis. S1PR2-deficient mice develop GCs that have no clear boundaries and when explanted LNs were studied by two-photon microscopy, S1PR2-deficient GC B-cells were observed moving out of the GC niche (Green *et al.*, 2011). In conjunction with other cues, S1PR2 is proposed to promote clustering of GC B-cells, demonstrated by dispersion of $GL7^{+}$ GC B-cells throughout lymphoid tissue when CXCL13-deficient mice were reconstituted with BM from a $S1PR2^{-/-}$ donor. The source of S1P, the ligand for S1PR2, is postulated to be stromal cells and S1P is thought to be present at a decreasing concentration gradient from outside the follicle to the centre, based on increased transcript levels for, and activity of, S1P-lyase in B-

cells (Green *et al.*, 2011). *In vitro* migration assays highlighted that low nM S1P concentrations were sufficient to inhibit GC B-cell, but not Fo B-cell, migration towards follicle chemoattractants CXCL12 and CXCL13, which indicated that the action of S1PR2 promotes the confinement of GC B-cells (Green *et al.*, 2011). Further, time-course experiments of immunised S1PR2-deficient mice have reported uncontrolled GC B-cell expansion and outgrowth (Cattoretti *et al.*, 2009; Green *et al.*, 2011). BrdU incorporation showed that GC B-cell proliferation was unaffected by S1PR2 deficiency, whereas flow cytometric analysis revealed that lack of S1PR2 signalling resulted in increased levels of phosphorylated, active, pro-survival kinase Akt and reduced apoptosis inferred by decreased active caspase-3 (Green *et al.*, 2011).

Early GC responses can be detected by histological methods as early as day 3.5-4 post immunisation (Zhang *et al.*, 2018; Roco *et al.*, 2019). Ag-activated B-cell blasts in early GCs displace $IgD^{+}IgM^{+}$ naïve Fo B-cells and by day 5 post immunisation the GC is established and has matured to possess two distinct microanatomical areas termed the dark zone (DZ) and light zone (LZ), named due to their histological appearance. GC B-cells in the DZ and LZ can be distinguished by inverse expression of CXCR4 and activation markers CD83 and CD86, with LZ GC B-cells being $CXCR4^{lo}$ $CD83^{Hi}$ $CD86^{Hi}$ (Victora *et al.*, 2010). Segregation of the GC B-cells in the DZ and LZ is mediated by stromal cell derived CXCL12 and FDC derived CXCL13, and their binding to cognate chemokine receptors CXCR4 and CXCR5, respectively (Allen *et al.*, 2004).

1.4 Affinity maturation, GC B-cell differentiation, and output.

Ab affinity maturation is a process of cellular Darwinian evolution and is accomplished by cyclical rounds of positive selection in the LZ for beneficial mutations introduced by activation-induced cytidine deaminase (AID) mediated SHM of GC B-cell BCR Ig heavy and light chain genes during rapid clonal expansion in the DZ. Concurrently, the lowest-affinity or self-reactive GC B-cell clones can apoptose as a result of non-selection or death by neglect (Figure 1.1).

Long-term humoral immunity is mediated by the egress of high-affinity GC matured (GCmat) PCs and memory B-cells (MBCs) from the GC. It has been shown that hundreds of distinct B-cell clones can seed a GC reaction (Tas *et al.*, 2016), which poses the question of how does efficient selection of the highest affinity B-cell clones proceed from this large heterogeneous pool of Ag-specific GC B-cells?

Initially, this was believed to be by simple competition for Ag displayed by FDC aided by Th cell interaction (MacLennan, 1994) with differentiation of MBCs from GC B-cells proposed to be stochastic (Smith *et al.*, 2000) as MBC BCRs were consistently of lower-affinity and harboured fewer mutations compared to PCs (Smith *et al.*, 1997). This notion has been challenged, as several studies provided evidence that GC B-cells are pre-disposed towards entering the MBC (Shinnakasu *et al.*, 2016; Suan *et al.*, 2017) or PC precursor (Kräutler *et al.*, 2017; Ise *et al.*, 2018) pools based upon their BCR affinity, with better selection for high affinity in PC precursors, whereas selection for MBC is more relaxed. Toboso-Navasa and colleagues have recently generated evidence which implicates MYC-MIZ1 transcription factor complexes as a molecular mechanism for this (Toboso-Navasa *et al.*, 2020). PC development and

movement has been tracked *in vivo* at the pre-GC, early and mid GC timepoints (Fooksman *et al.*, 2010), and it has recently been demonstrated that the peak output of GCmat PCs is within 2 days of GC formation (Zhang *et al.*, 2018). However, it is still not certain what the underlying mechanism(s) for selection and differentiation into GCmat PCs are.

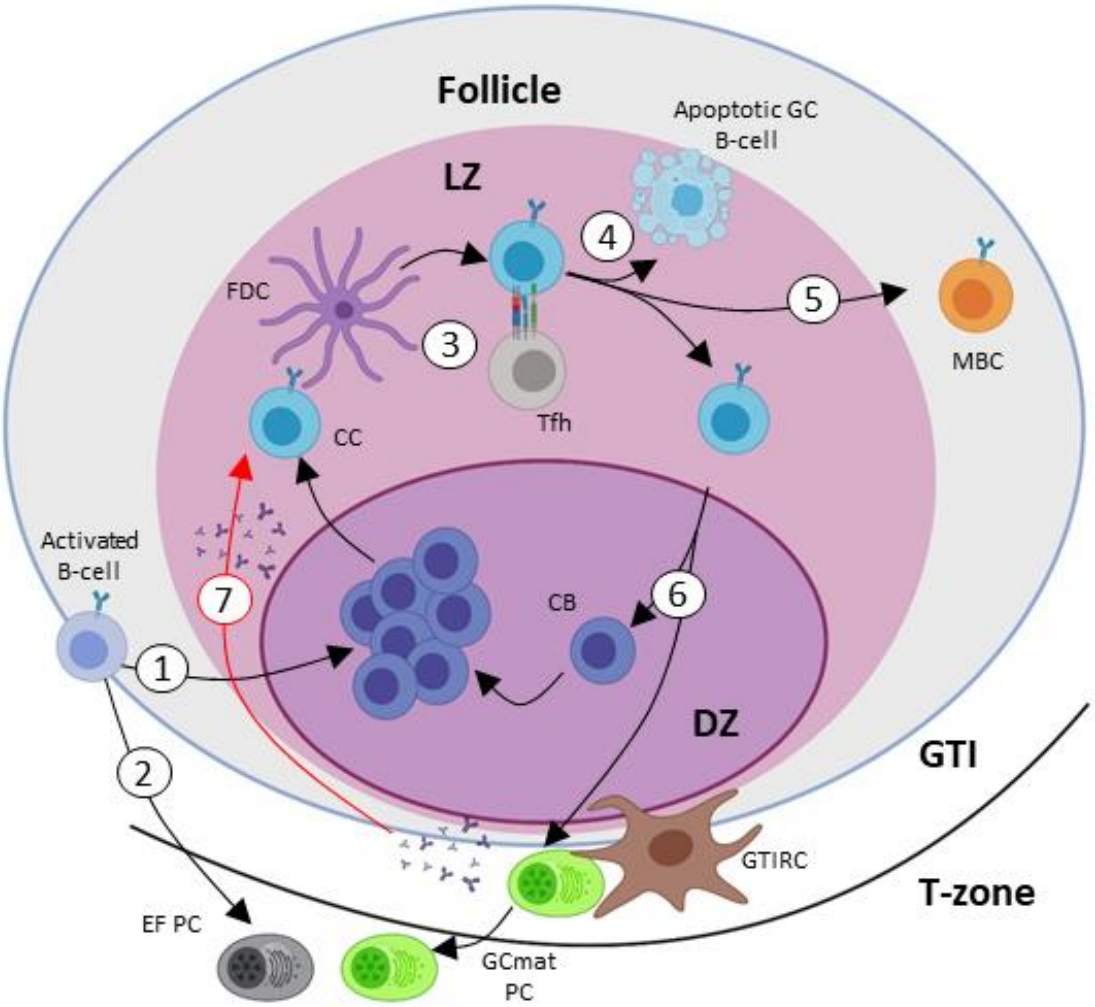

Figure 1.1 **Affinity maturation within the GC; the source of memory B-cells and high-affinity** p**lasma cells.** Ag-activated B-cells either acquire a GC B-cell phenotype and enter the DZ (1) or can terminally differentiate into EF PCs (2). GC selection mechanisms within the LZ (3) can result in death by apoptosis or neglect (4), differentiation and egress as a MBC precursor (5) or re-entry into the GC reaction with or without differentiation and egress as a GCmat PC (6). Antibody feedback (7). Light zone (LZ), dark zone (DZ), GC:T-zone interface (GTI), GTI reticular cell (GTIRC), memory B-cell (MBC), follicular dendritic cell (FDC), T follicular helper cell (Tfh), centrocyte (CC), centroblast (CB). Schematic created with BioRender.com.

There are three prevailing models for selection and differentiation: (i) asymmetric division, (ii) deterministic and (iii) deterministic – stochastic (Zhang *et al.*, 2018).

The asymmetric model (i) is supported by high resolution single cell image analysis of recently divided GC B-cells where asymmetric distribution of antigen (Thaunat *et al.*, 2012), Bcl6 and IL-21 receptor (Barnett *et al.*, 2012) were observed and by mathematical modelling (Meyer-Hermann *et al.*, 2012).

The deterministic model (ii) is based on cognate BCR:Ag interactions and strong bi-directional contact with Tfh cells and these events have been under intense scrutiny. The importance of Tfh cell help has been very well demonstrated by a series of studies where Ag was delivered to GC B-cells through the endocytic receptor DEC205 (CD205) independent of the BCR (Victora *et al.*, 2010; Gitlin, Shulman and Nussenzweig, 2014; Shulman *et al.*, 2014). More recently, through experiments involving gene expression and cell division tracking in response to defined doses of Ag, Finkin and colleagues demonstrated that the amount of Ag displayed by LZ GC B-cells to Tfh governs Tfh induced *Myc* expression in LZ GC B-cells and programs the number of DZ divisions (Finkin *et al.*, 2019). The CD40:CD40L axis has been recognised as a key signalling interaction between cognate B and Tfh cells (Han *et al.*, 1995; Victora and Nussenzweig, 2012; Zhang *et al.*, 2018). Zhang and colleagues have shown that even short-term 24 h blockade of CD40L can significantly decrease GCmat PC output (Zhang *et al.*, 2018), and others have confirmed that CD40 acts in a dose dependent manner to promote GC PC precursor formation (Ise *et al.*, 2018), however there is some evidence that CD40L blockade alone does not completely abrogate the formation of GCmat PCs (Kräutler *et al.*, 2017). Direct Tfh and GC B-cell cell-to-cell contact has been shown to be driven by CD40 mediated

upregulation of inducible T-cell co-stimulator ligand (ICOSL) (D. Liu *et al.*, 2015), intercellular adhesion molecule-1 (ICAM-1) and signalling lymphocytic activation molecule (SLAM) (Ise *et al.*, 2018), whereas GC B-cell Ephrin-B1 and Tfh EPHB4 or EPHB6 interaction acts to dissociate contact but enhance Tfh IL-21 production and PC output (Lu, Shih and Qi, 2017). Interactions between PD-1^{hi} Tfh and PD-L1 and PD-L2 expressing GC B-cells are required for GCmat PC output with the importance of these interactions shown in experiments in PD-1 deficient mice which showed both decreased long-lived PC output and IL-21 production by Tfh cells, although, importantly, the remaining PCs were of higher affinity (Good-Jacobson *et al.*, 2010). The role of Tfh derived IL-21 was revealed through sanroque mutation Tfh dysregulation (Vinuesa *et al.*, 2005) and further studies which involved mixed BM chimeras and IL-21 deficiency demonstrated that IL-21 acted in a GC B-cell intrinsic manner and was required for maximal Bcl6 expression and GCmat PC output (Linterman *et al.*, 2010; Zotos *et al.*, 2010). The importance of IL-21 in GCmat PC output was confirmed through IL-21/IL-21R knockout mice, or injection of soluble IL-21R or IL-21 (Zhang *et al.*, 2018). The role of direct BCR signalling during affinity selection and PC differentiation was thought not to be significant (Khalil, Cambier and Shlomchik, 2012). However, Kräutler and colleagues found that removal of Tfh cell help by blockade of CD40L alone did not abolish formation of GCmat PC precursors within the LZ and DZ GC B-cell compartments, whereas blocking cognate BCR:Ag interaction did, suggesting that BCR:Ag derived signals from high-affinity BCRs as well as display of peptide:MHCII plays an important role in PC differentiation (Kräutler *et al.*, 2017). Further, weak and transient GC B-cell BCR signal transduction via spleen tyrosine kinase (Syk) through the phosphatidylinositol-3-OH kinase (PI3K)-Akt axis was recently shown to be insufficient to inactivate and displace nuclear Foxo1 (Luo, Weisel and Shlomchik, 2018), a critical step for the transition from LZ to DZ phenotype (Dominguez-Sola *et al.*, 2015; Sander *et al.*, 2015). A

proposed molecular mechanism to regulate GC B-cell BCR signalling involves E3 ubiquitin ligase Cbl-mediated degradation of Syk (Li *et al.*, 2018; Davidzohn *et al.*, 2020), which can be alleviated by strong CD40 and BCR co-stimulation (Li *et al.*, 2018). Taken together, the integration of CD40 and BCR signals act to determine positive selection outcome. Strong combined CD40 and BCR signalling promotes c-Myc and IRF4 expression and Foxo1 inhibition, respectively, and further acts to alleviate Cbl-mediated degradation events of IRF4 and Syk, whereas intermediate signalling fails to achieve this and Foxo1 activity enables DZ re-entry (Li *et al.*, 2018; Luo, Weisel and Shlomchik, 2018; Ise and Kurosaki, 2019; Davidzohn *et al.*, 2020).

What GC external factors govern GCmat PC output? LZ GC B-cells test their new BCR by attempting to acquire Ag from immune complexes deposited on FDCs, therefore does Ab secreted from existing EF or GCmat PC feedback into GC selection stringency by replacing previous Ab in immune complex? Evidence for this mechanism was generated through administration of exogenous monoclonal antibodies of defined affinities which showed that GC output could be regulated through imposition of an increasing selection stringency by shielding GC B-cell access to Ag on FDC deposited immune complex (Zhang *et al.*, 2013). This process, termed antibody feedback, could potentially modulate adjacent and spatially distant GC reactions (Zhang *et al.*, 2013; Zhang, Garcia-Ibanez and Toellner, 2016). Further, immunohistology and gene expression analyses demonstrated that PBs resident in the GC:T-zone interface (GTI, Figure 1.1) express TACI (transmembrane activator and calcium-modulator and cyclophilin ligand interactor), a receptor for APRIL (a proliferation-inducing ligand), which is in-turn secreted by a newly identified population of GTI reticular cells (GTIRCs), and that blocking of either resulted in reduced GTI PBs (Zhang *et al.*, 2018). TACI

and B-cell maturation antigen (BCMA) are receptors which PBs sequentially express to high levels as they complete maturation to PCs (Bossen and Schneider, 2006), and APRIL can bind to both with high affinity in the nM range (Bossen and Schneider, 2006). Based on this evidence, Zhang and colleagues proposed the third model (iii); deterministic – stochastic (Zhang *et al.*, 2018), whereby LZ GC B-cells which have undergone successful Tfh selection, receive IL-21 and IL-4 and return to the DZ to differentiate into PCs. Whether this differentiation is due to asymmetric division, pre-determined by instructive signals, or due to contacts made between precursor GCmat PBs and chemokine (APRIL and IL-6) secreting GTIRCs, remains to be confirmed.

1.5 Transcriptional program for terminal B-cell differentiation.

In mature naïve B-cells, antigen-activated B-cells and GC B-cells, PAX5 plays an integral role in the regulation of the BCR heavy chain, CD79a, BCR co-receptors CD19 and CD21, and transcription factors IRF4, IRF8 and BACH2 (Nutt *et al.*, 2015). Together with Bcl-6, PAX5 upregulated IRF8 and BACH2 combine to repress *Prdm1* (encodes Blimp1) expression and inhibit PC differentiation in GC B-cells (Nutt *et al.*, 2015). However, IRF4 has a dose-dependent role in the GC; low-levels promote expression of *Aicda* and *Bcl6*, which facilitate GC B-cell fate, whereas high-levels inhibit *Bcl6* and upregulate *Prdm1* (Sciammas *et al.*, 2006; Ochiai *et al.*, 2013). Upon receipt of the required signals (discussed in Section 1.4), GC B-cell terminal differentiation into GCmat PCs is marked by a change in their transcription profile, mediated by high expression of IRF4 and de-repression of the transcription factors Blimp1 and XBP1 (Nutt *et al.*, 2015). In B-cell lineages Blimp1 is regarded as the 'master' regulatory transcription factor for mature differentiation of all antibody-secreting cells (Shapiro-Shelef *et al.*, 2003). Generation of the *Prdm1*$^{GFP/+}$ reporter strain highlighted that murine PBs could be

distinguished from mature PCs based on Blimp1 expression levels and this observation held true in humans (Kallies *et al.*, 2004). However, precisely how Blimp1 acts in concert with other regulators to control PC fate is to be completely elucidated, but the repressive action of Blimp1 on *Pax5*, *Bcl6* and other mediators of the mature B-cell programme provide an insight (Nutt *et al.*, 2015). XBP1 mediates the unfolded protein response (UPR) (Iwakoshi *et al.*, 2003) and due to the high Ig synthesis and associated endoplasmic reticulum stress of unfolded proteins, PCs rely on the UPR.

1.6 The duration of the Ab response hinges on survival of long-lived PCs (LLPCs).

The half-lives of the different Ab isotypes vary, but are typically ≤4-weeks, as demonstrated in human and murine studies in 1988 (Mankarious *et al.*, 1988; Vieira and Rajewsky, 1988). However, the calculated half-lives of vaccine induced Ag-specific Ab responses can extend up to 3000 years (Amanna, Carlson and Slifka, 2007). An early study in rats suggested that LLPCs could exist in the spleen, LNs, lamina propria and BM, with those residing in the BM calculated to have a lifespan >3 weeks (Ho *et al.*, 1986). A decade later, a series of murine studies by Manz and Slifka independently verified that Ag-specific PCs could persist within the BM for nearly 4 months without proliferation (Manz, Thiel and Radbruch, 1997; Manz *et al.*, 1998) and that BM resident Ag-specific PCs could be detected beyond 12 months post-immunisation (Slifka and Ahmed, 1996; Slifka *et al.*, 1998). More recently, Ag-specific PCs were demonstrated to persist for >10 years in the BM of rhesus macaques, with implications for the duration of human LLPCs as our lifespans are similar (Hammarlund *et al.*, 2017).

What licenses a PC to become a LLPC? An interplay between extrinsic and intrinsic factors must exist as Sze and colleagues demonstrated that intrinsic factors alone could not enable PC survival beyond the support capacity of the spleen (Sze *et al.*, 2000). The "PC niche" has been used to describe extrinsic factors that supported LLPCs (Manz and Radbruch, 2002; Radbruch *et al.*, 2006). Such niches exist in the BM, spleen, LN and gut associated lymphoid tissue (Ho *et al.*, 1986; Slifka and Ahmed, 1996; Manz, Thiel and Radbruch, 1997; Manz *et al.*, 1998; Slifka *et al.*, 1998; Sze *et al.*, 2000; Ellyard *et al.*, 2004; Mohr *et al.*, 2009; Bohannon *et al.*, 2016; Lemke *et al.*, 2016; Landsverk *et al.*, 2017) or at sites of inflammation (Cassese *et al.*, 2001). The PC isotype does not appear to be the determinant factor for longevity within the niche. Ag-specific IgM^+ PC have been shown to persist in the spleen for >1 year and can re-acquire this niche following adoptive transfer (Bohannon *et al.*, 2016). Similarly, Ag-specific IgA^+ PC were detected at least 9 months post-immunisation in the lamina propria but also within the BM (Lemke *et al.*, 2016). When resident within these specialist microenvironments, LLPCs interact both directly, through cell-to-cell contact, and indirectly, through soluble mediators, with stromal and hematopoietic cells (Khodadadi *et al.*, 2019; Lightman, Utley and Lee, 2019). APRIL, IL-6 and CXCL12 are prominent soluble mediators secreted locally within the niche. IL-6/IL-6R signalling on PC has been shown to improve survival and Ab titre of PC *in vitro* (Wols *et al.*, 2002; Cassese *et al.*, 2003) but is not detrimental to PC survival *in vivo* (Cassese *et al.*, 2003). CXCL12 has a dual function; it promotes PBs migration to the BM (Hauser *et al.*, 2002) and it acts as a survival factor (Cassese *et al.*, 2003). Immunofluorescence histology of BM sections from CXCR4/GFP reporter mice showed >90% PCs were in contact with CXCL12-expressing stromal cells (Tokoyoda *et al.*, 2004) which is supported by intravital imaging observations (Zehentmeier *et al.*, 2014). Moreover, fibroblasts and hematopoietic cells, especially eosinophils, are present within the niche and secret APRIL and IL-6 (Chu *et*

al., 2011; Chu and Berek, 2012; Kayaba *et al.*, 2018). More recently, a study identified fibronectin and YWHAZ as important mesenchymal stromal cell secreted survival factors, confirmed the importance of APRIL, IL-6 and hypoxic conditions for human PC survival in an *in vitro* culture system and found that cell-to-cell contact is not required for human PC survival *in vitro* (Nguyen *et al.*, 2018).

1.7 Existing transgenic strains to study the GC reaction and PC biology.

Transgenic mouse models that have been used to study GC B-cells, PC differentiation and PC kinetics utilise phenotype specific gene expression.

Irreversible commitment to terminal PC differentiation and fate are controlled by the transcriptional repressor *Prdm1*. The targeted knock-in *Prdm1*$^{GFP/+}$ mouse has been instrumental in understanding PC biology (Kallies *et al.*, 2004), with at least 25 published studies where an aspect of PC biology has been interrogated using this strain (Mouse Genome Informatic (MGI):3510704; URL: http://www.informatics.jax.org; accessed 08-Feb-2021). Recently, this has included comparative transcriptome analysis between bulk populations of splenic and BM PCs, GC, Fo and MZ B-cells (Shi *et al.*, 2015). Unlike the targeted *Prdm1*$^{GFP/+}$ allele, *Prdm1*^{YFP} is a transgenic model generated by random integration of a modified bacterial artificial chromosome (BAC) (Rutishauser *et al.*, 2009). The *Prdm1*^{YFP} model has not been as widely adopted with <10 published articles involving study of PCs (MGI:3839347; URL: http://www.informatics.jax.org; accessed 08-Feb-2021).

A variety of transgenic models have been used to interrogate aspects of GC biology. The Bcl6$^{YFP/wt}$ reporter model demonstrated the necessity of Bcl6 in GC formation and GC B-cell

phenotype (Kitano *et al.*, 2011). However, GC B-cells predominantly, but not exclusively express *Bcl6*, as 40% of non-immunised Ag-specific $B220^{+}$ B-cells expressed *Bcl6* but showed no detectable Bcl6 protein (Marshall *et al.*, 2011). Moreover, analysis of *Bcl6* transcript abundance using MyGeneset (Immunological Genome Project (Heng *et al.*, 2008), revealed that peripheral non-GC B-cells can express between 10% to 40% the level of *Bcl6* compared to GC B-cells. S1PR2 is expressed in non-hematopoietic (Price *et al.*, 2015; Petti *et al.*, 2020) and hematopoietic lineages (Green *et al.*, 2011; Shinnakasu *et al.*, 2016), with analysis from MyGeneset demonstrating that within hematopoietic cells *S1pr2* is highly upregulated in GC B-cells but is also expressed at moderate levels in subsets of granulocytes, macrophages, NK and stromal cells. Amongst peripheral B-cells, *S1pr2* is highly specific to GC B-cells and signalling of S1P through S1PR2 confines GC B-cells to the follicle centre (Green *et al.*, 2011). By using the *S1pr2*^{Venus} reporter mouse Moriyama and colleagues demonstrated that S1PR2 is also crucial for localisation, retention, and full expression profile of Tfh cells which are necessary to support the GC reaction (Moriyama *et al.*, 2014). These fluorescent reporter proteins are expressed under endogenous promoter control and are thus transient, only providing a snapshot of cells actively expressing *Bcl6* or *S1pr2*. Tracking or "fate mapping" GC experienced B-cells is made possible by transgenic mice that express Cre recombinase under the control of a GC-specific gene which are crossed with a suitable Cre inducible constitutive fluorescent protein reporter strain. The Cγ1-Cre transgenic mouse is such an example which, when bred to a Cre inducible constitutive EYFP reporter, labelled IgG1 isotype switched B-cells and was validated in GC responses (Casola *et al.*, 2006). Subsequently, Shinnakasu and colleagues developed a model with a tamoxifen inducible Cre recombinase (ERT2Cre) controlled by the *S1pr2* promoter and enhancer elements by random integration of a modified BAC (Shinnakasu *et al.*, 2016). When *S1pr2*^{ERT2Cre} mice were bred to the Cre-

inducible *Rosa26* controlled tdTomato reporter mouse (*Rosa26*^{LSLtdTomato}) (Madisen *et al.*, 2010), the resultant model enabled fate-mapping of all cells which were expressing *S1pr2* at the time of tamoxifen administration, and has provided insights into MBC (Shinnakasu *et al.*, 2016) and PC (Ise *et al.*, 2018) differentiation from the GC. Affinity maturation and GC dynamics have been visualised through the use of *Aicda*$^{ERT2Cre/wt}$.*Rosa26*$^{Confetti/Confetti}$ crosses that stochastically and permanently fluorescently labelled cells which expressed AID after tamoxifen induction (Tas *et al.*, 2016). Further, Zhang and colleagues used spleen sections from immunised *Aicda*$^{ERT2Cre/wt}$.*Rosa26*$^{Confetti/Confetti}$ and *Aicda*^{ERT2Cre}.*Rosa26*^{mTmG} mice, the latter intended to label only GC B-cells as plasma membrane localised EGFP (mG) switched, to study GCmat PBs by immunohistology in the GTI (Zhang *et al.*, 2018).

1.8 Near infrared (NIR) fluorescent proteins for *in vivo* studies.

Red and far-red fluorescent proteins (FPs), such as tdTomato (Campbell *et al.*, 2002) or mKate2 (Shcherbo *et al.*, 2009) have been used for various *in vivo* imaging applications and in transgenic animal reporter models (Winnard, Kluth and Raman, 2006; Madisen *et al.*, 2010; Vuletic *et al.*, 2015). Near infrared (NIR) wavelengths (λ) have improved tissue penetration compared to visible light, are minimally absorbed by haemoglobin and melanin, possess reduced auto fluorescence and decreased scattering by lipid-containing cell structures and therefore allow enhanced intravital imaging of live mammals and deep optical imaging of mammalian tissue samples (Weissleder, 2001). This makes FPs with excitation/emission spectra within the NIR 'optical window' of λ = 650 nm to 900 nm, valuable reporter tools for *in vivo* and *ex vivo* imaging applications.

Attempts to modify GFP-like FPs into suitable far-red reporters useful for *in vivo* mammalian studies have yielded numerous fluorescent proteins, including: E2-Crimson (Strack *et al.*, 2009), TagRFP657 (Morozova *et al.*, 2010), eqFP650 and eqFP670 (Shcherbo *et al.*, 2010). Of these, E2-Crimson and TagRFP657 possess the most red-shifted excitation maxima (Ex_{max}) at 611 nm but this is still suboptimal for deep *in vivo* imaging as it is outside the NIR optical window (Strack *et al.*, 2009; Morozova *et al.*, 2010). Further, the emission maximum (Em_{max}) of E2-Crimson is also outside the NIR optical window at 646 nm (Strack *et al.*, 2009), and both have reported photostability of ≤60 s (Strack *et al.*, 2009; Morozova *et al.*, 2010).

Light in the red/far-red spectrum is absorbed by a family of photosensor receptors, called phytochromes (Sharrock, 2008). These photoreceptors share a conserved core structure comprised of a Per/Arndt/Sim (PAS), cGMP phosphodiesterase/adenyl cyclase/FhlA (GAF) and phytochrome-specific (PHY) domain and require a linear tetrapyrrole chromophore as a co-factor (Wagner *et al.*, 2005). The PAS and GAF domains of these phytochromes are necessary and sufficient to form the chromophore binding domain (Wagner *et al.*, 2005). Bacteriophytochromes (BphP), were selected as the templates for engineering of new NIR FPs because biliverdin IXa (BV), which is incorporated as the chromophore, is an intermediate in mammalian heme catabolism (Rockwell and Lagarias, 2010) and endogenous in mammalian cells.

IFP1.4, derived from *Deinococcus radiodurans*, was the first reported NIR FP used for *in vivo* imaging, but required injection of exogenous BV (Shu *et al.*, 2009). iRFP713 is a dimeric NIR FP derived from *Rhodopseudomonas palustris Rp*BphP2 generated by Filonov and colleagues (Filonov *et al.*, 2011). iRFP713 represented a significant development in the development of

NIR FPs, as it was more red-shifted (iRFP713 Ex_{max}/Em_{max} 690/713nm compared to IFP1.4 Ex_{max}/Em_{max} 684/708 nm), had improved photostability, effective brightness *in vitro* and, critically, displayed fluorescence *in vivo* in mammalian tissue with endogenous concentrations of BV with at least 2-fold greater signal:noise ratio than mKate2, mNeptune, E2-Crimson and TagRFP657 (Filonov *et al.*, 2011). A repertoire of dimeric iRFP variants; iRFP670, iRFP682, iRFP702 and iRFP720, were engineered from *Rp*BphP6 and *Rp*BphP2 templates by rational design, targeted and random mutagenesis methods and enabled NIR multicolour imaging in living mice (Shcherbakova and Verkhusha, 2013). Further modifications guided by the crystal structures of *Rp*BphP3 (Yang *et al.*, 2007) and *Rp*BphP1 (Bellini and Papiz, 2012) have yielded a split dimeric reporter (iSplit713), monomeric iRFPs (miRFPs) and split monomeric derivatives (miSplit670) (Filonov *et al.*, 2011; Shcherbakova *et al.*, 2016; Matlashov *et al.*, 2020). To ensure clarity between monomeric and dimeric iRFPs within this thesis, dimeric iRFP670 will be referred to as diRFP670, dimeric iRFP713 as diRFP713 and so forth, whilst monomeric iRFP670 will be miRFP670. Multiple applications have been reported for iRFPs, including but not limited to: *in vivo* imaging of diRFP713 transgenic mice and rats, bimolecular fluorescence complementation (BiFC), biosensor development, and super-resolution microscopy (Shcherbakova and Verkhusha, 2013; M. T. Tran *et al.*, 2014; Shcherbakova *et al.*, 2016; Chernov *et al.*, 2017; Hock *et al.*, 2017; Richie *et al.*, 2017).

1.9 Transgenic mouse generation; from random integration to exquisite specificity.

The first transgenic mouse was developed by viral transduction of preimplantation embryos (Jaenisch, 1976). This was replaced by pronuclear microinjection (PNI) of small transgene segments which typically comprised the cDNA of interest with appropriate promoter and regulatory elements (Gordon *et al.*, 1980). PNI of BAC, typically >100 Kb, was developed to try to preserve the genomic context (i.e., inclusion of the promoter, enhancer, and regulatory elements) of the inserted transgene in order to try to better reproduce an endogenous expression profile. Engineering of BAC vectors was aided by the advent of recombineering (Murphy, 1998; Zhang *et al.*, 1998; Muyrers *et al.*, 1999). Transgenic mice made via PNI are limited by the random integration of the transgene which can disrupt endogenous gene expression at the integration site and lack of control of the copy number inserted per genome.

Successful *in vitro* culture of murine embryonic stem cells (ESCs) combined with evidence that cultured mammalian cells could mediate homologous recombination between exogenous DNA and the genome (reviewed (Bouabe and Okkenhaug, 2013)) enabled a plethora of transgenic mouse lines to be generated with precise genetic modifications. One locus that has been repeatedly targeted is the safe harbour locus, *Rosa26* (Friedrich and Soriano, 1991). A huge variety of transgenic mice have been generated by targeting to this locus, as there are currently >900 transgenic mouse line listed on the Mouse Genome Informatics (MGI) database annotated with *Rosa26* 'targeted allele' (URL: http://www.informatics.jax.org; accessed 05-Feb-21).

Knock-in gene targeting to loci of interest often has the goal of placing the inserted gene under the endogenous control of a specific gene. There are a variety of strategies available to achieve

this goal including insertion of the coding sequence to the endogenous start codon (ATG-fusion), use of self-cleaving 2A peptides to resolve two conjoined proteins post-translationally or use of an internal ribosome entry site (IRES) sequence to produce a bicistronic mRNA. IRES sequences and 2A peptides can be combined with a splice site acceptor if the incoming gene is targeted to an intronic region. When performing knock-in gene targeting (as well as other types of targeting e.g., knock-out) consideration must be given to whether the targeted locus exhibits haploinsufficiency, and/or the extent of the resultant phenotype (if known) in heterozygous or homozygous animals. All genetically modified mouse models require detailed characterisation. Traditional knock-in replacement targeting vectors (TVs) are comprised of a minimum of four segments; (i) a 5' homology arm (HA), (ii) DNA sequence of interest, (iii) an antibiotic selection cassette for positive selection flanked by site-specific recombination sites for later excision, for example, the LoxP/Cre or FRT/Flp systems, and (iv) a 3' HA. Inclusion of a negative selection cassette, such as Herpes Simplex Virus thymidine kinase (HSV-tk) or diphtheria toxin A fragment, can be included as a fifth segment in TV construction, cloned into the TV backbone outside of the HAs. For HSV-tk, ESC selection with ganciclovir results in toxicity to only those ESC clones with unwanted genomic integrations (Mansour, Thomas and Capecchi, 1988). ESC negative selection by diphtheria toxin A fragment does not require exogenous inducer, as the presence and expression of the cassette very efficiently inhibits protein synthesis and kills the ESCs (Yagi *et al.*, 1990).

Homologous recombination events are rare, occurring at a frequency of 10^{-3} to 10^{-4} relative to non-homologous recombination (Jasin and Berg, 1988). However, methods exist to improve the frequency of homologous recombination using the TV as an exogenous repair template. Such techniques include increasing HA length (Hasty, Rivera-Pérez and Bradley, 1991; Deng

and Capecchi, 1992), ensuring that HAs are isogenic to the ESC being used for the gene targeting, i.e., the HAs are cloned from genomic DNA of the mouse ESCs that will be targeted (Deng and Capecchi, 1992; Te Riele, Maandag and Berns, 1992), and linearising the TV prior to electroporation (Thomas, Folger and Capecchi, 1986).

A series of genome editing studies which began in *Saccharomyces cerevisiae* (Rudin, Sugarman and Haber, 1989; Plessis *et al.*, 1992), resulted in the use of mitochondrial endonuclease I-SceI from *S. cerevisiae* to edit the mouse genome (Rouet, Smih and Jasin, 1994; Choulika *et al.*, 1995). These groups found that I-SceI induced double-stranded breaks (DSB) increased the frequency of homologous recombination events that used an exogenous repair template and improved gene targeting efficiency (Rouet, Smih and Jasin, 1994; Choulika *et al.*, 1995). Further, the potential for designer nucleases was demonstrated by hybrid nucleases comprised of nonspecific DNA cleavage domains with DNA sequence specific zinc finger DNA binding domains and their use in Xenopus and Drosophila (Bibikova *et al.*, 2001, 2002). Following this, three nuclease systems which rely on protein-DNA interactions to guide nuclease activity to the desired DNA sequence have been developed to introduce DSB for genome engineering: meganucleases (Smith *et al.*, 2006), zinc finger nucleases (Urnov *et al.*, 2005; Miller *et al.*, 2007) and transcription activator-like effector nucleases, TALENs (Boch *et al.*, 2009; Moscou and Bogdanove, 2009; Christian *et al.*, 2010; Miller *et al.*, 2011). All three systems have limitations (Hsu, Lander and Zhang, 2014). However, the advent of the clustered regularly interspaced short palindromic repeats (CRISPR)/Cas9 system (Cong *et al.*, 2013; Mali *et al.*, 2013), has recently come to dominate the field. Originating from the prokaryotic adaptive immune system, the CRISPR/Cas9 system involves an endonuclease, a guide RNA (gRNA) and a protospacer adjacent motif (PAM). The gRNA is comprised of a scaffold and a 20-mer

nucleotide sequence that base pairs to the target DNA sequence (Jinek *et al.*, 2012). The PAM is located in the target genome immediately downstream (3') to the gRNA binding site and directs Cas9 to induce DSBs. Derivatives of the CRISPR/Cas9 system have been described which improve specific characteristics, for example, enhanced fidelity whilst maintaining editing efficiency (Casini *et al.*, 2018) and increasing accessible genomic targets by expanding PAM compatibility (Hu *et al.*, 2018).

The CRISPR/Cas9 system has been codon optimised for mammalian use (Mali *et al.*, 2013). Wang and colleagues reported that five genes could undergo efficient simultaneous editing in mouse ESCs and that microinjection of Cas9 mRNA, appropriate single gRNAs (sgRNAs) and small exogenous template oligos directly into mouse zygotes could generate correctly mutated mouse strains (Wang *et al.*, 2013). Soon after, Li and colleagues demonstrated the potential for CRISPR/Cas9 mediated enhanced ESC targeted knock-in efficiency for larger exogenous sequences by direct comparison to traditional homologous recombination targeting (Li *et al.*, 2014). They used a traditional TV which included 1 Kb and 4 Kb HAs, a neomycin resistance (neo^R) cassette and a C-terminal epitope fusion tag for *Mef2c*. Traditional positive G418 selection alone was compared to fluorescence associated cell sorting (FACS) of GFP^+ ESC clones after co-transfection with Cas9-GFP plasmid, appropriate sgRNA and TV, with no G418 selection. Genotype screening revealed enrichment in the CRISPR/Cas9 arm, as 19.6% (9/46) of ESCs were correctly targeted, whereas traditional ESC positive selection yielded only 4.2% (8/192) (Li *et al.*, 2014). The authors also demonstrated that CRISPR/Cas9 enrichment could substantially reduce the HA size requirement of the TV, as they successfully inserted a 720 bp GFP tag with only 100 bp of total homology in 4.3% (2/46) of ESC clones from the Cas9-GFP FACS enrichment regimen (Li *et al.*, 2014). Further, Zhang and colleagues describe efficient

CRISPR/Cas9 mediated mouse ESC knock-in of a larger DNA segments, namely a LacZ and neo^R cassette, using HAs both <800 bp in length (Zhang *et al.*, 2015). Recently, electroporation of zygotes with Cas9-gRNA ribonucleoprotein (CRISPR-EZ) has been reported to yield high efficiency for indel and point mutations and small insertions (Modzelewski *et al.*, 2018).

1.10 Methods for monoclonal antibody production.

Monoclonal antibodies (mAbs) can be produced by a variety of methodologies including permanent or transient immortalisation, high-throughput phage display, UCB Selected Lymphocyte Antibody Method (Babcook *et al.*, 1996; Tickle *et al.*, 2009) and ribosome display.

Hybridoma generation was the first methodology developed for production of mAb (Köhler and Milstein, 1975). Immunisation of a mammalian species with Ag of interest is followed by fusion of lymphocytes from secondary lymphoid tissue, such as spleen or LN, with polyethylene glycol to immortalised myeloma cells. The fusion partner cells are sensitive to hypoxanthine-aminopterin-thymidine (HAT) medium due to lack of the hypoxanthine-guanine phosphoribosyltransferase (HPRT) gene. HAT media selects only for fused hybridomas, which are HAT resistant due to the intact HPRT gene provided by the lymphocyte, and these undergo primary screening for Ag-specificity. Common primary screens involve enzyme-linked immunosorbent assays (ELISA), or FACS but these techniques are limited by epitope preservation and throughput capabilities, respectively. However, high-throughput cell-based image cytometer technologies are being developed which could also screen difficult to handle hydrophobic membrane proteins (Zhang *et al.*, 2017). Positive clones are selected, expanded and subjected to further downstream screening.

UCB Selected Lymphocyte Antibody Method does not fuse isolated Ag-specific B-cells to immortalised myeloma as the cell culture required for fusion and hybridoma cell line maintenance are not amenable to automation. Instead, B-cells are isolated from spleen, peripheral blood, LNs and/or BM and are transiently cultured *in vitro* for 5-7 days before automated primary screening and consolidation of primary hits onto master plates for freezing. Following secondary screens, B-cells are incubated with Ag on microscope slides and Ag-specific B-cells are isolated by a micromanipulator for amplification of variable heavy and light chains for sequencing (Babcook *et al.*, 1996; Tickle *et al.*, 2009).

Antibody phage display technology is a high-throughput screening system derived from phage display technology where protein of interest was fused to gene III (pIII) minor capsid protein of filamentous phage (Smith, 1985). An antibody library is constructed by amplifying the V_H and V_L chains of cDNA prepared from high-quality RNA and cloned into a phage display vector engineered to express the V_H and V_L as a single chain Fv (scFv) fused to pIII of M13 bacteriophage. Multiple rounds of panning, which involves screening (for example by ELISA), selection and propagation for Ag-specific bacteriophage, reduces the pool size of select Ag-binders, until a manageable panel of select binders remain which can be subjected to functional assays and further modification of the sequence encoding the scFv.

Despite the relative ease of genetic engineering and high-throughput nature of antibody phage display, parallel mAb production by hybridoma generation and phage display can be a useful strategy as mAbs that bind distinct epitopes and possess different mechanisms of actions can be identified (Rossant *et al.*, 2014).

Hybridoma generation and UCB Selected Lymphocyte Antibody Method both involve screening of large numbers of clones/isolated B-cells; which can exceed $1x10^9$ B-cells in a single antibody discovery campaign by the UCB method (Tickle *et al.*, 2009). Tools which can enrich for affinity matured clones would represent a significant advancement in mAb production.

1.11 General aims of MUTCHAP.

Long-lived affinity matured PCs are currently believed to be the key component of long lasting high-affinity antibody responses producing sterile immunity. Understanding the signals and mechanisms which underpin differentiation of GC B-cells into the precursors of GCmat PCs is an area of intense scrutiny; advancements here could have implications for vaccine development and/or efficacy. Further, there are currently no known markers to distinguish GCmat and EF PCs. Unique GCmat PC marker identification and validation could have translation application to streamline high quality mAb production by enrichment for affinity matured PCs prior to permanent or transient B-cell immortalisation.

Two linked, but distinct, strategies are described here that address these aims. Both utilise the inverse expression profiles of the GC B-cell specific gene, *S1pr2,* and the PC specific gene, *Prdm1,* to fluorescently label GCmat PCs.

Chapter 3 details the development of a novel fluorescent reporter model by breeding three existing validated transgenic mice. This new model is used to investigate and characterise the kinetics of GCmat PC formation in the primary immune response. Preliminary data from a hybridoma enrichment protocol using GC fate map mice to produce mAb warrants further investigation.

Chapter 4 outlines the generation and characterisation of a novel NIR split fluorescent reporter. It describes how CRISPR/Cas9 enhanced targeting was used to insert each component of this novel split reporter under the control of the endogenous promoters of *S1pr2* and *Prdm1* in

mouse ESCs. Finally, it details the progression made towards germline transmission of each targeted allele.

Chapter 2. Methods

2.1 Construction of fluorescent protein expression plasmids.

The rationale used to separate dimeric iRFP670 (diRFP670) into split-diRFP670 is detailed in Results Section 4.2.1.

Seamless cloning (Gibson Assembly; NEB E5510S) was used to construct: psplitd670PAS, psplitd670PAS-E, pm-splitd670PAS-E, psplitd670GAF, pK-splitd670GAF, pm-iSplit713PAS-E, pK-iSplit713GAF$_m$ and pm-EGFP from fluorescent protein sequences ordered as synthetic gBlocks (IDT) and pcDNA3.1 (Invitrogen) vector backbone. To construct plasma membrane targeted parental diRFP670 plasmid (pm-diRFP670), pm-splitd670PAS-E was PCR amplified excluding the E coil prior to seamless cloning with split-diRFP670 GAF amplified from pK-splitd670GAF to lack the sequence for the K coil and 4 residue overlap. Q5 site-directed mutagenesis (NEB; E0554S) was used to introduce FLAG and V5 epitope tag sequences into pm-splitd670PAS-E and pK-splitd670GAF plasmids, respectively, which generated pm-F-diSplit670PAS-E and pK-diSplit670GAF-V. Similarly, mutagenic PCR primers and Q5 site-directed mutagenesis were used to insert an E226Y amino acid substitution (residues numbered according to the original unmodified diRFP670 protein sequence) into pK-diSplit670GAF-V to generate pK-diSplit670GAF-V(E226Y). The details of each plasmid and the features contained in the translated product can be found in Table 2.1.

Plasmid name	Protein feature			Name of translated product	Encodes part of or entire fluorescent protein
	GGS-Coil-GGS	Plasma membrane tag	Epitope tag		
psplitd670PAS	-	-	-	split-diRFP670 PAS	split-diRFP670
psplitd670PAS-E	E	-	-	split-diRFP670 PAS-E	split-diRFP670 E/K
pm-splitd670PAS-E	E	Yes (GAP-43)	-	mem-split-diRFP670 PAS-E	mem-split-diRFP670
pm-F-diSplit670PAS-E	E	Yes (GAP-43)	FLAG	mem-FLAG-diSplit670 PAS-E	diSplit670
psplitd670GAF	-	-	-	split-diRFP670 GAF	split-diRFP670
pK-splitd670GAF	K	-	-	K-split-diRFP670 GAF	split-diRFP670 E/K mem-split-diRFP670
pK-diSplit670GAF-V	K	-	V5	K-diSplit670 GAF-V5	diSplit670
pK-diSplit670GAF-V(E226Y)	K	-	V5	K-diSplit670 GAF-V5(E226Y)	diSplit670 (E226Y)
pm-diRFP670	-	Yes (GAP-43)	-	mem-diRFP670	diRFP670
pm-iSplit713PAS-E	E	Yes (GAP-43)	-	mem-iSplit713 PAS-E	iSplit713
pK-iSplit713GAF$_m$	K	-	-	K-iSplit713 GAF$_m$	iSplit713
pm-EGFP	-	Yes (MARCKS)	-	mem-EGFP	EGFP

Table 2.1 **iRFP and EGFP plasmids.** GGS is glycine-glycine-serine flexible linker. E and K, are complementary coils comprised of pentameric repeats of a heptad sequence (De Crescenzo *et al.*, 2003). Plasma membrane tag GAP-43 is a *Mus musculus* codon-optimised 20-mer plasma-membrane targeting sequence from the GAP-43 protein (Richie *et al.*, 2017) and MARCKS is the plasma membrane targeting sequence used in the mTmG mouse (Muzumdar *et al.*, 2007). iSplit713 PAS and GAF$_m$ sequences are from Filonov and colleagues (Filonov and Verkhusha, 2013).

Highly competent *E.coli* (NEB C2987) were transformed according to the manufacturer's standard protocol and plated on 100 µg/mL ampicillin 2xTY agar selection plates which contained additional glucose. After overnight 37 °C incubation, individual isolates were picked and cultured in 200 µL of 2xTY media in a 96-well plate shaking at 190 RPM at 37 °C for 2 h. A colony PCR screen using 2x ReddyMix (Thermo Fischer Scientific; AB0575DCLDB) for correct 5' and 3' junction amplicons was set up using 1 µL of neat culture as template. Isolates with expected junction amplicons were prepared by miniprep (Qiagen; 27106) or Midiprep Plus (Qiagen; 12943) and sequenced.

2.2 Cell culture and transfection of cell lines (except mouse ESCs).

For media compositions please see Table 2.2. All cell culture media was 0.22 µm sterile filtered. HEK293T and Ad293 cells were cultured in R10 media. NIH-3T3 cells were cultured in D10 media. NS0 plasmacytoma cells were used as fusion partners for hybridoma generation and were cultured in R15 media prior to fusion. Subsequent hybridomas were cultured in hybridoma selection media. Cell lines were maintained at 37 °C in a humidified 5% CO_2 atmosphere.

Transfections were performed as described in the experiment using either Lipofectamine 2000 (Invitrogen; 11668027) or Lipofectamine 3000 (Invitrogen; L3000008) per the manufacturer's instructions using Opti-MEM reduced serum media (Gibco; 31985047).

Media Name	Composition
R10	RPMI-1640; (+) L-glutamine (Gibco; 21875034) • 10% v/v FBS • 100 U/mL penicillin and 100 µg/mL streptomycin (1X Pen/Strep)
D10	DMEM; (+) L-glutamine, (+) sodium pyruvate, (+) high glucose (Gibco; 41966029) • 10% v/v FBS • 1X Pen/Strep
R0	RPMI-1640; (+) L-glutamine (Gibco; 21875034) • 100 U/mL penicillin
R15	R0 media with: • 15% v/v FBS • Gentamycin at 20 µg/mL • Neomycin at 20 µg/mL • Chloramphenicol at 5 µg/mL
R20	R0 media with: • 20% v/v FBS
Hybridoma HAT selection media	R15 media with: • Hypoxanthine at 200 µM • Methotrexate at 1 µM (methotrexate is a closely related antifolate to historically used aminopterin) • Thymidine at 200 µM

Table 2.2 **Media composition for tissue culture**.

2.3 Flow cytometric assays with iRFPs.

Transfected HEK293T cell viability was assessed either by exclusion of 3 µM DAPI added immediately prior to acquisition or by staining with near IR fixable viability dye (Invitrogen; L10119) at 1:1000 in PBS.

Cells were formaldehyde fixed using Cytofix/Cytoperm buffer per the manufacturer's instructions (BD Biosciences; 554714). Sample fluorescence was measured immediately or after 24 h at 4 °C.

Intracellular complex stability was assessed by culture with either cycloheximide (CHX) (Sigma; C4859) at 20 µg/mL final concentration or DMSO control at 0.02% v/v final concentration.

For intracellular detection of epitope tags, CytoFix/CytoPerm buffer was used to fix and permeabilise cells before primary and secondary antibody staining steps. Please see Table 2.3 for antibody details.

Target	Host (Isotype)	Clone	Conjugate	Dilution	Supplier	Cat #
FLAG tag	Rabbit (IgG)	EPR20018-251	Purified	1:630	Abcam	ab205606
V5 tag	Rabbit (IgG)	1036H	Purified	1:500	R&D Systems	MAB8926
Isotype control	Rabbit (IgG)	Polyclonal	Purified	1:1667	R&D Systems	AB-105-C
Rabbit IgG	Goat	Polyclonal	FITC	1:500	BD	554020

Table 2.3 **Antibodies used for intracellular detection of epitope tags by flow cytometry.**

Data was acquired using either a BD LSRFortessa or LSRFortessa X-20 and FACSDiva v8 software. Near IR fluorescent proteins and near IR viability stain were excited using the 633 nm laser and detected using 670/14 nm or 670/30 nm (diSplit670/diRFP670), 730/45 nm or 722/44 nm filter sets (iSplit713) and 795/70 nm (near IR viability), EGFP was excited using the 488 nm laser and detected using the 525/50 nm filter set whilst DAPI was excited with the 360 nm laser and detected using a 450/50 nm filter set. Data analysis was performed in FlowJo v10.1 (BD Biosciences).

Effective brightness of diSplit670 or diRFP670 was quantified by dividing the geometric mean NIR signal intensity in NIR FP^+ cells by the co-transfected EGFP geometric mean signal intensity within the same population. To compare the brightness of diSplit670 and iSplit713, their effective brightness values were normalised by their excitation efficiency at 633nm and by emission filter set capture efficiency.

2.4 Cell preparation and mounting for microscopy.

Transiently transfected HEK293T cells were resuspended in 0.22 µm filtered 10% w/v bovine serum albumin (BSA) in PBS. Cytospin clips were prepared with Superfrost Plus microscope slides (Thermo; J1800AMNZ). A 100 µL aliquot of cells ($4x10^4$ cells) were attached to the slide by centrifugation at 400 RPM for 5 minutes at room temperature with low acceleration on a Cytospin 2 centrifuge (Shandon). Slides were air dried before fixation in 1% v/v formaldehyde (VWR; 11699455) in PBS at 4 °C in the dark for 15 minutes. Slides were DAPI counterstained (100 ng/mL in PBS) for 30 s before a #1 glass cover slip was mounted with

ProLong Diamond Antifade Mountant (Invitrogen; P36970) and dried overnight at room temperature in the dark.

2.5 Microscopy.

Confocal microscopy for cellular localisation.

Transiently transfected HEK293T cells were attached to slides as described in Section 2.4 and imaged using a Leica LSM880 Axio Observer with Airyscan Fast confocal microscope and a C-Apochromat 40x /1.2 W Korr FCS M27 objective. A beam splitter and appropriate emission filters were used to detect EGFP (488 nm beam and 498-560 nm emission filter) and diSplit670 (633 nm beam and 618-735 nm emission filter), whilst a 405 nm laser with 415-499 nm emission filter was used to detect DAPI. Dr Yang Zhang kindly imaged the slides, as COVID-19 restrictions prevented training to operate the confocal microscope. Images were analysed using Zen 3.2 Light Edition (Carl Zeiss Microscopy).

Epifluorescence microscopy for photo-bleaching and photostability assay.

Transiently transfected HEK293T cells were attached to slides as described in Section 2.4 and were imaged using a Leica DM6000 epifluorescence microscope with LASX software, a Y5 cube for NIR FP (Ex: 590-650 nm, Em: 662-738 nm), an A4 cube for DAPI (Ex: 340-380 nm, Em: 450-490 nm), and a L5 cube for EGFP (Ex: 460-500 nm, Em: 512-542 nm). Co-transfection with mem-EGFP was used to focus on cells with minimal bleaching of NIR FP before assay start. In total, 100 images cycles were captured 15 s apart for the 25-minute time-lapse, with an image taken in each of the three channels per cycle. Between image capture, the field of view was illuminated with the Y5 cube on full intensity to photo-bleach the NIR FPs. In ImageJ (Schneider, Rasband and Eliceiri, 2012), regions of interest (ROIs) were selected

around NIR FP expressing cells (n ≥ 35) and on cell-free background (n ≥ 10). Mean fluorescence values were extracted from each ROI over the time-lapse. At each time-point, background corrected fluorescence of each NIR FP ROI was normalised to its own maximum fluorescence intensity at cycle 1, t=0 s. Non-linear regression analysis of normalised fluorescence data was performed using GraphPad Prism v9.

2.6 Imaging in mice.

HEK293T cells were co-transfected with either diSplit670 or mem-diRFP670 and mem-EGFP at a 9:1 ratio of NIR FP:EGFP plasmids. After 48 h, cells were prepared in 100 µL of RMPI-1640 without phenol red (Gibco; 11835-063). The interscapular region of BALB/c cadavers were shaved before subcutaneous injection of transfected cells. Fluorescence measurements and images were acquired before and after cell injection with 640/20 nm excitation and 700/20 nm emission filters for NIR FPs and with 465/20 nm excitation and 520/20 nm emission filters for EGFP using an IVIS Spectrum and Living Image Software v4.2 (Perkin Elmer). Dr Juan Carlos Yam-Puc kindly performed the IVIS imaging as due to COVID-19 restrictions, only limited access was provided into the Birmingham Biomedical Services Unit (animal house). To remove background autofluorescence, new image sequences for each acquisition channel were created from images acquired before and after cell injection. Living Image Software 'Image Math' function was applied to this new sequence to generate an autofluorescence subtracted image using the function A-B*k and a ROI selected on the non-injected image that corresponded to a region that was not the interscapular site of injection. The parameters 'Colour Score Limits for A & B' and 'Results/Colour Scales Limits' were set to Auto. ROIs corresponding to cell injection sites were drawn on the autofluorescence corrected images and fluorescence measurements were extracted from those ROIs. The total radiant efficiency [p/s]

/ [µW/cm²] of diSplit670 or mem-diRFP670 was normalised for transfection efficiency by the corresponding EGFP signal for each ROI. Fluorescence intensity of diSplit670 compared to mem-diRFP670 was reported as a percentage of mem-diRFP670.

2.7 Preparation of genomic DNA.

Genomic DNA (gDNA) was extracted from cells and prepared for PCR analyses by overnight incubation of the cells at 55 °C within the tissue culture well or plate, or as a cell pellet, with gDNA lysis buffer comprised of; proteinase K at final concentration 0.1 mg/mL diluted in Viagen Direct PCR(cell) Lysis reagent (Viagen, 302-C).

2.8 Pre-validation of CRISPR/Cas9 single guide RNAs in NIH-3T3 cell line.

CRISPR/Cas9 single guide RNA (sgRNA) sequences were selected as consistent high scorers across multiple design tools and were assessed for off-target interactions using Cas-OFFinder (Bae, Park and Kim, 2014) (Table 2.4). Mutagenic substitution primers were designed using NEBaseChanger v1.2.7 (URL: http://nebasechanger.neb.com/) to enable cloning of the sgRNA sequence into the sgRNA scaffold of pD1301-AD vector (Atum), which also contains the constitutively high expression CMV promoter controlled Cas9-T2A-DasherGFP cassette. sgRNA sequences were introduced by Q5 site-directed mutagenesis and transformed 5α *E. coli* (NEB C2987) were selected on 2xTY agar impregnated with 50 µg/mL kanamycin and glucose. Kanamycin resistant isolates were cultured and used as template for colony PCR screen of the sgRNA scaffold region. PCR amplicons were sequenced, and correct isolates were prepared by miniprep.

sgRNA design algorithm	**Reference**
GPP sgRNA Designer	(Doench *et al.*, 2016)
ChopChop	(Labun *et al.*, 2016)
Cas-Designer	(Bae, Park and Kim, 2014; Park, Bae and Kim, 2015)
Cas-OFFinder	(Bae, Park and Kim, 2014)
CRISPR.mit.edu	Tool accessed prior to shut down

Table 2.4 **Online tools accessed to design *S1pr2* and *Prdm1* specific CRISPR/Cas9 sgRNA sequences.**

Mouse NIH-3T3 cells were seeded in 24-well plates at $4x10^4$ cells/well 24 h before transfection with Lipofectamine 3000. Cells were transfected with either pD1301-AD containing the sgRNA of interest or pmaxGFP Positive Control Vector (Lonza). After 30 h, GFP^+ cells were bulk sorted by fluorescence-associated cell sorting (FACS) using a FACSAria II (BD) into D10 media in a 96-well plate and expanded for 72 h. gDNA was prepared and used as template for the T7 endonuclease E1 assay (described in Section 2.9). FACS was kindly performed by Dr Guglielmo Rosignoli or Owen Wyatt (AstraZeneca).

2.9 T7 Endonuclease 1 (T7E1) assay.

Target genomic regions were PCR amplified in a 40 µL Bio-X-Act Short Mix reaction (Bioline) with 2% v/v DMSO and primers at 0.5 µM final concentration. The desired amplicons were gel purified (Table 2.5). Annealing reactions were set up, hybridised and subject to the T7E1 assay (Table 2.6). Reactions were ended by addition of 1.5 µL of 0.25 M EDTA. Samples were analysed on 1% w/v agarose gels and semi-quantitative measurements of CRISPR/Cas9 sgRNA activity were made by band intensity analysis using ImageJ software (described in Section 2.10).

Genomic target	**Strand**	**Sequence (5' → 3')**	**Expected amplicon (bp)**
S1pr2 exon 2 3'UTR	Sense Anti-sense	GATGTTGCTGGTCCTCAGAC GAAGCTGTGGATTTAGGCCTC	925
Prdm1 intron6-7	Sense Anti-sense	TGGCTTGAGCACCATGAACAAC CCGTTCTCCACTGTGCACTC	803
Prdm1 exon 8	Sense Anti-sense	GTGTATCCAGTAGGAGTGCAGG GCTCAACACTCTCATGTAAGAGG	1002

Table 2.5 **Primers pairs to amplify genomic regions that contain sgRNA targets.**

Component	**Annealing reaction**		
DNA (ng)	400		
10x NEBuffer 2 (µL)	2		
Nuclease-free dH_20	To 19 µL		
Hybridisation	**Temperature (°C)**	**Ramp Rate (°C / s)**	**Time (minutes)**
Initial denaturation	95	N/A	5
Annealing	95-85 85-25	-2.0 -0.1	
Hold	4		∞
Component	**T7E1 reaction**		
Annealing reaction (µL)	19		
T7 Endonuclease 1 (NEB; M0302S) (µL)	1		
Incubation time (minutes)	15		
Incubation temperature (°C)	37		

Table 2.6 **Protocol for the T7 Endonuclease I (T7E1) assay**.

2.10 Gel/blot intensity analysis.

Protein or DNA band intensity was analysed in a semi-quantitative manner using the Plot Lanes function of ImageJ. Signal intensity was calculated as the area under user defined peaks (Figure 2.1A). Comparative signal intensity was determined as the quotient of experimental band signal intensity to that of the control/comparator band (Figure 2.1B).

Alternatively, where indicated, DNA band intensity was analysed using Gene Tools software (Syngene).

Figure 2.1 **Example of band intensity analysis used to determine semi-quantitative efficacy of CRISPR/Cas9 sgRNAs by the T7E1 assay**. (A) Left, plotted lanes contain the regions of interest (ROIs) on the DNA gel or protein blot. Right, corresponding intensity profiles for each ROI. User defined segments are used to measure areas under the peaks (coloured areas). Inset, quantification of the user defined coloured areas in Plot 1. (B) Semi-quantitative comparative signal intensity analysis (marked as percentage) is calculated as the quotient of area 2 (red; value 843) and area 1 (blue; value 9811), providing an estimated efficacy for *Prdm1* exon 8 3'UTR sgRNA 4. Single peaks in profile plots represent either a single product or multiple indistinguishable products (by size), indicating non-specific (NS) sgRNA did not target CRISPR/Cas9 to this genomic region as there is only a single peak in Plot 2.

2.11 Precipitation and sterilisation of DNA for electroporation.

One volume of linearised or circular plasmid DNA was added to 0.1 volumes of 3 M sodium acetate pH 5.2 and 2.5 volumes of isopropanol. The solution was mixed to precipitate the DNA before centrifugation at 13,000 RPM for 10 minutes at room temperature. The supernatant was discarded, and 1 mL of 70% v/v ethanol was added to the tube before inversion to sterilise the precipitated DNA pellet. The sterile DNA was centrifuged at 13,000 RPM for 5 minutes at room temperature. The ethanol was carefully removed, and allow the pellet to air-dry, before resuspension in sterile PBS. The final steps were performed in a Class II safety cabinet to ensure sterility of the linearised DNA.

2.12 Mouse ESC tissue culture, electroporation and colony picking.

C57BL/6 JM8 A3.N1 ESCs (Pettitt *et al.*, 2009) were either cultured on tissue culture plates coated with 0.1% w/v gelatin or sparsely coated with proliferation inactivated mouse embryonic fibroblasts (MEFs) (Taconic-Artemis), at densities shown in Table 2.7. Gelatin coated plates were used when RNA or protein was to be extracted from ESCs or to minimise and dilute carried over MEF gDNA for PCR assays of targeted ESCs. To render MEFs replication deficient, cells were expanded for two passages in MEFs media (Advanced DMEM, 10% v/v FCS, 1% v/v GlutaMAX) before a 3 h treatment with 10 µg/mL mitomycin C in MEFs media.

Tissue Cultures type	**MEFs/well (cell No.)**
96-well	$1x10^4$
6-well	$2.5x10^5$
10-cm	$1.5x10^6$

Table 2.7 **Quantities of MEFs used to prepare sparsely coated plates for mouse ESC culture**.

JM8 A3.N1 ESCs were cultured in a humidified 37 °C incubator with CO_2 at 7.5% in either non-selection or selection media (Table 2.8), as detailed in the text. The media was changed daily. All centrifugation steps for ESC tissue culture were at 1100 RPM for 5 minutes at room temperature, and cells were harvested by trypsin enzymatic digestion.

Component	**Supplier (and Category #)**	**Final concentration**
DMEM	Gibco	N/A
Glutamax	Gibco (35050-038)	1X
HEPES	Gibco	0.02 M
NEAA	Gibco (11140-035)	1X
β mercaptoethanol	Gibco	0.1 mM
Pansera ES	Pan Biotech (P30-2602)	N/A
LIF (Leukaemia Inhibitory Factor)	EMD Millipore (ESG1107)	1500 Units/mL
(Optional) – for selection media only		
G418	Invitrogen (10131-011)	200 µg/mL
Puromycin	Gibco	1.0-1.75 µg/mL

Table 2.8 **Mouse ESC tissue culture media composition**.

For ESC electroporation, 100 µL of sterile PBS which contained a total of 10 µg of sterile DNA was added to an electroporation cuvette and placed on ice. ESCs were harvested, counted, resuspended at $5x10^6$ cells/mL and 1-2 $x10^7$ ESCs per electroporation were transferred into separate 15 mL Falcon tubes. Cells were centrifuged, resuspended in 650 µL PBS, transferred into pre-cooled electroporation cuvettes which contained the DNA of interest or PBS control, mixed and rested on ice for a further 5 minutes. Electroporations were performed using an exponential protocol at 240 V and 500 µF with a Gene Pulser II (Bio-Rad). After electroporation, cells were rested on ice for 5 minutes before recovery in pre-warmed ESC non-selection media and plating onto a MEF-coated plate. Antibiotic selections were initiated 24 h after electroporation.

To pick ESC colonies the ESC media was replaced with PBS. A 20 µL pipette was used to cut around the colonies and set to aspirate the colony along with PBS. Individual colonies were transferred into separate wells of a 96-well plate which contained trypsin. ESC colonies were dissociated by incubation at 37 °C and mixed to single cell suspension. Single cell ESC suspensions were transferred to a flat-bottom 96-well plate coated with MEFs and cultured.

2.13 Validation of *S1pr2* and *Prdm1* specific CRISPR/Cas9 sgRNAs in JM8 A3.N1 ESCs.

An all-in-one CRISPR/Cas9(Puro) plasmid was used which expressed Cas9 and puromycin from a bicistronic message and possessed a unique MluI restriction site within the sgRNA scaffold where the sgRNA sequence could be inserted. For each sgRNA, a 70 bp oligonucleotide was designed to include the 20-mer sgRNA sequence flanked by 25 bp of homology to all-in-one CRISPR/Cas9(Puro) plasmid. Seamless cloning (HiFi DNA assembly) was used to insert the 70-mer single-stranded oligonucleotide into MluI linearised all-in-one CRISPR/Cas9(Puro). Cloning was confirmed by: (i) restriction digests which demonstrated the removal of unique MluI site, and (ii) sequencing.

To confirm pre-validated sgRNA sequences in JM8 A3.N1 ESCs, *S1pr2* exon 2 3'UTR, *Prdm1* intron6-7 or *Prdm1* exon 8 3'UTR specific all-in-one CRISPR/Cas9(Puro) plasmids were NheI linearised, sterilised and 10 µg of each plasmid electroporated into ESCs before stable puromycin selection. For the positive antibiotic selection control, ESCs were electroporated with 10 µg of KpnI linearised pUC19-CAGG-Puro plasmid (kind gift of AstraZeneca). For the negative antibiotic selection control PBS only was used. For each tested all-in-one

CRISPR/Cas9(Puro) plasmid, ten aliquots of $8.0x10^5$ electroporated ESCs were plated onto MEFs coated 6-well plates. For antibiotic selection controls, two aliquots of $8.0x10^5$ electroporated ESCs were plated. Puromycin selection was tested over a range of concentrations for the all-in-one CRISPR/Cas9(Puro) plasmid (0, 1.0, 1.25, 1.5, 1.75 µg/mL puromycin), whereas the selection controls were tested only at the highest concentration (1.75 µg/mL puromycin). Selection was performed for 7 days until puromycin-resistant ESC colonies were counted. ESCs from the positive selection condition were harvested and frozen to be used as the wild-type (negative) control for an αCas9 Western blot. ESC colonies that received all-in-one CRISPR/Cas9(Puro) plasmids were picked and further expanded for 11 days in puromycin selection media before preparation of gDNA or cell lysate for T7E1 assay or Western blot, respectively.

2.14 Construction of targeting vectors and plasmids to optimise PCR genotype assays for targeted insertions to *S1pr2* and *Prdm1* loci.

Targeting vectors (TVs) were constructed for targeted insertion of mem-FLAG-diSplit670 PAS-E to *S1pr2* exon 2 3'UTR or K-diSplit670 GAF-V5 to *Prdm1* intron6-7 or *Prdm1* exon 8 3'UTR. Construction was achieved by seamless cloning involving PCR amplicons with homology overlaps, single-stranded oligonucleotide bridges and restriction enzyme digests. NEBuilder online tool (URL: https://nebuilder.neb.com/#!/) was used to design the primers to introduce homology overlaps onto the ends of each PCR amplicon necessary for seamless cloning. All seamless cloning assembly and transformation steps described below were conducted using HiFi DNA Assembly mix (NEB) and Stellar chemically competent *E.coli* (Takara) according to the manufacturer's protocol.

S1pr2 exon 2 3'UTR TV iteration 1 (no positive antibiotic selection cassette):

The mem-FLAG-diSplit670 PAS-E sequence and pcDNA3.1 backbone were PCR amplified in separate reactions from pm-F-diSplit670PAS-E. gDNA from WT JM8 A3.N1 ESCs was used to amplify the 1118 bp 5' HA and 967 bp 3' HA from either side of the sgRNA cut site in the 3' UTR of *S1pr2* exon 2. PCR amplified internal ribosome entry site (IRES) sequence was a kind gift of AstraZeneca. These five fragments were assembled by seamless cloning. Transformed bacterial isolates were selected on ampicillin plates, screened by colony PCR and TV assemblies were validated by restriction digests and sequencing. Iteration 1 TV is referred to as *S1pr2* TV(v1) in Figure 2.2A and later text.

Finalised *S1pr2* exon 2 3'UTR TV (includes floxed neo^R selection cassette):

A floxed neo^R cassette was cloned into *S1pr2* TV(v1) immediately 5' to the IRES sequence. Cloning required: (i) *S1pr2* TV(v1) linearised at the unique NotI site at the 5' end of the IRES sequence and treated with shrimp Alkaline Phosphatase (NEB; M0371L) to prevent vector backbone self-ligation; (ii) PCR amplified neo^R cassette (which contained a PGK-gb2 promoter and a single LoxP sequence at the 5' end, kind gift of AstraZeneca); and (iii) a single-stranded synthetic oligonucleotide comprised of a LoxP sequence flanked by homology to the 3' end of the PCR amplified neo^R cassette and IRES end of the NotI linearised TV from (i). These three fragments were assembled by seamless cloning. Transformed bacteria were selected on kanamycin plates; functional eukaryotic/prokaryotic PGK-gb2 promoter confers bacterial kanamycin resistance. Kanamycin-resistant isolates were screened by colony PCR and assemblies were validated by restriction digests and sequencing. The pcDNA3.1 backbone also contains a neo^R cassette and, therefore, to prevent aberrant homologous recombination events in ESCs this unwanted neo^R cassette required removal. Excision was achieved by double digest

using unique XmaI / BstBI restriction sites flanking the vector backbone neo^R cassette. Re-assembly of TV was accomplished by seamless cloning with a single-stranded synthetic oligonucleotide bridge which restored the unique XmaI restriction site. Transformed bacterial isolates were selected on ampicillin plates, screened by colony PCR and TV assemblies were validated by restriction digests and sequencing. The *S1pr2* TV with floxed neo^R cassette is referred to as *S1pr2* TV(final) in Figure 2.2A and later text.

Prdm1 exon 8 3'UTR TV iteration 1 (no positive antibiotic selection cassette):

The K-diSplit670 GAF-V5 sequence and pcDNA3.1 backbone were PCR amplified in separate reactions from pK-diSplit670GAF-V. gDNA from WT JM8 A3.N1 ESCs was used to amplify the 1001 bp 5' HA and 1006 bp 3' HA from either side of the sgRNA cut site in the 3' UTR of *Prdm1* exon 8. PCR amplified IRES sequence (AstraZeneca) was used as described previously. These five fragments were assembled by seamless cloning. Transformed bacterial isolates were selected on ampicillin plates, screened by colony PCR and TV assemblies were validated by restriction digests and sequencing. *Prdm1* exon 8 iteration 1 TV is referred to as *Prdm1* exon 8 TV(v1) in Figure 2.2B and later text.

Finalised *Prdm1* exon 8 3'UTR TV (includes floxed neo^R selection cassette):

A floxed neo^R cassette was cloned into *Prdm1* exon 8 TV(v1) immediately 5' to the IRES sequence as described for *S1pr2* TV(final), except that NotI linearised *Prdm1* exon 8 TV(v1) was used as the template. Excision of the pcDNA3.1 vector backbone neo^R cassette was performed as described for *S1pr2* TV(final) to generate *Prdm1* exon 8 TV(final) (Figure 2.2B and later text).

Prdm1 intron6-7 TV iteration 1 (no positive antibiotic selection cassette):

The K-diSplit670 GAF-V5 sequence and pcDNA3.1 backbone were PCR amplified in separate reactions from pK-diSplit670GAF-V. gDNA from WT JM8 A3.N1 ESCs was used to amplify the 999 bp 5' HA and 894 bp 3' HA from either side of the sgRNA cut site in the 3' UTR of *Prdm1* exon 8. The adenoviral major late transcript splice acceptor (Ad SA) (Friedrich and Soriano, 1991) was synthesised as a gBlock (IDT). PCR amplified IRES sequence was a kind gift of AstraZeneca. These six fragments were assembled by seamless cloning. Transformed bacterial isolates were selected on ampicillin plates, screened by colony PCR and TV assemblies were validated by restriction digests and sequencing. *Prdm1* intron6-7 iteration 1 TV is referred to as *Prdm1* intron6-7 TV(v1) in Figure 2.2C and later text.

Finalised *Prdm1* intron6-7 TV (includes floxed neo^R selection cassette):

A floxed neo^R cassette was cloned into *Prdm1* intron6-7 TV(v1) immediately 5' to the IRES sequence as described for *S1pr2* and *Prdm1* exon 8 TV(final) except that NotI linearised *Prdm1* intron6-7 TV(v1) was used as the template. The *Prdm1* intron6-7 TV(v1) did not possess a unique XmaI restriction site flanking the pcDNA3.1 vector backbone neo^R cassette but had a unique SexAI restriction site. SexA1 is sensitive to methylation by dcm methylase and required *Prdm1* intron6-7 TV(v1) plasmid to be prepared from dcm$^-$ *E.coli*. To achieve this *Prdm1* intron6-7 TV(v1) was transformed into Oneshot INV100 *E.coli* (Invitrogen, #C717103). Double digest with SexAI / BstBI restriction enzymes excised the vector backbone neo^R cassette. Re-assembly of TV was accomplished by seamless cloning with a single-stranded synthetic oligonucleotide bridge which restored the unique BstBI restriction site. Transformed bacterial isolates were selected on ampicillin plates, screened by colony PCR and TV assembly was validated by restriction digests and sequencing to generate *Prdm1* intron6-7 TV(v2) (Figure

2.2C and later text). Following collaborative discussions with Taconic Biosciences the short HAs of *Prdm1* intron6-7 TV(v2) were lengthened to maximise the likelihood of positive outcome from the single gene targeting experiment. First, the length of the 5' HA was extended to 4.0 Kb by seamless cloning with: (i) PCR linearised *Prdm1* intron6-7 TV(v2) and (ii) a PCR amplicon containing a further 3021 bp of 5' homology from the *Prdm1* locus of BAC clone RP23-145G7. Bacterial isolates were screened by colony PCR and TV assembly was validated by restriction digests and sequencing to generate *Prdm1* intron6-7 TV(v3). Finally, the length of the 3' HA was extended to ~2.3 Kb by seamless cloning with: (i) PCR linearised *Prdm1* intron6-7 TV(v3) and (ii) a PCR amplicon containing a further 1465 bp of 3' homology from the *Prdm1* locus of BAC clone RP23-145G7. Bacterial isolates were screened by colony PCR and TV assembly was validated by restriction digests and sequencing. The *Prdm1* intron6-7 TV with floxed neo^R cassette and longer HAs is referred to as *Prdm1* intron6-7 TV(final) in Figure 2.2C and later text.

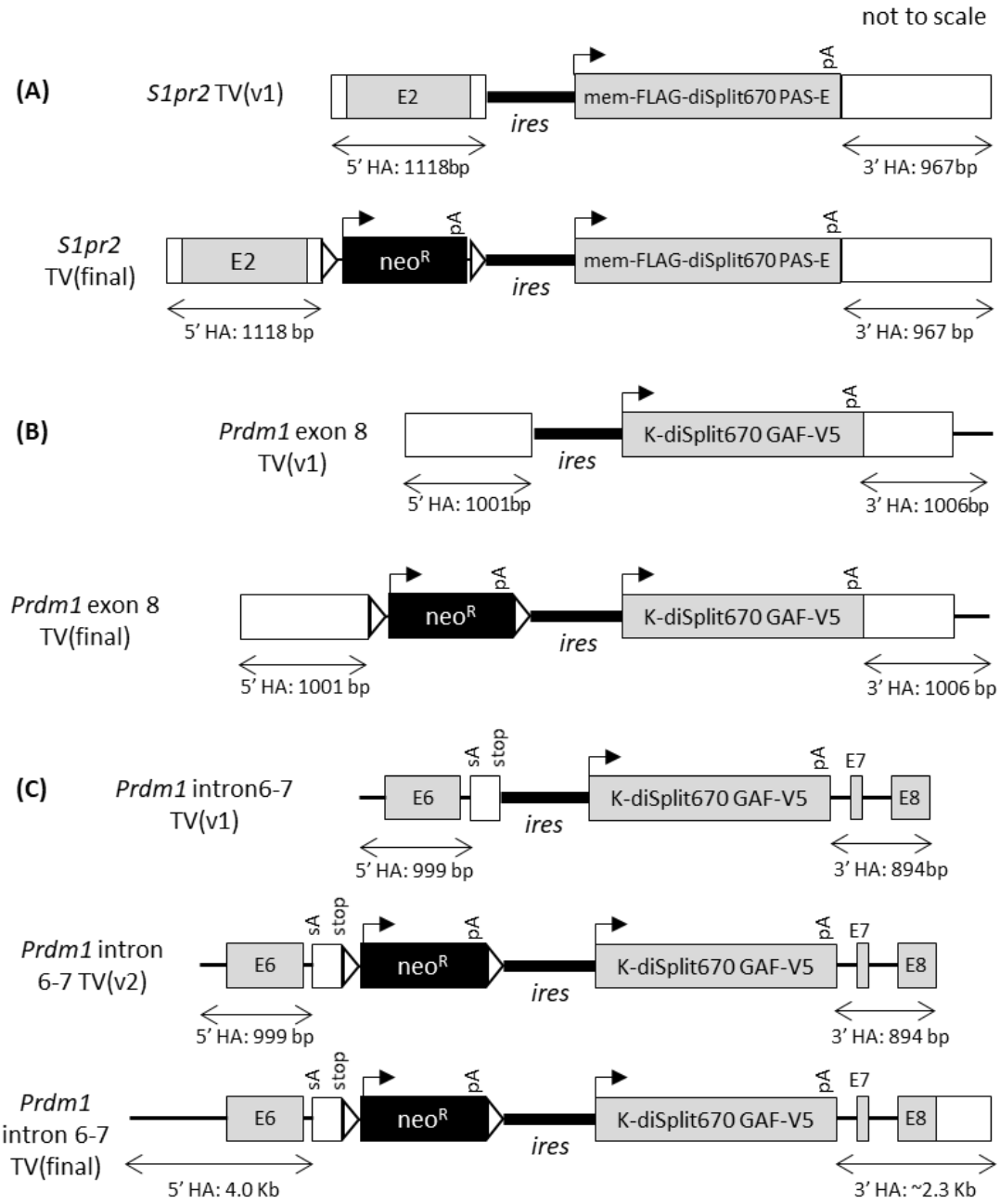

Figure 2.2 **Schematic of targeting vector.** Iterations of targeting vectors as described in Section 2.14 for *S1pr2* (A), *Prdm1* exon 8 (B) and *Prdm1* intron6-7 (C). Genomic introns (thin black lines) and exons as boxes (open for untranslated regions (UTRs), grey shaded with exon number "EX" for protein coding regions), 5' and 3' homology arm (HA, double arrow-headed lines), LoxP sequences (open black triangles), neomycin antibiotic selection cassette (neo^R), internal ribosome entry site (*ires*, thick black line), black filled arrowhead depicts translation from initial methionine and stop indicates STOP codon, bovine growth hormone polyadenylation site (pA), cDNA for transgene (grey box with diSplit670 label).

Plasmids to optimise PCR genotyping assays for *S1pr2* or *Prdm1* targeted knock-in events.

Separate plasmids were generated that mimicked the expected 5' or 3' junctions of targeted genomic loci. These plasmids are referred to as 5'-Expected and 3'-Expected and were constructed for each of the three loci (schematic overview Figure 2.3). These plasmids enable optimisation of genotyping PCR primer sets to be used for screening ESCs for correct targeting events. Seamless cloning assembly described below was followed by transformation into chemically competent *E.coli* and purified plasmids were validated by restriction digest and sequencing.

S1pr2 5'-Expected plasmid was assembled by seamless cloning of: (i) PCR linearised pm-F-diSplit670PAS-E, (ii) an extended 5' HA (1767 bp) amplified from WT JM8 A3.N1 ESC gDNA, and (iii) PCR amplified IRES (AstraZeneca). A floxed neoR cassette was inserted by the same method as described for *S1pr2* TV(final).

S1pr2 3'-Expected plasmid was assembled by seamless cloning of: (i) PCR linearised pm-F-diSplit670PAS-E, and (ii) an extended 3' HA (1615 bp) amplified from WT JM8 A3.N1 ESC gDNA.

5'-Expected plasmids for *Prdm1* exon 8 and *Prdm1* intron6-7 were assembled by seamless cloning of: (i) PCR linearised pK-diSplit670GAF-V, (ii) extended 5' HAs (1918 bp and 1494 bp, respectively) amplified from WT JM8 A3.N1 ESC gDNA, and (iii) PCR amplified IRES (AstraZeneca). A floxed neoR cassette was inserted by the same method as described for *Prdm1* exon 8 or *Prdm1* intron6-7 TV(final).

3’-Expected plasmids for *Prdm1* exon 8 and *Prdm1* intron6-7 were assembled by seamless cloning of: (i) PCR linearised pK-diSplit670GAF-V, and (ii) an extended 3’ HAs (1520 bp and 1394 bp, respectively) amplified from WT JM8 A3.N1 ESC gDNA.

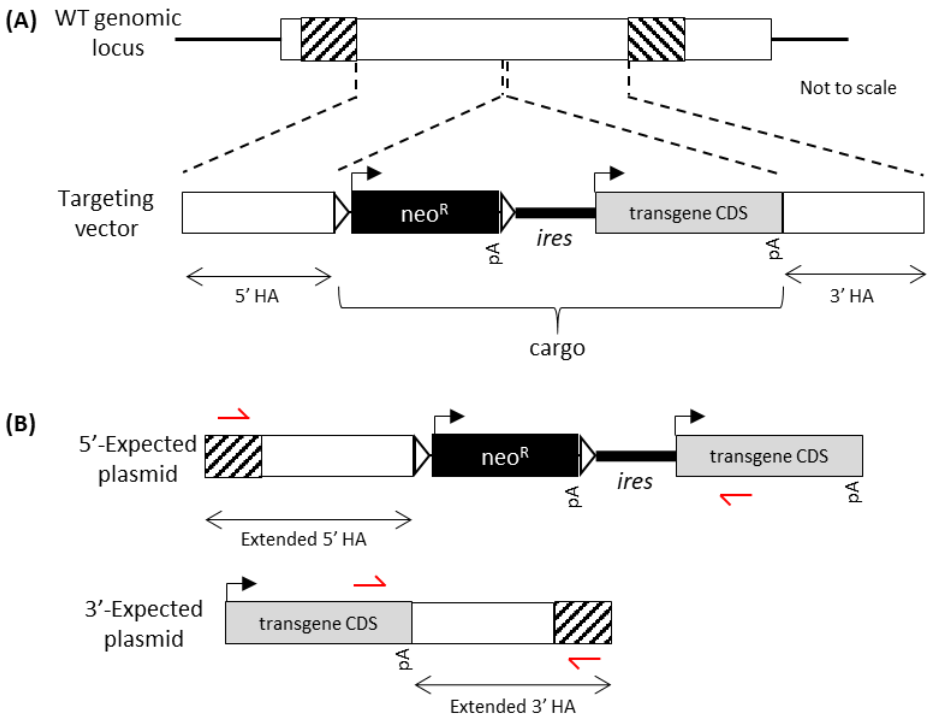

Figure 2.3 **Schematic of standard targeting vector containing antibiotic selection cassette and plasmids which enabled optimisation of PCR genotyping assays.** (A) Top, wild-type (WT) genomic locus with intron (thin black lines) and exon (box) sequences. Dashed lines indicate homology between genomic sequences and targeting vector (TV) homology arms (HAs). Pattern filled boxes represent sequence that is immediately 5’ (left) or 3’ (right) of the HAs included in the TV. Bottom, standard TV including 5’ and 3’ HAs, LoxP sequences (black triangles), neo selection cassette (neo^R), internal ribosome entry site (*ires*, thick black line), polyadenylation site (pA) and cDNA for transgene (transgene CDS). (B) Top, 5’-Expected plasmid contains the TV cargo sequence, 5’ HA and additional 5’ homology to the genomic loci. Bottom, 3’-Expected plasmid contains the TV transgene CDS and 3’HA and additional 3’ homology to the genomic loci. This enables optimisation of PCR genotyping primers (red arrows) able to detect correct targeted knock-in events by amplification of the expected 5’ or 3’ junctions.

2.15 *In vitro* assay to assess functionality of LoxP sequences flanking the neo^R cassette of targeting vectors.

SW106 *E. coli* possess an arabinose inducible Cre recombinase gene (Warming *et al.*, 2005). *S1pr2* TV(final) was used to transform arabinose induced electrocompetent SW106 *E. coli* by Gene Pulser Xcell (Bio-Rad) on an exponential setting; 1800 V, 25 µF, 200 Ω. Transformed cells were plated on 2xTY agar plates that contained either 100 µg/mL ampicillin or 50 µg/mL kanamycin and incubated at 37 °C overnight. Bacterial isolates were counted, picked and cultured for 2 h at 37 °C in a shaking incubator to act as template for colony PCR for the neo^R cassette (Table 2.9). PCR amplicons were analysed on a 1% w/v agarose gel. Plasmids were prepared by miniprep for selected isolates. For restriction digests, a 25 µL reaction contained 2.5 µL of 10X CutSmart Buffer (NEB, B7204S), 0.5 µL of HindIII restriction enzyme (NEB R3104S), 0.5 µL of EcoRI restriction enzyme (NEB R3101S) and as DNA substrate either 2 µL of plasmid from transformed SW106 or 1 µL of parental *S1pr2* TV(final) used for the transformation. The reaction volume was made up to 25 µL using dH_20.

Target	**Primer**	**Strand**	**Sequence (5' → 3')**	**Expected amplicon (bp)**
Left (5') junction	MJP-138 VC-18	Sense Anti-sense	GATCCCCTATGGTGCACTCTCA TGGCCGATCCCATGGTTTAG	1860
Right (3') junction	VC-19 MJP-14	Sense Anti-sense	TCTCTAGAGCTCGCTGATCAGCCTC ATGTGGATCGGCTCGCGATC	1074

Table 2.9 **Primers used to screen for the presence of floxed neo^R cassette in transformed SW106 *E. coli*.**

2.16 PCR assays for the wild-type (WT) and targeted knock-in allele at the *S1pr2* locus in ESCs.

Multiple sets of potential genotyping primer pairs were screened against the loci specific 5'-Expected or 3'-Expected plasmids which contain additional genomic homology not included in their corresponding TVs (Figure 2.3). The most promising primer pairs were tested in a titration assay to assess the limit of detection when WT JM8 A3.N1 ESC gDNA was spiked with 5'-Expected or 3'-Expected plasmids in a 10-fold serial dilution (Figure 2.4). The presence of WT JM8 A3.N1 ESC gDNA is to mimic the "dirty" conditions of crude ESC lysates that will be the real experimental PCR template. The PCR assay was comprised of 50 ng of WT JM8 A3.N1 ESC gDNA spiked with 1 µL of either 5'-Expected or 3'-Expected plasmid, 2% v/v DMSO, primers at 0.5 µM final concentration (Table 2.10), 10 µL of 2X MyFi Mix (Bioline; BIO-25050) and dH_20 to a final reaction volume of 20 µL.

The PCR genotype assay for targeted knock-in events from antibiotic resistant ESCs consisted of 1 µL of ESC gDNA crude extract, 2% v/v DMSO, optimised primers at 0.5 µM final concentration (Figure 2.4 and Table 2.10), 10 µL of 2X MyFi Mix and dH_20 to a final reaction volume of 20 µL. PCR amplicons were first analysed on a low-resolution 96-lane 2% w/v agarose E-gel (Invitrogen). Lanes with putative positive clones were run on higher-resolution 1% w/v agarose gels for confirmation of amplicon size.

The PCR assay for the WT *S1pr2* allele consisted of 1 µL of ESC gDNA crude extract, 2% v/v DMSO, Bio-X-Act Short Mix (Bioline), the loci specific primers used for the corresponding T7E1 assay (Table 2.6) and dH_20 to a 20 µL final volume.

Target	Junction	Primer	Strand	Sequence (5’ → 3’)	Expected amplicon (bp)
S1pr2	3’	Ge19 Ge18	Sense Anti-sense	GGTCGATCTCACCTCCTGCGAT CAGCACAAGGAGGACATCTGGG	1887
S1pr2	5’	Ge21 Ge24	Sense Anti-sense	TGCAGTCCCATTCAGAGTCCCT CTCGTCGTTCTTCTCCACCTGC	3791
Prdm1 exon 8	3’	Ge15 Ge16	Sense Anti-sense	AAGAAAAGGTTTCCGCACTCAA TTGGTCTTGGAAACTAAGCAGC	2116
Prdm1 exon 8	5’	Ge29 Ge30	Sense Anti-sense	GTCCTCTGGCCATTCTTTGT TCTTTCAGCGCGCTCACTTT	3632
Prdm1 intron6-7	5’	Ge6 Ge2	Sense Anti-sense	CAAGAGAGAGTACAGCGTGAAAG CTTCGAGCGACTTCAGTTCTTT	3770

Table 2.10 **Sequences for optimised PCR genotyping primers for targeted insertion of transgenes at *S1pr2* or *Prdm1* loci**. Related to Figure 2.4.

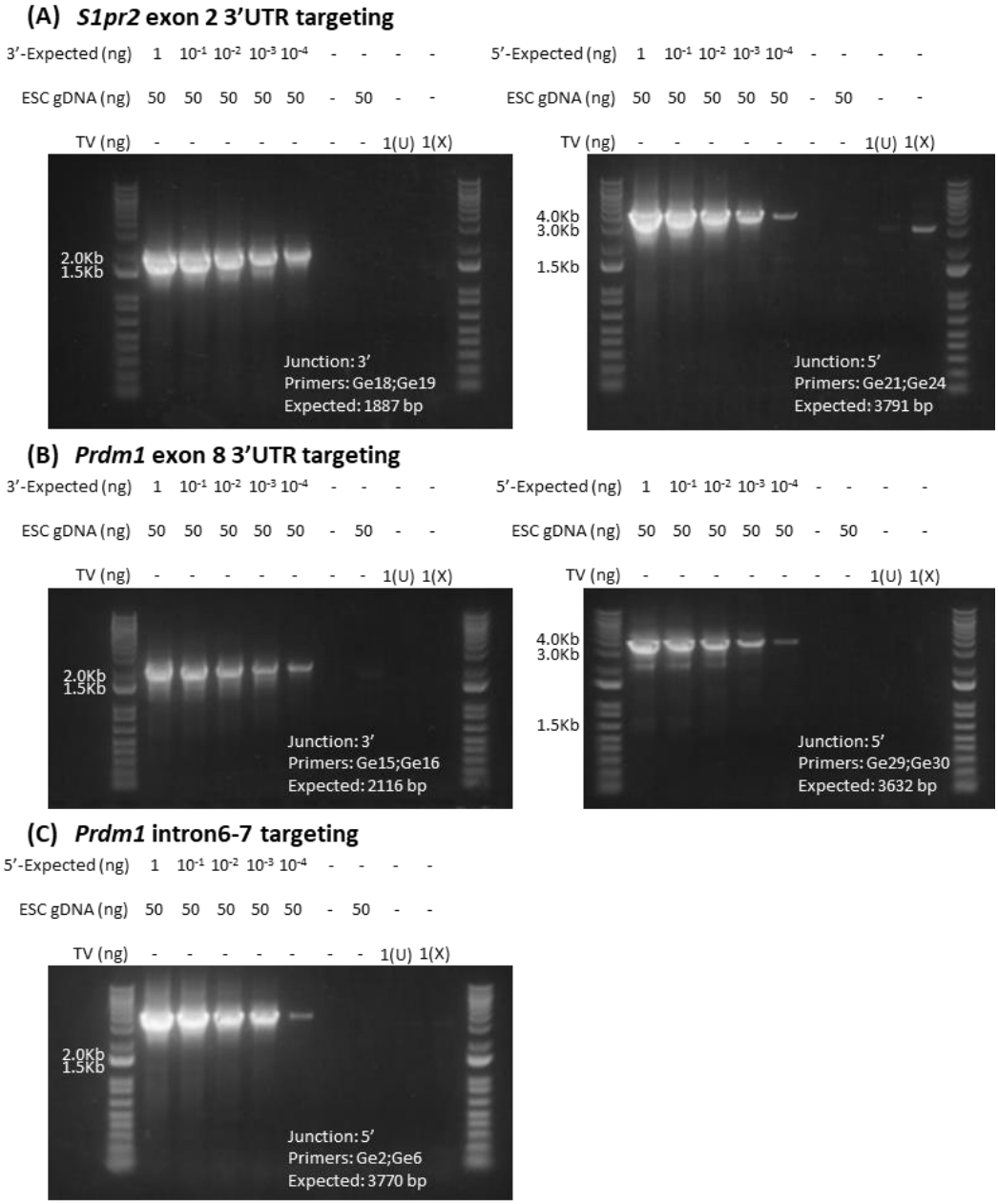

Figure 2.4 **Optimisation of PCR genotyping primers to detect the junctions of targeted knock-ins at *S1pr2* and *Prdm1* loci**. Assessment of the sensitivity and specificity of PCR genotyping primers to detect the junctions of targeted knock-in events. (A) *S1pr2* exon 2 3'UTR genotyping assay for 3' junction and 5' junction. (B) *Prdm1* exon 8 3'UTR genotyping assay for 3' junction and 5' junction. (C) *Prdm1* intron6-7 genotyping assay for 5' junction. Plasmids used are denoted as either 3'-Expected or 5'-Expected and contain additional genomic homology beyond the homology included in the TVs as detailed in Figure 2.3. Uncut (U) and XmaI linearised (X) TV were used as PCR controls to exclude non-specific primer binding to the relevant TV. JM8 A3.N1 ESC gDNA included to replicate "dirty" conditions of crude extracts from ESC colonies that will require PCR genotyping and to exclude non-specific amplicons from mouse gDNA.

2.17 PCR screen for genomic integration of all-in-one CRISPR/Cas9(Puro) plasmid.

PCR primer sets designed to bind to all-in-one CRISPR/Cas9(Puro) plasmid between the puromycin resistance cassette and pUC origin of replication were assessed by *in silico* PCR (UCSC in silico PCR (Kent *et al.*, 2002)) to exclude primers with predicted non-specific amplicons from the mouse genome. The limit of detection for candidate primers was assessed by PCR assay where 50 ng of WT JM8 A3.N1 ESC gDNA was spiked with all-in-one CRISPR/Cas9(Puro) plasmid in a 10-fold serial dilution. The optimised PCR primers are detailed in Table 2.11.

PCR screen assays for unwanted genomic integration of all-in-one CRISPR/Cas9(Puro) plasmid in targeted *S1pr2*$^{\text{diSplit670PAS}}$ ESC clones included no template controls (NTC) and controls for non-specific binding to *S1pr2* TV(final).

Primer	**Strand**	**Sequence (5' → 3')**	**Expected amplicon (bp)**
PuroIntScr1F	Sense	GCAGCAACAGATGGAAGGCC	596
PuroIntScr2R	Anti-sense	GGGAGAAAGGCGGACAGGTATC	

Table 2.11 **Optimised primers to screen for random integration events of the all-in-one CRISPR/Cas9(Puro) plasmid.**

2.18 Copy number assessment of the targeted knock-in transgene.

The copy number of the antibiotic positive selection neo^R cassette was assessed by qPCR in triplicate. Reactions comprised 1 µL of ESC gDNA as template, a PrimeTime qPCR Assay (IDT) with FAM-conjugated probe and neo^R cassette specific primers (Table 2.12), VIC-conjugated mouse *Tfrc* reference assay (Thermofisher; 4458367) and Taqman Fast Universal PCR Master Mix, no UNG (Thermofisher, 4352042). Data was acquired using a 7900HT Fast Real-time PCR Systems machine (Applied Biosystems) and analysed using CopyCaller v2.1 software (Applied Biosystems).

Target	**Strand**	**Sequence (5' → 3')**
Neo^R cassette	Sense	ACTTCCATTTGTCACGTCCTG
	Antisense	ACACATTCCACATCCACCG

Table 2.12 **Primer sequences used for targeted knock-in transgene copy number**.

2.19 Gene expression analysis in mouse ESCs.

Targeted ESC clones were harvested from 0.1% w/v gelatin coated plates. Total RNA was extracted with the RNeasy Mini Kit (Qiagen) and contaminating gDNA was removed by a minimum of one 'routine' DNaseI treatment (DNA-free™ DNA Removal Kit, Invitrogen). cDNA was prepared using High-Capacity cDNA Reverse Transcriptase kit without RNase Inhibitor (Applied Biosystems). Gene expression data was acquired in triplicate by qPCR using appropriate primers (Table 2.13), SYBR Green PCR Master Mix (Thermofisher, 4309155) and a 7900HT Fast Real-time PCR Systems machine. Primers designed *de novo* to detect *Prdm1* and *S1pr2* expression were tested on cDNA prepared from WT JM8 A3.N1 ESCs and MEFs to ensure that gene expression in ESCs was higher than MEFs so that contamination by residual feeder MEFs did not confound analysis (Figure 2.5A). For ESCs, gene expression was

compared to *Pou5f1* (Figure 2.5B), a typical ESC gene marker (Do *et al.*, 2013). No template (NTC; dH_20 only) and minus reverse transcriptase (-RT) controls were included for each primer pair or for the total RNA, respectively.

cDNA specificity	Strand	Sequence (5' → 3')	Expected amplicon (bp)	*De novo* or Published
S1pr2	Sense Anti-sense	GACCGAGCACAGCCAACAGTCTC CATGGTGGGGCTCAGTGGCC	147	*De novo*
Prdm1	Sense Anti-sense	TGTGGTATTGTCGGGACTTTGCGG TCACGCTGTACTCTCTCTTGGGGA	159	*De novo*
Actb (β-actin)	Sense Anti-sense	CGCCACCAGTTCGCCATGGA TACAGCCCGGGGAGCATCGT	106	(Lambooy *et al.*, 2017)
Pou5f1	Sense Anti-sense	TTGGGCTAGAGAAGGATGTGGTT GGAAAAGGGACTGAGTAGAGTGTGG	217	(Do *et al.*, 2013)

Table 2.13 **qPCR primer sequences**. *De novo* designed primers were selected using the Primer3 (Kõressaar *et al.*, 2018) and screened for predicted non-specific amplicons in the mouse genome by *in silico* PCR (UCSC in silico PCR tool (Kent *et al.*, 2002).

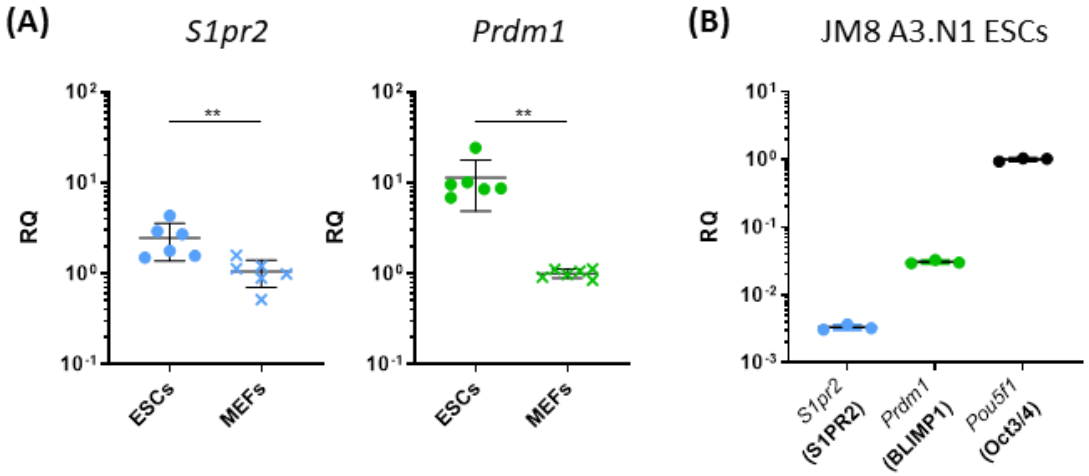

Figure 2.5 **Gene expression assessment in wild-type C57BL/6 JM8 ESCs and MEFs**. (A) Relative quantification (RQ) of *S1pr2* and *Prdm1* expression in WT JM8 A3.N1 ESCs to MEFs compared by Mann-Whitney test. (B) Comparison of *S1pr2* and *Prdm1* expression in JM8 ESCs to transcription factor *Pou5f1* highly expressed at the ESC stage. Proteins encoded by the genes are denoted in brackets. For gene expression 5 ng of cDNA template was used.

2.20 Chromosome counting of targeted ESCs.

Targeted ESCs were plated at $1x10^5$ cells/well on a MEFs coated 6-well plate. The next day, ESCs were incubated with non-selection ESC media supplemented with colcemid at 200 ng/mL for 2 h (Sigma; 10295892001), prior to harvest centrifugation at 1100 RPM for 3 minutes. Cell pellets were resuspended in 5 mL of 75 mM KCl solution, added dropwise with constant agitation, for an incubation at room temperature for 15 minutes, before centrifugation at 1100 RPM for 3 minutes. Pellets were resuspended in 5 mL of fixative (3:1 ratio absolute methanol:absolute acetic acid) added dropwise with constant agitation. Cells were incubated for 30 minutes at room temperature before centrifugation and fresh fixative added. Cells were incubated at -20 °C overnight then centrifuged and resuspended in the ~100 µL residual fixative remaining after centrifugation. Cells were then added dropwise from height to pre-cooled microscope slides to break the cell membrane. Slides were air dried, then stained with 2% v/v Giemsa stain (Sigma-Aldrich; Accustain Giemsa Stain), imaged using a Leica DFC295 microscope with 40x objective and 10x digital zoom and analysed using Leica application suite (LAS).

2.21 Western blots.

SDS-PAGE and western blots performed at AstraZeneca. *S1pr2*$^{\text{diSplit670PAS}}$ ESCs clones were expanded in 0.1% w/v gelatin coated 6-well plates, trypsinised and centrifuged at 1100 RPM for 5 minutes at 4 °C. Cell lysates were prepared in 150 µL radio-immunoprecipitation assay (RIPA) lysis buffer (Thermofisher, 89900) with 1X protease/phosphatase inhibitor cocktail (Cell Signalling, 5872). Lysates were incubated at 4 °C for 30 minutes with constant agitation (end-over-end wheel rotor) before centrifugation at 13,000 RPM for 20 minutes at 4 °C. The supernatant was harvested and rested for a further 30 minutes on ice. Protein concentration was

determined by BCA assay (Invitrogen, 23225). Cell lysate was prepared in Bolt LDS Sample Buffer (Novex; B0007) and NuPAGE reducing agent (Invitrogen; NP0009) and incubated at 70 °C for 10 minutes. Appropriate controls were also denatured. For α-FLAG epitope tag this was an *E. coli* whole cell lysate containing a 41 kDa recombinant protein expressing 11 epitope tags (Abcam; ab5395). For α-Cas9 this was 200 ng of purified recombinant *S. pyogenes* Cas9 (kind gift of AstraZeneca). Denatured samples (20 µg) were loaded onto a Bolt 4-12% Bis-Tris Gel (Invitrogen; NW04125BOX) with SeeBlue Plus 2 (Invitrogen, LC5925) and Odyssey One-colour Protein MW Marker (Li-Cor; 928-40000) pre-stained protein molecular weight markers. Gels were run at 200 mV with Bolt MES Running Buffer (Invitrogen, B000202). Gels were transferred by iBlot (Invitrogen) onto iBlot PVDF membrane (Invitrogen, IB401001). All subsequent incubation steps, unless otherwise stated, were performed at room temperature on a rotary platform. PVDF membranes were incubated for 1 h in block buffer (PBS, 0.1% v/v Tween-20, 5% w/v marvel milk powder), before three 10-minute washes with PBS/T (PBS, 0.1% v/v Tween-20) and one 10-minute wash with PBS. Primary detection antibody diluted in block buffer was incubated overnight at 4 °C (Table 2.14). After washing, secondary detection antibody in block buffer was incubated for 1 h. A final wash was performed before image acquisition using the Odyssey Clx with Image Studio software (Li-COR) at 700 nm or 800 nm emission. Cas9 protein expression was analysed in ImageJ.

SDS-PAGE and western blots performed at UoB. Transfected HEK293T cell lysates were prepared as detailed above, except a different protease inhibitor cocktail was used (Sigma; P8430). Sample was prepared in NuPAGE LDS sample buffer (Invitrogen, NP0007) and dithiothreitol to 25 mM final concentration and incubated at 70 °C for 10 minutes. Denatured samples (25 µg) were loaded onto a NuPAGE 4-12% gradient Bis-Tris gel (Invitrogen;

NP0321) with pre-stained molecular weight ladder (Biolegend; 773301) and MagicMark XP Western Protein Standard (Invitrogen; LC5602). Gels were run at 200 mV in NuPAGE MES SDS Running Buffer (Novex NP0002). Samples were transferred onto PVDF membranes (Merck; IPVH08100) by wet transfer in NuPAGE Transfer Buffer (Novex; NP0006) for 2 h at 30 V. Efficiency of the transfer was assessed by Coomassie Blue stain of the gel (Invitrogen; LC6060) and by Ponceau S stain of the PVDF membrane (Sigma; P7170). Before immunoblotting the PVDF membrane was de-stained using 0.1 M NaOH and rinsed with dH_20. Immunoblotting was performed as described above except Tris Buffered Saline (TBS) was used instead of PBS. Image acquisition was performed using a ChemiDoc Imaging System (Bio-Rad) with emission filter sets for IRDye680 (715/30 nm) and IRDye800 (835/50 nm) and analysed using Image Lab Standard Edition v6.0.1 (Bio-Rad).

NativePAGE and western blots performed at UoB. Transfected HEK293T cell lysates were prepared in Pierce™ IP Lysis Buffer (Invitrogen; 87787) with 1X protease cocktail inhibitor (Sigma; P8430). BCA assay determined cell lysate protein concentration and 25 µg was prepared with Novex Tris-Glycine Native Sample Buffer (Invitrogen, LC2673). Samples and unstained NativeMark protein standard (Invitrogen; LC0725) were loaded into Novex 4-12% gradient Tris-Glycine Gels (Invitrogen; XP04122BOX) and run at 200 mV in Novex Tris-Glycine Native Running Buffer (Invitrogen; LC2672). After electrophoresis, gels were incubated in 0.1% w/v SDS for 15 minutes. Wet transfer onto PVDF membranes was achieved with Novex Tris-Glycine Transfer Buffer (Novex; LC3675) and transfer conditions of 30 V for 2 h. To improve fixation of soluble non-denatured proteins, the PVDF membrane was air dried immediately after wet transfer. Efficiency of the transfer was assessed by Coomassie Blue stain of the gel and by Ponceau S stain of the PVDF membrane. Before immunoblotting the PVDF

membrane was de-stained using 0.1 M NaOH and rinsed with dH_20. Immunoblotting and image acquisition was performed as described for SDS-PAGE at UoB.

Primary and secondary antibodies used for Western blots are detailed in Table 2.14.

Target	Host (Isotype)	Clone	Conjugate	Dilution	Supplier	Cat #
α-tubulin	Rabbit (IgG)	EP1332Y	Purified	1:5000	Abcam	ab52866
GAPDH	Mouse (IgG1)	GA1R	Purified	1:3000	Invitrogen	MA5-15738
FLAG tag	Rabbit (IgG)	EPR20018-251	Purified	1:5000	Abcam	ab205606
V5 tag	Rabbit (IgG)	Polyclonal	Purified	1:5000	Abcam	ab9116
Cas9 (*S.pyogenes*)	Mouse (IgG1)	7A9-3A3	Purified	1:1000	Thermofisher	MA1-201
Rabbit IgG	Goat	Polyclonal	IRDye 680RD	1:15000	Li-COR	925-68071
Rabbit IgG	Donkey	Polyclonal	IRDye 680RD	1:15000	Abcam	ab216779
Mouse IgG	Goat	Polyclonal	IRDye 800CW	1:15000	Li-COR	925-32210
Mouse IgG	Goat	Polyclonal	IRDye 800CW	1:15000	Abcam	ab216772

Table 2.14 **Primary and secondary antibodies used for detection in Western blot assays**.

2.22 Mycoplasma PCR screen.

The LookOut Mycoplasma PCR detection kit (Sigma; MP0035) was used according to manufacturer's protocol with JumpStart Taq DNA polymerase (Sigma; D9307). Briefly, supplied PCR tubes for samples and the negative PCR control contain two sets of primers; one set for an internal control (expected product 481 bp) and the other set is specific for mycoplasma

DNA (expected product 260 bp). Supplied PCR tubes for the PCR positive control contain the internal control and mycoplasma specific primers as well as mycoplasma DNA template. Heat inactivated ESC culture supernatant (2 µL) or dH_20 were added to the sample and negative PCR control tubes, respectively. Following thermocycler amplification, the samples were analysed on a 1.2% w/v agarose gel.

2.23 Chimera generation and germline transmission of *S1pr2*^{diSplit670PAS} ESC clones.

Chimera generation at UoB: Andrea Bacon (Transgenic Operator) performed microinjections, blastocyst transfers and chimera coat assessments. Blastocysts were isolated from superovulated C57BL/6J females after mating with C57BL/6J males. Blastocysts were placed in a drop of M2 media (Sigma; M7167) with 15% v/v FBS under mineral oil before targeted *S1pr2*^{diSplit670PAS} ESCs were injected into each blastocyst with TransferTip (ES) (Eppendorf; 930001040) micro-injection pipette. After recovery, 16-19 blastocysts were transferred to either the fallopian tubes or uterus of 0.5-2.5 days post coitum (dpc) pseudo-pregnant CD1 females. Coat colour contribution of *S1pr2*^{diSplit670PAS} targeted C57BL/6 JM8 A3.N1 ESCs with agouti coat (Pettitt *et al.*, 2009) to host C57BL/6J black coat colour was used to measure chimerism.

In vitro fertilisation (IVF) at UoB BMSU: BMSU staff harvested spermatozoa from the single *S1pr2*^{diSplit670PAS} chimera to fertilise oocytes from C57BL/6N females. Transfer into C57BL/6N surrogate females.

PCR genotyping: Spermatozoa from the male *S1pr2*^{diSplit670PAS} chimera was PCR screened for presence of targeted *S1pr2*^{diSplit670PAS} allele. Platinum Direct PCR Universal Master Mix (Invitrogen; A44647100) was used according to manufacturer's instructions. Multiplex PCR assays to detect the neo^{R} cassette or the 3' junction of *S1pr2*^{diSplit670PAS} allele were performed with an internal control for CD79b (Table 2.15).

Target	**Sequence (5' → 3')**	**Expected amplicon (bp)**
3' *S1pr2*^{diSplit670PAS} junction	GGTCGATCTCACCTCCTGCGAT CAGCACAAGGAGGACATCTGGG	1887
neo^{R} cassette	CGATCAGGATGATCTGGACG CAAGCTCTTCAGCAATATCACG	239
CD79b	GAGACTCTGGCTACTCATCC CCTTCAGCAAGAGCTGGGGAC	585

Table 2.15 **Primers for PCR genotype of *S1pr2*^{diSplit670PAS} chimera and for detection of germline transmission.**

2.24 Generation of *Prdm1*^{diSplit670GAF} targeted mice.

Prdm1 intron6-7 TV(final) and pre-validated *Prdm1* intron6-7 sgRNA 3 (Table 4.3) were sent to Taconic Biosciences for targeted insertion into C57BL/6NTac ESCs.

Generation of targeted knock-in ESCs at Taconic: For traditional homologous recombination mediated targeted knock-in, *Prdm1* intron6-7 TV(final) was introduced into ESCs by electroporation with subsequent G418 selection. For CRISPR/Cas9 enhanced targeting, plasmids were introduced by nucleofection. PCR screens were performed to detect ESC clones with the desired targeted knock-in and to exclude those with random genomic integrations. Multiple southern blot assays were used to further characterise targeted knock-in ESC clones.

Chimera generation at Taconic: Blastocysts were isolated from superovulated BALB/C females after mating with BALB/c males. Blastocysts were placed in a drop of DMEM media with 15% v/v FBS under mineral oil before 10-15 targeted *Prdm1*^{diSplit670GAF} ESCs were injected into each blastocyst with a flat tip, piezo actuated microinjection-pipette. After recovery, blastocysts were transferred to each uterine horn of pseudo-pregnant females. Coat colour contribution of targeted C57BL/6NTac ESCs with black coat colour to host BALB/c white coat was used to measure chimerism.

IVF performed at Taconic: Cryopreserved spermatozoa from *Prdm1*^{diSplit670GAF} chimeras and oocytes from C57BL/6NTac females were used for IVF. Pseudo-pregnant females received two-cell embryos into their oviducts. Germline transmission was confirmed by PCR genotyping.

2.25 Details of wild-type and transgenic mice used in this project.

Mice were housed and bred under specific pathogen-free conditions at the University of Birmingham's Biomedical Services Unit (BMSU). Ethical approval for all animal experiments was granted and procedures were conducted under Home Office Project License PEAE5FA92 or PP8702596. At the time of immunisation all experimental mice were between 6 and 21 weeks of age.

BALB/c mice were purchased by BMSU and were Schedule 1 culled prior to injections for IVIS experiments.

Prdm1$^{GFP/+}$ mice were a kind gift from Stephen Nutt, WEHI, Melbourne, Australia. These mice have a targeted insertion within intron6-7 of the *Prdm1* locus comprised of a splice site acceptor, IRES and EGFP cDNA. Fluorescence is driven by the endogenous *Prdm1* promoter and regulatory elements. The targeted knock-in produces a non-functional truncated Blimp1 protein and is pre-natal lethal if the embryo is homozygous for the targeted allele (Kallies *et al.*, 2004).

S1pr2^{ERT2Cre} mice were a kind gift from Tomohiro Kurosaki, RIKEN Center for Integrative Medical Sciences, Yokohama, Kanagawa, Japan. Briefly, the sequence which encodes the ERT2-Cre fusion protein was inserted into exon 2 of the *S1pr2* gene on a BAC clone (RPCI23.C-168D6) using the Red recombination system. Transgenic *S1pr2*^{ERT2Cre} mice were generated by PNI of the targeted BAC into C57BL/6 zygotes (Shinnakasu *et al.*, 2016).

Rosa26^{LSLtdTomato} mice are a Cre-inducible fluorescent reporter strain (obtained from the Jackson Laboratory, Cat # 007914). These mice have a Cre conditional tdTomato expression allele targeted to the *Rosa26* locus. Cre excision removes the floxed STOP cassette (LSL) located immediately upstream of the tdTomato sequence and results in permanent constitutive tdTomato expression (Madisen *et al.*, 2010).

Rosa26^{mTmG} mice are a two-colour fluorescent Cre-inducible reporter strain (obtained from the Jackson Laboratory, Cat # 007576). Mice constitutively express a plasma membrane tagged tdTomato (mT) fluorescent protein from the *Rosa26* locus. Upon crossing with a Cre-expressing strain, the LoxP flanked mT sequence is excised, enabling the downstream plasma membrane tagged EGFP (mG) cassette to be expressed (Muzumdar *et al.*, 2007).

Aicda^{ERT2Cre} mice were a kind gift from C-A Reynaud, Institute Necker, Paris, France. Briefly, the sequence which encodes the ERT2-Cre fusion protein replaced exon 2 of *Aicda* locus by targeted knock-in. This creates a non-functional *Aicda* allele, and mice must be heterozygous for the transgenic allele to possess functional AID protein (Dogan *et al.*, 2009).

2.26 Immunisations and *in vivo* treatment with antibodies or chemicals.

Immunisations.

The primary immune response to sheep red blood cell (SRBC) immunisation was used to study the kinetics of GCmat PC output. SRBCs in Alsever's (TCS Biosciences, SB068) were washed three times in sterile PBS before resuspension at $1x10^9$ SRBC/mL in PBS. A single 200 µL dose ($2x10^8$ SRBCs) was injected intravenous (i.v.) via the tail vein.

T-cell dependent immune responses were induced by immunisation with hapten-protein conjugate; NP_{24}-KLH (4-hydroxy-3-nitrophenylacetyl conjugated to Key Limpet Hemocyanin, Biosearch Technologies, N-5060-5) or NP-CGG (chicken gamma globulin) conjugated in the lab. To prepare alum precipitated reagent for immunisation, alum (9% w/v $KAl(S0_4)_2$ in sterile dH_20) and reagent were mixed at a 1:1 ratio. The pH was adjusted to between pH 6.5 and pH 7.0 using 10 M NaOH. The solution was protected from light and incubated for 60 minutes on an end-over-end rotator at room temperature before centrifugation at 2000 RPM for 5 minutes. The pellet was washed twice with sterile PBS before being resuspended to the desired concentration in sterile PBS; for intraperitoneal (i.p.) injections this was 50 µg / 200 µL dose and for subcutaneous (s.c.) injections on the plantar surface of the foot 20 µg / 20 µL dose. If

required, $5x10^6$ chemically inactivated *Bortedella pertussis* (Wako, 022-08301) was added per dose.

In vivo treatments

For transgenic mice which contained the transgene encoding ERT2-Cre protein, Cre recombinase activity was induced by administration of a single 200 µL dose of 30 mg/mL tamoxifen (i.e., 6 mg tamoxifen/dose) by oral gavage at the indicated time before tissues were prepared for analysis. To prepare 10 mL of 30 mg/mL tamoxifen solution, 300 mg of tamoxifen powder (Sigma, T5648) was added to 200 µL of absolute ethanol before addition of 9.8 mL of corn oil. The solution was protected from light, regularly mixed by vortex and incubated in a 42 °C water bath until the tamoxifen had completely dissolved.

Soluble decoy TACI receptor fusion protein (mTACI-Fc) was administered to inhibit TACI signalling (Zhang *et al.*, 2018). mTACI-Fc contains the extracellular mouse TACI domain fused to the Fc portion of mouse IgG2c. A single 100 µg/ 200 µL PBS dose of mTACI-Fc or control mouse IgG2c (mFc control) was administered i.v. 24 h or 48 h before tissue analysis.

2.27 Mouse tissue and sample preparation.

Serum was obtained by cardiac puncture immediately before schedule 1 cull of mice. Whole blood was incubated for 1 h at 37 °C before centrifugation at 13,000 RPM for 5 minutes at room temperature. The serum (supernatant) was carefully aspirated from the RBC layer and stored at -20 °C.

Spleens were taken aseptically and placed in ice cold RPMI-1640 media before being weighed. If spleens were to be analysed by both flow cytometry and immunofluorescence histology, they were weighed before and after cutting the tissue into the required sections. To obtain a single cell suspension for flow cytometry, spleens were gently passed through a 70 µm filter into a 6-well plate containing cold RPMI-1640. Cells were transferred to a 15 mL conical tube, centrifuged at 1400 RPM for 5 minutes at 4 °C, resuspended in RPMI-1640 media and placed on ice.

Bone marrow (BM) cell suspensions were prepared from the tibia and fibula. Excess tissue was removed before flushing the BM contents into a 6-well plate with needle and syringe and mechanical disruption by pipetting and passing through a 70 µm filter. Cells were then resuspended as already described.

All cell counts were performed manually using the trypan blue exclusion method and a haemocytometer.

2.28 Flow cytometry of primary mouse cells.

Cell-surface staining

Single cell suspensions were plated in a V-bottomed 96-well plate and centrifuged at 1400 RPM, 4 °C for 5 minutes. Samples were resuspended in 100 µL of αCD16/CD32 FcR block (Invitrogen; 14-0161-82) diluted 1:200 in flow cytometry buffer (PBS, 2% v/v FBS, 2mM EDTA) for 20 minutes at 4 °C to block non-specific FcγRIII and FcγRII binding. Cell-surface marker specific antibody cocktails were diluted in flow cytometry buffer or, if multiple Brilliant Violet (BV) conjugated dyes were included in the stain panel, Brilliant Stain Buffer (BD Biosciences; 563794) at 50 µL/sample well. After blocking, cell-surface markers were stained

for 20 minutes in the dark at 4 °C, washed and incubated for 20 minutes in the dark at 4 °C in fixable near infrared viability dye (Invitrogen; L10119). Samples were washed twice in flow cytometry buffer before data acquisition.

Compensation controls

Compensation controls were selected as appropriate from: i) intrinsically non-fluorescent single colour stained splenocytes, ii) non-stained intrinsically fluorescent cells from the appropriate immunised or naïve transgenic mouse, iii) stained compensation beads (BD Biosciences; 552845) or iv) GFP BrightComp eBeads™ Compensation Bead Kit (Invitrogen; A10514).

Data acquisition and analysis

Flow cytometric data was acquired on a LSRFortessa X-20 using FACSDiva software (BD Biosciences) and analysed offline using FlowJo v10 (BD Biosciences)

Antibody list

The details of all antibodies included for flow cytometric analysis of primary mouse cells are included in (Table 2.16).

Specificity	Clone	Isotype	Conjugation	Supplier	Cat #
CD3	145-2C11	Armenian Hamster IgG	PE-Cy7	BD	560591
CD4	GK1.5	Rat IgG2a, κ	APC	eBioscience	17-0041
CD4	GK1.5	Rat IgG2a, κ	Alexa700	Invitrogen	56-0041
CD8	53-6.7	Rat IgG2a, κ	APC	eBioscience	17-0081
CD8	53-6.7	Rat IgG2a, κ	PerCP-Cy5.5	eBioscience	45-0081
CD11b	M1/70	Rat IgG2b, κ	BV510	Biolegend	101245
CD11c	N418	Armenian Hamster IgG1 κ	APC	eBioscience	17-0114
CD11c	HL3	Armenian Hamster IgG1 λ	PE-Cy7	BD	558079
CD19	1D3	Rat IgG2a κ	eFluor450	eBioscience	48-0193
CD19	1D3	Rat IgG2a κ	BUV737	BD	612781
CD19	1D3	Rat IgG2a κ	FITC	eBioscience	11-0193
CD21	7G6	Rat IgG2b κ	BV605	BD	563176
CD23	B3B4	Rat IgG2a, κ	PE-Cy7	eBioscience	25-0232
CD38	90	Rat IgG2a, κ	PerCP-Cy5.5	Biolegend	102722
CD43	S7	Rat IgG2a, κ	Biotin	BD	553269
CD45R (B220)	RA3-6B2	Rat IgG2a, κ	BV510	Biolegend	103247
CD45R (B220)	RA3-6B2	Rat IgG2a, κ	BUV395	BD	
CD86	GL1	Rat IgG2a, κ	PE-Cy7	eBioscience	25-0862
CD93	AA4.1	Rat IgG2b, κ	Biotin	eBioscience	13-5892
CD93	AA4.1	Rat IgG2b, κ	PerCP-Cy5.5	Biolegend	136512
CD95 (Fas)	Jo2	Hamster IgG	PE-Cy7	BD	557653
CD95 (Fas)	Jo2	Hamster IgG	BV605	BD	740367
CD138	281-2	Rat IgG2a, κ	BV711	Biolegend	142519
CD138	281-2	Rat IgG2a, κ	BV421	Biolegend	142508
CD184 (CXCR4)	2B11	Rat IgG2b κ	Biotin	eBioscience	13-9991
CD184 (CXCR4)	2B11	Rat IgG2b κ	APC	eBioscience	17-9991
CD267 (TACI)	8F10	Rat IgG2a κ	Alexa647	BD	558453
IgD	11-26c.2a	Rat IgG2a κ	BV421	Biolegend	405725
IgG1	A85-1	Rat IgG1, κ	Biotin	BD	553441
IgG1	Polyclonal	Goat IgG	FITC	Southern Biotech	1070-02
IgG	Polyclonal	Goat F(ab')2	APC	eBioscience	17-4010

IgM	Polyclonal	Goat IgG	FITC	Southern Biotech	1021-02
IgM	RMM-1	Rat IgG2b κ	PE-Cy7	Biolegend	406514
IgM	RMM-1	Rat IgG2b κ	PerCP-Cy5.5	Biolegend	406511
Blimp1	5E7	Rat IgG2a κ	BV421	BD	564270
Streptavidin			BV421	Biolegend	405226
Streptavidin			APC	eBioscience	17-4317
Streptavidin			BV605	Biolegend	405226
Streptavidin			BV711	Biolegend	405241

Table 2.16 **Antibodies used to analyse primary mouse cells.**

2.29 Enzyme linked immunosorbent assay (ELISA).

Samples for ELISA analyses were either culture supernatant or mouse sera. Flat-bottomed Maxisorp 96-well plates (Thermofisher, 442404) were coated overnight with 100 µL of antigen (Table 2.17) diluted in ELISA coating buffer (Table 2.18) at 4 °C. Unless otherwise stated, plates were washed with ELISA wash buffer before the next reagent was added. To prevent non-specific binding, 200 µL of block buffer was incubated for 1 h at 37 °C (Table 2.18). Sample was added to each well as appropriate. For single end-point analyses (e.g., hybridoma mAb analysis) undiluted sample was added to a single well. For analysis of serum, samples were pre-diluted in ELISA dilution buffer (Table 2.18) and added to the first well before serial dilution. For a 1 in 3 serial dilution, 150 µL of sample was added to the first well with 50 µL aspirated and mixed in the next well which contained 100 µL of dilution buffer. This was repeated until the necessary dilution factor had been achieved and each sample well had a final volume of 100 µL. Samples were incubated for 1.5 h at 37 °C in a humidified chamber. Alkaline phosphatase-conjugated secondary detection antibody was added at 100 µL per well (Table 2.19) and incubated for 1 h at 37 °C. SigmaFast p-Nitrophenyl phosphate reagent (Sigma, N2770) was added at 100 µL/well and colour development was measured at 405 nm using a SpectraMax ABS Plus plate reader (Molecular Devices).

Reagent	Coating concentration	Supplier	Category #
NP_2-BSA	5 µg/mL	Prepared in-house	N/A
NP_{14}-BSA	5 µg/mL	Biosearch Technologies	N-5050H-10
NP_{24}-KLH	5 µg/mL	Biosearch Technologies	N-5060-5
OVA	5 µg/mL	Sigma	
Goat α-mouse κ	1:1000	Southern Biotech	1050-01
Goat α-mouse λ	1:1000	Southern Biotech	1060-01

Table 2.17 **Reagents used to coat ELISA plates**.

Buffer	Component	Final concentration
Coating	Na_2CO_3	0.018M
	$NaHCO_3$	0.035M
	dH_20	1X
Wash	PBS	1X
	Tween-20	0.05% v/v
Blocking	PBS	1X
	BSA	1% w/v
Dilution	PBS	1X
	BSA	1% w/v
	Tween-20	0.05% v/v

Table 2.18 **Buffer compositions for use in ELISA protocol.**

Specificity	Species	Concentration	Conjugation	Supplier	Category #
IgM (mouse)	Goat	1:2000	AP	Southern Biotech	1020-04
Total IgG (mouse)	Goat	1:2000	AP	Southern Biotech	1030-04

Table 2.19 **Secondary detection antibodies for ELISA.** AP – alkaline phosphatase.

2.30 Hybridoma generation and screening.

Traditional hybridoma generation. The protocol for traditional hybridoma fusion is outlined in Figure 2.6. To ensure NS0 fusion partner cells were sensitive to HAT selection, cells were cultured for 5 days in R15 media supplemented with 20 µM of 6-thioguanine before continued culture in standard R15 media. Three days before fusion, R15 media was replaced with HAT selection media (Table 2.2) on a test flask of NS0 cells to confirm HAT sensitivity and requirement of functional HPRT gene. On the day of fusion, mouse spleen(s) were aseptically collected, perforated with a needle and flushed with RPMI-1640 before a single cell suspension was obtained through a 40 µm cell strainer. Splenocytes and NS0 cells were washed twice with R0 media, combined at a 5:1 splenocyte:NS0 ratio, then aspirated to dryness. Over the next 5 minutes, 1 mL pre-warmed polyethene glycol (PEG; Stemcell Technologies; 03806) was added slowly over the first 60 s to the cells with constant mixing, followed by a further 60 s of mixing only, and finally slow dilution of the PEG by addition of 20 mL of R0 media during the remaining time. Fusions were rested for 5 minutes at 37 °C before centrifugation and resuspension in R20 media. Fusions were further rested for 15 minutes. Fused cells were diluted into R15 media then plated at 150 µL/well in flat bottomed 96-well plates and incubated at 37 °C in a non-humidified 5% $C0_2$ incubator. HAT selection was initiated 24 h post-fusion. From day 11 post-fusion, manual observation for hybridoma colony growth was made using an inverted light microscope. Supernatant from wells with visible hybridoma colonies were screened by ELISA. Antibody expressing hybridomas were expanded for further testing of Ag specificity.

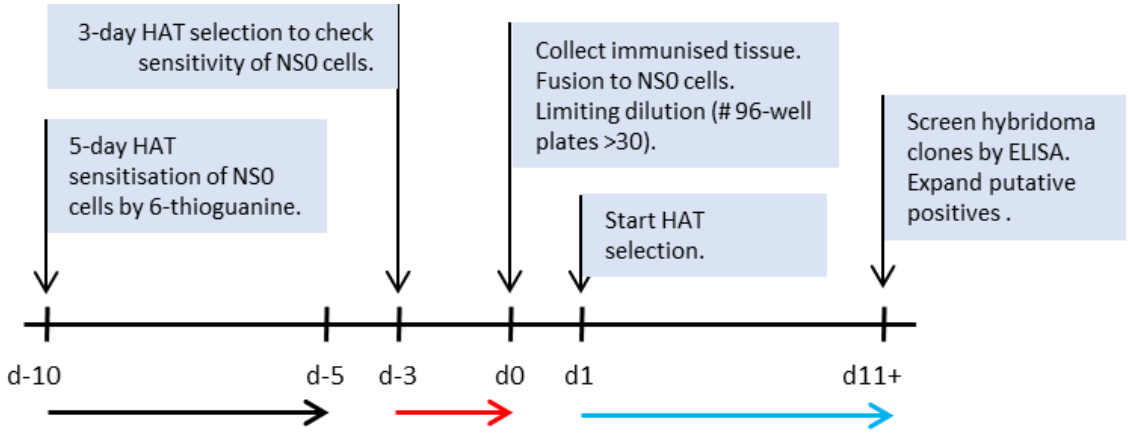

Figure 2.6 **Traditional protocol for fusion, selection and screening to generate hybridomas expressing Ag-specific mAbs**. NS0 plasmacytoma cells are sensitised to HAT selection by growth in media containing 6-thioguanine (black arrow). Prior to fusion an aliquot of NS0 cells is subject to 72 h HAT selection (red arrow) to confirm requirement for functional HPRT gene. Cells from immunised secondary lymphoid tissue (e.g., spleen or LNs) of hyperimmunised mice are fused to HAT sensitive NS0 fusion partners and plated by limiting dilution in preparation for HAT selection which is initiated 24 h later (blue arrow). Wells are checked for hybridoma colony growth manually with microscope and the supernatant of wells containing hybridomas are screened by ELISA. Putative Ag-specific hybridoma clones are expanded and further characterised.

Protocol A – Micro-fusion of isolated affinity matured cells: GCmat PCs and GC B-cells from a single hyperimmunised spleen were isolated by FACS. Scaled down PEG based fusions were performed with altered cell ratios and 250 µL instead of 1 mL of PEG. NS0 plasmacytoma cells were added at a 30:1 ratio to GCmat PCs whereas GC B-cells and NS0 cells were combined at a 1:1 ratio. Fusions were added to a single or six wells of a flat bottomed 96-well plates, respectively, and HAT selection was initiated 24 h post-fusion.

Protocol B – Traditional fusion with altered HAT selection and FACS enrichment: Fusion to NS0 cells was performed as per traditional hybridoma generation, but instead of limiting dilution for HAT selection in 96-well plates, the fused cells were split between T75 flasks. HAT selection was initiated 24 h post fusion and after 10 days hybridoma cells were harvested,

treated with αCD16/CD32 FcR Block, stained with α-mouse IgM-FITC and α-mouse IgG-APC for 15 minutes at room temperature and stained with fixable NIR viability dye. Live hybridoma clones that were non-negative for cell-surface IgM or IgG were index single cell-sorted into flat bottomed 96-well plates that contained $3x10^4$ HAT sensitive NS0 cells to condition the media. HAT selection was resumed 24 h post cell-sort. Wells were screened for post-sort expansion of hybridoma colonies from 10 days after isolation by observation under light microscope. The supernatant from wells with expanded hybridoma colonies were screened by ELISA. The FACS stain profile of index sorted single cells was analysed on FlowJo v10.

The FACS was kindly performed by Dr Adriana Flores-Langarica of the University of Birmingham Flow Cytometry Services using a FACSAria Fusion cell sorter (BD).

2.31 Statistical analysis.

All statistical analyses were conducted on GraphPad Prism v9. Data were assessed for Gaussian distribution and the appropriate parametric or non-parametric tests were performed and described in the Figure legend. Significance (p) values are indicated throughout as; "ns" for not significant, * for $0.01 \leq p < 0.05$, ** for $0.001 \leq p < 0.01$, *** for $0.0001 \leq p < 0.001$ and **** for $p < 0.0001$.

Chapter 3. Investigating Germinal Centre matured Plasma Cells

3.1 Introduction

3.1.1 The kinetics of GCmat PC output.

Two recent studies have shed light on the kinetics of GC output. First, Weisel and colleagues postulated that the GC switches from preferential early output of MBC to LLPC output at later stages (Weisel *et al.*, 2016). They used BrdU pulse labelling to study when Ag-specific MBC or PC were preferentially output in an artificial system used to induce a synchronous GC response that involved adoptive transfer of NP-specific B1-8i cells into AM14 transgenic mice where the recipient has a single BCR specificity to rheumatoid factor that cannot react to immunising antigen NP-CGG (Weisel *et al.*, 2016). All mice were analysed at week 8 post-immunisation and flow cytometric analysis of $BrdU^+$ NP-specific cells MBC in the spleen indicated that peak output of MBC occurred between day 6 to day 8 after immunisation, whereas peak detection of $BrdU^+$ NP-specific PCs resident in the BM did not occur until days 24-26 (Weisel *et al.*, 2016). However, ELISpot data showed that NP-specific $IgG1^+$ PCs in the spleen peaked by day 11, and the subsequent decline in the Ag-specific splenic PC compartment was concurrent with a steady accumulation in the Ag-specific PCs in the BM, which peaked and plateaued almost 2-weeks later, in-line with the flow cytometric observations (Weisel *et al.*, 2016). In a later study, Zhang and colleagues used wild-type and GC-specific fluorescent reporter tissues to study PBs formed at the earliest stages of the GC reaction by immunohistology (Zhang *et al.*, 2018). Using either sheep red blood cell (SRBC) or carrier primed NP-carrier immunisation, they demonstrated that the peak output of PBs exiting the GC relative to GC size was 5 days after immunization, before the GC had reached peak size (Zhang *et al.*, 2018). This study also showed that the microanatomical pathway of emigration for PCs

was via the GC T zone interface (GTI). Further, experiments involving administration of soluble blockers of CD40L, IL-21, and IL-21R$^{-/-}$ mice, all important for Tfh cell mediated selection of the precursors of GCmat PBs, confirmed a decline in detected GTI PBs at this earliest stage (Zhang *et al.*, 2018). Taken together, these studies suggest that either GTI PBs observed at the earliest timepoint differentiate locally without migration to the BM or that GCmat PCs occupy local PC niches in the secondary lymphoid tissue first with migration to the BM survival niche later (Sze *et al.*, 2000; Weisel *et al.*, 2016; Zhang *et al.*, 2018). In both scenarios high affinity antibody secreted locally by early GCmat PC output could serve to increase the affinity selection threshold within the GC reaction by replacing previous antibody on FDC deposited immune complex with those of higher affinity, as shown by administration of exogenous Ag-specific antibody of varying affinity (Zhang *et al.*, 2013; Zhang, Garcia-Ibanez and Toellner, 2016). This early GCmat PC output, which can reside in local splenic PC niches long-term (Bohannon *et al.*, 2016), could provide this antibody feedback.

3.1.2 The limitations of existing transgenic fluorescent reporter mice for study of GCmat PCs.

Study of the kinetic output of GCs and PC biology by either flow cytometry, histology or by *in vivo* imaging, can be facilitated by specific fluorescent protein reporter systems. Existing models used for this purpose each have their own limitations.

The involvement of Blimp1 (encoded by *Prdm1*) in terminal differentiation of PC has been known for nearly three decades (Turner, Mack and Davis, 1994). Functional *Prdm1* is essential for differentiation of B-cells into antibody secreting PCs (Shapiro-Shelef *et al.*, 2003) and is highly expressed in PCs (Marshall *et al.*, 2011). The generation of the targeted knock-in

Prdm1$^{GFP/+}$ fluorescent reporter mouse showed that Blimp1 expression increased as immature plasmablasts differentiate into mature PCs (Kallies *et al.*, 2004). The *Prdm1*$^{GFP/+}$ fluorescent reporter model is very well characterised and has been extensively used for the study of PC biology (discussed in Section 1.7), but targeted insertion created a non-functional *Prdm1* allele which cannot be bred homozygous due to the essential requirement of Blimp1 for proper embryo development (Kallies *et al.*, 2004; Mould *et al.*, 2012; Yamashiro *et al.*, 2016). There are alternative transgenic mice which possess a fluorescent reporter controlled by *Prdm1*, for example, *Prdm1*^{EYFP} (Rutishauser *et al.*, 2009) and *Prdm1*^{mVenus} (Ohinata *et al.*, 2008). Both transgenic mice were generated by random integration of a BAC and either have not been extensively used, in the case of *Prdm1*^{EYFP}, or not used at all, in the case of and *Prdm1*^{mVenus}, for study of PCs. Without aid of a fluorescent reporter system, the only current methods to identify and characterize GC derived PC is via the histological location (Fooksman *et al.*, 2010; Zhang *et al.*, 2018), their mutations (Smith *et al.*, 1997; Sze *et al.*, 2000) or by BrdU labelling (Sze *et al.*, 2000; Weisel *et al.*, 2016).

Several gene reporter models were used to identify GC lineage cells. The Cγ1-Cre targeted knock-in model (Casola *et al.*, 2006) is a mouse where Cre recombinase is inserted downstream of the IgG1 heavy chain locus. This is transcribed during induction of CSR to IgG1, as this is associated with strong induction of IgG1 heavy chain germline transcription. In combination with Cre-inducible EYFP expression, Cγ1-Cre can label >85% of GC B-cells 10-14 days post immunisation with T-D antigen (Casola *et al.*, 2006). However, as the Cre recombinase is constitutively expressed under endogenous Cγ1 control, this limits the model to the study of PCs induced by Th2 responses (Bergstedt-Lindqvist *et al.*, 1984; Stevens *et al.*, 1988) and is not broadly applicable to all antigens. The *Aicda*^{ERT2Cre} transgenic model (Dogan *et al.*, 2009)

relies on the expression of *Aicda*, which encodes AID, preferentially occurring within GC B-cells. However, AID is involved in the independent processes of CSR and SHM (Muramatsu *et al.*, 2000). Non-coding mRNA germline transcripts (GLTs) are transcribed from regions upstream of all Ig except for IgD and their expression precedes Ig recombination with constant heavy chain regions (Stavnezer, 1996). The notion of CSR occurring primarily in the GC was maintained despite accumulating evidence of GLT detection and CSR events occurring: (i) before the onset of the GC response (Toellner *et al.*, 1996; Marshall *et al.*, 2011; Zhang *et al.*, 2018), (ii) within B-cells differentiating extrafollicular (García De Vinuesa *et al.*, 1999), and (iii) the observation that isotype switched Ab titres were unaffected in mice with defective GC responses (Kitano *et al.*, 2011). A recent study by Roco and colleagues used flow cytometry, immunofluorescence histology and single cell qPCR to demonstrate that GLT expression peaks during B-cell activation prior to GC formation when *Bcl6* and *Aicda* are at their peak, that *Aicda* mRNA can be detected 24 h before EF PC or GC B-cells, that there are comparable levels of isotype switched cells in the EF PC and early GC B-cell compartments, and that GLTs remained diminished throughout GC reactions measured out to day 18 post immunisation (Roco *et al.*, 2019). Further, using SRBC immunised Cγ1-Cre.*Rosa26*^{mTmG} mice they observed IgG1 switched mGFP^{+} cells by day 2 after immunisation at the T:B border (Roco *et al.*, 2019). This means that fate-mapped cells produced by both the Cγ1-Cre and *Aicda*^{ERT2Cre} models are labelled prior to GC experience. Hence, for these transgenic models this limits the specific identification of true GCmat PCs at the earliest stages of the GC response, when GCmat PC output is at its peak, to histological methods which rely on location in the GTI (Zhang *et al.*, 2018).

The transient reporters *S1pr2*$^{Venus/wt}$ and Bcl6$^{YFP/wt}$ have been used to study GC reactions, however, mice bred homozygous for these knock-in alleles cannot be used for immunological studies of "normal" GC dependent responses (Kitano *et al.*, 2011; Moriyama *et al.*, 2014). The targeting vector used to generate *S1pr2*^{Venus} replaced the first 498 bp of protein coding sequence creating a non-functional allele. Phenotype analysis revealed that 40% of *S1pr2*$^{Venus/Venus}$ mice display neurological impairments and die by 3-5 weeks of age in seizure-like positions, but the remaining adult mice would display impaired GC responses as they are S1PR2 deficient (Green *et al.*, 2011; Moriyama *et al.*, 2014). This phenotype could in part be attributed to the function(s) that S1PR2 has in numerous non-hematopoietic cell types, for example regulating epithelial and mesenchymal stem cell differentiation (Price *et al.*, 2015; Petti *et al.*, 2020). Adult mice homozygous for the Bcl6-YFP chimeric protein, Bcl6$^{YFP/YFP}$, are healthy but have significantly reduced GC B-cell and Tfh cell numbers (Kitano *et al.*, 2011). Further, the spectral characteristics of *S1pr2*$^{Venus/wt}$, Bcl6$^{YFP/wt}$ and Bcl6-YFP GC reporter mice mean that crosses with current *Prdm1* reporters are either entirely unfeasible (for the *Prdm1*^{EYFP} mouse (Rutishauser *et al.*, 2009)), or would be generate a system where it would be very difficult to correctly resolve GC and recently differentiated GCmat PC populations by fluorescence detection methods if crossed with the *Prdm1*$^{GFP/+}$ reporter.

Within peripheral B-cell lineages, *S1pr2* expression is highly specific for both LZ and DZ GC B-cells (Green *et al.*, 2011; Shinnakasu *et al.*, 2016). Shinnakasu and colleagues created the *S1pr2*^{ERT2Cre} mouse by random integration of a modified BAC which contained and ATG fusion of ERT2Cre to *S1pr2* exon 2 (Shinnakasu *et al.*, 2016). This approach leaves the endogenous *S1pr2* alleles intact and thus removes both the potential impact of reduced S1PR2 expression in non-hematopoietic cell types (Price *et al.*, 2015; Petti *et al.*, 2020) and the known deleterious

effects exhibited by homozygous *S1pr2*$^{Venus/Venus}$ mice (Moriyama *et al.*, 2014). These mice have been used to fate map and study GC output by combination with Cre-inducible fluorescent reporters (Shinnakasu *et al.*, 2016; Ise *et al.*, 2018). The specificity and inducible capability to timestamp and fate map all GC-experienced cells, with predicted minimal impact to normal S1PR2 function, makes the *S1pr2*^{ERT2Cre} model the best current option for studying GC B-cells and their progeny (Shinnakasu *et al.*, 2016; Ise *et al.*, 2018).

3.1.3 Objectives and Aims.

The objective of this Chapter was to highlight the necessity for a novel fluorescent reporter model which could specifically distinguish between EF and GCmat PCs during the peak of GCmat PC output in the early GC, and to then design and validate such a model to interrogate basic immunology questions regarding PC differentiation but also test whether high affinity mAb production could be expedited.

The aims were as follows:

1. Test the usefulness of the *Aicda*^{ERT2Cre}.*Rosa26*^{mTmG} model for the study of GCmat PCs during the peak PC output in the early GC response.
2. Design, breed and validate a novel transgenic fluorescent reporter model by combining existing GC-specific (*S1pr2*) and PC-specific (*Prdm1*) transgenic alleles to study GCmat PCs at any time-point.
3. Test whether mice with fluorescent reporting of GC experience can used to streamline production of mAbs.

3.2 Results

3.2.1 The limitations of the *Aicda*$^{ERT2Cre/+}$.*Rosa26*^{mTmG} model for studying GCmat PCs.

Amongst other models, Zhang and colleagues used immunised *Aicda*$^{ERT2Cre/+}$.*Rosa26*^{mTmG} mice to study GCmat PBs in the GTI by immunofluorescence histology at the earliest time after GC onset (Zhang *et al.*, 2018). Although *Aicda* is expressed during CSR and in B-cells prior to differentiation into GC B-cells (Marshall *et al.*, 2011; Roco *et al.*, 2019), we wanted to test the usefulness of *Aicda*$^{ERT2Cre/+}$.*Rosa26*$^{mTmG/+}$ model for study of GCmat PCs at the earliest stage after GC formation by flow cytometry. To do this we immunised *Aicda*$^{ERT2Cre/+}$.*Rosa26*$^{mTmG/+}$ mice with SRBC i.v. and labelled all cells expressing *Aicda* within a 48 h window before analysis (Figure 3.1).

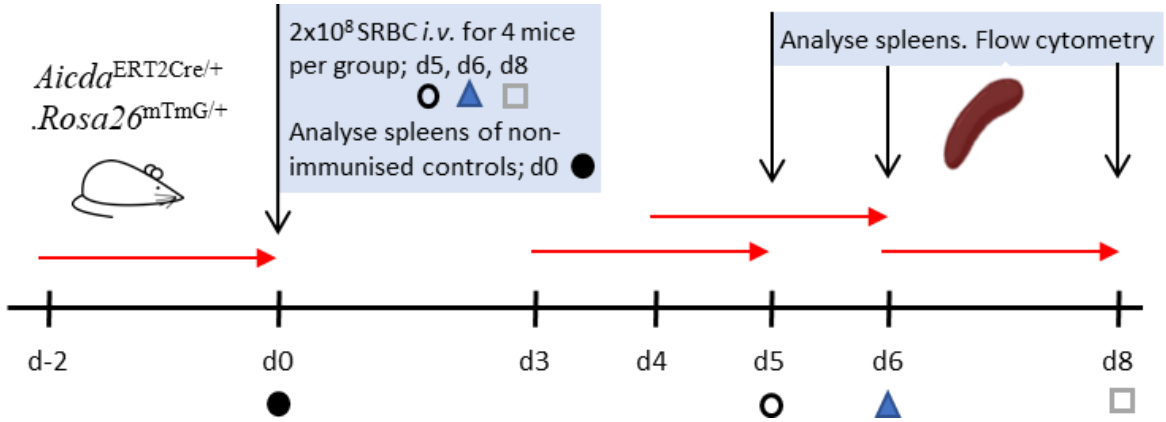

Figure 3.1 **Experimental protocol to assess whether *Aicda*$^{ERT2Cre+}$.*Rosa26*^{mTmG} mice are suitable to study GCmat PCs at the earliest time after GC onset**. Mice were immunised, or not, with SRBC i.v. and received a single 6 mg oral dose of tamoxifen (red arrow) 48 h prior to tissue analysis. Control mice were naïve, non-immunised but received 48 h tamoxifen treatment. Splenocytes were analysed at the indicated time-point post-immunisation.

By day 5 post-immunisation the size of the splenic GC response was significantly greater than background GC size, and this remained steady to day 8 (Figure 3.2A-B). Analysis of GC B-cell DZ (CXCR4^{Hi} CD86^{Lo}) and LZ (CXCR4^{Lo} CD86^{Hi}) phenotypes shows that, as expected

(MacLennan *et al.*, 1990), there is an initial proliferation of blasting GC DZ cells on day 5 which reduces after 24 h and remains steady (Figure 3.2C-E). In-line with the histology data of Zhang and colleagues (Zhang *et al.*, 2018), the efficiency of *Aicda* promoter controlled, tamoxifen induced Cre recombinase activity in GC B-cells was low, as fewer than 30% of DZ and LZ GC B-cells had switched from constitutive mTomato to mGFP expression at all time-points analysed (Figure 3.2F-G). Further, less than 25% of IgG1 switched GC B-cells were also mGFP switched (Figure 3.3A-B). As expected, the total PC response declined significantly from day 5 post-immunisation (Figure 3.3C) as the extrafollicular response was resolved and those short-lived PCs died. mGFP expression was even lower in PCs, with only 11.5% of all PCs being mGFP positive 5 days after immunisation. As there is only minor follicular activity between 3-5 days post immunisation (Zhang *et al.*, 2018), this should mainly reflect *Aicda* expression during EF PC generation. mGFP expression decreased significantly by over 6-fold on days 6 and 8 (Figure 3.3D). This very low mGFP expression rate was also reflected in IgG1 switched PCs (Figure 3.3E). These results indicate that despite a 48 h tamoxifen labelling window there was neither efficient induction of mGFP during extrafollicular PC generation from day 3-5, although this is known to be associated with *Aicda* expression (Marshall *et al.*, 2011; Roco *et al.*, 2019). In early GC B-cells from day 5 of the response there was also low efficiency of mGFP induction, despite *Aicda* being repeatedly induced in GC B cells and being crucial for GC affinity maturation (Figure 3.2F-G). Inefficient Cre recombinase induced mGFP expression could be explained by: (i) low levels of *Aicda*^{ERT2Cre} expression, (ii) inefficient Cre mediated recombination between the LoxP sites flanking the mTomato sequence, or (iii) a combination of (i) and (ii). Tas and colleagues have reported between 40-50% of Cre mediated recombination 72 h after a single 15 mg dose of tamoxifen given to *Aicda*^{ERT2Cre}.*Rosa26*^{Confetti} mice (Tas *et al.*, 2016). The distance between LoxP sites which flank the target sequence for

recombinase mediated excision also influences recombination efficiency, which was demonstrated by Vooijs and colleagues who bred multiple floxed alleles to a *Rosa26*^{ERT2Cre} mouse (Vooijs, Jonkers and Berns, 2001). Our data indicates that the *Aicda*$^{ERT2Cre/+}$.*Rosa26*$^{mTmG/+}$ model is an inefficient method to label a significant part of GCmat PC at the peak of their generation, but it is not clear which transgenic allele is limiting this.

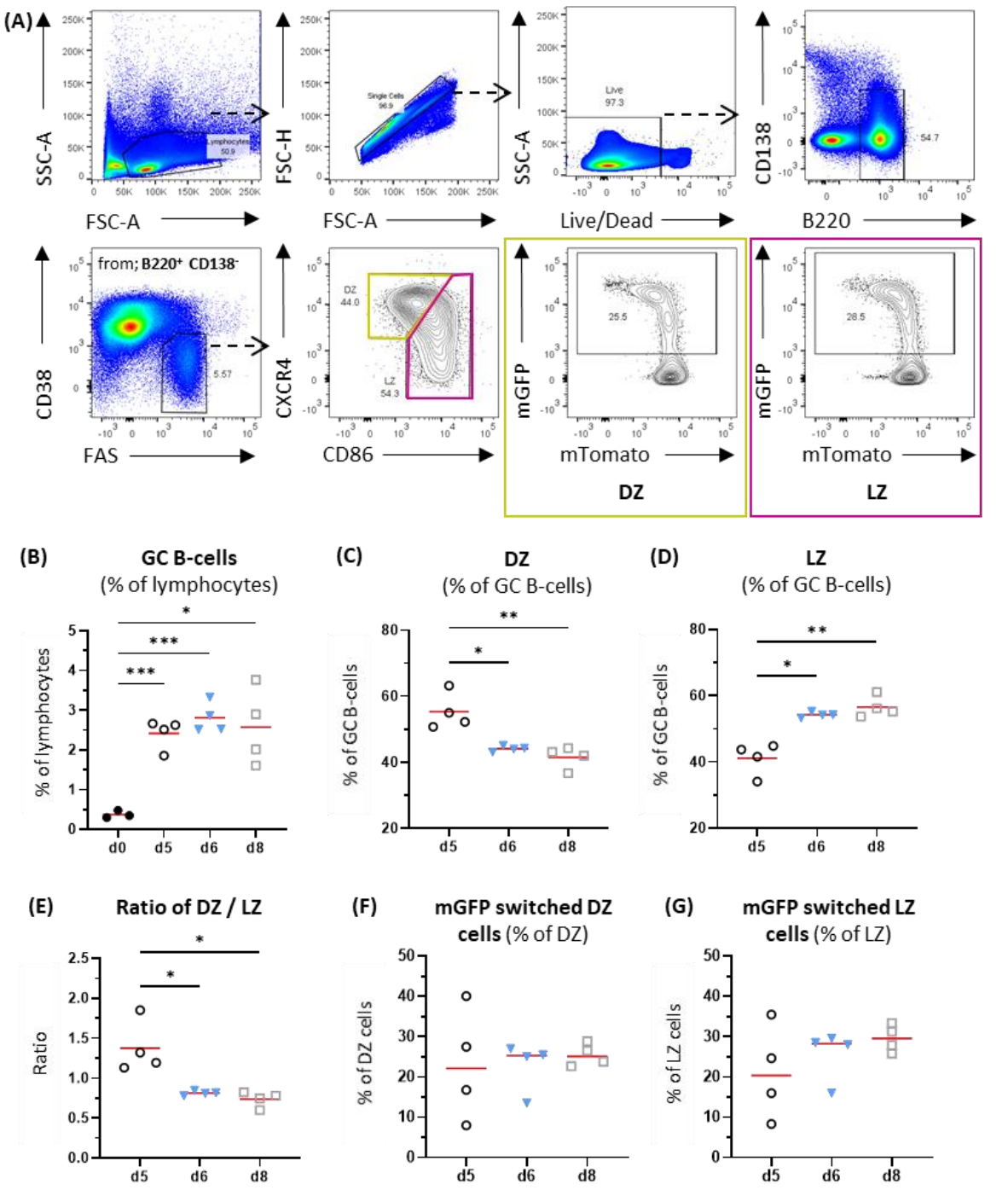

Figure 3.2 **Low levels of GC fate-mapping displayed by the *Aicda*$^{ERT2Cre/+}$.*Rosa26*^{mTmG} model**. Flow cytometric analysis of splenic GC B-cell phenotypes from immunised *Aicda*$^{ERT2Cre/+}$.*Rosa26*$^{mTmG/+}$ mice (Figure 3.1). Representative gating **(A)**. Analysis of GC B-cells **(B)**, DZ GC B-cells **(C)**, LZ GC B-cells **(D)**, ratio of DZ to LZ GC B-cells **(E)** and levels of tamoxifen induced *Aicda*-ERT2Cre fate mapping in the DZ **(F)** and LZ **(G)**. Data from one experiment, each symbol represents an individual mouse. Brown-Forsythe & Welch ANOVA with unpaired Welch's t-test (B, C, D, E) and Kruskal-Wallis with uncorrected Dunn's test (F, G).

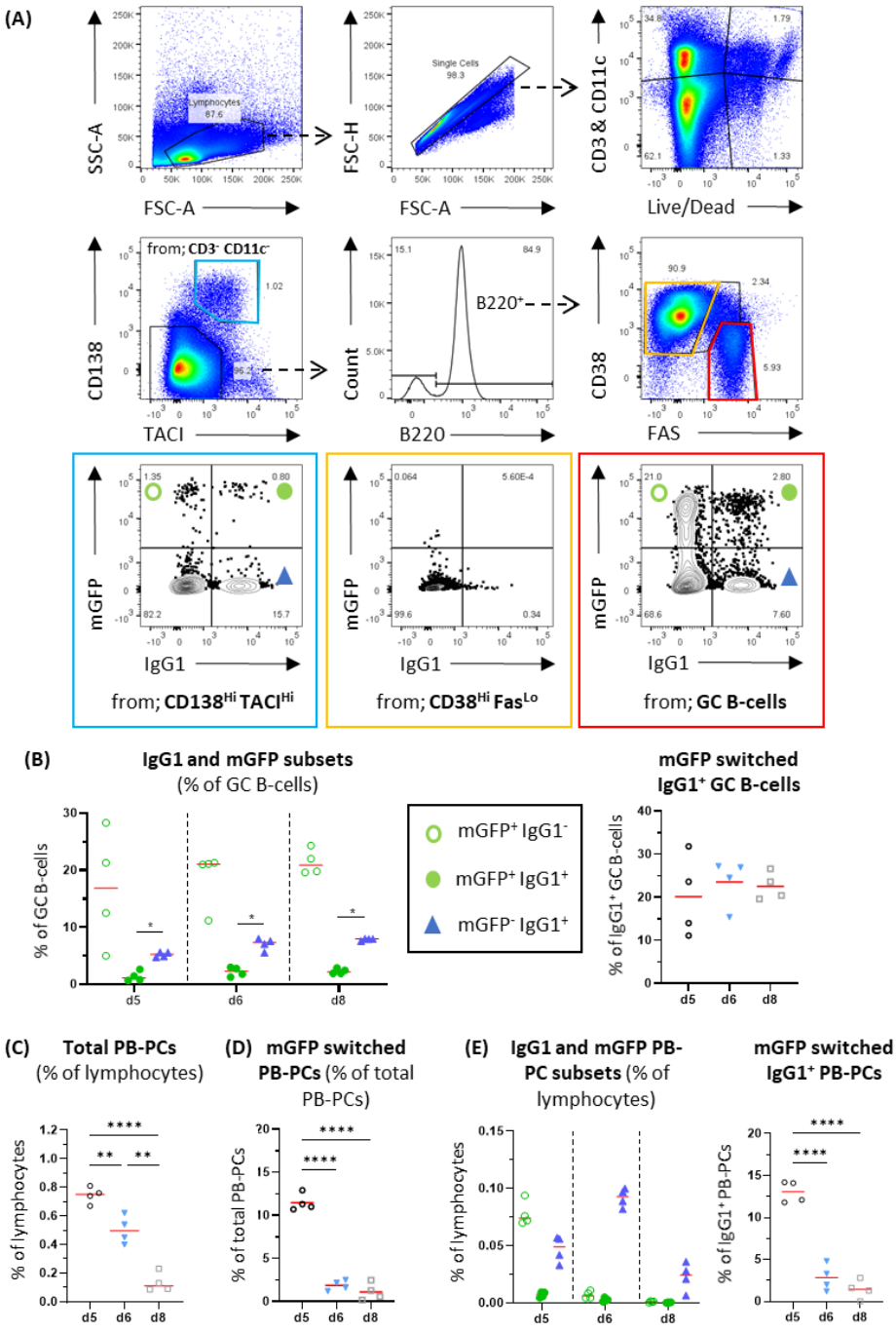

Figure 3.3 **Further evaluation of GCs and PCs in the *Aicda*$^{ERT2Cre/+}$.*Rosa26*^{mTmG} model.** Analysis of splenic PB/PCs and GC B-cells from immunised *Aicda*$^{ERT2Cre/+}$.*Rosa26*$^{mTmG/+}$ mice (Figure 3.1). Representative gating **(A)**. Analysis of GC B-cell IgG1 isotype and mGFP switch rates **(B, left)** and the level of mGFP expression amongst IgG1^{+} **(B, right)**. Total PC response **(C)**, level of mGFP switched PCs **(D)**, PC IgG1 isotype and mGFP switch rates **(E, left)** and the level of mGFP expression amongst IgG1^{+} PCs **(E, right)**. Data from one experiment, each symbol represents an individual mouse. Brown-Forsythe & Welch ANOVA with unpaired Welch's t-test (C-E) and Mann-Whitney test between mGFP^{+} IgG1^{+} and mGFP^{-} IgG1^{+} populations only (B).

3.2.2 The kinetics of Cre inducible fluorescent reporter systems.

To test whether the inefficient labelling of GCmat output at the earliest stage of the GC formation in the *Aicda*$^{ERT2Cre/+}$.*Rosa26*$^{mTmG/+}$model is due to inefficient Cre expression or inefficient Cre-mediated recombination of the mTmG reporter, we used different combinations of inducible Cre and floxed fluorescent reporters. For this we generated *Aicda*$^{ERT2Cre/+}$.*Rosa26*^{LSLtdTomato} and *S1pr2*^{ERT2Cre}.*Rosa26*^{LSLtdTomato} mice and used *Aicda*$^{ERT2Cre/+}$.*Rosa26*$^{mTmG/+}$ mice as a comparator which displayed low efficiency of fate mapping. Mice were immunised with SRBC i.v. before pulse-chase with a single dose of tamoxifen on day 5 after immunisation (Figure 3.4). This time-point was selected for administration of tamoxifen as a compromise between fully formed GCs with intermediate GCmat PC output expected in the 48 h up to day 7 (Zhang *et al.*, 2018) and minimising labelling of activated B-cells undergoing CSR, as the majority of SRBC-specific splenic B-cells would have been activated before day 5 (Sze *et al.*, 2000; Roco *et al.*, 2019).

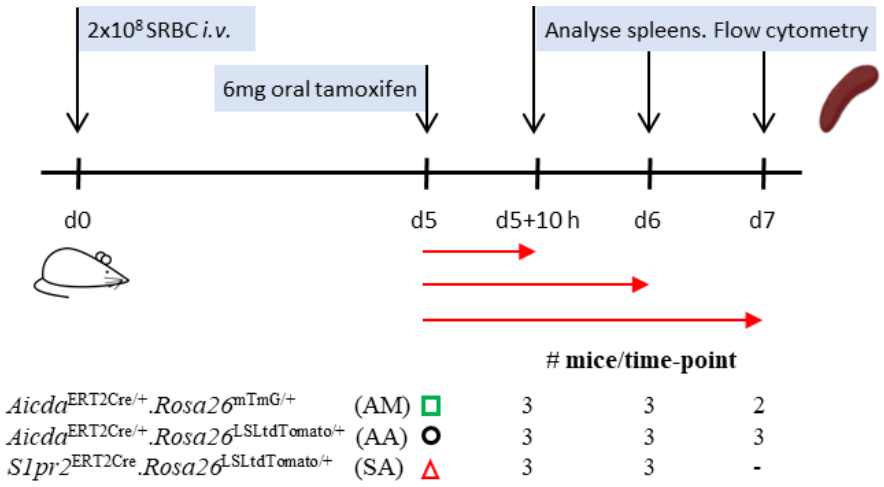

Figure 3.4 **Experimental protocol to assess the kinetics of GC fate map labelling for various tamoxifen inducible fluorescent reporter models.** All mice were immunised with SRBC intravenous and received a single 6 mg dose of tamoxifen by gavage 5 d after immunisation to fate map *Aicda* or *S1pr2* expressing cells within the next 10 h, 24 h, or 48 h (red arrows).

Aicda$^{ERT2Cre/+}$.*Rosa26*$^{mTmG/+}$ mice displayed both slow kinetics and poor levels of GC B-cell fate mapping after 48 h, with only 4.4% of GC B-cells mGFP switched 10 h after tamoxifen induction which only increased to 30.3% after 48 h (Figure 3.5A and B), in-line with previous data (Figure 3.2F-G). However, *Aicda*$^{ERT2Cre/+}$.*Rosa26*$^{LSLtdTomato/+}$ mice demonstrated fast and efficient fate mapping with 63.2% of GC B-cells tdTomato^{+} only 10 h after tamoxifen induction, a 14-fold improvement compared to *Aicda*$^{ERT2Cre/+}$.*Rosa26*$^{mTmG/+}$ mice (Figure 3.5A-B). By 24 h, tdTomato^{+} fate mapped GC B-cells constituted more than 90% of total GC B-cells for *Aicda*$^{ERT2Cre/+}$.*Rosa26*$^{LSLtdTomato/+}$ mice, 4-fold more efficient than *Aicda*$^{ERT2Cre/+}$.*Rosa26*$^{mTmG/+}$ mice (Figure 3.5A-B). It is unlikely that fluorescent protein maturation is the cause for this observed difference, as EGFP has a maturation half time ~ 4-fold faster than tdTomato at 37 °C (Iizuka, Yamagishi-Shirasaki and Funatsu, 2011; Piatkevich and Verkhusha, 2011). Further, it is unlikely that the level of *Aicda* driven Cre recombinase expression is the cause, as the *Aicda*$^{ERT2Cre/+}$.*Rosa26*^{LSLtdTomato} model showed fast and efficient FP induction. This highlighted that the rate- and efficiency-limiting step for fate mapping in the *Rosa26*^{mTmG} model is likely to be Cre-mediated recombination between distant LoxP sites (Vooijs, Jonkers and Berns, 2001), which are separated by 1653 bp containing the mTomato DNA sequence (Muzumdar *et al.*, 2007). The higher efficiency in *Rosa26*$^{LSLtdTomato/+}$ mice is probably due to the fact that the LoxP sequences are only separated by a STOP codon (Vooijs, Jonkers and Berns, 2001; Madisen *et al.*, 2010). Similarly, the *S1pr2*^{ERT2Cre}.*Rosa26*$^{LSLtdTomato/+}$ model displayed quick and efficient fate mapping, with 44.8% of GC B-cells tdTomato^{+} 10 h after induction, rising to 72.7% after 24 h (Figure 3.5A-B). This is in-line with published kinetic fate mapping data (Shinnakasu *et al.*, 2016). Although the GC fate map kinetics for the *S1pr2*^{ERT2Cre}.*Rosa26*$^{LSLtdTomato/+}$ model were not quite as fast as *Aicda*$^{ERT2Cre/+}$.*Rosa26*$^{LSLtdTomato/+}$ mice 10 h after tamoxifen induction, the difference in the

frequency of tdTomato^{+} GC B-cells was less than 20%, and this difference was maintained at 24 h post induction (Figure 3.5B). This could be explained by different levels of Cre expression between the models. Further, when either of the ERT2Cre reporters was combined with *Rosa26*^{LSLtdTomato} they fate mapped at least 3-fold more CD138^{Hi} B220$^{Lo/Int}$ PBs-PCs at either 10 h or 24 h post-induction compared to the *Aicda*^{ERT2Cre}.*Rosa26*^{mTmG} model (Figure 3.5C), highlighting that the *Rosa26*^{LSLtdTomato} model is better suited to quickly labelling GCmat output than the *Rosa26*^{mTmG} model. Despite the *Aicda*$^{ERT2Cre/+}$.*Rosa26*$^{LSLtdTomato/+}$ model displaying a modest increase in speed of GC B-cell fate mapping than the *S1pr2*^{ERT2Cre}.*Rosa26*^{LSLtdTomato} model, the specificity of *S1pr2* expression within B-cells to GC B-cells (Green *et al.*, 2011; Shinnakasu *et al.*, 2016) and not to class-switched extrafollicular cells (Marshall *et al.*, 2011; Roco *et al.*, 2019), means that in downstream assays tamoxifen administration on either day 3 or day 4 post-immunisation should ensure that the majority of genuine GCmat PCs are identified at the peak of their output from the early GC. In retrospect, an experiment that could have provided definitive evidence that the *S1pr2*^{ERT2Cre} transgenic model was superior to the *Aicda*^{ERT2Cre} model for labelling GCmat PCs, would have been to analyse the BCRs of single cell sorted tdTomato^{+} PCs for accumulation of high-affinity mutations and overall mutational burden from *S1pr2*^{ERT2Cre}.*Rosa26*^{LSLtdTomato} and *Aicda*$^{ERT2Cre/+}$.*Rosa26*$^{LSLtdTomato/+}$ mice at day 5 of a T-dependent response to the model hapten NP.

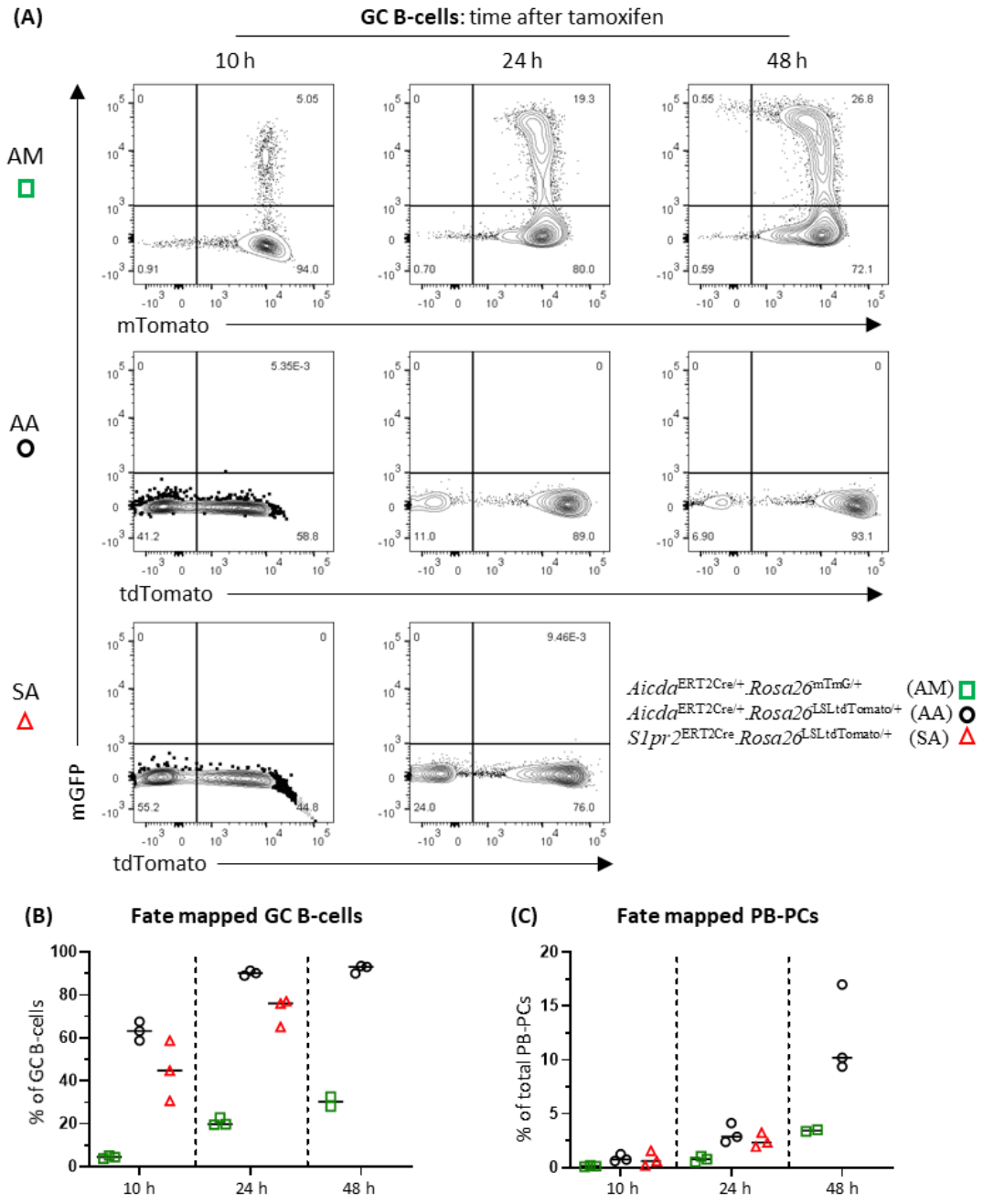

Figure 3.5 **The *Rosa26*$^{\text{LSLtdTomato}}$ inducible reporter displays quicker and more efficient fate map capability than the *Rosa26*$^{\text{mTmG}}$ model**. Kinetic analysis of inducible permanent fate mapping to primary SRBC response in the spleens of *Aicda*$^{\text{ERT2Cre/+}}$.*Rosa26*$^{\text{mTmG/+}}$ (AM, open green squares), *Aicda*$^{\text{ERT2Cre/+}}$.*Rosa26*$^{\text{LSLtdTomato}}$ (AA, open black circles) and *S1pr2*$^{\text{ERT2Cre}}$.*Rosa26*$^{\text{LSLtdTomato}}$ (SA, open red triangles) mice by flow cytometry (Figure 3.4). Representative 2D plots of fate mapped GC B-cells (CD138$^{\text{Lo}}$ B220^{+} CD38$^{\text{Lo}}$ Fas^{+}) at each time-point for each genotype **(A)**. Summary of fate map efficiency within GC B-cells **(B)** and all PB-PCs (CD138$^{\text{Hi}}$ B220$^{\text{Lo/int}}$) **(C)**. Data from one experiment, each symbol represents an individual mouse. Insufficient *S1pr2*$^{\text{ERT2Cre}}$.*Rosa26*$^{\text{LSLtdTomato}}$ mice (SA, open red triangles) were available for assessment at 48 h time-point.

3.2.3 Rationale and development of the High-Affinity LOw-affinity (HALO) PC model.

We desired an *in vivo* fluorescent reporter model that could specifically identify GCmat PCs by flow cytometric and microscopy techniques. This would allow to interrogate signals, mechanisms and interactions which drive differentiation of high affinity GC B-cells. This could also become a useful tool for antibody discovery.

The tamoxifen inducible *S1pr2*^{ERT2Cre} transgenic mouse (Shinnakasu *et al.*, 2016) is currently the most suitable model for GC B-cell fate mapping (discussed in Section 3.1.2), and we confirmed quick and efficient fate mapping in a preliminary experiment with early GC output (Figure 3.5B). This supported the use of this gene to label GC B-cells and their recent differentiated progeny. The decision as to which Cre recombinase-inducible FP reporter to use was influenced by the kinetics and efficiency of Cre recombinase induction and compatibility with the available options for fluorescent PC reporter models. The *Rosa26*^{Confetti} allele (Snippert *et al.*, 2010) has previously been used to study GC clonality and GC output (Tas *et al.*, 2016; Zhang *et al.*, 2018). The Confetti allele uses the brainbow FP cassette comprised of GFP, YFP, RFP and CFP (Livet *et al.*, 2007) and therefore cannot be combined with any of the existing *Prdm1* reporter strains, *Prdm1*$^{GFP/+}$ or *Prdm1*^{EYFP}. Moreover, Cre recombination was only detected in 40-50% of GC B-cells 72 h after tamoxifen induction in *Aicda*^{ERT2Cre}.*Rosa26*^{Confetti} (Tas *et al.*, 2016) suggesting that, similar to the *Rosa26*^{mTmG} model (Figure 3.2 and Figure 3.5), the extent Confetti labelled GCmat PCs would be limited due to distance between LoxP sequences (Vooijs, Jonkers and Berns, 2001). The *Rosa26*^{LSLtdTomato} model has demonstrated superior recombination speed and efficiency to the *Rosa26*^{mTmG} model (Figure 3.5B, Figure 3.2F-G and (Zhang *et al.*, 2018)). Further, others have already used the combination of the

S1pr2^{ERT2Cre} and *Rosa26*^{LSLtdTomato} alleles to study GC progeny and demonstrated that this works at high efficiency (Shinnakasu *et al.*, 2016; Ise *et al.*, 2018).

With the selections for tamoxifen inducible Cre and Cre-inducible fluorescent reporters made, the final step was the choice of which PC-specific *Prdm1* controlled fluorescent reporter to incorporate. Despite non-viable homozygous breeding (discussed in Section 3.1.2), the *Prdm1*$^{GFP/+}$ allele (Kallies *et al.*, 2004) is very well characterised and established for study of PC biology in comparison to the BAC transgenic *Prdm1*^{EYFP} model ((Rutishauser *et al.*, 2009; Fooksman *et al.*, 2010) and discussed in Section 1.7). Therefore, *Prdm1*$^{GFP/+}$ was selected for inclusion into the breeding strategy.

A breeding strategy was devised which combined *S1pr2*^{ERT2Cre} and *Rosa26*^{LSLtdTomato} mice, generating an intermediary "GC fate mapper" mouse, with subsequent breeding to *Prdm1*$^{GFP/+}$ mice (Figure 3.6A). After tamoxifen induction, this novel combination of alleles (Figure 3.6A) should simultaneously delineate GC B-cells, EF PCs and GCmat PCs (Figure 3.6B). This predicted ability to distinguish between high affinity GCmat PCs and non-affinity matured low-affinity EF PCs underpins the designation of this novel model; the High-Affinity LOw-affinity (HALO) PC mouse. This proposed model has a number of benefits, including the ability to: a) study GCmat PCs at the peak of their output from the early GC with the ability to distinguish them from EF PCs, b) identify and isolate GCmat PCs by FACS without manipulation with fluorochrome conjugated antibody labelling, and c) identify GCmat PCs by intravital imaging without additional of exogenous fluorochrome labelled antibodies.

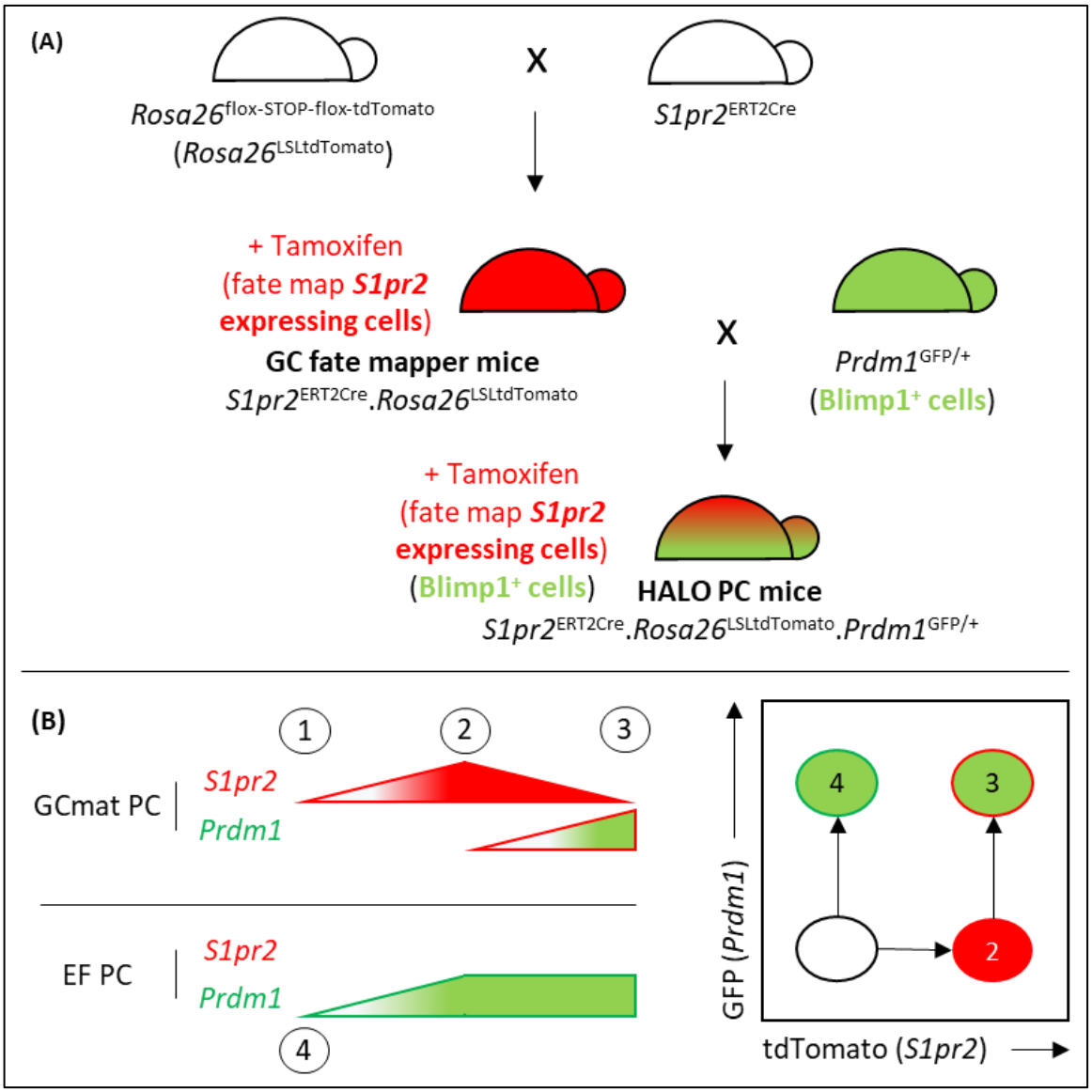

Figure 3.6 **Breeding strategy to generate HALO (High-Affinity and LOw-Affinity marked) PC mice**. **(A)** Breeding schematic for GC fate mapper and HALO PC mice. In both models, tamoxifen administration induces permanent tdTomato expression in cells currently expressing *S1pr2* promoter controlled ERT2Cre. In HALO PC mice, *Prdm1* expressing cells are GFP^{+}. **(B, left)** Schematic detailing gene expression level (shape height), reporter fluorescence intensity (gradient of shape fill) and permanent fate map colour(s) (shape line and fill colour). **(B, right)** 2D schematic flow cytometric plot to demonstrate the predicted populations which can be distinguished intrinsically within HALO PC mice after tamoxifen administration during an immune response; antigen activated B-cell (1), GC B-cell (2), GC matured (GCmat) PC (3) and extrafollicular (EF) PC (4).

Our initial breeding strategy was to generate sufficient HALO PC mice for multiple pairs of HALO PC mice to be interbred. This was hypothesised to achieve the highest percentage of offspring carrying all three alleles. During the 16 months when generation of HALO PC mice was possible (Dec-2018 to Mar-2020), 35 HALO PC mice were successfully weaned (Table 3.1). Attempts to interbreed HALO PC mice resulted in unsuccessful weaning of 37 pups (Table 3.1). Although *Prdm1*$^{GFP/GFP}$ is prenatal embryonic lethal (Kallies *et al.*, 2004), our breeding showed that two *Prdm1*$^{GFP/+}$ heterozygous parents could produce live offspring. However, it is not clear if resorption of *Prdm1*$^{GFP/GFP}$ embryos within the womb had a detrimental effect on the remainder of the litter *in utero*, or on the ability of the mother to wean the pups. Retrospective analysis of breeding suggested that interbreeding parents which both carry the *Rosa26*^{LSLtdTomato} and either the *S1pr2*^{ERT2Cre} or the *Prdm1*$^{GFP/+}$ was the most efficient approach, with 77% of pups born to such allelic combinations being successfully weaned. As such, further breeding pairs employed this approach. Despite lower than anticipated breeding efficiency at the outset, 15 HALO PC mice were available for experiments to validate the novel combination of these transgenic alleles before March 2020 (Table 3.1). However, no additional mice were available for the remainder of 2020 due to COVID-19 lockdowns and the requirement for all colonies to be reduced to only the minimum number of breeding pairs to maintain stocks of transgenic alleles.

Breeding pairs	
# of pairs that <u>could</u> produce HALO PC	**# of pairs that were <u>not productive</u>: either no litters or no pups that survived past weaning (%)**
32	11 (34%)

HALO PC mice and their use (until colony crash Mar-2020)			
# of mice born	**# of mice used for breeding**	**# of mice for experiments**	**# of mice died of unrelated issue before use**
35	19	15	1

Breeding pairs where both parents are HALO PC mice			
# of pairs	**# of pairs that produced litters (%)**	**# of litters born**	**# of mice that survived beyond weaning (pups born)**
5	4 (80%)	11	0 (37)

Table 3.1 **Breeding of HALO PC mice**. Analysis of the breeding programme to produce HALO PC mice from mating of the first pair capable of producing HALO PC pups (Dec-2018) until colony crash at the start of the UK COVID-19 pandemic restrictions (end of March-2020).

3.2.4 The efficiency of GCmat PC labelling using *S1pr2*^{ERT2Cre}.*Rosa26*^{LSLtdTomato} mice.

The *S1pr2*^{ERT2Cre}.*Rosa26*^{LSLtdTomato} model has been used to investigate gene expression of GC output and LZ GC B-cell fractions at the late stages of the GC response (Ise *et al.*, 2018), but not during the peak of PC output from the early GC (Zhang *et al.*, 2018). Whilst breeding of the triple transgenic HALO PC mouse was underway, we wanted to use double transgenic intermediates ("GC fate mapper" mice; Figure 3.6A) to validate our experimental system to induce and study maximal GCmat PC output from the early GC. To do this we induced SRBC immunised or naïve *S1pr2*^{ERT2Cre}.*Rosa26*^{LSLtdTomato} with a single dose of tamoxifen for 48 h before analysing the response for GCmat PCs in the spleen and BM (Figure 3.7).

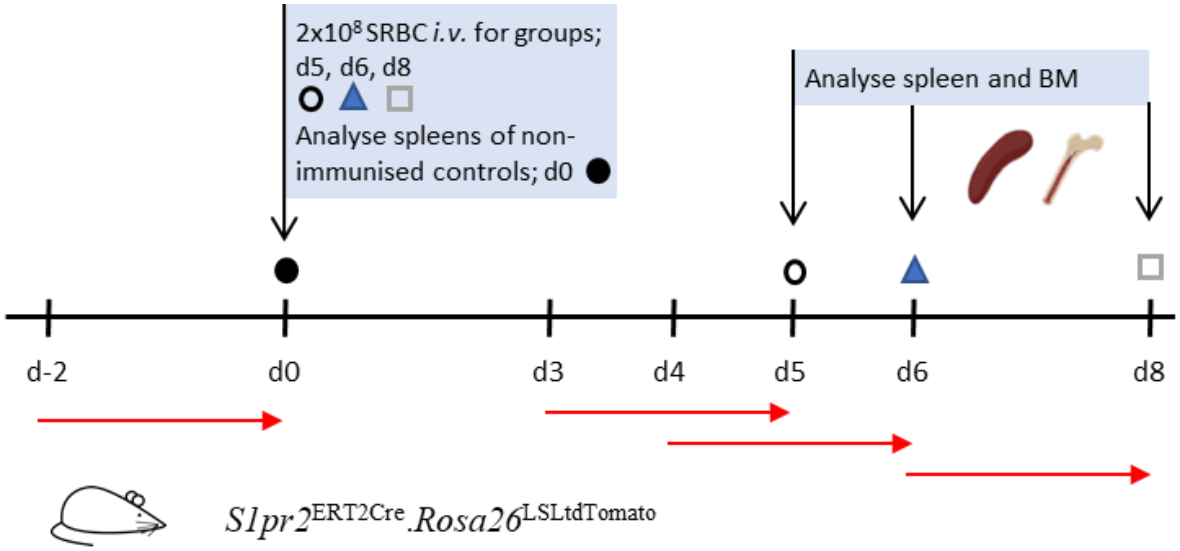

Figure 3.7 **Experimental protocol to validate experimental system to evaluate GCmat PCs from the early GC**. Naïve or SRBC i.v. immunised mice received a single 6 mg dose of tamoxifen by gavage 48 h prior (red arrow) to tissue analysis at the indicated time-point in the primary response or naïve background control (d0). As a control for the specificity of Cre recombinase activity, a single mouse in the d5 response group did not receive tamoxifen. Spleens were partitioned, with ~1/3 used for flow cytometry and the remainder formaldehyde fixed and frozen. BM lymphocytes were analysed by flow cytometry only.

As expected (Zhang *et al.,* 2018), splenic GCs formed by day 5 of primary SRBC immunisation (Figure 3.8A-B) and in immunised *S1pr2*^{ERT2Cre}.*Rosa26*^{LSLtdTomato} mice very high levels of GC B-cells, exceeding 85%, were fate mapped 48 h after a single dose of tamoxifen (Figure 3.8C). As expected, (MacLennan *et al.,* 1990), and like *Aicda*$^{ERT2Cre/+}$.*Rosa26*$^{mTmG/+}$ mice (Figure 3.2C-E), the DZ:LZ ratio indicated a larger DZ compartment on day 5 which was reduced on days 6 and 8 (Figure 3.8D).

In addition to the combined extrafollicular and GCmat CD138^{Hi} TACI^{Hi} PC response and GCmat PC response alone, we wanted to explore the phenotypes of GCmat PCs during the early GC response. Pracht and colleagues have defined three PC maturation stages based upon sequential loss of B220 and CD19 expression: B220^{+} CD19^{+} represent plasmablasts (P1), B220^{-} CD19^{+} as early PCs (P2) and fully differentiated B220^{-} CD19^{-} mature PCs (P3) (Pracht *et al.*, 2017). The splenic CD138^{Hi} TACI^{Hi} PC response was analysed for the proportions of EF and GC-experienced cells and their maturity (Figure 3.9). As expected, the total splenic CD138^{Hi} TACI^{Hi} PC response peaked at days 5 and 6 post primary i.v. SRBC immunisation and decreased to background by day 8 (Figure 3.10A-B). The proportion of GCmat PCs in the spleen rose after day 5, concurrent with the resolution of the EF PC response (Figure 3.10C). Interestingly, the peak accumulation of GCmat PCs measured by flow cytometry was at day 6 (Figure 3.10D-E) and there was no decrease in the frequency of GCmat PCs between days 6 and 8 (Figure 3.10D). This peak was 24 h later than determined by identification of GTI PBs by histology (Zhang *et al.*, 2018). Loss of spatial information by flow cytometry could account for these differences. Histological methods can identify nascent GC emigrant immature GTI PBs as a snapshot of GCmat PC output at that exact time-point, whereas flow cytometric measurements will identify both these GTI PBs as well as those mature GCmat PCs that have

migrated to splenic PC niches. The ratio of GCmat PC output to GC size was increased for cells labelled between days 4-6 and days 6-8 compared to the days 3-5 (Figure 3.10F), consistent with a peak in output during the early stage after GC formation.

Maturity analysis using B220 and CD19 expression (Figure 3.9) showed that, as expected, the proportion of GCmat P1 PBs within the total EF and GCmat P1 PB compartment rose as the extrafollicular response resolved (Figure 3.11A). However, the proportion of GCmat P1 PBs of all GCmat PB-PCs remained steady during all tamoxifen labelling windows at ~50% (Figure 3.11B). The GCmat P1 PB compartment reflected the overall GCmat PC response as it was significantly larger at day 6 than at day 5 and displayed an increasing output ratio compared to GC size as the immune response progressed (Figure 3.11C-F). The frequency and proportions of GCmat early P2 PCs ($B220^{-}$ $CD19^{+}$) were similar to GCmat P1 PBs (data not shown). Similarly, the proportion of GCmat mature P3 PCs of total mature P3 PCs rose as time progressed (Figure 3.11G). Like GCmat P1 PBs, the proportion of GCmat P3 mature PCs peaked at day 6, however, this then significantly decreased 48 h later (Figure 3.11H-L). This decrease in mature splenic GCmat P3 PCs is not unexpected, as local PC niches could have reached maximum capacity (Sze *et al.*, 2000) and these mature PCs could have started to migrate to the BM niches.

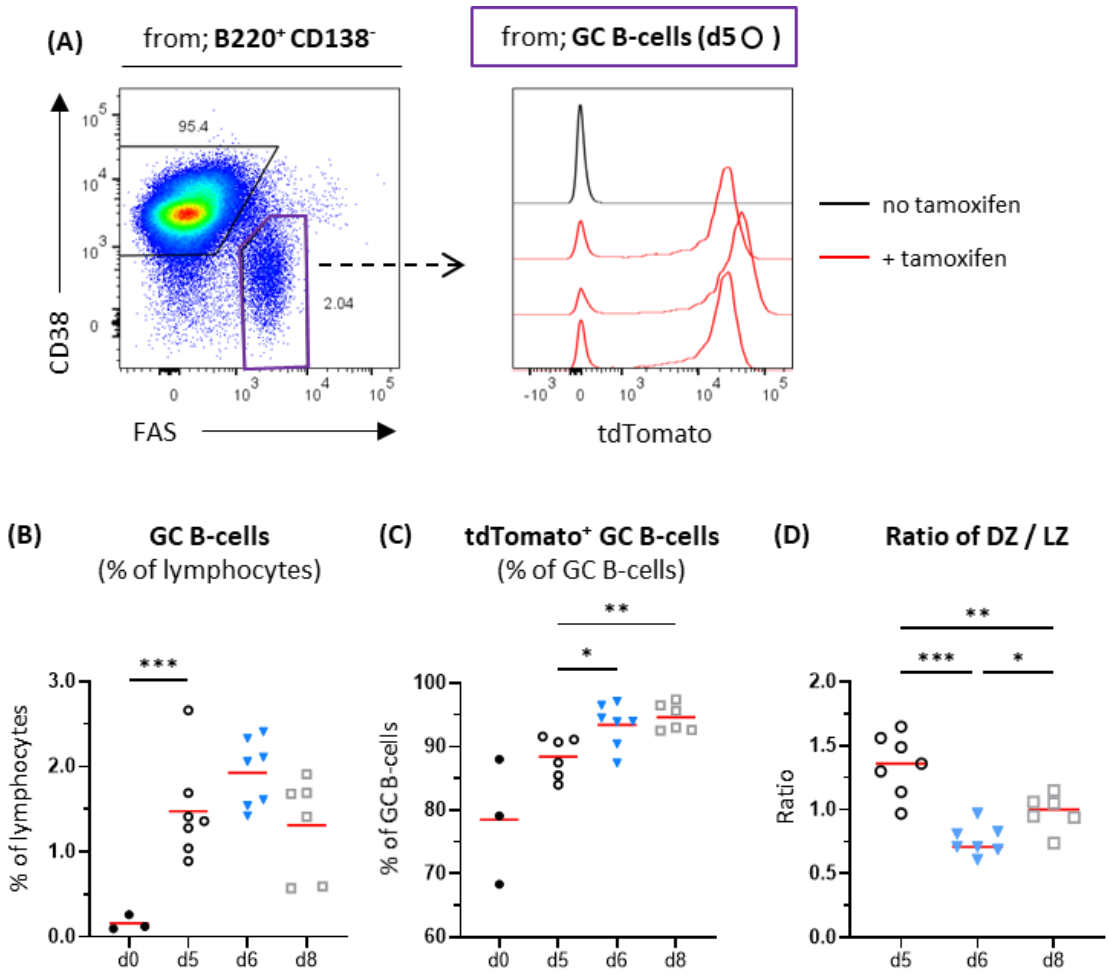

Figure 3.8 **Validation of our experimental system in *S1pr2*^{ERT2Cre}.*Rosa26*^{LSLtdTomato} mice; evaluation of the GC response**. Representative gating for splenic GC B-cells (B220^{+} CD138^{-} CD38^{Lo} Fas^{+}) from the primary SRBC response on day 5 showing tdTomato expression ± administration of tamoxifen **(A)**, GC size **(B)**, efficiency of tamoxifen induced GC B-cell fate mapping 48 h after a single oral 6 mg dose excluding the no tamoxifen control **(C)**, and GC DZ:LZ ratio **(D)**. Experimental protocol outlined in Figure 3.7. Data from two experiments, each symbol represents an individual mouse. Brown-Forsythe & Welch ANOVA with unpaired Welch's t-test for (B-D).

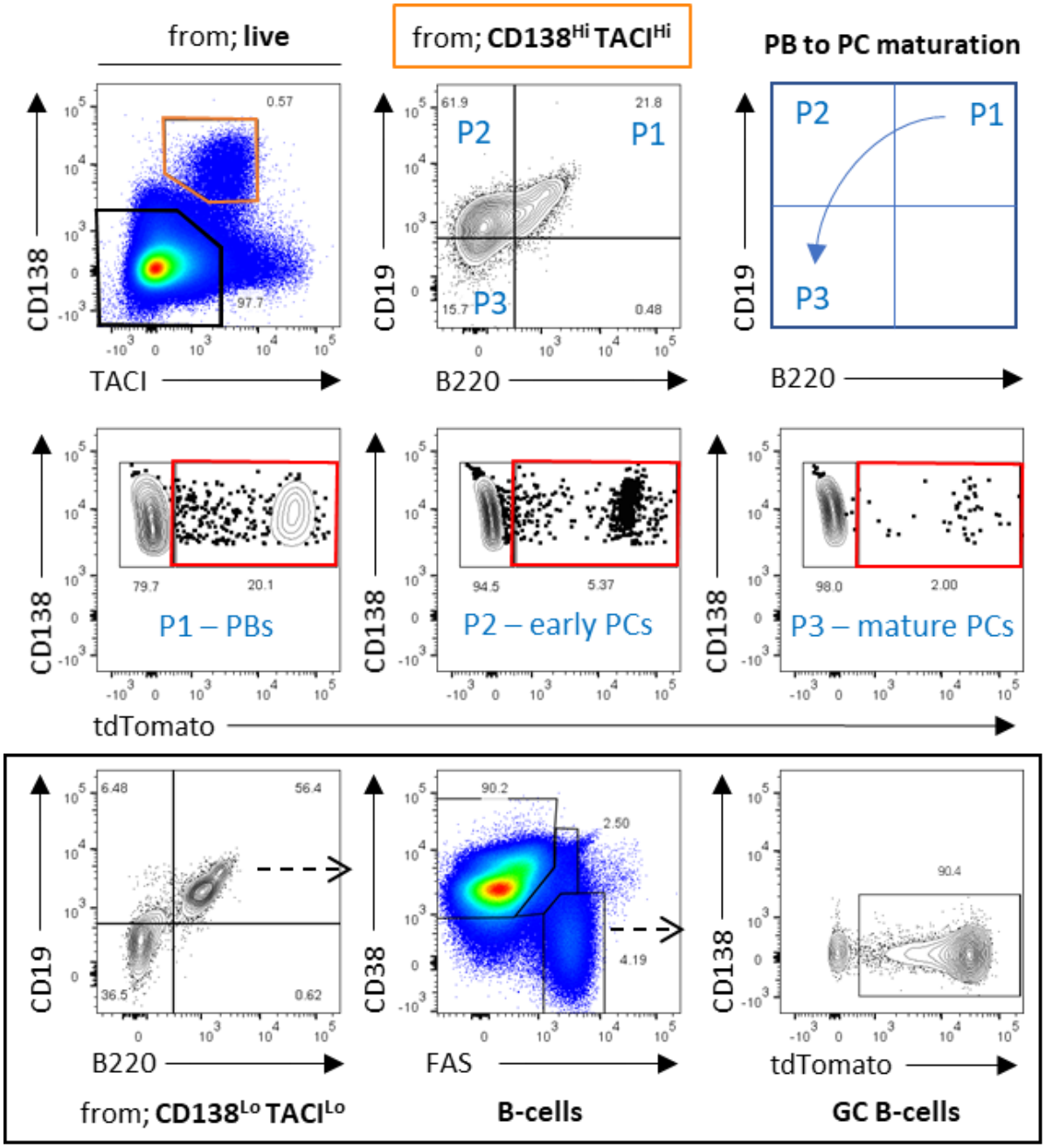

Figure 3.9 **Gating strategy for splenic PC response to validate our experimental system in *S1pr2*^{ERT2Cre}.*Rosa26*^{LSLtdTomato} mice.** Representative flow cytometric gating strategy from a *S1pr2*^{ERT2Cre}.*Rosa26*^{LSLtdTomato} mouse at day 6 of the primary SRBC response to evaluate the maturity and GC experience of the CD138^{Hi} TACI^{Hi} PB-PC response from the experimental protocol outlined in Figure 3.7. Maturity of PB-PCs was assessed by B220 and CD19 expression with populations labelled; P1 PBs (B220^{+} CD19^{+}), P2 early PCs (B220^{-} CD19^{+}) or P3 mature PCs (B220^{-} CD19^{-}) (Pracht *et al.*, 2017), with the B220 and CD19 gates set using expression on in CD138^{Lo} TACI^{Lo} (non-PCs). The gate for tdTomato expressing CD138^{Hi} TACI^{Hi} PCs was set using tdTomato expression in GC B-cells.

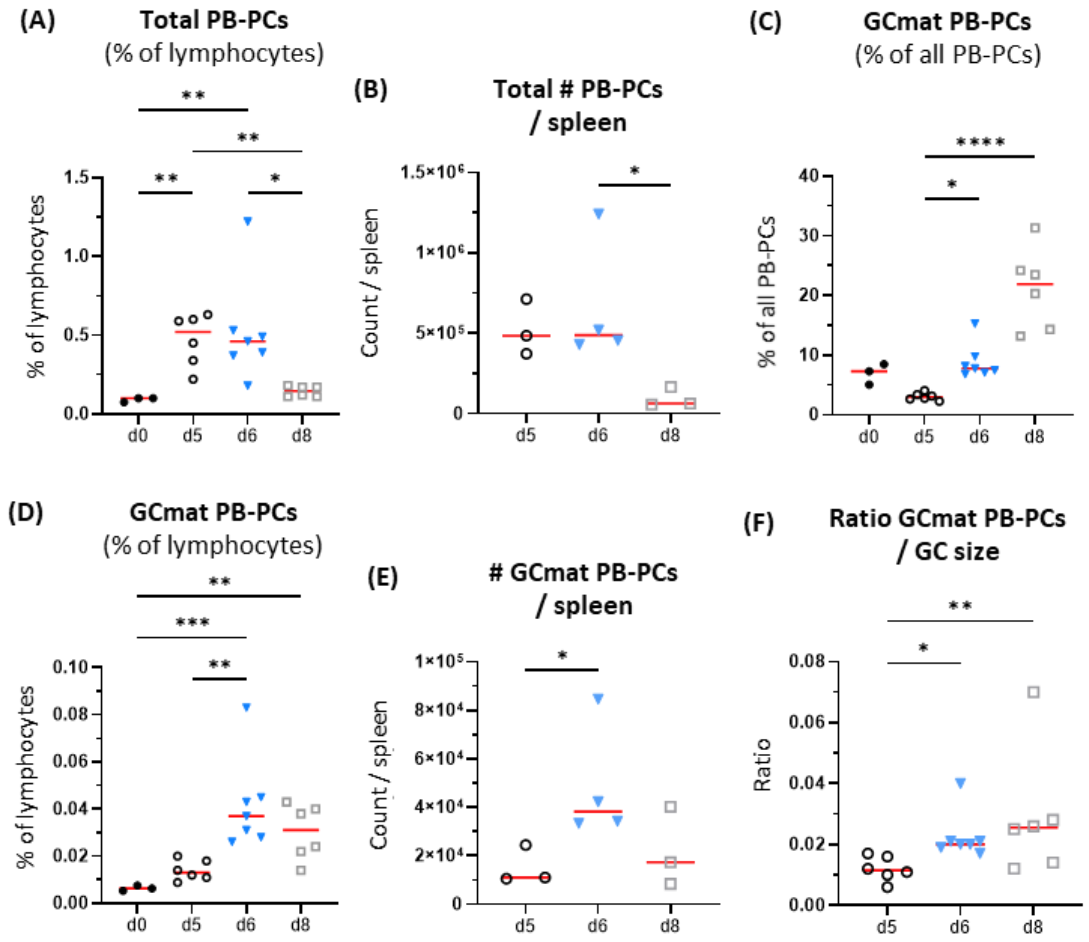

Figure 3.10 **Evaluation of the early splenic PC response in *S1pr2*^{ERT2Cre}.*Rosa26*^{LSLtdTomato} mice.** Combined CD138^{Hi} TACI^{Hi} EF and GCmat PC response **(A-B)**, GCmat PC response alone **(D-E)** and ratio of the output of affinity matured CD138^{Hi} TACI^{Hi} PCs to GC size **(F)**. Experimental protocol outlined in Figure 3.7. Data from two experiments, each symbol represents an individual mouse. Kruskal-Wallis multiple comparisons with uncorrected Dunn's test (A-F). Absolute numbers of splenic cells only available from 1 of 2 independent experiments.

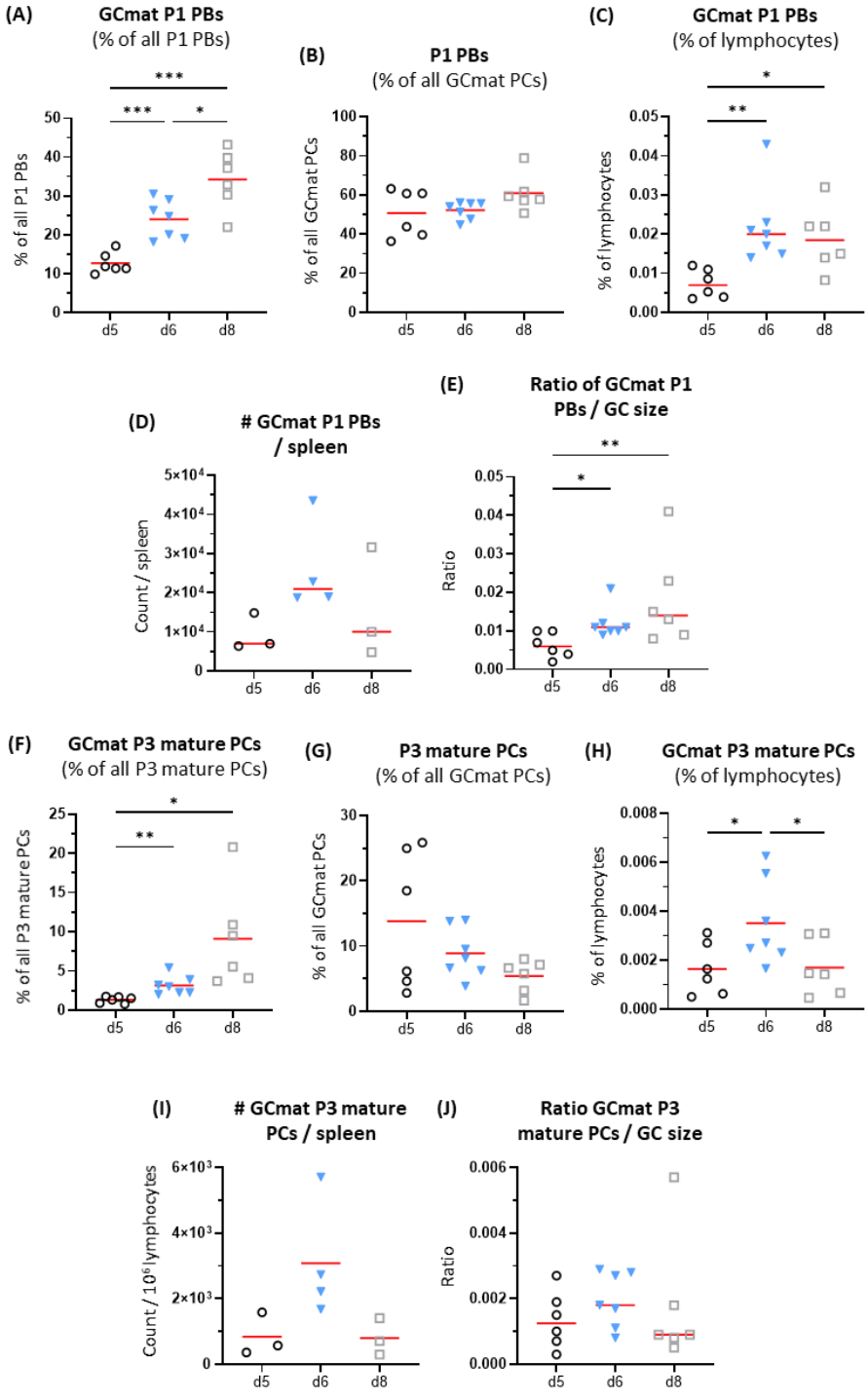

Figure 3.11 **Maturity of the early affinity matured SRBC splenic PC response in *S1pr2*^{ERT2Cre}.*Rosa26*^{LSLtdTomato} mice.** Analysis of CD138^{Hi} TACI^{Hi} GCmat B220^{+} CD19^{+} P1 PBs (A-E) and GCmat B220^{-} CD19^{-} P3 PCs (F-J). Experimental protocol outlined in Figure 3.7. Data from two experiments, each symbol represents an individual mouse. Brown-Forsythe & Welch ANOVA with unpaired Welch's t-test (A-B and F-J) or Kruskal-Wallis multiple comparisons with uncorrected Dunn's test (C-E). Absolute numbers of splenic cells only available from 1 of 2 independent experiments.

To understand the migration kinetics of GCmat PCs to the BM, total and GCmat BM PCs were analysed (Figure 3.12A). The total BM PC proportions remained unchanged compared to background after induction of immune response, however the variability is quite high and only three naïve mice were studied (Figure 3.12B-C). Further, there was no increase in the proportion of GCmat PCs compared to that observed in non-immunised controls despite the ongoing strong splenic GC response (Figure 3.10D-F). This lack of increase could be explained by retention of newly differentiated and GC emigrant PCs (within the previous 48 h) within local splenic PC niches; the influence of isotype on which PC niche is preferentially occupied; or that homeostatic PC turnover in the BM may remain unchanged during the acute phase of immune response (Sze *et al.*, 2000; Bohannon *et al.*, 2016; Lemke *et al.*, 2016; Xu, Barbosa and Calado, 2020).

The BrdU labelling experiments performed by Weisel and colleagues indicated preferential MBC output from early splenic GCs, with peak MBC output between days 6-8 post-immunisation which was over 2-fold greater than MBC output between days 3-5 (Weisel *et al.*, 2016). In our experimental protocol, GC B-cells and progeny from the previous 48 h are labelled tdTomato^{+} (Figure 3.13A). Our results suggest that there is only a modest increase in the proportion of tdTomato^{Hi} splenic MBCs between days 4-6 or days 6-8 compared to days 3-5 (Figure 3.13B-D). Interestingly, we did not observe an increase in MBC output to GC size nor to GCmat PC output when GC fate mapping was induced between days 3-5, days 4-6 or days 6-8 (Figure 3.13E-F). This suggests that GCmat MBC output during the early GC response remained constant, with 2-3 GCmat MBCs for each GCmat PC (Figure 3.13F). Potential reasons for differences in the kinetics of MBC response could lie in the experimental setup. We used transgenic fluorescent reporter mice which label all GC-derived output and

have a WT BCR repertoire, whereas Weisel and colleagues used an Ag-specific system designed to synchronise GC onset through adoptive transfer of limiting numbers of NP-specific transgenic B-cells into transgenic host mice with fixed rheumatoid factor specific B-cells meaning no GC contribution from host B-cells (Weisel *et al.*, 2016).

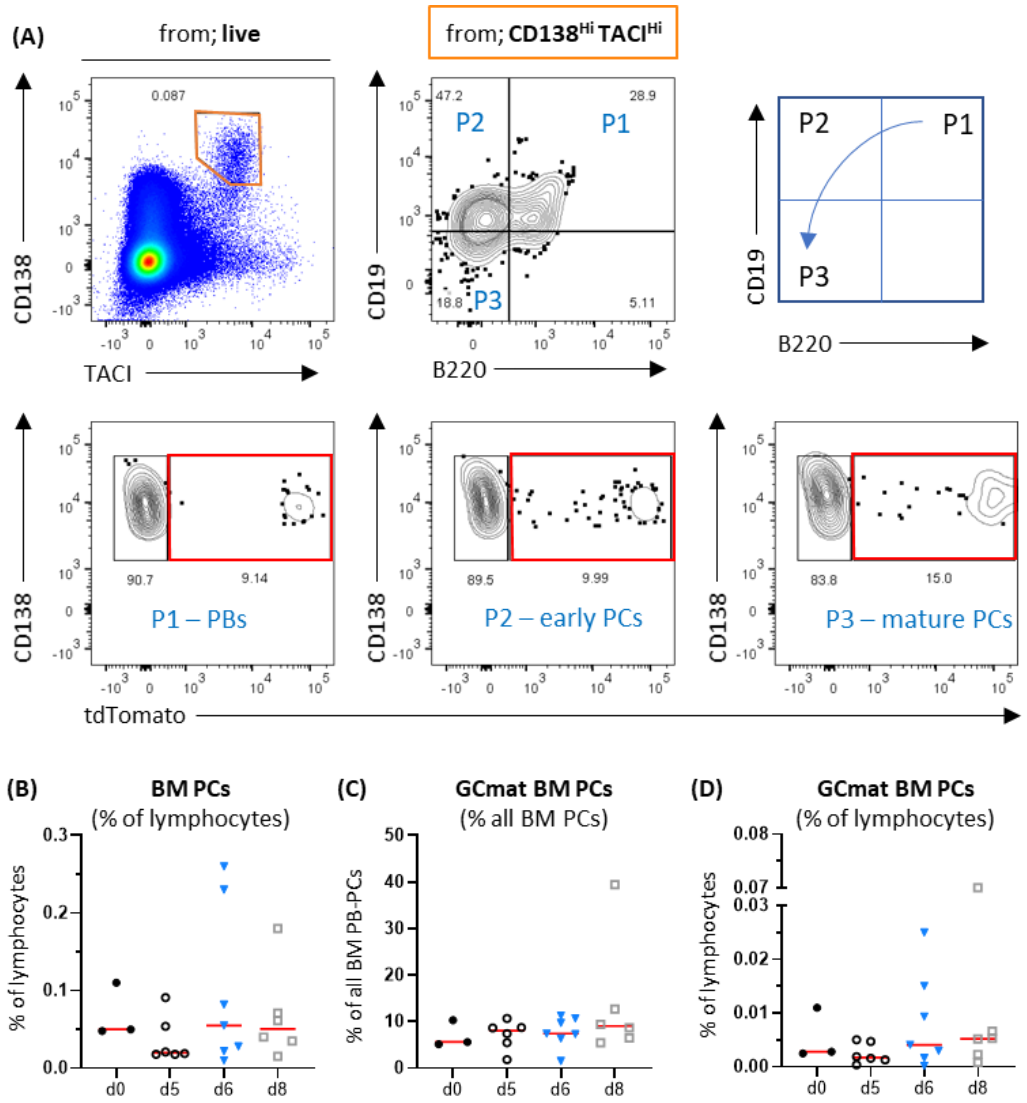

Figure 3.12 **Analysis of affinity matured PC accumulation in the BM in *S1pr2*^{ERT2Cre}.*Rosa26*^{LSLtdTomato} mice.** Gating scheme to identify CD138^{Hi} TACI^{Hi} BM PCs, their maturity and the proportion of GC-experienced PCs 48 h after tamoxifen induction during primary immune response **(A)**. Total BM PC **(B)** and GCmat PC response **(C-D)**. Experimental protocol outlined in Figure 3.7. Data from two experiments, each symbol represents an individual mouse. Kruskal-Wallis multiple comparisons with uncorrected Dunn's test (B-D).

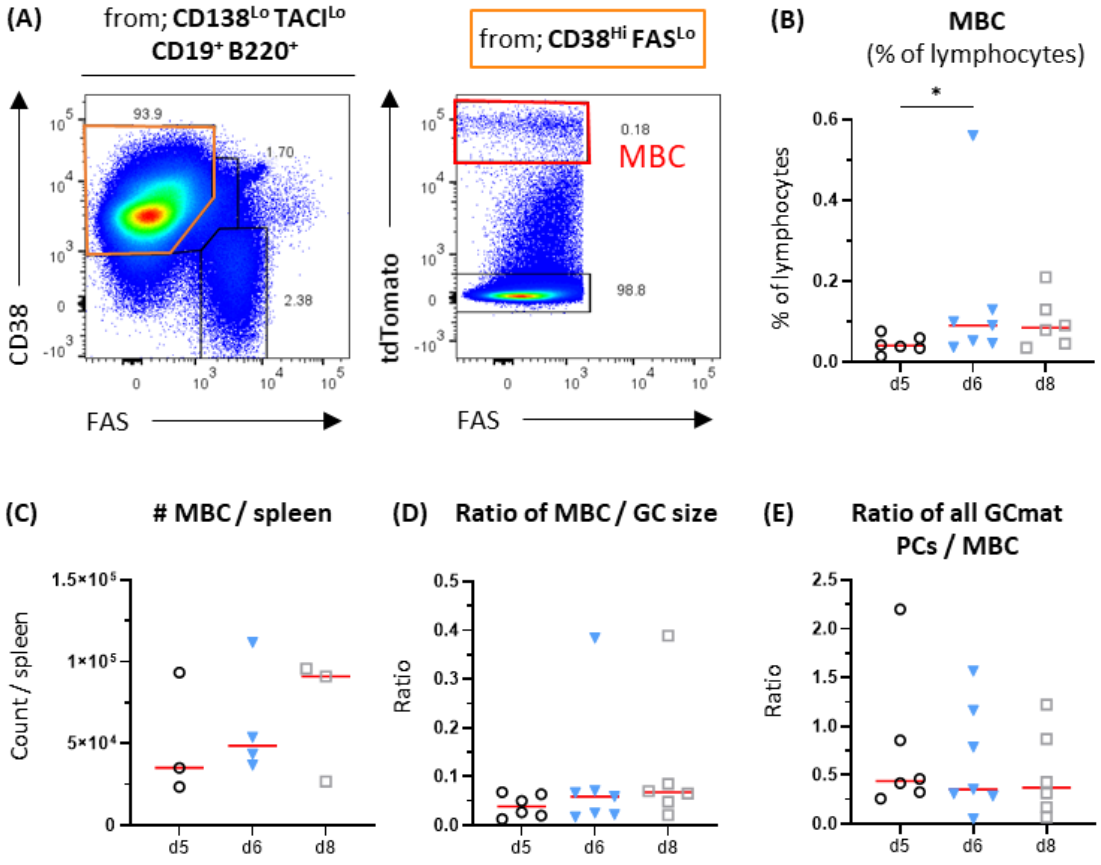

Figure 3.13 **Analysis of MBCs and comparison of productive GC outputs during the early GC response in *S1pr2*^{ERT2Cre}.*Rosa26*^{LSLtdTomato} mice.** Representative gating (of mouse from day 6 of response) to identify MBCs as CD138^{Lo} TACI^{Lo} B220^{+} CD19^{+} CD38^{Hi} FAS^{Lo} tdTomato^{Hi} **(A)**. MBC proportions and absolute numbers **(B-C)**. MBC output ratios compared to GC size **(D)** and total CD138^{Hi} TACI^{Hi} GCmat PCs **(E)**. Experimental protocol outlined in Figure 3.7. Data from two experiments, each symbol represents an individual mouse. Kruskal-Wallis multiple comparisons with uncorrected Dunn's test (B-E). Absolute numbers of splenic cells only available from 1 of 2 independent experiments.

3.2.4.1 A role for CD38 expression during emergence of PC from GCs?

We wanted to obtain an unbiased view of the B-cell differentiation stages contained within the whole population of cells that expressed *S1pr2* within the tamoxifen induction window. To do this all tdTomato expressing cells were first selected before any phenotype specific marker combinations were analysed (Figure 3.14A). As expected, most cells with *S1pr2* induced tdTomato expression were GC B-cells and 2.5% of cells expressed high levels of TACI and CD138, identifying them as PCs (Figure 3.14A). Interestingly, there was a small population of tdTomato expressing $CD138^{int}$ $TACI^{int}$ cells (Figure 3.14A). Initial analysis of cell size suggested that these tdTomato expressing $CD138^{int}$ $TACI^{int}$ cells were blasts, which more closely resembled the cell size of $CD138^{Hi}$ $TACI^{Hi}$ PCs than either GC B-cells or MBCs (Figure 3.14B). Further, phenotype analysis of these tdTomato expressing $CD138^{int}$ $TACI^{int}$ cells revealed high levels of B220 expression and significantly elevated CD19 expression compared to both GC B-cells and MBCs (Figure 3.15A-B), which suggests an activated and differentiating state involving BCR signalling (Tedder, Inaoki and Sato, 1997; Hermiston, Xu and Weiss, 2003; Del Nagro *et al.*, 2005). These tdTomato expressing $CD138^{int}$ $TACI^{int}$ cells also expressed CD38 (Figure 3.15C), which was unexpected as murine GC B-cells and terminally differentiated PCs do not express CD38 (Oliver, Martin and Kearney, 1997). Moreover, this CD38 expression was at significantly higher levels than GC B-cells, GCmat $CD138^{Hi}$ $TACI^{Hi}$ P1 PBs, and strikingly, was of similar intensity shown by GCmat MBCs where CD38 re-expression is expected (Figure 3.15C).

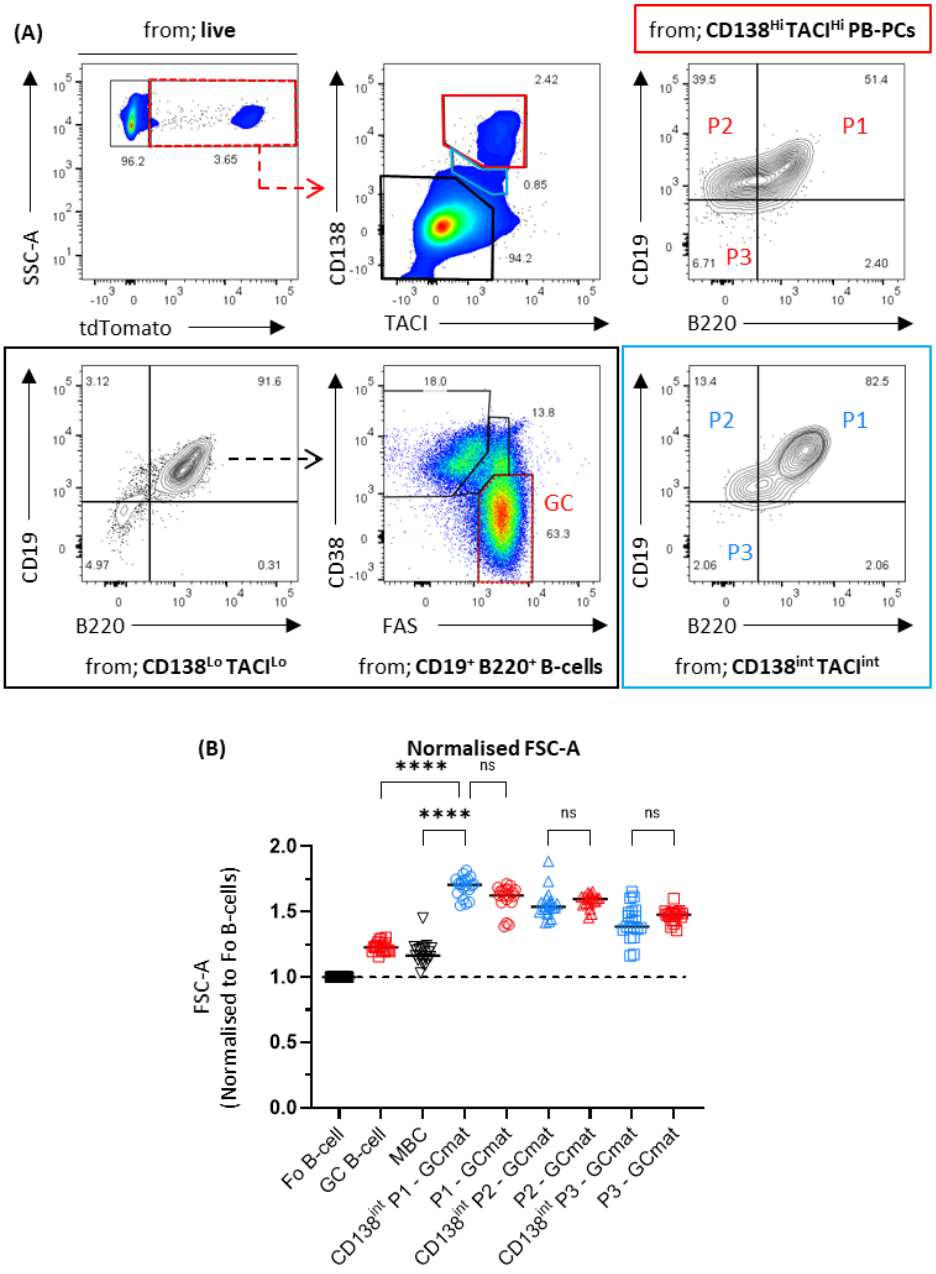

Figure 3.14 **Identification of a potential population of transitioning tdTomato^{+} PB-PCs.** **(A)** Representative gating for splenic populations that have expressed *S1pr2* since tamoxifen induction, with GCmat tdTomato expressing CD138^{int} TACI^{int} cells highlighted cyan. Gate for B220 and CD19 expression set from CD138^{Lo} TACI^{Lo} cells in Figure 3.9. P1 (B220^{+} CD19^{+}), P2 (B220^{-} CD19^{+}) and P3 (B220^{-} CD19^{-}) as per Figure 3.12A. **(B)** Assessment of cell size (FSC-A) normalised to follicular (Fo) B-cells. Fo B-cells (CD138^{Lo} TACI^{Lo} B220^{+} CD19^{+} CD38^{Hi} Fas^{Lo} tdTomato^{-}), GC B-cells (CD138^{Lo} TACI^{Lo} B220^{+} CD19^{+} CD38^{Lo} Fas^{Hi} tdTomato^{+}), and MBC (CD138^{Lo} TACI^{Lo} B220^{+} CD19^{+} CD38^{Hi} Fas^{Lo} tdTomato^{+}). Experimental protocol outlined in Figure 3.7. The indicated cell populations were pooled from all analysed time-points. Data from two experiments, each symbol represents an individual mouse. Kruskal-Wallis multiple comparisons with uncorrected Dunn's test (B).

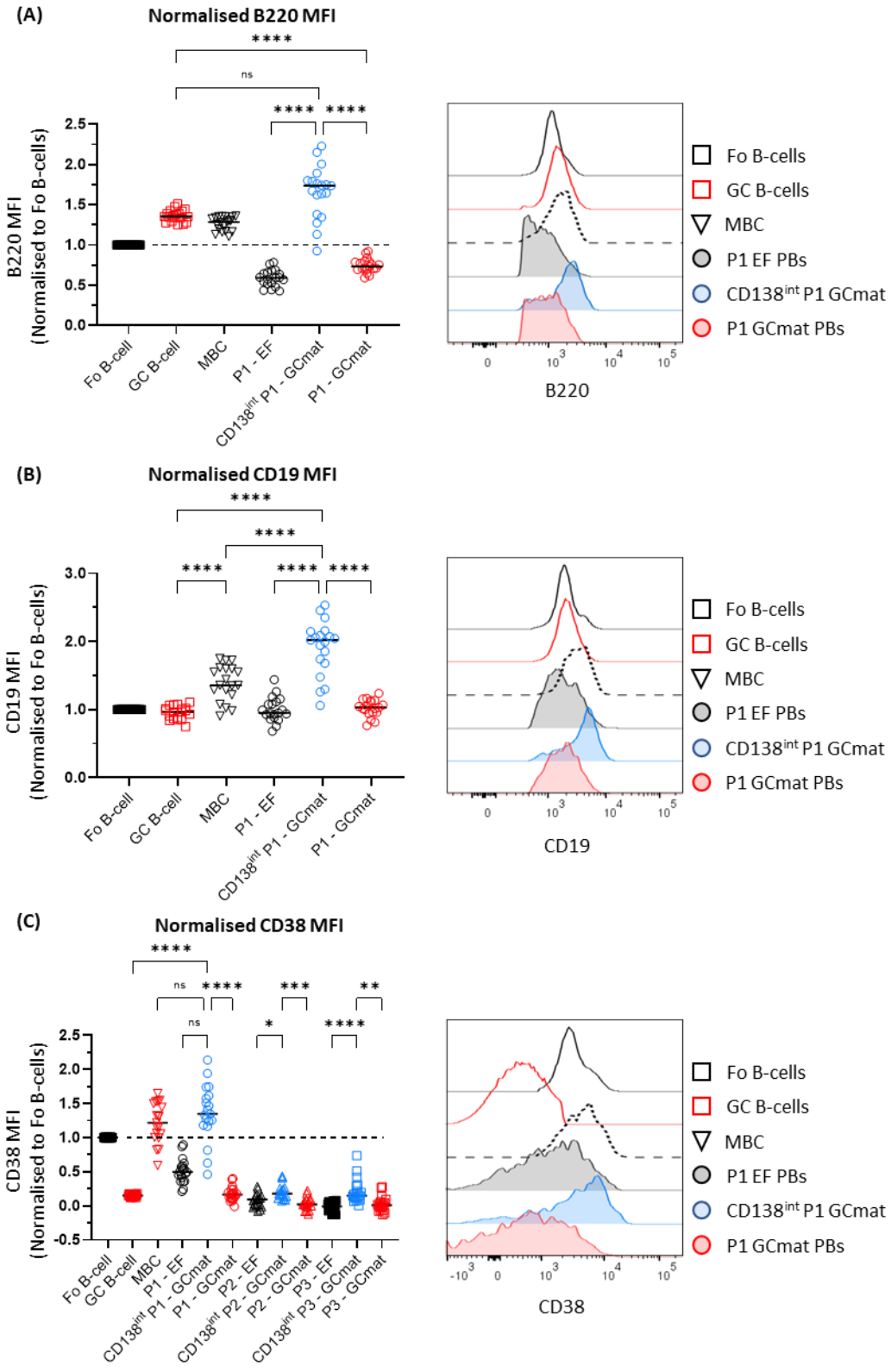

Figure 3.15 **Phenotype evaluation of CD138^{int} TACI^{int} tdTomato^{+} expressing cells**. Normalised expression of cell-surface markers B220 **(A)**, CD19 **(B)** and CD38 **(C)** with example histograms from individual mice. Fo B-cells (CD138^{Lo} TACI^{Lo} B220^{+} CD19^{+} CD38^{Hi}

Fas^{Lo} $tdTomato^{-}$), GC B-cells ($CD138^{Lo}$ $TACI^{Lo}$ $B220^{+}$ $CD19^{+}$ $CD38^{Lo}$ Fas^{Hi} $tdTomato^{+}$), MBC ($CD138^{Lo}$ $TACI^{Lo}$ $B220^{+}$ $CD19^{+}$ $CD38^{Hi}$ Fas^{Lo} $tdTomato^{+}$), $CD138^{int}$ P1 GCmat ($CD138^{int}$ $TACI^{int}$ $B220^{+}$ $CD19^{+}$ $tdTomato^{+}$), P1 GCmat ($CD138^{Hi}$ $TACI^{Hi}$ $B220^{+}$ $CD19^{+}$ $tdTomato^{+}$), P1 EF (extrafollicular; markers as P1 GCmat except $tdTomato^{-}$), P2 GCmat ($CD138^{Hi}$ $TACI^{Hi}$ $B220^{-}$ $CD19^{+}$ $tdTomato^{+}$), P2 EF (extrafollicular; markers as P2 GCmat except $tdTomato^{-}$), P3 GCmat ($CD138^{Hi}$ $TACI^{Hi}$ $B220^{-}$ $CD19^{-}$ $tdTomato^{+}$), P3 EF (extrafollicular; markers as P3 GCmat except $tdTomato^{-}$). Data from two experiments, each symbol represents an individual mouse. Cell populations were pooled from response time-points described in the experimental protocol (Figure 3.7). Kruskal-Wallis multiple comparisons with uncorrected Dunn's test (A and C). Brown-Forsythe & Welch's ANOVA with unpaired Welch's t-test (B).

Could short-lived CD38 re-expression be required for precursors of GCmat PCs to exit the GC microenvironment? Using *S1pr2*^{Venus} reporter mice, Laidlaw and colleagues have described marker combinations for early and mature GC B-cells as well as cells entering or exiting the GC reaction (Laidlaw *et al.*, 2017). They found ~2% of cells exiting the GC (defined as IgD^{Lo} $GL7^{+}$ FAS^{+} Ephrin-$B1^{+}$ *S1pr2*^{Lo} $CD38^{Hi}$) were also $CD138^{+}$ (Laidlaw *et al.*, 2017), suggesting that a small proportion of GCmat PC precursors leaving the GC can show high levels of CD38 expression. Moreover, they also mention unpublished findings where they identify this same $CD138^{+}$ population amongst $CD38^{Hi}$ cells emerging from the GC using *Prdm1*$^{GFP/+}$ mice (Laidlaw *et al.*, 2017).

Due to their tdTomato, CD138 and TACI expression and similar size to GCmat $CD138^{Hi}$ $TACI^{Hi}$ PCs, these tdTomato expressing $CD138^{int}$ $TACI^{int}$ cells are likely to be transitioning GCmat PCs and will from now on be referred to as GCmat $CD138^{int}$ $TACI^{int}$ Tr PB-PCs. Population analysis of GCmat $CD138^{int}$ $TACI^{int}$ Tr PB-PCs revealed a frequency of between 1-2 in 10,000 splenic lymphocytes (Figure 3.16A-B) and that their output compared to GC size remained unchanged or increased slightly until the end of the experiment day 8 post immunisation (Figure 3.16C). Maturity analysis using B220 and CD19 expression revealed

that the majority subset of GCmat CD138^{int} TACI^{int} Tr PB-PC cells are at P1 plasmablast stage throughout the period tested (until day 8) (Figure 3.16D), which is compatible with the hypothesis that this is a transient differentiation stage of PB-PC precursors. Moreover, the frequency of GCmat CD138^{int} TACI^{int} Tr P1 remained unchanged during the period tested (Figure 3.16E). To understand whether there was a preference for GCmat MBC or CD138^{int} TACI^{int} tdTomato expressing Tr cells from the early GC, and how this affected the overall combined GCmat PC to GCmat MBC response, we assessed their output ratios. This showed that GC output preference did not change over the course of the analysis and that GCmat MBC output was 2-fold higher than PC (Figure 3.16F-G).

Investigation of this population of GCmat CD138^{int} TACI^{int} Tr PB-PCs for expression of the Blimp1^{GFP} reporter in the HALO PC model will help to understand whether these are bone fide GC-experienced PCs with a transitioning phenotype at an early terminal differentiation stage (Figure 3.17). Furthermore, it will inform whether transient CD38 re-expression could be involved in PC precursor emergence from the GC.

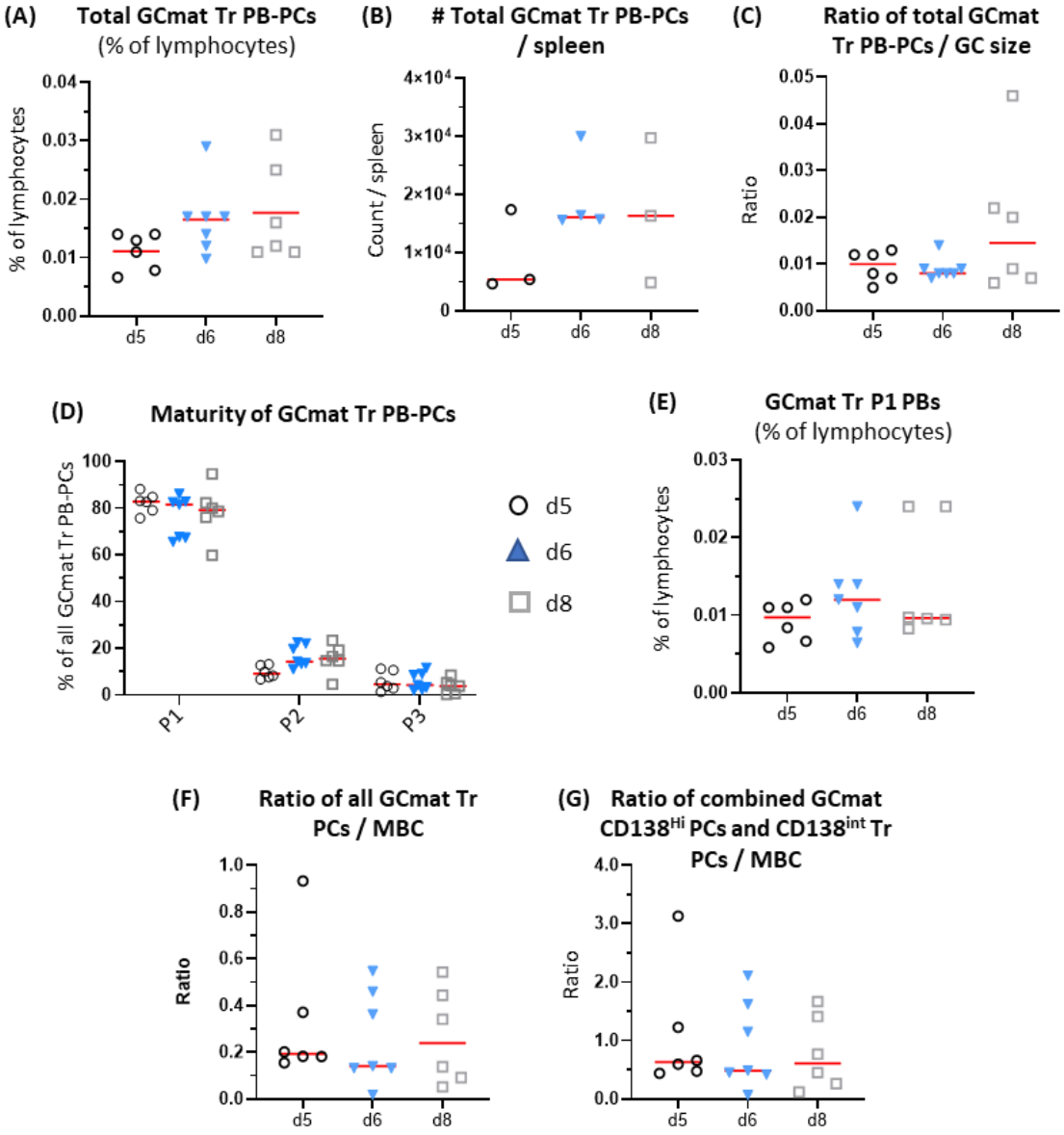

Figure 3.16 **Population analysis of tdTomato^{+} splenic suspected transitioning PB-PCs**. Response in the spleen. Analysis of the proportions and absolute numbers of total GCmat CD138^{int} TACI^{int} transitioning (Tr) PB-PCs **(A-C)**. Maturity of GCmat CD138^{int} TACI^{int} Tr PB-PCs defined as P1 (B220^{+} CD19^{+}), P2 (B220^{-} CD19^{+}), P3 (B220^{-} CD19^{-}) **(D)**. Frequency of GCmat CD138^{int} TACI^{int} Tr P1 PBs in the spleen **(E)**. Analysis of the GCmat Tr CD138^{int} TACI^{int} response to MBC alone **(F)** or combined GCmat CD138^{Hi} TACI^{Hi} PC and GCmat Tr CD138^{int} TACI^{int} response to MBC output **(G)**. Experimental protocol outlined in Figure 3.7. Data from two experiments, each symbol represents an individual mouse. Brown-Forsythe & Welch's ANOVA with unpaired Welch's t-test (A and D). Kruskal-Wallis multiple comparisons with uncorrected Dunn's test (B-C and E-G).

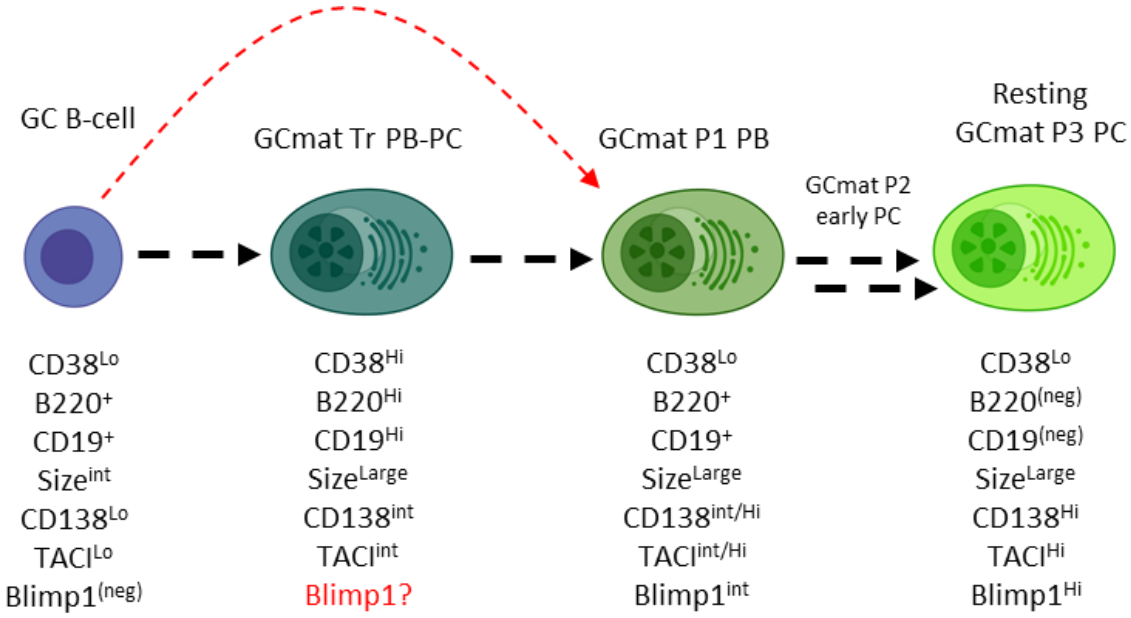

Figure 3.17 **Schematic detailing a potential differentiation progression from GC B-cells to terminally differentiated GC-experienced PCs**. GC B-cells positively selected and instructed toward terminal differentiation and output as GCmat PCs could transition through a highly activated state with high expression of CD38, B220 and CD19 with upregulated CD138 and TACI (GCmat Tr PB-PC), before concomitant downregulation of CD38, B220 and CD19 and high expression of classical PC markers CD138 and TACI. Undetermined Blimp1 expression in GCmat Tr PB-PCs (highlighted red with question mark). Dashed thick black arrows indicate favoured, sequential route of differentiation whereas dashed red arrow (upper) represents GC-experienced PC output without the transitioning stage. Model derived from phenotype analyses in Figure 3.14 and Figure 3.15. Schematic created with BioRender.com.

3.2.5 *Prdm1* dependent GFP expression in the HALO PC mouse allows simultaneous detection of GC derived and EF PC responses.

After successful combination of the three alleles to generate the novel HALO PC transgenic mouse (Figure 3.6 and Table 3.1), we set out to: a) confirm that GC B-cells, GCmat PCs and EF PCs populations were faithfully labelled by the (inducible) fluorescent reporters and could be distinguished from the earliest stages of GC formation and GC derived cellular output, and b) to test whether the newly identified tdTomato expressing CD138^{int} TACI^{int} transitioning (Tr) cells were indeed transitioning GCmat PCs (Figure 3.14, Figure 3.15 and Figure 3.17). To do this, we used our validated experimental protocol to study peak GCmat PC output from the early GC in HALO PC mice (Figure 3.18). *Prdm1*$^{GFP/+}$ and *S1pr2*^{ERT2Cre}.*Rosa26*^{LSLtdTomato} single positive control mice were included to enable correct gating and flow cytometric compensation of true FP^{+} cells.

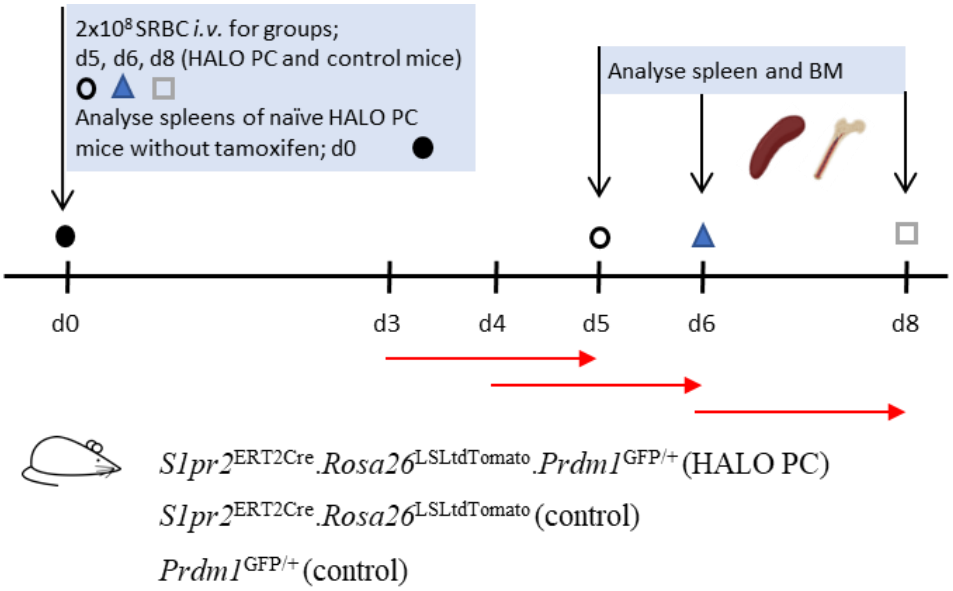

Figure 3.18 **Experimental system used to validate HALO PC mice and investigate GCmat PCs from the early GC response**. HALO PC mice were immunised with SRBC i.v. and received a single 6 mg dose of tamoxifen by gavage 48 h prior (red arrow) to tissue analysis on

day 5, 6 or 8 of the primary immune response. Naïve HALO PC mice without tamoxifen administration were included as background non-induced controls. Control mice (*S1pr2*^{ERT2Cre}.*Rosa26*^{LSLtdTomato} and *Prdm1*$^{GFP/+}$) were identically immunised and treated with tamoxifen. Spleens were partitioned, with ~1/3 used for flow cytometry and the remainder formaldehyde fixed and frozen. For immunised mice splenic and BM lymphocytes were analysed by flow cytometry, whereas only the splenic lymphocytes were analysed for naïve non-induced HALO PC mice.

3.2.5.1 Characterising B-cells subsets in the HALO PC model.

Two of the transgenic alleles (*Prdm1*$^{GFP/+}$ and *Rosa26*^{LSLtdTomato}) that were combined to produce the HALO PC model were generated by targeted insertion to the mouse genome and are well characterised (Kallies *et al.*, 2004; Madisen *et al.*, 2010) with phenotype data available on MGI. When the knock-in *Prdm1*$^{GFP/+}$ allele is heterozygous there are no reported abnormalities to the mouse immune system ((Kallies *et al.*, 2004) and MGI:3510704; URL: http://www.informatics.jax.org; accessed 10-Jan-2020). There are also no reported immune defects for the knock-in *Rosa26*^{LSLtdTomato} allele ((Madisen *et al.*, 2010); MGI:3809524; URL: http://www.informatics.jax.org; accessed 10-Jan-2020). The *S1pr2*^{ERT2Cre} was generated by random genomic integration of a modified BAC, contains two wild-type *S1pr2* alleles and, likely due to the specificity of *S1pr2* for GC B-cells, no comment has been made on the B-cell compartment which are pre-GC (Shinnakasu *et al.*, 2016; Ise *et al.*, 2018). Although there are no reported disruptions to developing or peripheral B-cell subsets, for due diligence, we analysed these compartments in immunised HALO PC mice and compared them to immunised *S1pr2*^{ERT2Cre}. *Rosa26*^{LSLtdTomato} and *Prdm1*$^{GFP/+}$ mice.

Developing B-cell subsets in the BM were analysed for CD43, B220, IgM and IgD expression (Tung *et al.*, 2004). Early B-cells (Hardy Fractions A-C) are identified as B220$^{Lo/int}$ CD43^{+}

whereas small pre-B-II-cells, immature B-cells, and mature recirculating B-cells (Hardy Fractions D, E and F, respectively) are $B220^{+}$ $CD43^{-}$ and distinguished by IgD and IgM expression (Figure 3.19A). Although the frequency of pre-B-cells and immature B-cells were slightly reduced in immunised HALO PC mice (Figure 3.19B), there was no impact on the composition of the Hardy Fractions D-F compared to either the *S1pr2*^{ERT2Cre}. *Rosa26*^{LSLtdTomato} or *Prdm1*$^{GFP/+}$ mice (Figure 3.19C). Transitional and mature peripheral B-cell subsets in the spleen were initially separated by B220 and CD93 expression and then by either IgD or CD21 and CD23 expression (Figure 3.20A). As anticipated, there were no obvious differences or trends present in the transitional (T1 or T2+T3) or mature (Fo or MZ) B-cell compartments of HALO PC mice compared to either *S1pr2*^{ERT2Cre}.*Rosa26*^{LSLtdTomato} or *Prdm1*$^{GFP/+}$ control mice (Figure 3.20B-D). We concluded that, as expected, there was no deleterious impact upon B-cell compartments when these three transgenic alleles are combined in the HALO PC mouse.

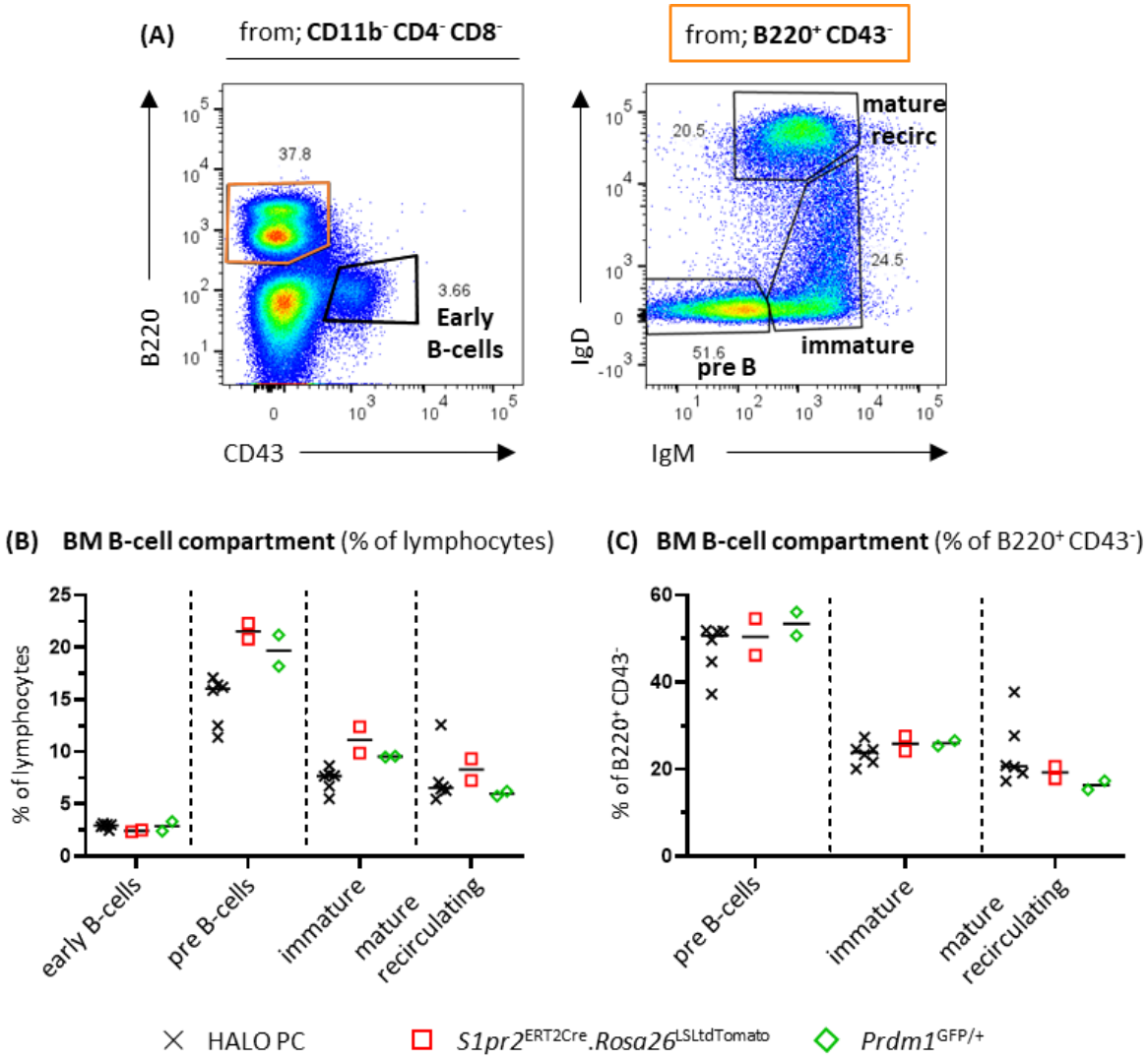

Figure 3.19 **Analysis of developing B-cell subsets in the bone marrow of HALO PC mice**. Representative gating strategy to assess the proportions of BM developing early B-cells ($CD43^+$ $B220^-$), pre-B cells ($CD43^-$ $B220^+$ IgM^- IgD^-) and immature B-cells ($CD43^-$ $B220^+$ IgM^+ $IgD^{Lo/int}$) and recirculating mature follicular B-cells ($CD43^-$ $B220^+$ IgM^+ IgD^+). Results displayed are collated from HALO PC mice on day 5 and day 6 of primary SRBC immune response, with three HALO PC mice and a single control mouse of each genotype per time-point (experimental protocol; Figure 3.18). Each symbol represents an individual mouse.

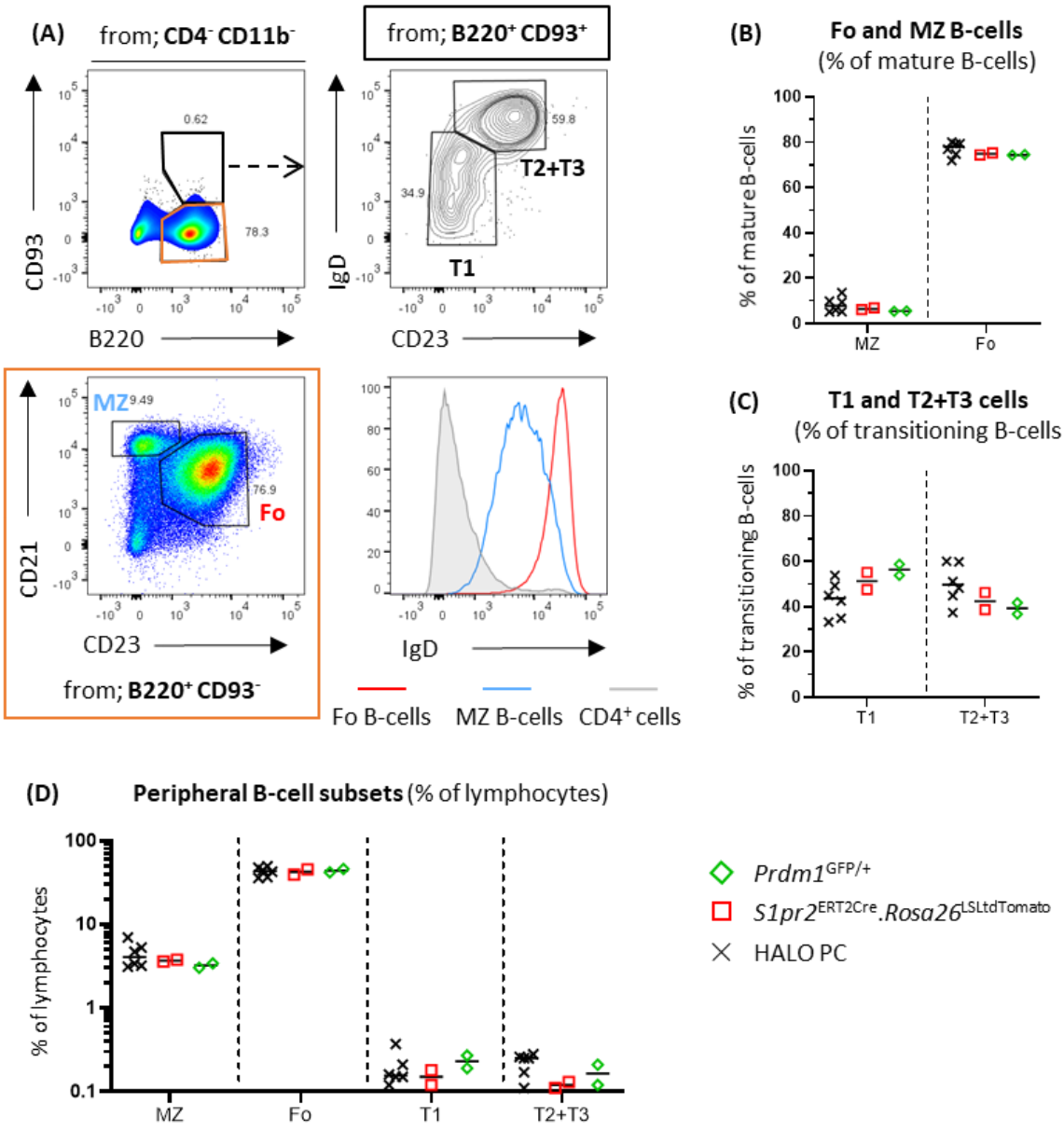

Figure 3.20 **Phenotype analysis of peripheral B-cell subsets in HALO PC mice**. Representative gating strategy to assess the proportions of splenic transitional T1 cells ($CD93^{+}$ $B220^{+}$ $CD23^{Lo}$ IgD^{Lo}), transitional T2+T3 cells ($CD93^{+}$ $B220^{+}$ $CD23^{Hi}$ IgD^{Hi}), MZ ($CD93^{-}$ $B220^{+}$ $CD23^{Lo}$ $CD21^{Hi}$) and follicular (Fo) B-cells ($CD93^{-}$ $B220^{+}$ $CD23^{Hi}$ $CD21^{int}$). Results displayed are collated from HALO PC mice on day 5 and day 6 of primary SRBC immune response, with three HALO PC mice and a single control mouse of each genotype per time-point (experimental protocol; Figure 3.18). Each symbol represents an individual mouse.

3.2.5.2 CD11b expression on maturing PCs.

As well as its critical function in PC biology (Shapiro-Shelef *et al.*, 2003; Kallies *et al.*, 2004), Blimp1 is also involved in the differentiation and/or maintenance of CD8 T-cells and regulatory T cells (Martins *et al.*, 2006; Kallies *et al.*, 2009; Rutishauser *et al.*, 2009), development of natural killer (NK) cells (Kallies *et al.*, 2011) and tolerogenic function in dendritic cells (Kim *et al.*, 2011). Therefore, to improve identification of Blimp1-expressing B lineage cells in the HALO PC mouse, antibodies against CD3ε and CD11b were included in the flow cytometry panel as dump channels to exclude T-cells, most myeloid cells and natural killer (NK) cells (Hey and O'Neill, 2012; Bachmann Link *et al.*, 2014). However, bimodal separation of BM lymphocytes into $CD11b^{-}$ or $CD11b^{+}$ led to a loss of a large proportion of the BM $CD138^{Hi}$ $TACI^{Hi}$ PCs (top row, Figure 3.21A). Testing PC marker expression in the $CD3^{-}$ CD11b expressing population identified bone fide $CD138^{Hi}$ $TACI^{Hi}$ $Blimp1^{GFP}$ expressing PCs, which suggested that PCs can express CD11b (bottom row, Figure 3.21A). To test whether there was correlation between PC maturity and upregulated CD11b, $CD138^{Hi}$ $TACI^{Hi}$ PCs were gated from $CD3^{-}$ BM lymphocytes and CD11b was assessed against $Blimp1^{GFP}$ and B220 (Figure 3.21B). This showed that as $Blimp1^{GFP}$ expression increased and B220 expression decreased, the levels of CD11b increased (Figure 3.21B), consistent with CD11b upregulation as PCs matured. Similar results were obtained when the standard CD11b bimodal gating strategy was applied to splenocytes from immunised HALO PC mice (Figure 3.22A) or when CD11b expression was assessed in splenic $CD138^{Hi}$ $TACI^{Hi}$ PCs (Figure 3.22B). Further, splenic $CD138^{int}$ $TACI^{int}$ Tr cells, proposed to be transitioning PCs at an early stage of PC differentiation, displayed the lowest levels of CD11b expression (Figure 3.22B and C). Furthermore, comparison of spleen $CD138^{int}$ $TACI^{int}$ Tr cells and $CD138^{Hi}$ $TACI^{Hi}$ PCs to BM

CD138^{Hi} TACI^{Hi} PCs showed that the BM resident PCs expressed the most CD11b (Figure 3.22C), consistent with PCs in the BM being more mature (Kallies *et al.*, 2004).

It was unexpected to find that CD11b surface expression correlated with PC maturity as analysis of *Itgam* gene expression (which encodes CD11b) on MyGeneset (Immunological Genome Project (Heng *et al.*, 2008)) revealed minimal expression in conventional B-2 cell derived PB or PC populations compared to granulocytes, macrophages or NK cells. However, there are reports that *Itgam* gene expression and cell surface CD11b protein are present in a proportion of cells exiting the GC (Laidlaw *et al.*, 2017), in IgA^{+} PCs from the intestinal Lamina Propria (iLP) (Kunisawa *et al.*, 2013) and in BM PCs (Wilmore, Jones and Allman, 2017). Further, unpublished immunofluorescence histology data from our lab has suggested that there could be CD11b expression on a minority of IRF4^{+} PCs located in the extrafollicular foci of the spleen of wild-type C57BL/6 mice 5 d post-immunisation with SRBC (Figure 3.23). CD11b has a large array of reported ligands, one of which is fibronectin, a mesenchymal stromal cell secreted factor which can aid the survival and *in vitro* culture of PCs (Yakubenko *et al.*, 2001; Arnaout, 2016; Nguyen *et al.*, 2018). Does CD11b upregulation of a proportion of GCmat output represent increased survival potential, perhaps by aiding migration to areas secreting survival factors? Testing for the expression of CD11b on spleen sections from SRBC immunised HALO PC mice by immunofluorescence histology would help to confirm the spatial context of CD11b expression of PCs.

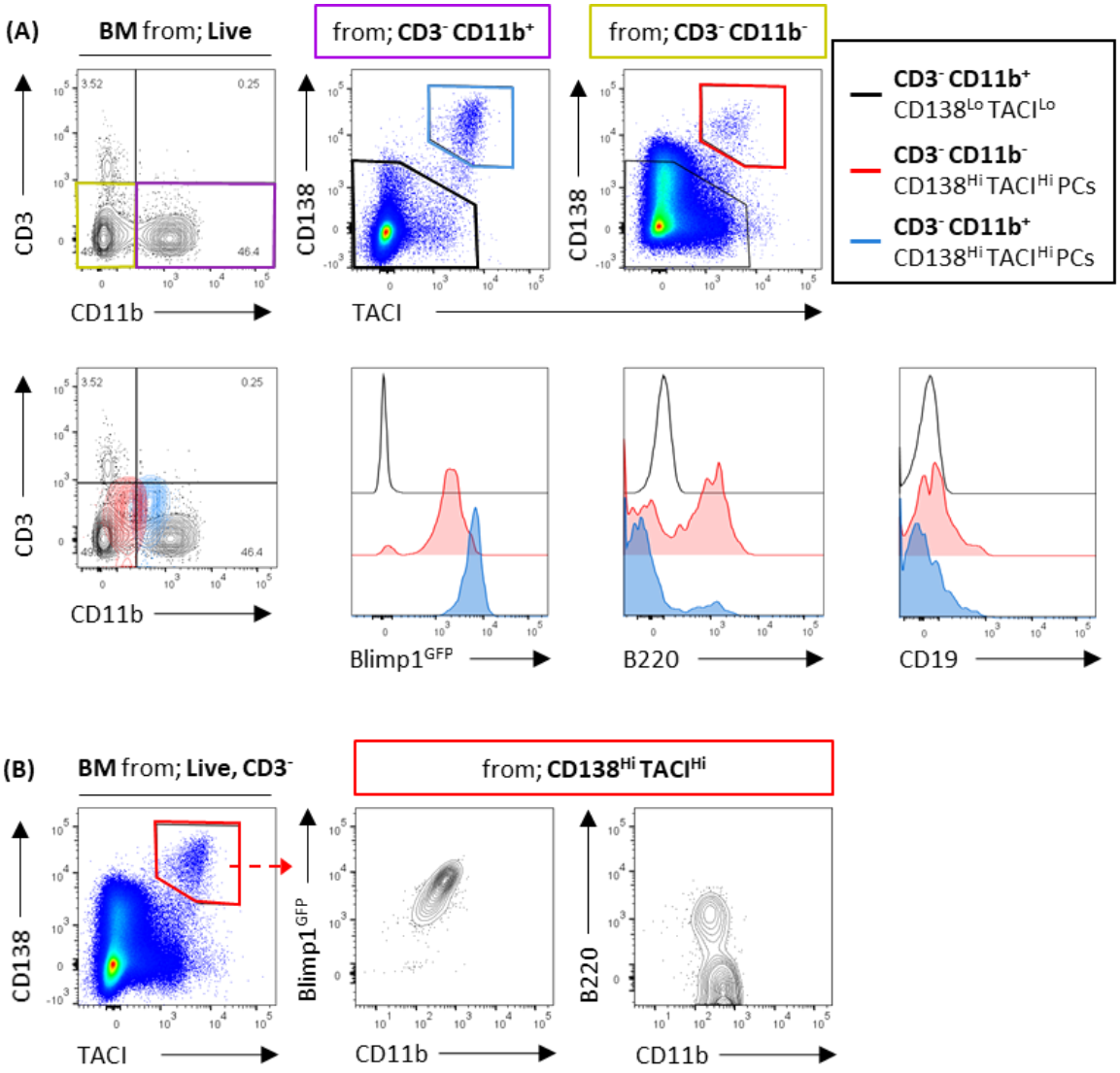

Figure 3.21 **BM PCs show an upregulation in CD11b as maturity increases**. **(A)** Top row, representative standard gating strategy in HALO PC mice to exclude $CD3^+$ T-cells and $CD11b^+$ myeloid cells from BM lymphocytes. Bottom row, assessment for $Blimp1^{GFP}$, B220 and CD19 expression in $CD3^-$ CD11b expressing $CD138^{Lo}$ $TACI^{Lo}$ cells (black), $CD3^-$ CD11b negative $CD138^{Hi}$ $TACI^{Hi}$ PCs (red) and $CD3^-$ CD11b expressing $CD138^{Hi}$ $TACI^{Hi}$ PCs (blue). Key for histograms is enclosed in black box. **(B)** Alternative gating strategy on the same BM sample shown in (A); $CD138^{Hi}$ $TACI^{Hi}$ PCs are gated from $CD3^-$ cells (left) before $CD138^{Hi}$ $TACI^{Hi}$ PCs are assessed for CD11b expression against $Blimp1^{GFP}$ (middle) and B220 (right). Flow cytometric data from a day 8 SRBC immunised HALO PC mouse (Figure 3.18).

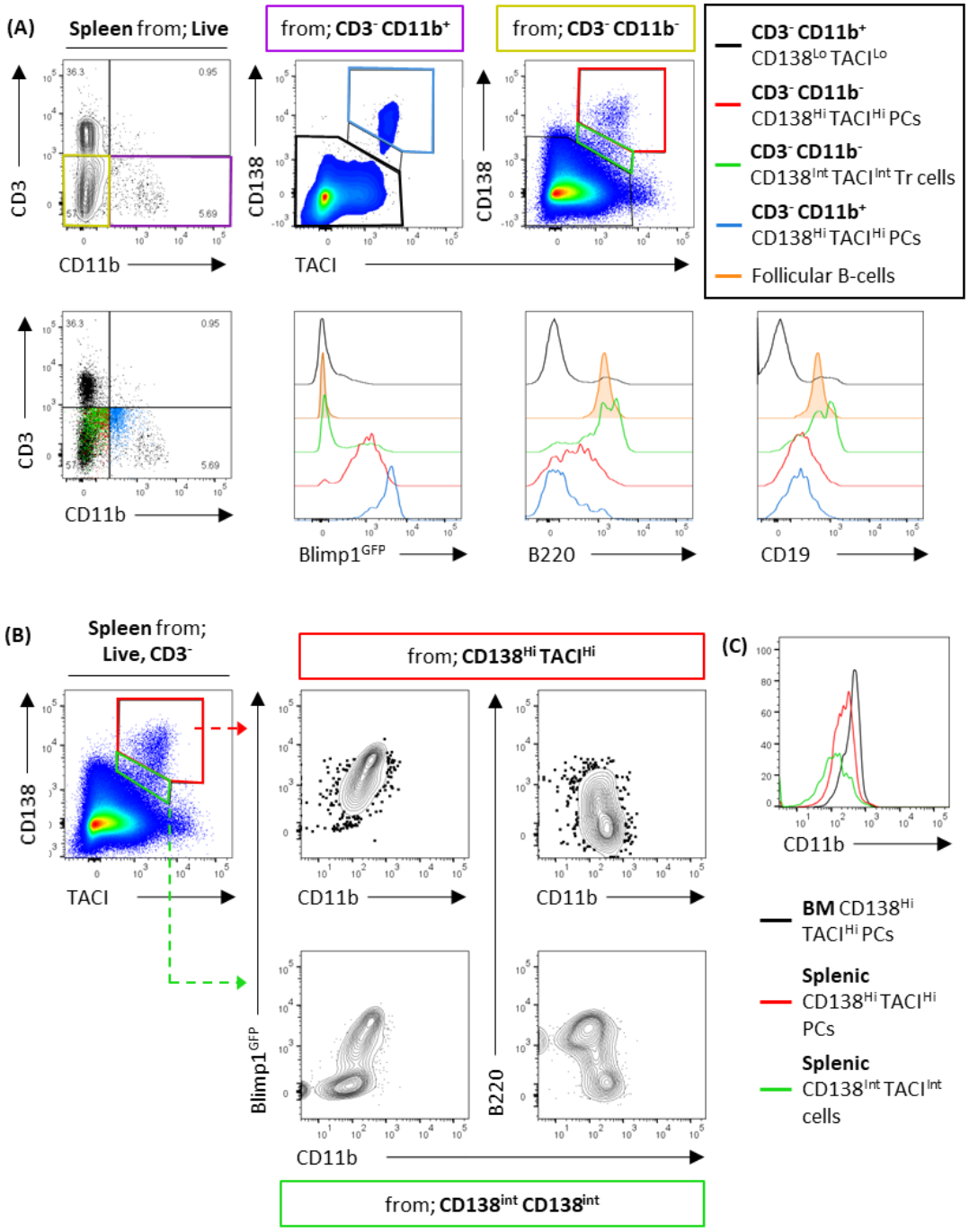

Figure 3.22 **CD11b expression correlates with maturing PCs in the spleen**. **(A)** Top row, representative standard gating strategy in HALO PC mice to exclude $CD3^+$ T-cells and $CD11b^+$ myeloid cells from splenic lymphocytes. Bottom row, assessment for $Blimp1^{GFP}$, B220 and CD19 expression in $CD3^-$ CD11b expressing $CD138^{Lo}$ $TACI^{Lo}$ cells (black), $CD3^-$ CD11b negative $CD138^{Hi}$ $TACI^{Hi}$ PCs (red), $CD3^-$ CD11b negative $CD138^{int}$ $TACI^{int}$ Tr cells, $CD3^-$ CD11b negative $CD138^{Lo}$ $TACI^{Lo}$ $B220^+$ $CD19^+$ $CD38^{Hi}$ Fas^{Lo} tdTomato negative Follicular B-cells and $CD3^-$ CD11b expressing $CD138^{Hi}$ $TACI^{Hi}$ PCs (blue) Key for histograms is enclosed in black box. **(B)** Alternative gating strategy on the same spleen sample shown in (A); $CD138^{Hi}$ $TACI^{Hi}$ PCs and $CD138^{int}$ $TACI^{int}$ Tr cells are gated from $CD3^-$ cells (left) before

CD138^{Hi} TACI^{Hi} PCs are assessed for CD11b expression against Blimp1^{GFP} (middle column) and B220 (right column). **(C)** CD11b expression in BM and spleen CD138^{Hi} TACI^{Hi} PCs and spleen CD138^{int} TACI^{int} Tr cells from the same mouse. Flow cytometric data from a day 8 SRBC immunised HALO PC mouse.

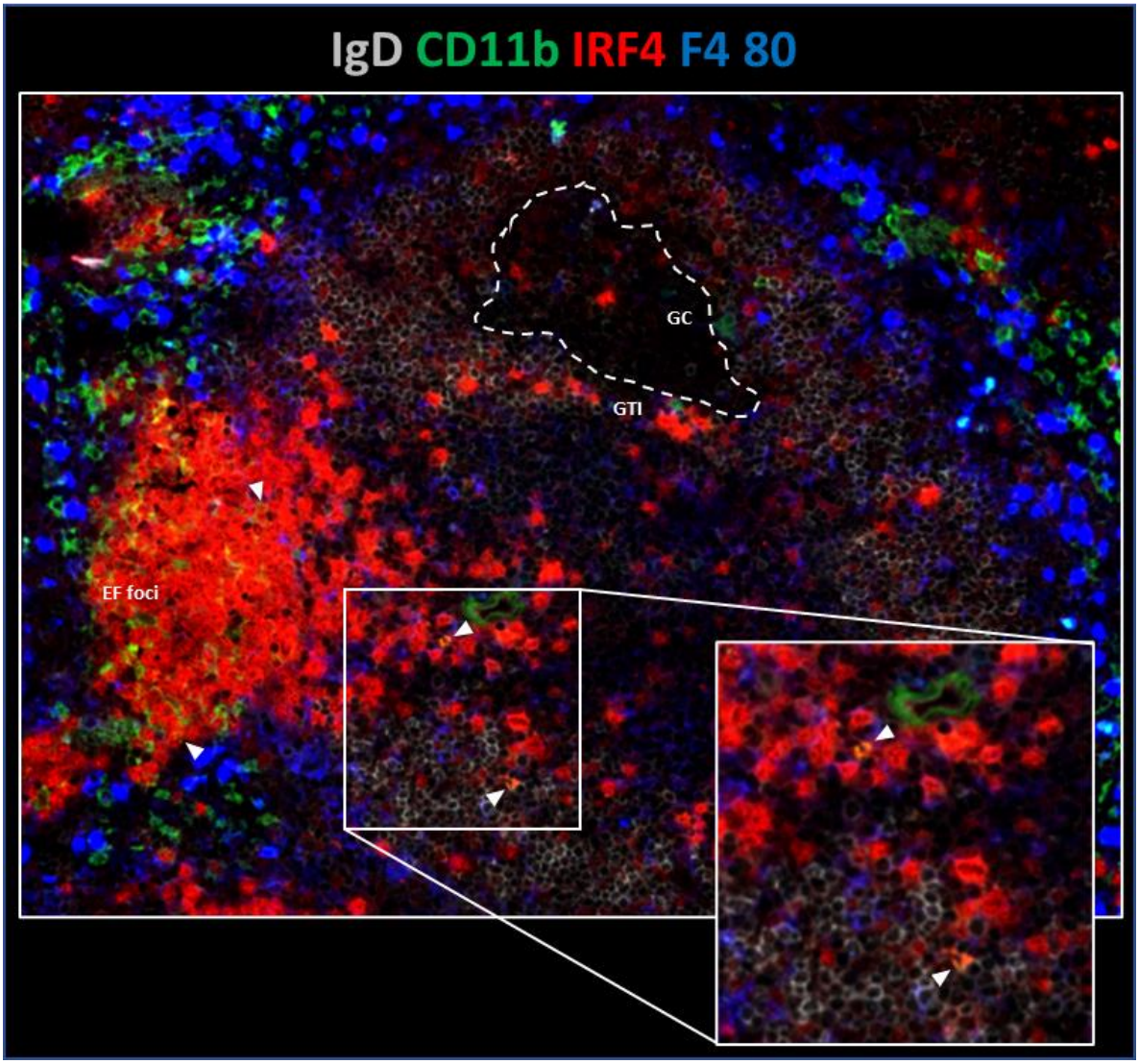

Figure 3.23 **Immunofluorescence histology suggested that CD11b expression could be present on a fraction of splenic PCs.** Spleen section from a wild-type C57BL/6 mouse 5 d post-immunisation with SRBC i.v. Sectioning, staining, and imaging performed by Dr Yang Zhang. Image acquired with Slide Scanner Axio Scan.Z1 (Zeiss) at 20x magnification. Boundaries of the GC (dashed white lines), as well as the GC:T-zone interface (GTI) and extrafollicular foci (EF foci) are indicated. White arrow heads indicate cells which are co-expressing CD11b and IRF4.

3.2.5.3 Investigation of GC B-cell subsets in HALO PC mice during the early GC response identified CD38 (re)-expression in Blimp1^{GFP} expressing GC B-cells.

We next sought to characterise the GC response. HALO PC mice demonstrated efficient GC B-cell fate mapping and early GC responses with magnitudes consistent with those observed in *S1pr2*^{ERT2Cre}.*Rosa26*^{LSLtdTomato} mice (Figure 3.24A-B and Figure 3.8) The DZ:LZ ratio in HALO PC mice changed in a similar pattern with a skew towards centroblasts at day 5, the ratio being reduced at 6 d after immunization, and slightly more DZ B cells at 8 days, although this was not a statistically significant due to the small number of HALO PC mice available for study (Figure 3.24C-D).

Imaging and flow cytometric studies have used *Prdm1* controlled FP reporters to identify and study proposed PC precursor cells in the GC (Fooksman *et al.*, 2010; Kräutler *et al.*, 2017; Zhang *et al.*, 2018; Radtke and Bannard, 2019). However, these studies focus on imaging and cell dynamics (Fooksman *et al.*, 2010; Zhang *et al.*, 2018), population dynamics after immunological intervention (Kräutler *et al.*, 2017), or transcriptional changes and differentiation capacity (Radtke and Bannard, 2019). Bcl6-YFP mice have been used to identify and study a subset of LZ GC B-cells that were Bcl6^{Lo} IRF4^{Hi} CD69^{Hi} and which contain higher affinity PC precursors (Ise *et al.*, 2018). This LZ subset displayed a predisposition to upregulate *Prdm1* after *in vitro* IL-21 stimulation, but notably, did not yet express *Prdm1 in vivo* and displayed no significant association in gene expression patterns with mature GCmat PBs when comparing RNA-seq data by principal component analysis (Ise *et al.*, 2018). To test whether precursors of PCs were detectable in the GCs of HALO PC mice, we undertook flow cytometric population and cell-surface phenotype analysis of the Blimp1^{GFP} expressing GC B-cell DZ and LZ compartments (Figure 3.25A). Cell frequency analysis indicated that, although

rare, with only 1-2 per 20,000 lymphocytes, the proportion of DZ Blimp1^{GFP} expressing cells increased as the response progressed (Figure 3.25B-C). The scarcity of PC precursors was consistent with the low frequencies of Blimp1^{GFP} expressing GC B-cell subsets reported by others during the early stage of primary responses in the spleen or LN (Fooksman *et al.*, 2010; Kräutler *et al.*, 2017), or throughout the entire response (days 7, 14 and 21) when identified as LZ Bcl6^{Lo} IRF4^{Hi} CD69^{Hi} precursors (Ise *et al.*, 2018). B220 expression was elevated on the Blimp1^{GFP} expressing DZ and LZ GC B-cells compared to the Blimp1^{GFP} negative DZ and LZ GC B-cells (Figure 3.25D), which suggests an activated differentiating state (Hermiston, Xu and Weiss, 2003). Interestingly, this corresponded with increased CD38 expression, as DZ Blimp1^{GFP} expressing cells displayed almost 2-fold greater CD38 expression compared to DZ Blimp1^{GFP} negative cells, rising to 30% the expression level of Fo B-cells (Figure 3.25E). LZ Blimp1^{GFP} expressing cells displayed a similar pattern of B220 and CD38 expression (Figure 3.25D-E). Blimp1^{GFP}, B220 and CD38 co-expression all coincided with a significant increase in cell size (Figure 3.25A and E) and upregulation of traditional PC lineage marker CD138 (Figure 3.25F-G), particularly in a subset of Blimp1^{GFP} expressing LZ and DZ cells (middle histogram, Figure 3.25A). This data suggested that Blimp1^{GFP} expressing DZ and LZ subsets have recently been positively selected into the initial stages of the pathway towards PC lineage. Like for CD138^{int} TACI^{int} tdTomato expressing Tr cells (Figure 3.15C), CD38 re-expression in Blimp1^{GFP} expressing GC B-cells was unexpected as it is accepted that murine GC B-cells do not express CD38 (Oliver, Martin and Kearney, 1997). However, CD38 has been shown to act in synergy with BCR signalling to decrease the threshold for BCR responses (Lund *et al.*, 1996). Further, activated CD38 can act through the nuclear factor (NF)-κB pathway to induce c-Rel and RelA (p65) expression (Kaku *et al.*, 2002) and the balance between these two NF-κB proteins regulates GC B-cell maintenance or Blimp1 up-regulation and induction of PC

differentiation, with RelA critically required for PC differentiation (Heise *et al.*, 2014; Roy *et al.*, 2019). This makes it likely that a transient CD38 re-expression in high-affinity GC B-cells promotes integration of strong BCR-Ag induced signals and CD40 propagated NF-κB signals to promote initiation of PC differentiation.

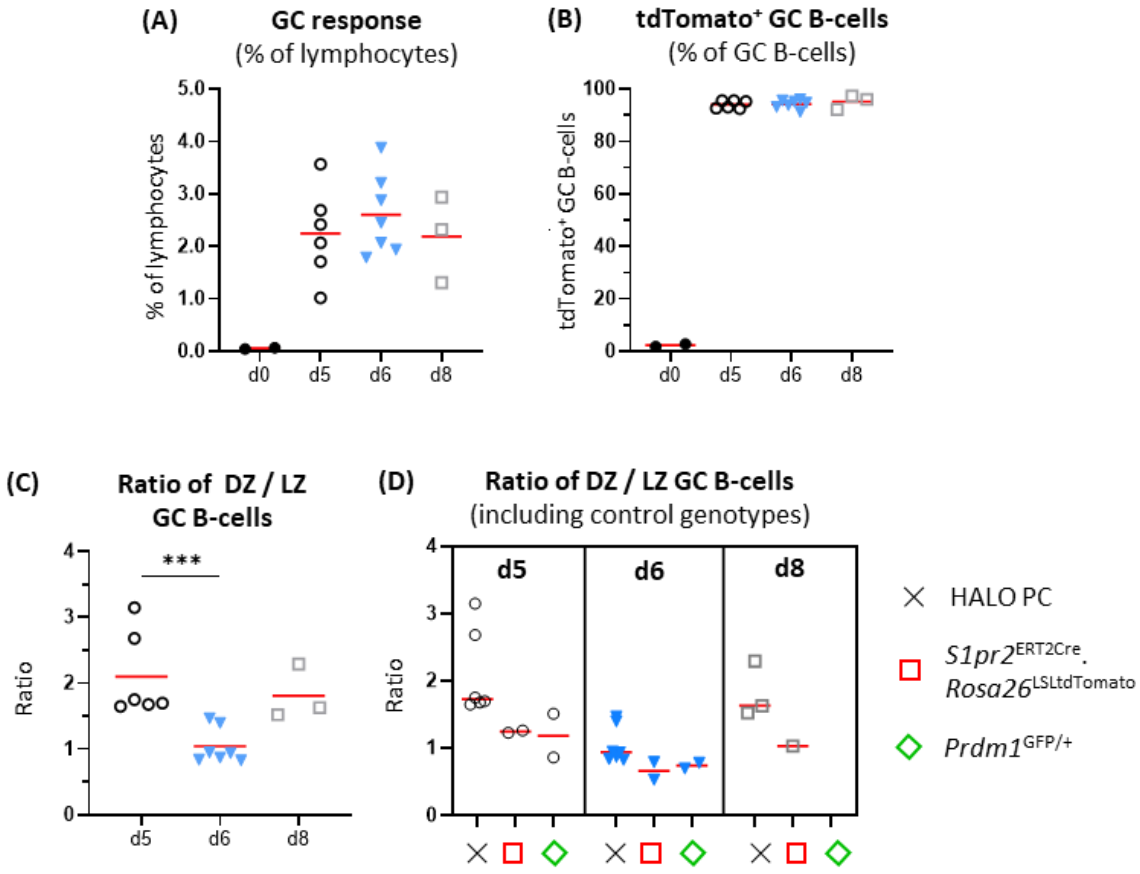

Figure 3.24 **Overview of the early splenic GC response and subsets in HALO PC mice**. Analysis of the early GC response in the primary immune response of SRBC immunised HALO PC mice, as per experimental protocol in Figure 3.18. **(A)** Size of the GC B-cell ($CD138^{Lo}$ $TACI^{Lo}$ $B220^{+}$ $CD19^{+}$ $CD38^{Lo}$ Fas^{Hi}) response. **(B)** Efficiency of 48 h tamoxifen induction in fate mapping GC B-cells on day 5, 6, 8 or background in non-induced naïve HALO PC mice (d0). Phenotypic analysis of the GC for DZ and LZ compartments **(C-D)**. Data from three experiments. No *Prdm1*$^{GFP/+}$ mice were available for analysis at day 8. Brown-Forsythe & Welch's ANOVA with uncorrected Welch's t-test (A). Kruskal-Wallis test with uncorrected Dunn's test (B and C).

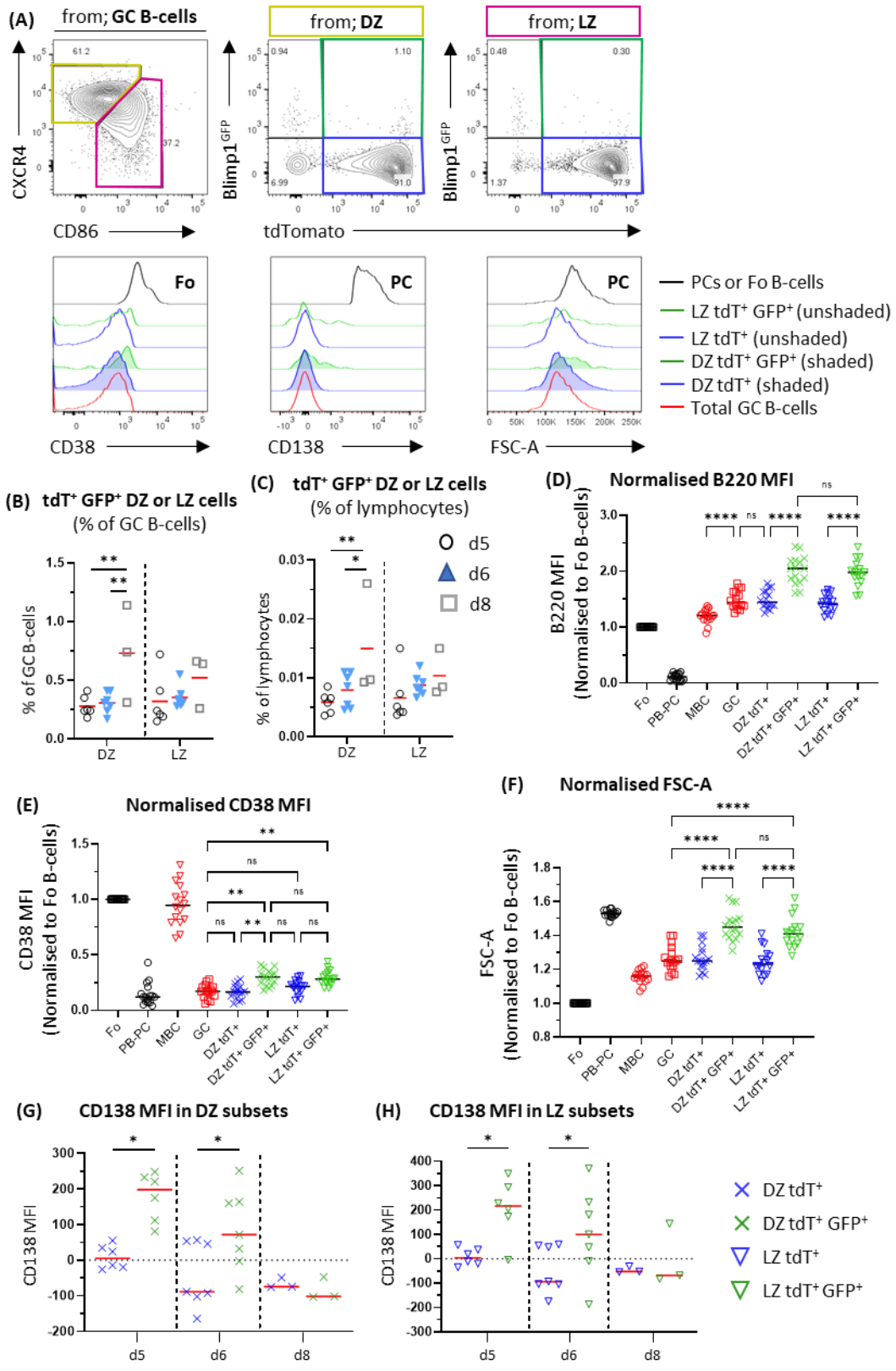

Figure 3.25 **Phenotype analysis of Blimp1^{GFP+} GC B-cell subsets in the early GC response.** **(A)** Representative gating for identification of DZ (CXCR4^{Hi} CD86^{Lo}) and LZ (CXCR4^{Lo} CD86^{Hi}) from CD138^{Lo} B220^{+} CD38^{Lo} FAS^{Hi} GC B-cells, with subsequent analysis for

Blimp1^{GFP+} and tdTomato^{+} (tdT^{+}) subsets and population analysis for CD38 or CD138 expression and cell size. Fo B-cells (CD138^{Lo} B220^{+} CD38^{Hi} Fas^{Lo} tdTomato^{-}) and PB-PC (CD138^{Hi} B220$^{Lo/int}$ Blimp1^{GFP+} tdTomato^{-}). Frequency of Blimp1^{GFP+} tdT^{+} DZ **(B)** and LZ **(C)** GC B-cells. Phenotypic analysis for B220 **(D)**, CD38 **(E)**, cell size **(F)** in Blimp1^{GFP+} or Blimp1^{GFP-} tdT^{+} DZ and LZ GC B-cells, total GC B-cells, Fo B-cells, PB-PC, MBC (CD138^{Lo} B220^{+} CD38^{Hi} Fas^{Lo} tdTomato^{+}). **(G-H)** CD138 expression in Blimp1^{GFP+} or Blimp1^{GFP-} tdT^{+} DZ and LZ GC B-cells. Data from three experiments. Experimental protocol outlined in Figure 3.18. Two-way ANOVA with Tukey's multiple comparisons (B-C). Kruskal-Wallis with uncorrected Dunn's test (E, G-H). Brown-Forsythe & Welch ANOVA with unpaired Welch's t-test (D-E).

3.2.5.4 Investigation of GCmat CD138^{Hi} TACI^{Hi} PC output from the early GC in HALO PC mice.

We designed the HALO PC mouse to be able to distinguish EF and GCmat PCs (Figure 3.6B). To test whether this was the true at the early stages of the GC response, we analysed tdTomato (tdT) expression in splenic CD138^{Hi} TACI^{Hi} PCs at day 5, 6, or 8 post primary SRBC immunisation (Figure 3.26A). PCs were found to express low to intermediate levels of CD11b as terminal differentiation progressed (Figure 3.21 and Figure 3.22), therefore, for all subsequent flow cytometric analyses where CD11b was included, CD11b$^{Lo/Int}$ represents a gate that was set to include all PCs and to exclude CD11b^{Hi} myeloid cells.

The magnitude and kinetics of the total CD138^{Hi} TACI^{Hi} PC response were as expected (Figure 3.26B) and were consistent with the observations in *S1pr2*^{ERT2Cre}.*Rosa26*^{LSLtdTomato} mice (Figure 3.10). As hypothesised (Figure 3.6B), the HALO PC model can resolve GCmat PCs (GFP^{+} tdT^{+}) from EF PCs (GFP^{+} tdT^{-}), with less than 10% of CD138^{Hi} TACI^{Hi} GCmat PCs negative for Blimp1^{GFP} (Figure 3.26A and C). The proportion of GCmat CD138^{Hi} TACI^{Hi} PB-PCs in the total splenic PC response increased as the resolution of the extrafollicular phase continued (Figure 3.26D) providing further confidence that the immune response of HALO PC mice progressed as expected. HALO PC mice displayed similar frequencies and absolute numbers of GCmat CD138^{Hi} TACI^{Hi} PB-PCs fate mapped between days 4-6 and days 6-8 compared to *S1pr2*^{ERT2Cre}.*Rosa26*^{LSLtdTomato} mice, but in HALO PC mice there was no difference in the frequency of GCmat CD138^{Hi} TACI^{Hi} PB-PCs labelled during days 3-5 compared to days 4-6 (Figure 3.26D-E and Figure 3.10). Moreover, the frequency and absolute numbers of fate mapped GCmat CD138^{Hi} TACI^{Hi} P1 PBs peaked during the earliest labelling window (days 3-5) with subsequent decline (Figure 3.26G-I), which could be due to the decrease in volume of

PC niche available to support PCs after the acute extrafollicular phase has resolved (Sze *et al.*, 2000).

We also analysed the accumulation of GCmat CD138^{Hi} TACI^{Hi} PCs in the BM (Figure 3.27A-B). Consistent with preliminary findings (Figure 3.12), there was no significant increase in the proportion of affinity matured PCs resident in the BM (Figure 3.27C-D). However, there was a potential trend towards an increase of PCs fate mapped between days 6-8 (Figure 3.27C-D), but due to COVID-19 restrictions and curtailed breeding, sufficient HALO PC mice were not available to further evaluate this time-point.

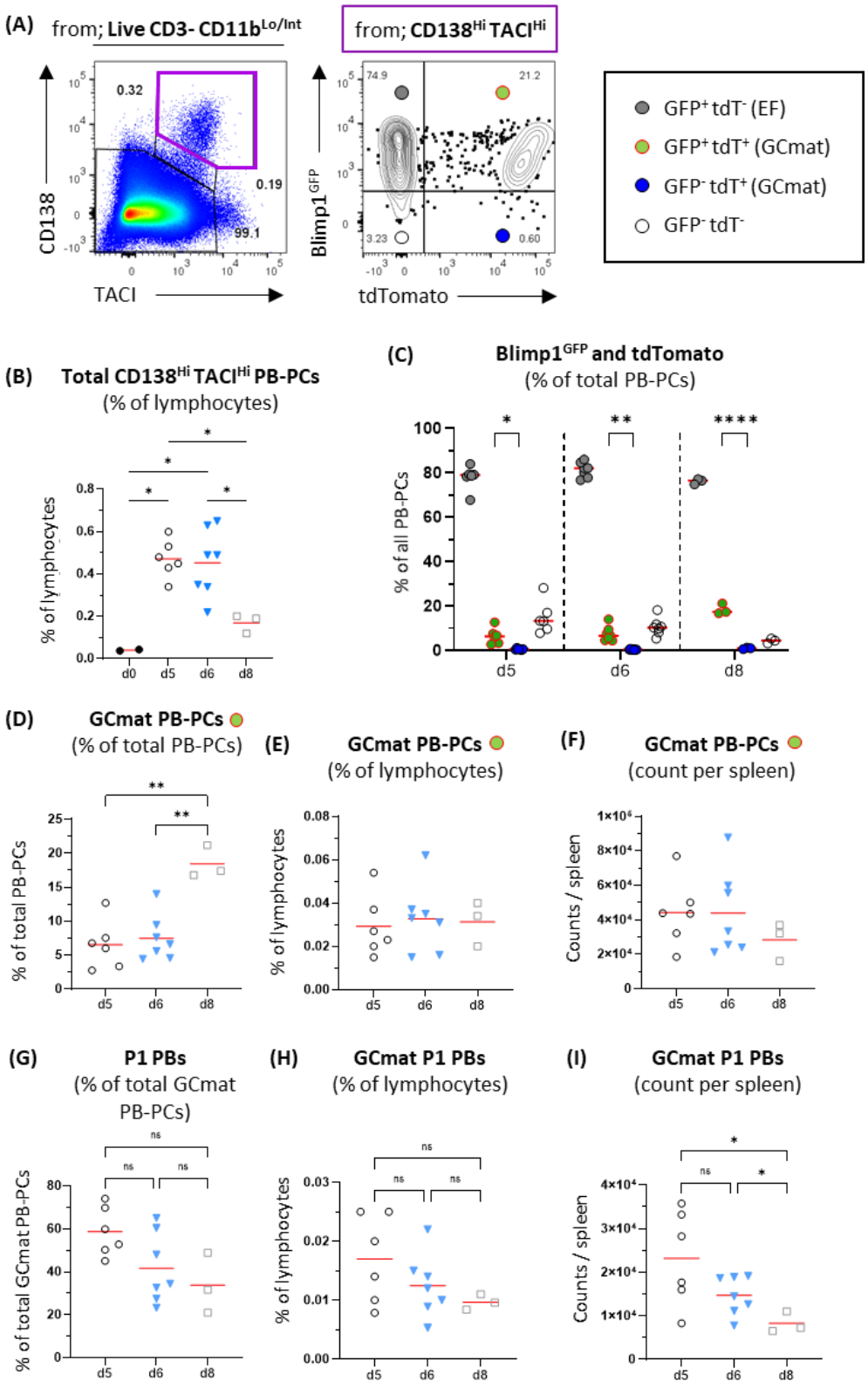

Figure 3.26 **The HALO PC model can distinguish extrafollicular and GC-experienced PCs**. **(A)** Representative flow cytometric gating of Blimp1^{GFP} and tdTomato expression in CD138^{Hi} TACI^{Hi} PB-PCs in the spleen of SRBC immunised HALO PC mice. The CD11b$^{Lo/Int}$

gate was set to include all PCs as identified in Figure 3.22 and discussed in Section 3.2.5.2 CD11b expression on maturing PCs.3.2.5.2 CD11b expression on maturing PCs. Size of the total CD138^{Hi} TACI^{Hi} PC response **(B)** and proportions of Blimp1^{GFP} and tdTomato (tdT) expressing PCs **(C)**. Frequency of GCmat CD138^{Hi} TACI^{Hi} PB-PCs from total CD138^{Hi} TACI^{Hi} PCs **(D)** or lymphocytes **(E)**. GCmat CD138^{Hi} TACI^{Hi} PB-PCs absolute numbers **(F)**. P1 PBs (B220^{+} CD19^{+}) gated as shown in Figure 3.12A. Frequency of GCmat CD138^{Hi} TACI^{Hi} P1 PBs from total GCmat PCs **(G)** or lymphocytes **(H)**. GCmat CD138^{Hi} TACI^{Hi} P1 PB absolute numbers **(I)**. Experimental protocol outlined in Figure 3.18. Kruskal-Wallis with uncorrected Dunn's test (B). Two-way ANOVA with Tukey's multiple comparisons (C). Brown-Forsythe & Welch ANOVA with unpaired Welch's t-test (D-I).

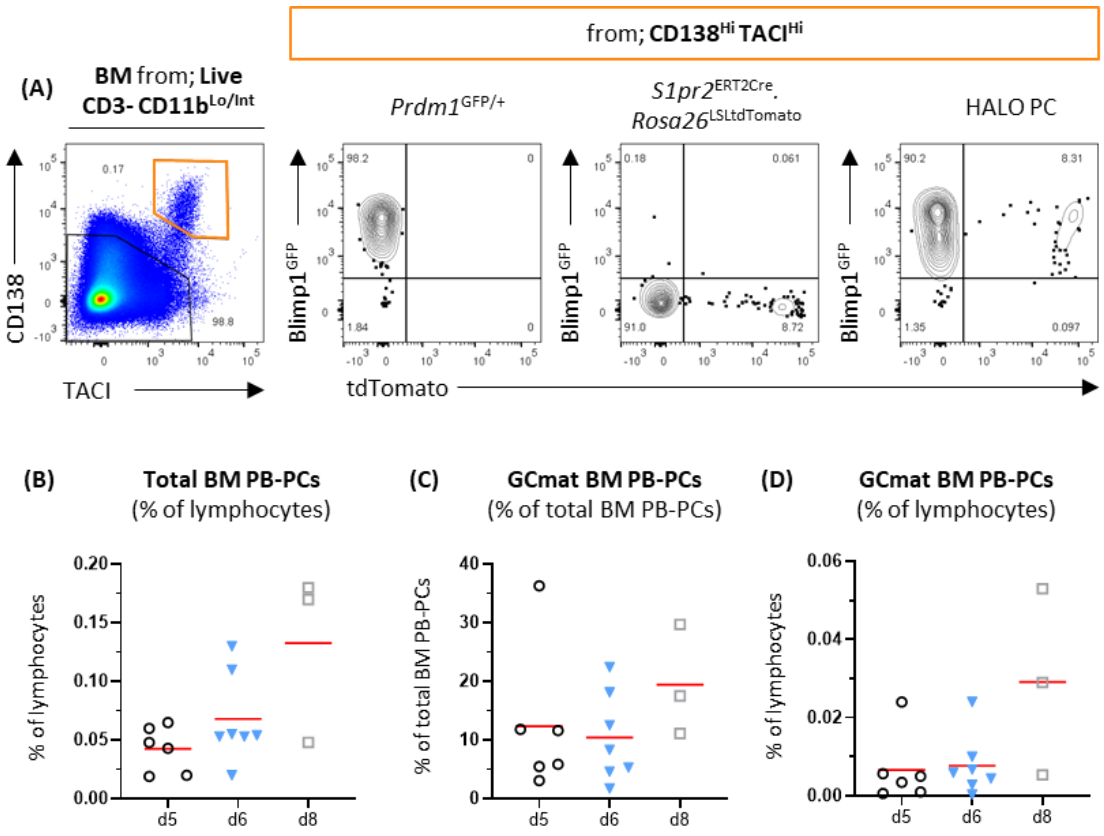

Figure 3.27 **Accumulation of GCmat PCs in the bone marrow**. Flow cytometric gating of CD138^{Hi} TACI^{Hi} BM PCs with Blimp1^{GFP} and tdTomato expression in HALO PC and control mice (A). Analysis of total BM PCs (B), and GCmat PCs (C-D). Experimental protocol outlined in Figure 3.18. Brown-Forsythe & Welch ANOVA with unpaired Welch's t-test (B). Kruskal-Wallis test with uncorrected Dunn's test (C-D).

3.2.5.5 Investigation of GC-experienced CD138^{int} TACI^{int} transitioning (Tr) cells and MBCs and understanding their output kinetics from the early GC.

Whilst analysing the GCmat output from *S1pr*^{2ERT2Cre}.*Rosa26*^{LSLtdTomato} mice we identified a population of CD138^{int} TACI^{int} tdTomato expressing cells (Figure 3.14A) which we proposed to be transitioning (Tr) PCs based on cell size and cell-surface marker expression (Figure 3.15 and Figure 3.17). With the HALO PC mouse we had the ability to test these tdTomato expressing CD138^{int} TACI^{int} Tr cells for expression of Blimp1^{GFP} to ascertain if they were bone fide PC precursors and could represent a highly activated transitioning state of positively selected GC B-cells instructed toward terminal differentiation (Figure 3.17). We therefore expanded the phenotype analysis to include Blimp1^{GFP} expression (Figure 3.28A), as well as cell surface marker expression and cell size (Figure 3.28B-E). To ensure that CD138^{int} TACI^{int} Tr cells analysed were GC-experienced, we restricted the analysis of CD138^{int} TACI^{int} cells negative for Blimp1^{GFP} to those that were tdTomato^{Hi} (tdT^{Hi}). We did not include CD138^{int} TACI^{int} Tr cells expressing neither Blimp1^{GFP} nor tdTomato in the analysis as they are neither GC-experienced nor are they (yet) showing commitment to the PC lineage, whereas for double or single FP+ CD138^{int} TACI^{int} Tr cells, information on these parameters is provided by FP status. The CD138^{int} TACI^{int} tdT^{Hi} Blimp1^{GFP} negative cells were similar in size to CD138^{Hi} TACI^{Hi} GCmat Blimp1^{GFP} expressing PCs and were significantly larger than both their CD138^{int} TACI^{int} tdT^{+} Blimp1^{GFP} expressing Tr counterparts and Blimp1^{GFP} expressing GC B-cells (Figure 3.29A). Cell surface marker analysis revealed high expression of CD38, B220 and CD19 by CD138^{int} TACI^{int} tdT^{Hi} Blimp1^{GFP} negative Tr cells (Figure 3.29B-D). Irrespective of Blimp1^{GFP} status, tdTomato expressing CD138^{int} TACI^{int} Tr cells displayed significantly elevated CD38 expression (at least 2-fold higher) compared to Blimp1^{GFP} expressing GC B-cells (Figure 3.29B). Strikingly, for the CD138^{int} TACI^{int} tdT^{Hi} Blimp1^{GFP}

negative Tr population CD38 expression was no different to GCmat MBC expression levels (Figure 3.29B). Although CD38 expression in CD138^{int} TACI^{int} tdT^{+} Blimp1^{GFP} expressing Tr P1 PBs was lower than the CD138^{int} TACI^{int} tdT^{Hi} Blimp1^{GFP} negative Tr population, it was still at 54% of Fo B-cells; more than 3-fold higher than GC B-cells and 2-fold greater than Blimp1^{GFP} expressing GC B-cells (Figure 3.29B). These results suggest that CD38 re-expression may be transient as GC-experienced PC precursors initiate differentiation and exit from the GC but is dispensable as differentiation progresses and the canonical PC gene regulatory network is engaged. Expression of B220, an isoform of protein tyrosine phosphatase CD45 implicated in B-cell differentiation and BCR signal modulation (Hermiston, Xu and Weiss, 2003), was similar to Blimp1^{GFP} expressing GC B-cells and elevated compared to Blimp1^{GFP} negative GC B-cells (Figure 3.29C). However, as tdTomato expressing CD138^{int} TACI^{int} tdT^{Hi} Tr cells acquired Blimp1^{GFP} expression and progressed down the PC lineage, this spike in B220 expression decreased rapidly (Figure 3.29C). Further, CD19 expression was also elevated in these CD138^{int} TACI^{int} tdT^{Hi} Blimp1^{GFP} negative Tr cells but also significantly decreased after Blimp1^{GFP} expression (Figure 3.29D). CD19 forms a co-receptor involved in decreasing the BCR signalling threshold (Tedder, Inaoki and Sato, 1997; Del Nagro *et al.*, 2005), and so these results are consistent with the requirement of strong BCR signalling, as well as Tfh mediated signals, for GC B-cell PC fate induction (Luo, Weisel and Shlomchik, 2018).

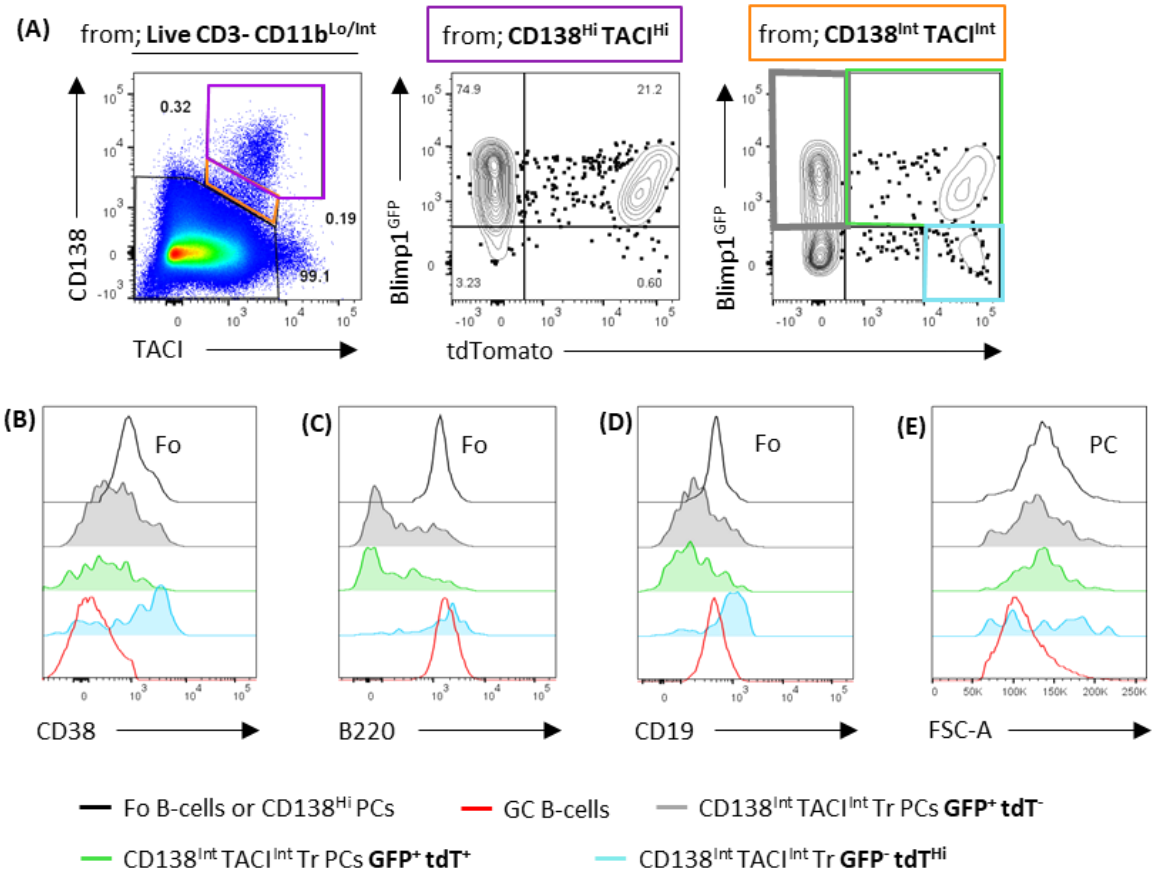

Figure 3.28 **Initial phenotype insights into *S1pr2* experienced CD138^{int} TACI^{int} transitioning PCs**. **(A)** Representative flow cytometric gating from spleen to identify populations of interest from CD138^{int} TACI^{int} Tr cells: GFP^{+} tdT^{-} (grey, EF Tr PCs), GFP^{+} tdT^{+} (green, GCmat Tr PCs) and GFP^{-} tdT^{Hi} (cyan, proposed to be earliest differentiation state of GCmat PCs). **(B-E)** Representative histograms of populations from a single immunised HALO PC mouse for cell surface marker expression (B-D) and cell size (E). Experimental protocol outlined in Figure 3.18.

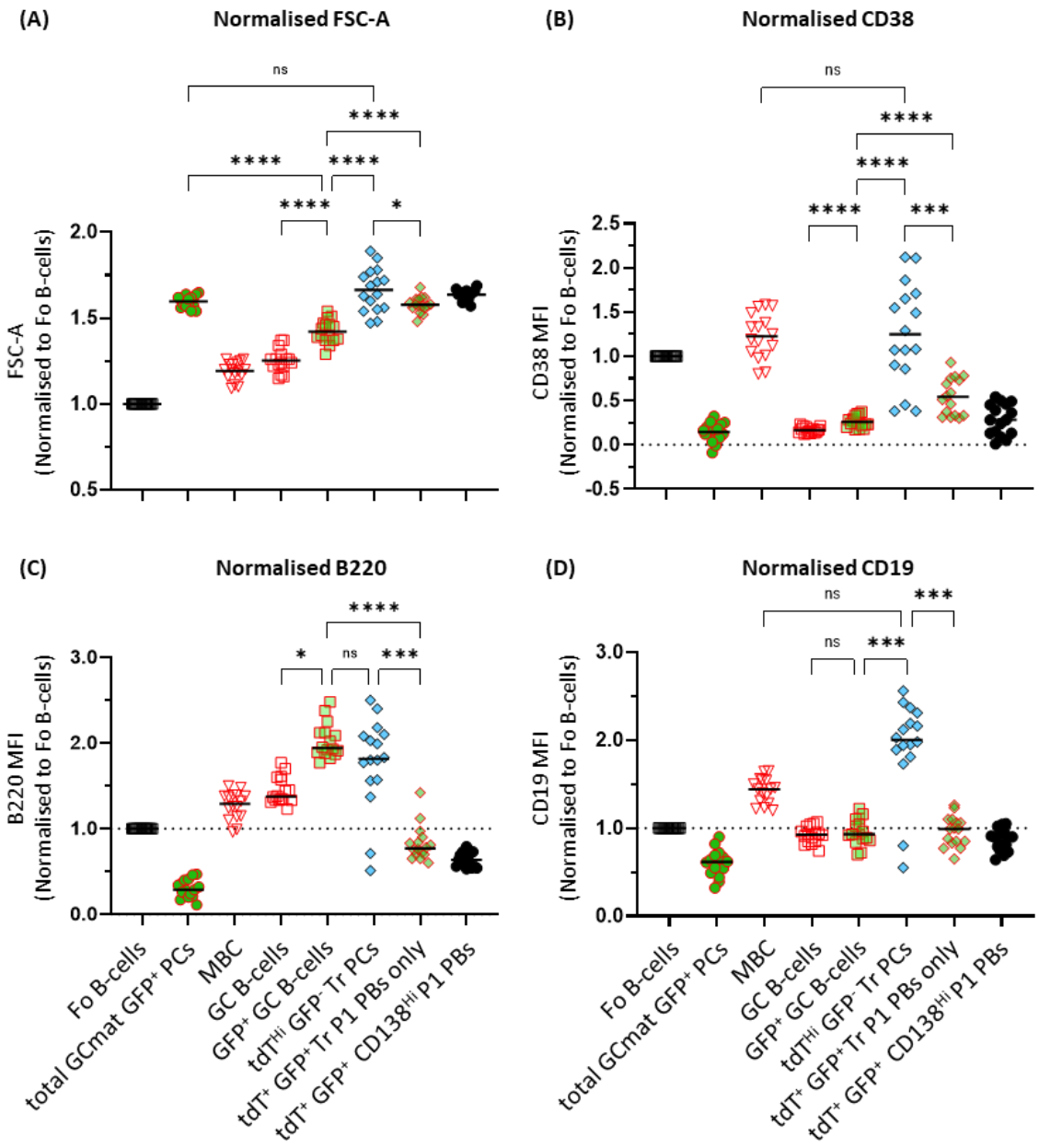

Figure 3.29 **Phenotype analysis of *S1pr2* experienced, GC matured CD138^{int} TACI^{int} transitioning PCs**. Analysis of cells size **(A)** and cell surface marker expression **(B-D)**. Fo B-cells (CD138^{Lo} TACI^{Lo} B220^{+} CD19^{+} CD38^{Hi} Fas^{Lo} tdTomato^{-}), total GCmat GFP^{+} PCs (CD138^{Hi} TACI^{Hi} tdTomato^{+} Blimp1^{GFP} expressing), MBC (CD138^{Lo} TACI^{Lo} B220^{+} CD19^{+} CD38^{Hi} Fas^{Lo} tdTomato^{+}), GFP^{+} GC B-cells (CD138^{Lo} TACI^{Lo} B220^{+} CD19^{+} CD38^{Lo} Fas^{Hi} tdTomato^{+} Blimp1^{GFP} expressing), tdT^{Hi} GFP^{-} Tr PCs (CD138^{int} TACI^{int} tdTomato^{Hi} Blimp1^{GFP} negative irrespective of B220 and CD19), tdT^{+} GFP^{+} Tr P1 PBs only (CD138^{int} TACI^{int} B220^{+} CD19^{+} tdTomato^{+} Blimp1^{GFP} negative), , tdT^{+} GFP^{+} CD138^{Hi} P1 PBs (CD138^{Hi} TACI^{Hi} B220^{+} CD19^{+} tdTomato^{+} Blimp1^{GFP} expressing) Experimental protocol outlined in Figure 3.18. Brown-Forsythe & Welch ANOVA with unpaired Welch's t-test (A-B). Kruskal-Wallis with uncorrected Dunn's test (C-D).

B220 expression and cell size suggested that CD138^{int} TACI^{int} tdT^{Hi} Tr cells represented an intermediate between Blimp1^{GFP} expressing GC B-cells and CD138^{Hi} TACI^{Hi} GCmat PCs. However, the lack of Blimp1^{GFP} expression and equivalent CD38 expression to MBCs could have meant that these cells were a GCmat MBC sub-population with unexpectedly high CD138 and TACI expression contaminating the CD138^{int} TACI^{int} gate. The staining intensities for CD138 and TACI (MFI values) range from 0 to >10^3 within the CD138^{Lo} TACI^{Lo} gate (Figure 3.28A). Although CD138^{int} TACI^{int} tdT^{Hi} Blimp1^{GFP} negative Tr cells and GCmat MBCs (CD138^{Lo} TACI^{Lo} B220^{+} CD19^{+} CD38^{Hi} Fas^{Lo} tdT^{Hi}) populations are contained within either the CD138^{int} TACI^{int} or CD138^{Lo} TACI^{Lo} gates, respectively, to test whether the arbitrary placement of flow cytometry gates had separated a single population of GCmat MBCs with variable CD138 and TACI staining intensities and protein expression, we analysed the fold-change in staining intensities between CD138^{int} TACI^{int} tdT^{Hi} Blimp1^{GFP} negative Tr cells, GCmat MBCs and control populations (Figure 3.30A-B). CD138^{int} TACI^{int} tdT^{Hi} Blimp1^{GFP} negative Tr cells expressed at least 16-fold greater CD138 than GCmat MBCs (Figure 3.30A) and at least 3-fold more TACI (Figure 3.30B). These substantial fold-changes in CD138 and TACI expression supported our conclusion that arbitrary flow cytometric gate placement had not separated a single GCmat MBC population with variable CD138 and TACI but that CD138^{int} TACI^{int} tdTomato expressing Tr cells are an intermediary stage of GCmat PC differentiation. Further, TACI expression of CD138^{int} TACI^{int} tdT^{Hi} Blimp1^{GFP} negative Tr cells was only 81% that of their CD138^{int} TACI^{int} tdT^{+} Blimp1^{GFP} expressing Tr PC counterparts, consistent with the former population being of an earlier PC differentiation stage (Figure 3.30B). Taken together, these data suggest that CD138^{int} TACI^{int} GCmat Tr PB-PCs represent a highly activated population of GCmat PC precursors which require transient CD38

re-expression before Blimp1 driven changes to gene expression and progression of terminal differentiation (Figure 3.31).

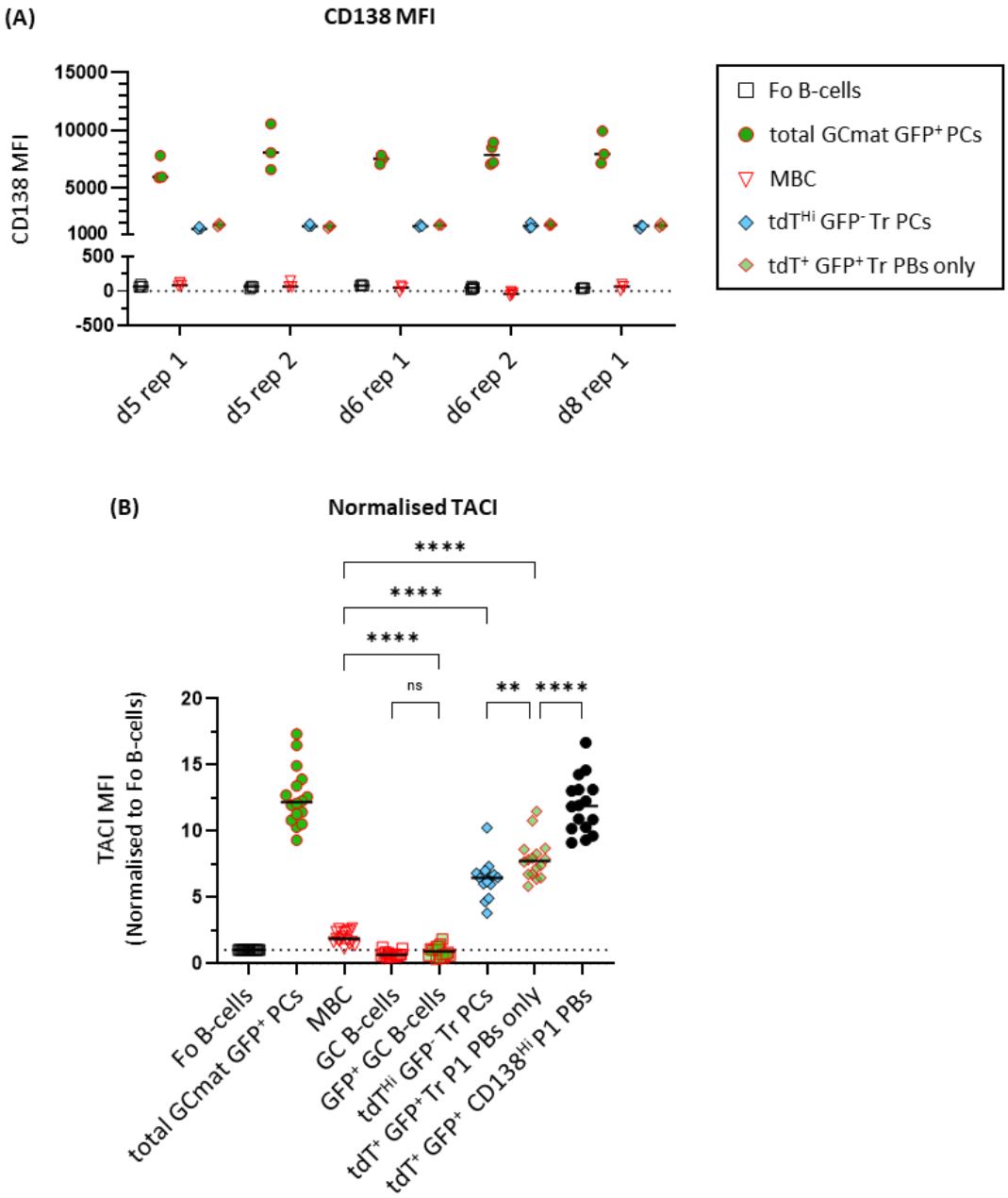

Figure 3.30 **CD138^{int} TACI^{int} tdTomato expressing Tr cells are not MBC**. Analysis of PC lineage markers CD138 **(A)** and TACI **(B)**. In (A), d5 rep 1 represent cell populations from the first independent repeat of the d5 response in HALO PC mice, d5 rep 2 from the second independent repeat etc. Fo B-cells (CD138^{Lo} TACI^{Lo} B220^{+} CD19^{+} CD38^{Hi} Fas^{Lo} tdTomato^{-}), total GCmat GFP^{+} PCs (CD138^{Hi} TACI^{Hi} tdTomato^{+} Blimp1^{GFP} expressing), MBC (CD138^{Lo} TACI^{Lo} B220^{+} CD19^{+} CD38^{Hi} Fas^{Lo} tdTomato^{+}), GFP^{+} GC B-cells (CD138^{Lo} TACI^{Lo} B220^{+} CD19^{+} CD38^{Lo} Fas^{Hi} tdTomato^{+} Blimp1^{GFP} expressing), tdT^{Hi} GFP^{-} Tr PCs (CD138^{int} TACI^{int} tdTomato^{Hi} Blimp1^{GFP} negative irrespective of B220 and CD19), tdT^{+} GFP^{+} Tr P1 PBs only (CD138^{int} TACI^{int} B220^{+} CD19^{+} tdTomato^{+} Blimp1^{GFP} negative), tdT^{+} GFP^{+} CD138^{Hi} P1 PBs (CD138^{Hi} TACI^{Hi} B220^{+} CD19^{+} tdTomato^{+} Blimp1^{GFP} expressing). Experimental protocol outlined in Figure 3.18. Brown-Forsythe & Welch ANOVA with unpaired Welch's t-test (B).

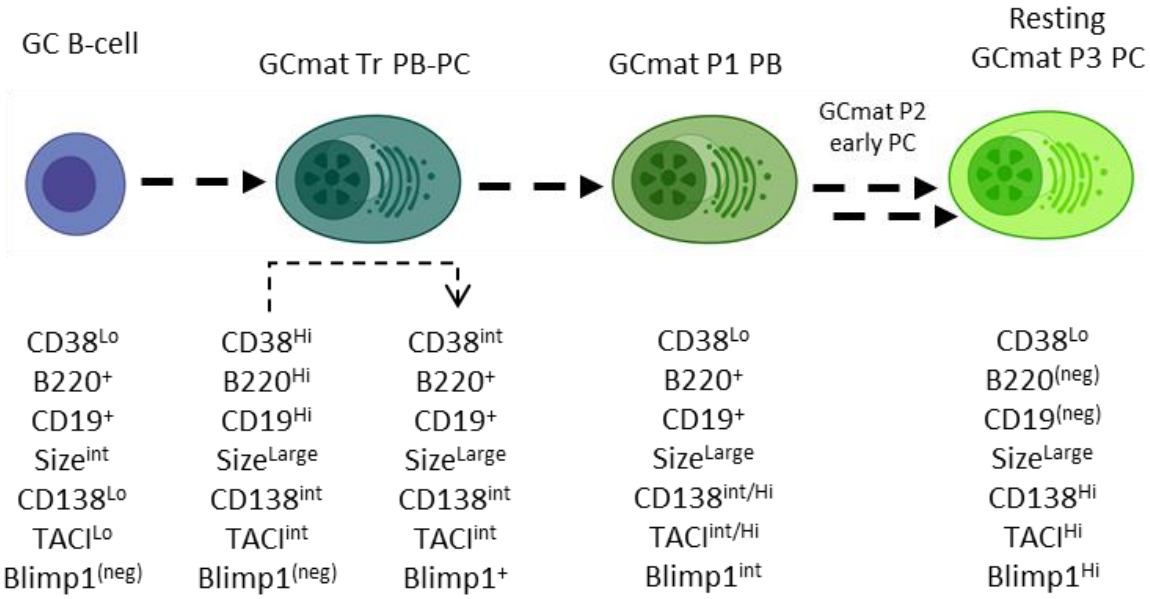

Figure 3.31 **Analysis from the HALO PC mice suggests that CD138^{int} TACI^{int} GCmat Tr PB-PCs are a bone fide population of GC-experienced PC precursors**. The schematic depicts a differentiation pathway where GC B-cells which have undergone positive selection and have been instructed toward terminal differentiation, transition through a highly activated state before increased expression of canonical PC transcription factor Blimp1 acts to co-ordinate the necessary gene regulatory network to drive terminal differentiation. Dashed thick black arrows indicate this favoured, sequential route of differentiation. Model derived from phenotype analyses from Figure 3.14, Figure 3.15, Figure 3.28, Figure 3.29 and Figure 3.30. Schematic created with BioRender.com.

To test whether CD138^{int} TACI^{int} Tr cells were responding in a manner similar to CD138^{Hi} TACI^{Hi} PCs we analysed the magnitude and kinetics of the total (extrafollicular and GCmat) CD138^{int} TACI^{int} Tr population over the duration of the immune response studied. Population analysis confirmed the expected decrease in numbers by day 8 (Figure 3.32A-B), which mirrored the CD138^{Hi} TACI^{Hi} PC response Figure 3.26). Total GCmat CD138^{int} TACI^{int} Tr PB-PCs labelled between days 3-5, days 4-6 or days 6-8 was stable (Figure 3.32C) with a frequency of ~0.01% of lymphocytes (Figure 3.32D). Classification of GCmat CD138^{int} TACI^{int} Tr cells either expressing Blimp1^{GFP} or not by B220 and CD19 expression

demonstrated that $B220^{-}$ cells (early P2 PC or mature P3 PC equivalents) were almost absent in the $CD138^{int}$ $TACI^{int}$ tdT^{Hi} $Blimp1^{GFP}$ negative Tr PB-PCs, but were present at almost 40% in the GCmat $CD138^{int}$ $TACI^{int}$ tdT^{+} $Blimp1^{GFP}$ expressing Tr PB-PCs (Figure 3.32E), consistent with $CD138^{int}$ $TACI^{int}$ tdT^{Hi} $Blimp1^{GFP}$ negative Tr PB-PCs possessing an early PC differentiation state. Cell-sorting and gene expression analysis of key genes associated with lineage commitment would help to confirm that $CD138^{int}$ $TACI^{int}$ tdT^{Hi} $Blimp1^{GFP}$ negative Tr cells are early differentiating PCs and not GCmat MBC precursors.

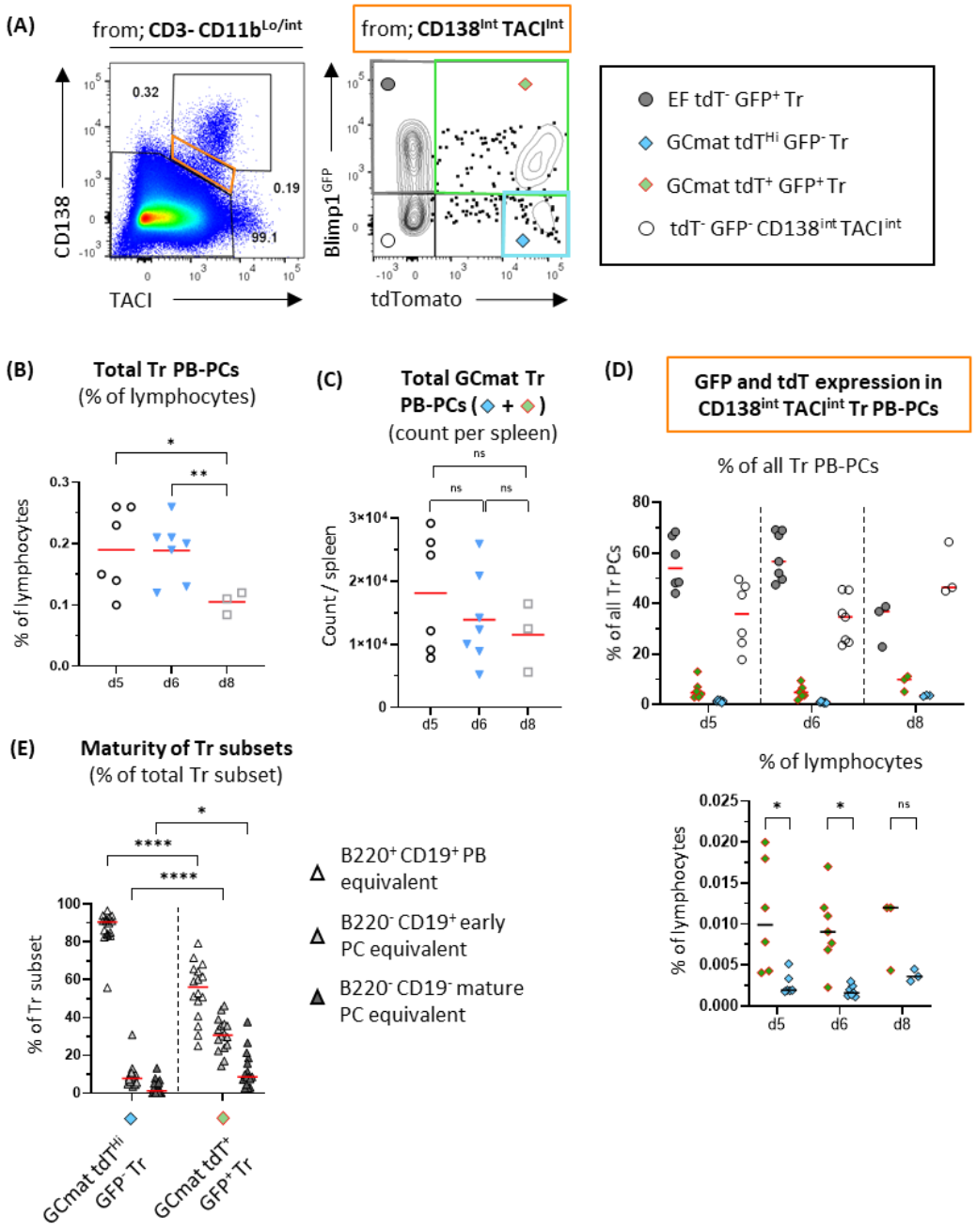

Figure 3.32 **Frequency and maturity analysis of GC-experienced Tr PCs**. Populations of CD138^{int} TACI^{int} Tr PB-PCs separated by Blimp1^{GFP} and tdTomato expression **(A)**. Analysis of total CD138^{int} TACI^{int} Tr PB-PCs **(B)**, total GCmat CD138^{int} TACI^{int} Tr PB-PCs **(C)**, or CD138^{int} TACI^{int} Tr PB-PCs by Blimp1^{GFP} and tdTomato expression; GFP^{-} tdT^{-} (open circle), EF GFP^{+} tdT^{-} (grey circle), GCmat GFP^{-} tdT^{Hi} (cyan diamond) and GCmat GFP^{+} tdT^{+} (green filled diamond with red outline) **(D)**. Classification of Blimp1^{GFP} negative (GFP^{-}) and Blimp1^{GFP} expressing (GFP^{+}) GCmat Tr PB-PCs according to B220 and CD19 expression **(E)**. Experimental protocol outlined in Figure 3.18. Brown-Forsythe & Welch ANOVA with unpaired Welch's t-test (B-C). Two-way ANOVA with Tukey's multiple comparisons (D). Sidak's multiple comparisons (E).

The magnitude of the GC-experienced MBC response fate mapped during each labelling window was unchanged at ~0.1% of splenic lymphocytes (Figure 3.33A). The earliest time-point was not entirely consistent with preliminary data from the early GC response using SRBC immunised *S1pr2*^{ERT2Cre}.*Rosa26*^{LSLtdTomato} mice (Figure 3.13B-C), but followed the general pattern that the magnitude of GC output in HALO PC mice was unchanged at all time-points of the early GC response compared to preliminary data in *S1pr2*^{ERT2Cre}.*Rosa26*^{LSLtdTomato} mice (Figure 3.26E and Figure 3.10E).

To investigate whether the early GC had preferential output we analysed the ratios of GC-experienced PCs and MBCs in the spleen (Figure 3.33). Efficiency of MBC generation remained unchanged with ~15-20 GC B-cells per MBC (Figure 3.33B), in-line with data reported by Shinnakasu and colleagues (Shinnakasu *et al.*, 2016). The size of the total GCmat CD138^{Hi} TACI^{Hi} PC compartment compared to GC size also remained unchanged (Figure 3.33C), however, there was a decline in output of immature GCmat CD138^{Hi} TACI^{Hi} P1 PBs commensurate with an increase in the GCmat CD138^{Hi} TACI^{Hi} P3 mature PC compartment (Figure 3.33D-E). There were consistent ratios of GCmat CD138^{Hi} TACI^{Hi} PCs and CD138^{int} TACI^{int} PCs to MBC during the early splenic GC reaction with 2-3 MBCs present for each PC (Figure 3.33F-H). The steady nature of the GC output ratios do not support a preference for MBC output from the early GC (Shinnakasu *et al.*, 2016; Weisel *et al.*, 2016), but are consistent with an early burst of high-affinity output from the GC with subsequent decline to a steady state (Zhang *et al.*, 2018). Spatial analysis of GTI PBs and GCmat PCs resident/migrating to PC foci in the splenic red pulp (Sze *et al.*, 2000) would provide further context of GC output efficiency at these time-points.

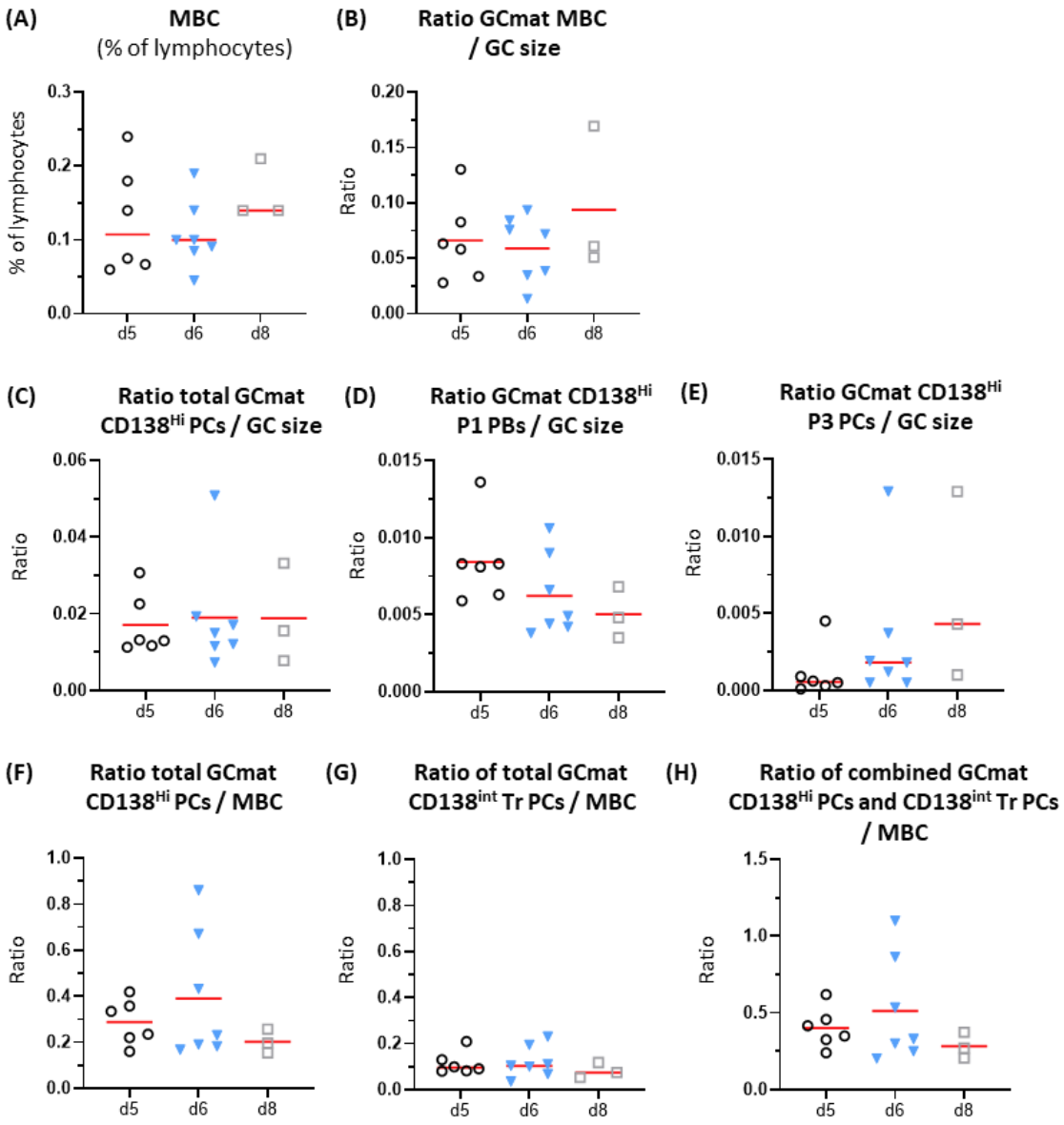

Figure 3.33 **Understanding the kinetics of GC matured output in the early GC response**. Frequency of GCmat MBCs **(A)**. Analysis of GCmat MBCs **(B)**, total GCmat CD138^{Hi} TACI^{Hi} PCs **(C)**, GCmat CD138^{Hi} TACI^{Hi} P1 PBs only **(D)** or GCmat CD138^{Hi} TACI^{Hi} P3 PCs only **(E)** to GC size. Analysis of either total GCmat CD138^{Hi} TACI^{Hi} or total GCmat CD138^{int} TACI^{int} Tr PCs to MBCs alone **(F and G)** or combined **(H)**. Experimental protocol outlined in Figure 3.18. Kruskal-Wallis test with uncorrected Dunn's test (A, C, E, G). Brown-Forsythe & Welch ANOVA with unpaired Welch's t-test (B, D, F, H).

3.2.6 Modulation of GCmat PC output.

A novel population of GTI reticular cells (GTIRCs) have recently been shown to interact with and support GTI PBs (Zhang *et al.*, 2018). Gene expression and flow cytometry confirmed that GTIRCs expressed high levels of *April* and *Il-6*, as well as increased amounts of adhesion molecules ICAM-1, VCAM-1 and CD44 (Zhang *et al.*, 2018). APRIL is a ligand for the TACI receptor (Bossen and Schneider, 2006), and APRIL signalling through TACI is critical for the survival and output of PCs (Peperzak *et al.*, 2013; Zhang *et al.*, 2018). TACI expression is enriched on GTI PBs and mature PCs residing in the PC niches, and the importance of this signalling interaction to facilitate GTI PBs was demonstrated by quantified immunohistology where decreased GTI PB output was detected following treatment with a soluble fusion protein decoy receptor that can bind TACI ligands BAFF and APRIL (mTACI-Fc) or with an α-APRIL neutralising antibody (Zhang *et al.*, 2018).

To test the role of TACI signalling for GCmat PC output, we administered mTACI-Fc or control mouse IgG2c (mFc) to SRBC immunised, tamoxifen treated GC reporter mice and quantified the response by flow cytometry (Figure 3.34). Administration of tamoxifen 3 days after immunisation was chosen as GC B-cells and GC structures are detected between 3-4 d post-immunisation (Zhang *et al.*, 2018; Roco *et al.*, 2019), and we wanted to test TACI signal blockade on the total GC output from this earliest stage. As a reduction of GCmat PC output after inhibition of TACI signalling was tested, one-tailed statistical analysis was appropriate to analyse PC numbers. Due to the COVID-19 pandemic we have only been able to perform this experiment once so far with four mice per group.

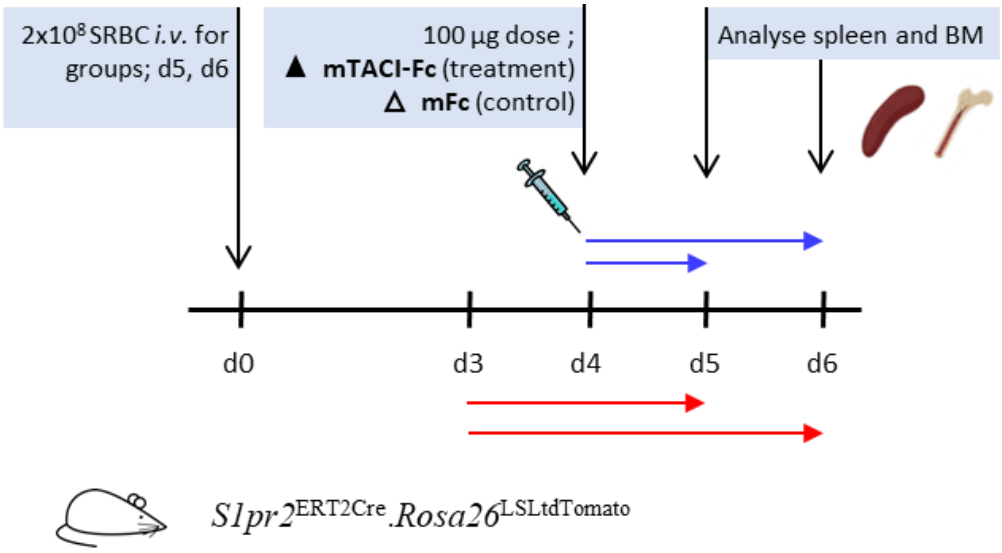

Figure 3.34 **Experimental system to evaluate TACI signalling and GCmat PC output**. *S1pr2*^{ERT2Cre}.*Rosa26*^{LSLtdTomato} mice were immunised with SRBC i.v. and received a single 6 mg dose of tamoxifen three days later. Mice were administered a single i.v. dose of soluble decoy receptor fusion protein (mTACI-Fc) or control mouse IgG2c (mFc control) either 24 h or 48 h prior (blue arrows) to tissue analysis on either 5 d or 6 d post-immunisation. Spleens were partitioned, with ~1/3 used for flow cytometry and the remainder formaldehyde fixed and frozen.

As expected, (Zhang *et al.*, 2018), neither mTACI-Fc blockade from day 4 to 5 nor from day 4 to 6 was detrimental to GC size, frequency of tdTomato expressing GC B-cells, or DZ:LZ ratio (Figure 3.35A-C). The total PC numbers decreased between days 5 and 6 in mTACI-Fc treated mice, and there was a slight reduction in total numbers of PCs after mTACI-Fc treatment (Figure 3.35D-E). While the extrafollicular response decayed towards day 6, the proportion of GCmat PCs in the spleen increased from 5 to 6 d after immunisation, and this was irrespective of treatment (Figure 3.35F). The frequency, absolute number per spleen and GC output efficiency of GCmat PCs had all declined after 48 h of mTACI-Fc blockade (Figure 3.35G-I), confirming the critical role of TACI signalling for GC-derived PB output (Zhang *et al.*, 2018).

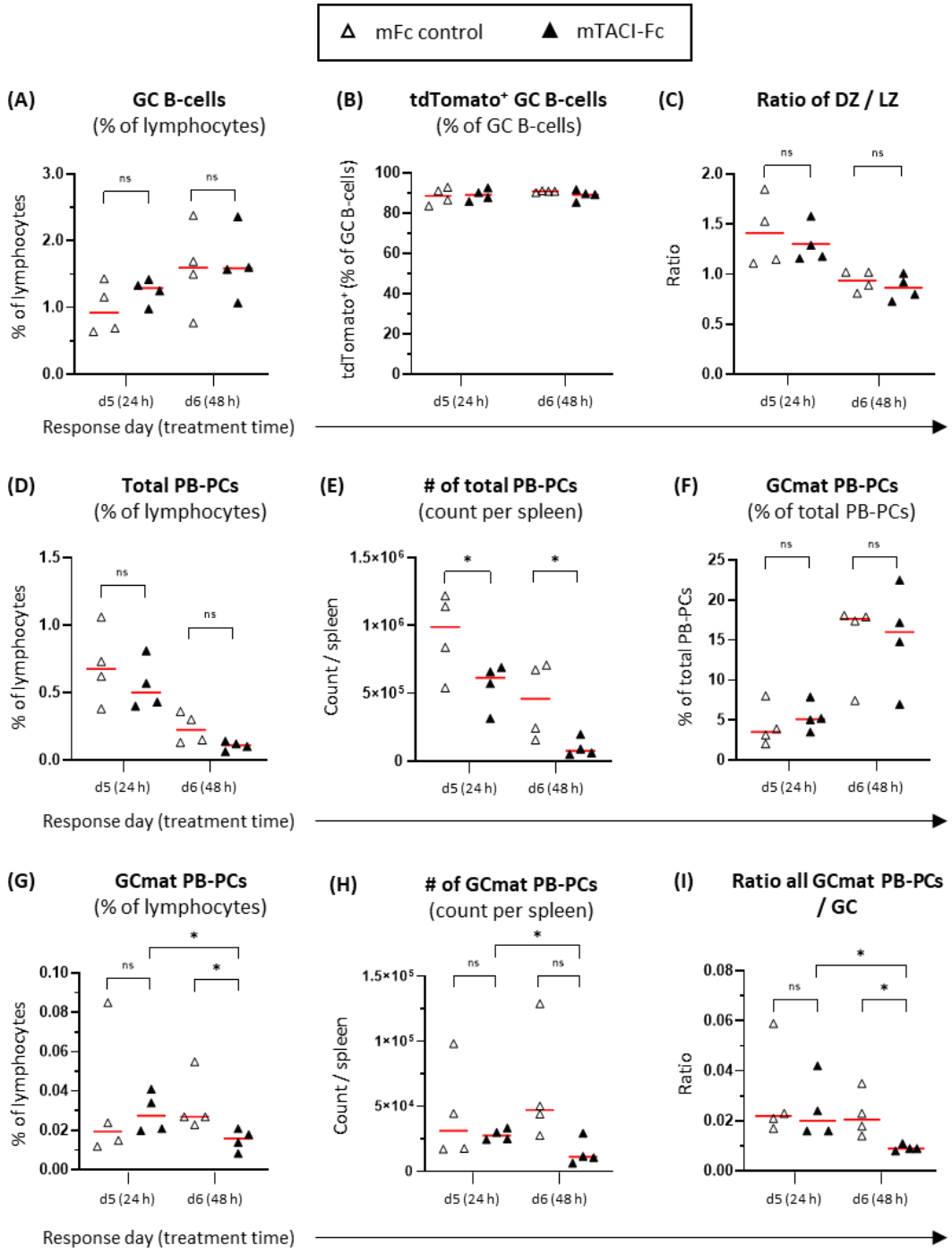

Figure 3.35 **Evaluation of TACI ligand blockade on the splenic immune response**. Evaluation of TACI signalling inhibition on the GC B-cell response **(A-B)** and DZ:LZ composition **(C)**. Analysis of the total extrafollicular and GCmat CD138^{Hi} TACI^{Hi} PB-PC response **(D-E)** or GCmat PC compartment alone **(F-H)** and the efficiency of GCmat CD138^{Hi} TACI^{Hi} PC production **(I)**. Experimental protocol defined in Figure 3.34. Data from one experiment, each symbol represents an individual mouse. Two-tailed unpaired Welch's t-test (A and C). One-tailed unpaired Welch's t-test (D, E, H) or one-tailed Mann-Whitney test (F, G, I).

GTI PBs have been shown to be an early differentiation stage recently emergent from the adjacent GC (Zhang *et al.*, 2018). Having observed an overall decline in GCmat PCs and efficiency in their output (Figure 3.35G and I), we wanted to assess whether this was reflected in the compartments which represented early affinity matured PC differentiation states; a) GCmat CD138^{Hi} TACI^{Hi} P1 PBs and b) GCmat CD138^{int} TACI^{int} Tr PCs. While 24 h mTACI-Fc treatment did not lead to a significant decline in the frequency or GC output of GCmat CD138^{Hi} TACI^{Hi} P1 PBs, there was a significant reduction when TACI ligands were blocked for 48 h (Figure 3.36A-C), consistent with the overall reduction of GCmat CD138^{Hi} TACI^{Hi} PCs (Figure 3.35I). Unexpectedly, there was no change in the composition, frequency or GC output efficiency of GCmat CD138^{int} TACI^{int} Tr PCs, neither in the frequencies and numbers of all CD138^{int} TACI^{int} Tr PCs (Figure 3.36D-F), nor in the numbers of GCmat CD138^{int} TACI^{int} Tr P1 PBs (Figure 3.36G-I). If these GCmat CD138^{int} TACI^{int} tdT^{Hi} Tr PCs represent a transitioning population acquiring terminal PC phenotype after recent exit from the GC both the unchanged frequency and GC output ratio are inconsistent with this. Lack of decline could be reconciled by levels of TACI expression between the CD138^{Hi} TACI^{Hi} and CD138^{int} TACI^{int} populations, with CD138^{int} TACI^{int} Tr cells less dependent on TACI signals at their current stage of differentiation. Quantification of the GTI PBs by immunohistology of the fixed spleen sections would help to resolve this.

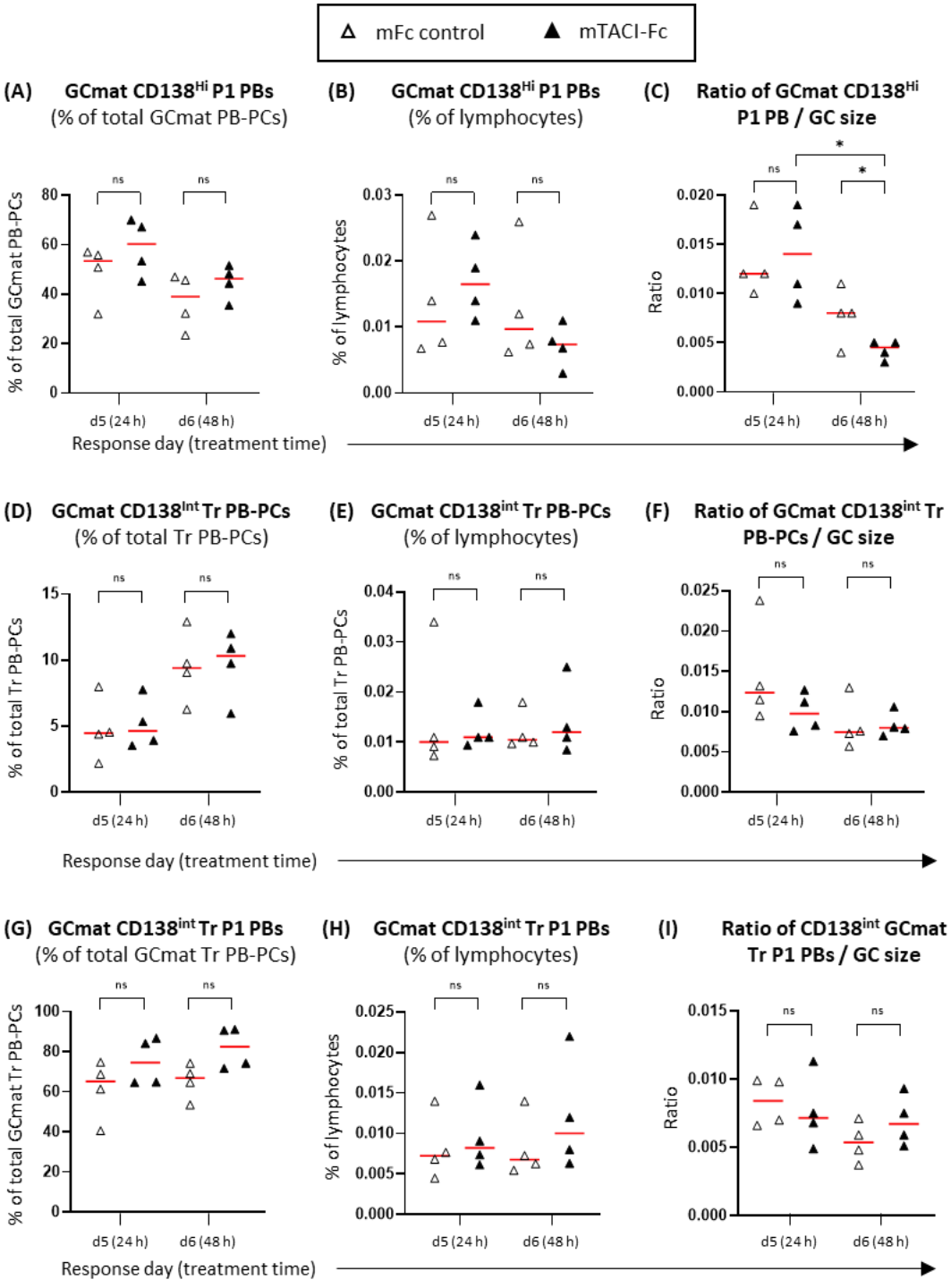

Figure 3.36 **Impact of TACI ligand blockade upon the immature and Tr GCmat splenic PC compartments**. Proportion **(A, D, G)**, magnitude **(B, E, H)** and GC production efficiency **(C, F, I)** of GCmat CD138^{Hi} TACI^{Hi} B220^{+} CD19^{+} P1 PBs (A-C), total GCmat CD138^{int} TACI^{int} Tr PCs **(D-F)** or just the early stage GCmat CD138^{int} TACI^{int} B220^{+} CD19^{+} Tr P1 PBs **(G-I)**. Experimental protocol defined in Figure 3.34. Data from one experiment, each symbol represents an individual mouse. One-tailed unpaired Welch's t-test (A-D and F-I). One-tailed Mann-Whitney test (E).

As expected, there was no significant change in the frequency of GC-experienced tdTomato expressing MBCs after mTACI-Fc treatment (Figure 3.37A-B). Further, 48 h of TACI signal blockade caused a reduction in the output of GCmat CD138^{Hi} TACI^{Hi} PCs to GCmat MBC (Figure 3.37C) which is consistent with the specific effect TACI blockade to TACI^{Hi} PCs (Figure 3.35G).

The numbers of GCmat PC in the BM at this early stage of the response were very small, and there was no significant increase in cells from 5 d to 6 d after immunisation. Accordingly, no significant effects on BM PC were observed after 24 h or 48 h of mTACI-Fc treatment (Figure 3.38A-C).

Taken together these data suggest that the observations made by immunohistology at the GTI border, derived from observations of the spatial distribution of cells (Zhang *et al.*, 2018), can be broadly reproduced using GC fate mapping *S1pr2*^{ERT2Cre}.*Rosa26*^{LSLtdTomato} mice and flow cytometry. To strengthen these conclusions, the experiment requires repeating, and confirmation of these results should be made by immunofluorescence histology on the formaldehyde fixed and frozen spleen tissues.

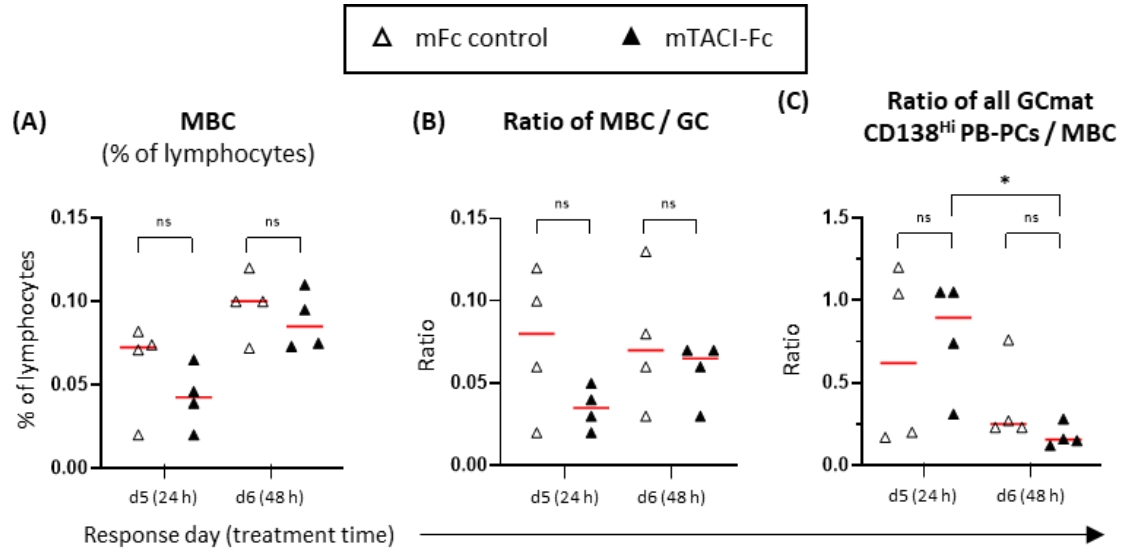

Figure 3.37 **Output of MBC from the early GC was unaffected by TACI ligand blockade**. Frequency **(A)** and efficiency **(B)** of GCmat MBC (CD138^{Lo} TACI^{Lo} B220^{+} CD19^{+} CD38^{Hi} Fas^{Lo} tdTomato^{Hi}) output. **(C)** Efficiency of GCmat CD138^{Hi} TACI^{Hi} PCs to GCmat MBC output. Experimental protocol defined in Figure 3.34. Data from one experiment. Each symbol represents a mouse. One-tailed unpaired Welch's t-test (A and B). One-tailed Mann-Whitney test (C-E).

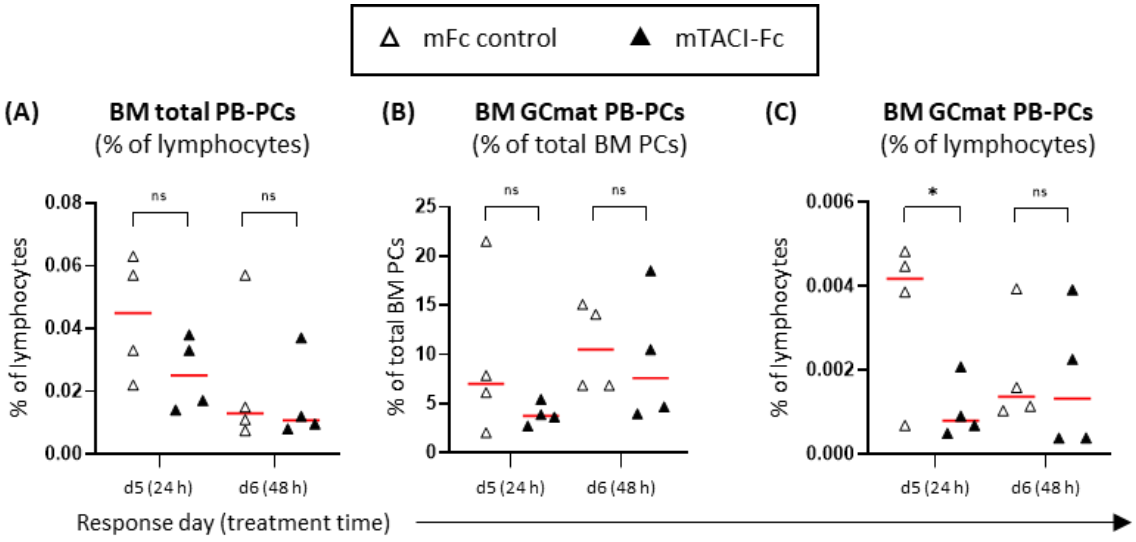

Figure 3.38 **TACI signal blockade during the early GC response did not impact GCmat PCs in resident in the BM**. **(A)** Frequency of total CD138^{Hi} TACI^{Hi} PCs in the BM. Proportion **(B)** and frequency **(C)** of recently GC experienced CD138^{Hi} TACI^{Hi} PCs in the BM. Experimental protocol defined in Figure 3.34. Data from one experiment, each symbol represents an individual mouse. One-tailed Mann-Whitney test (A). One-tailed unpaired Welch's t-test (B and C).

3.2.7 Can mice reporting GCmat PC generation be used to streamline the production of high affinity monoclonal antibodies?

The traditional method for mAb production is through random hybridoma generation using splenocytes of immunised mice (Köhler and Milstein, 1975). Downstream screening for myeloma clones producing antigen-specific high affinity and class switched antibody is labour and resource intensive. Typically, fusion of a single immunised mouse spleen with NS0 fusion partners requires limiting dilution into and screening of more than thirty 96-well plates. Efforts to streamline hybridoma generation have involved altered HAT selection protocols with subsequent single cell-sorting of hybridomas to enrich for cell-surface expression specific for the antigen. This has been demonstrated for haptens or the production of OVA-specific antibodies (H. Liu *et al.*, 2015; Dippong *et al.*, 2017). We hypothesised that hybridoma generation could be further streamlined through the use of mice with a fluorescent reporter of GC maturation.

To assess whether hybridomas could be enriched for clones derived from fusions between an GCmat splenic B-cells and NS0 fusion partner, we tested three protocols on NP_{24}-KLH prime-boost immunised, tamoxifen-treated GC fate mapper mice (Figure 3.39). All mice received tamoxifen 48 h prior to tissue collection in order to label *S1pr2*-expressing B-cells. Tamoxifen treatment after secondary immunisation should label both GCmat B cells derived from virgin Ag-specific naïve B-cells that received help from primed T-cells (Toellner *et al.*, 1996) and Ag-specific MBCs undergoing a recall response and re-entering the GC response (Bende *et al.*, 2007; Dogan *et al.*, 2009; Mcheyzer-Williams *et al.*, 2015). The spleen from a single mouse (M1) underwent traditional hybridoma fusion 72 h after booster immunisation and was subject to limiting dilution and HAT selection in over thirty 96-well plates (Protocol M1 Figure 3.39).

The two alternate enrichment protocols used spleens 120 h after boost to enable capture of GC experienced cells. Protocol M2 involved cell sorting either (i) $CD3^{-}$ $CD4^{-}$ $CD11b^{Lo/int}$ GCmat $CD138^{Hi}$ $TACI^{Hi}$ $tdTomato^{+}$ PCs, or (ii) $CD138^{Lo}$ $TACI^{Lo}$ $B220^{+}$ $CD38^{Lo}$ IgD^{Lo} GC B-cells, and separate scaled-downed "micro-fusions" of each of these GC-experienced populations (Figure 3.39). Protocol M3 involved a traditional fusion of the entire spleen but limiting dilution in multi-well plates was replaced by HAT selection in three T75 flasks with subsequent single cell sorting and expansion of hybridoma clones based on cell-surface BCR expression (Figure 3.39). The use of GC fate mapper mice meant that for all three protocols, NP-specific hybridomas identified by ELISA of hybridoma culture supernatants could be analysed for tdTomato expression to correlate affinity measurements to GC experience.

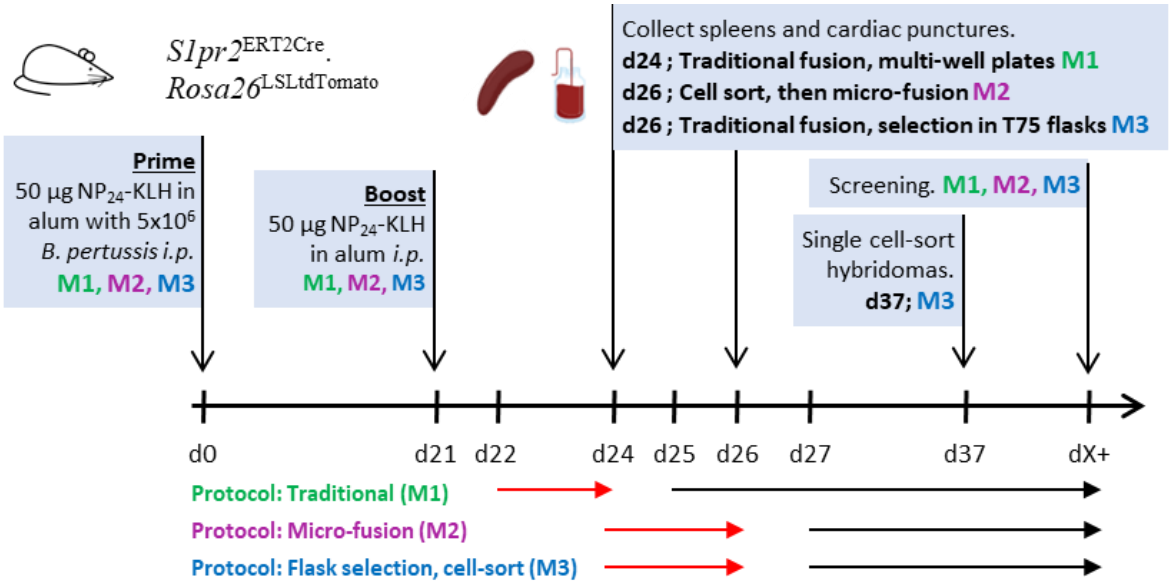

Figure 3.39 **Experimental protocol to test modified fusion and selection protocols to enrich for affinity matured hybridomas**. *S1pr2*^{ERT2Cre}.*Rosa26*^{LSLtdTomato} mice were immunised with insoluble NP_{24}-KLH i.p. in a prime-boost regimen. All mice received a single 6 mg dose of tamoxifen by oral gavage 48 h prior to tissue collection (red arrow). Entire spleen from mouse M1 used for traditional fusion and HAT selection protocol in multi-well plates 72 h after boost. Tissues from M2 and M3 collected 120 h after boost. dX represents ongoing analyses. Protocol M2 involved cell-sorting bulk $CD138^{Hi}$ $TACI^{Hi}$ $tdTomato^{+}$ PCs or $CD138^{Lo}$ $TACI^{Lo}$ $B220^{+}$ $CD38^{Lo}$ IgD^{Lo} GC B-cells from the spleen for separate micro-fusions. Protocol M3 involved

traditional fusion of the entire spleen with altered HAT selection performed in T75 flasks rather than multi-well plates with single cell hybridoma sorting and expansion after 10 days. HAT selection initiated 24 h after fusions (black arrow). Downstream screening as appropriate based on hybridoma growth.

As expected, all mice displayed an affinity matured NP-specific response after prime-boost compared to an early (day 8) primary immune response to NP (Figure 3.40A-D). For the traditional fusions (protocols M1 and M3) splenocytes are 5-fold more abundant than NS0 cells (see Section 2.30). However, for protocol M2, two separate micro-fusions were performed using either 1651 cell-sorted GCmat CD138^{Hi} TACI^{Hi} PCs with excess NS0 fusion partners (at a 1:30 splenocyte:NS0 ratio) or 164,405 cell-sorted GC B-cells with NS0 fusion partners at ~1:1 ratio. These ratios of NS0 cells were chosen to increase the likelihood of splenocytes and NS0 plasma membranes fusing as they are mixed in the polyethene glycol (PEG) fusing agent. Conditions for the micro-fusions proved unfavourable as no hybridomas grew following HAT selection (data not shown). Unfortunately, due to the COVID-19 restrictions there has been no opportunity to repeat the micro-fusions to optimise this protocol. However, despite the pandemic ending the ending the experiment prematurely, fusions for the traditional hybridoma protocol M1 or for protocol M3 yielded viable hybridomas for further analysis (Table 3.2, Figure 3.41 and Figure 3.42). The traditional protocol (M1) produced hybridoma colony growth in 3.6% of wells after limiting dilution selection (111 / 3072 wells). Primary screening for secretion of IgM or IgG revealed 11.8% (13 / 111) expressed Ig, but only a single hybridoma clone specifically bound NP with low affinity (Table 3.2).

# wells with hybridoma growth (% of total wells)	**Primary screen # hybridomas expressing IgM or IgG** (% of hybridomas)	**# hybridomas expressing low-affinity NP-specific IgM** (% of hybridomas)	**# hybridomas expressing NP-specific IgG** (% of hybridomas)
111 (3.6%)	13 (11.8%)	1 (0.9%)	0 (0%)

Table 3.2 **Summary of traditional hybridoma protocol output and screening for NP-specific mAbs**. Traditional protocol using protocol M1 Figure 3.39. Fused splenocytes:NS0 cells were plated in 32 separate 96-well plates. Primary screen of supernatants for total IgM or IgG on anti-κ and anti-λ coated ELISA plates. Further screens made on NP_{14}-BSA and NP_2-BSA coated plates for the affinity of NP-specific hybridomas. Screening against irrelevant antigen (OVA) was used to exclude non-specific binders (this excluded a further hybridoma, data not shown).

For protocol M2, on day 10 of flask based HAT selection all hybridoma cells were harvested, stained with α-IgM and α-IgG antibodies and single cell sorted based on surface BCR expression independent of tdTomato expression (Figure 3.41A-C). Hybridoma cell-sorting was performed with cell-surface BCR expression in this initial experiment with the aim to perform post-hoc analysis for clones that were GC-experienced by analysis of tdTomato expression from the index cell sort data. Further experiments were planned to repeat this protocol using single cell sorting based entirely on tdTomato expression. As expected, <1.0% of hybridomas were live following 10 days of HAT selection (Figure 3.41C). Visual assessment identified three hybridomas which had successfully re-expanded by day 18 post cell-sort (the day before UK national COVID-19 lockdown) (Figure 3.42A), all of which were secreting IgM mAb (Figure 3.42B). Correlation of the expanded hybridoma clones with index cell-sort data identified that all three were derived from B-cells not expressing *S1pr2* within the 48 h prior to tissue acquisition (Figure 3.42C). This does not exclude the possibility that these cells could have been GC-experienced during the primary immune response, as fate mapping of GC-experienced cells was only performed for the 48 h window before tissue collection (Figure 3.39). Of the three re-expanded IgM producing hybridomas only clone B-P5H5 was NP-specific and

demonstrated avidity to NP as it could bind to both high and low NP haptenation ratios (Figure 3.42D). Comparison to in-house NP-specific IgM clones with known affinity was not possible due to COVID-19 lockdown. Analysis of the index sorted cells revealed that 47.5% (228 /480) of the hybridomas co-expressed tdTomato indicating GC experience at the time of fusion (96-well plates 2 and 5 are representative and depicted Figure 3.42C). Whether these tdTomato expressing hybridoma cells would have re-expanded given further time after single cell-sorting is unknown as the experiment was cut short due to COVID-19 lockdown.

These initial attempts at alternate enrichment protocols yieled mixed results. Cell numbers and conditions for scale-down micro-fusions (protocol M2) require careful optimisation. However, protocol M3 demonstrated that nearly half of cell-surface IgM/IgG expressing single cell sorted hybridomas were GC experienced, which suggests further experiments in this direction should be promising. Potential enhancements to protocol M3 which should be tested include: a) boost immunisations performed with soluble antigen lacking adjuvant, b) administration of tamoxifen 72 h after all immunisations to fate map a larger proportion of GC progeny, and c) single cell sort hybridomas soley on the basis of tdTomato expression. Further, conditions into which single hybridoma cells are sorted require optimistion to boost survival and post-sort expansion. Unfortunately, identification of the three hybridoma clones which expanded after single cell sorting occurred the day before the University closed for the COVID-19 pandemic lockdown. ELISA screens to determine mAb secretion, isotype and specificity were conducted on the morning before closure. This prevented any further analyses and continued cell culture to assess whether additional single cell sorted hybridomas could re-establish colonies or modifications to the protocol to be tested. The suspension of mouse breeding at the University

of Birmingham (UoB) and cull of most mouse stocks during lockdown prevented subsequent *in vivo* experiments for the rest of the year.

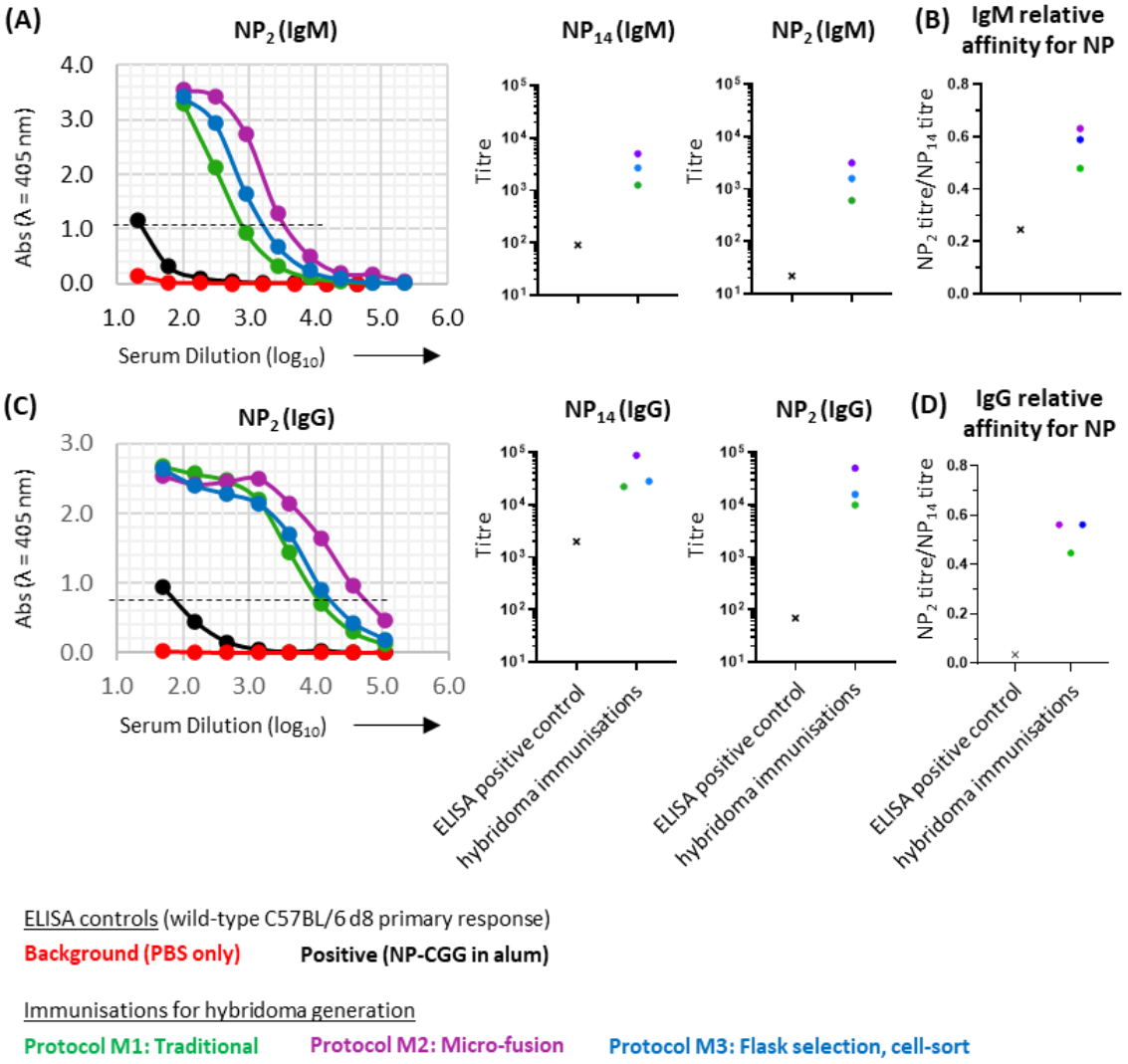

Figure 3.40 **Assessment of immunisation protocol to induce affinity matured NP-specific response**. Serum obtained from cardiac puncture of NP_{24}-KLH prime-boost immunised *S1pr2*^{ERT2Cre}.*Rosa26*^{LSLtdTomato} mice (Figure 3.39) were assessed for NP-specificity by ELISA. **(A)** Dilution curve for high affinity IgM isotype NP-specific ELISA (left), low affinity IgM NP-specific titre (middle), and high affinity IgM NP-specific titre (right). **(B)** Relative NP affinity of IgM response. **(C)** Dilution curve for high affinity IgG isotype NP-specific ELISA (left), low affinity IgG NP-specific titre (middle), and high affinity IgG NP-specific titre (right). **(D)** Relative NP affinity of IgG response. For NP-specific positive control, serum from a wild-type C57BL/6 mouse at day 8 of a primary response to s.c. immunisation with 20 µg NP-CGG in alum was used. For NP binding background non-specific control, serum from a wild-type C57BL/6 mouse 8 d after immunisation with PBS only. Dashed black lines indicate threshold used to determine relative titres.

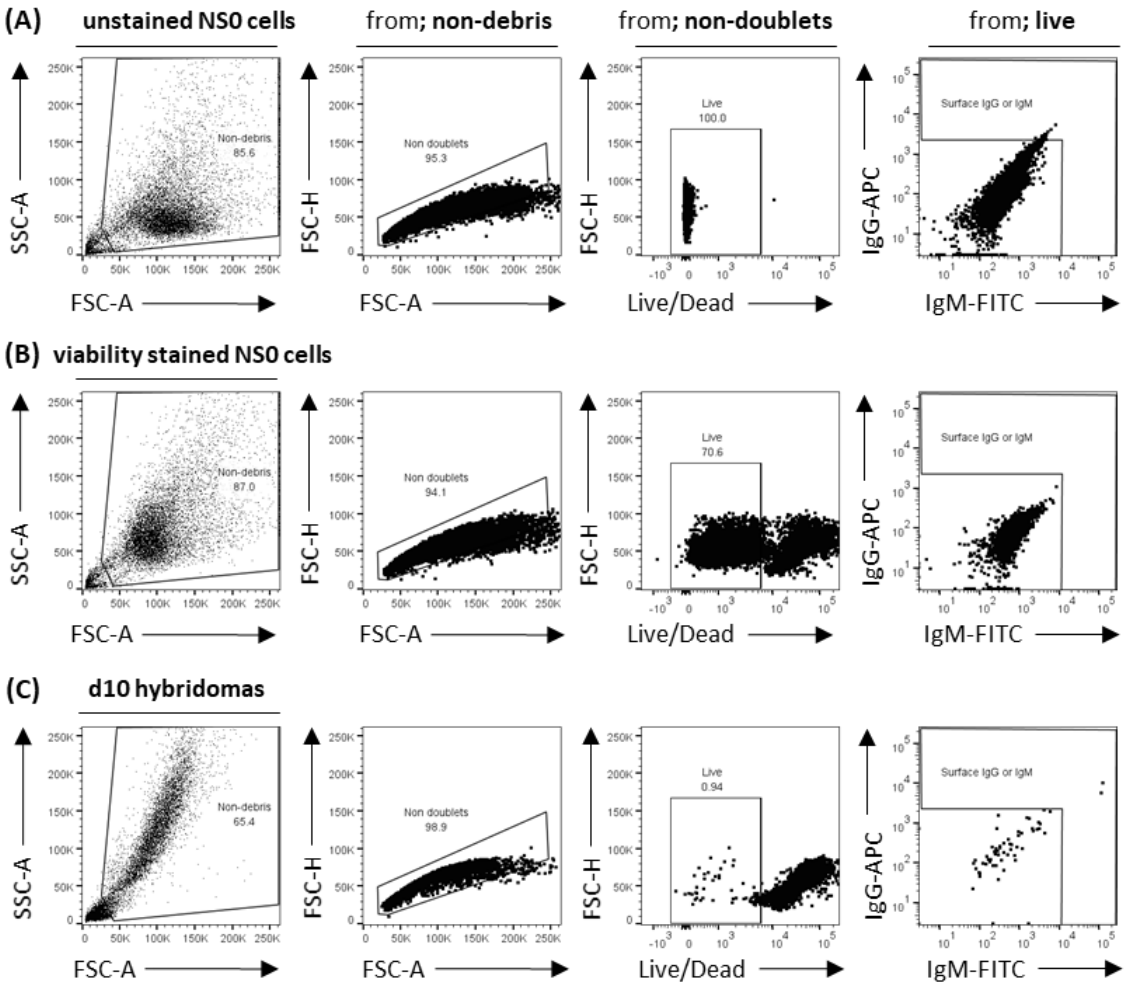

Figure 3.41 **Single cell sorting of hybridoma cells from protocol B**. Gating strategy used to sort single viable, cell-surface IgM or IgG expressing hybridoma cells by FACS into 96-well plates which contained $3x10^4$ NS0 cells to condition the media. HAT selection resumed 24 h after cell sort and continued during expansion. Hybridoma cells from protocol M3 10 d after starting HAT selection in T75 flasks. Experiment protocol outlined in Figure 3.39. Plots for 10,000 unstained NS0 fusion partner cells only **(A)**, heat-shock treated NS0 cells stained with viability dye only **(B)** and fully stained hybridoma cells 10 d after HAT selection **(C)**. Cell-surface IgM or IgG gate set using non-negative cells from live NS0 (B, far right).

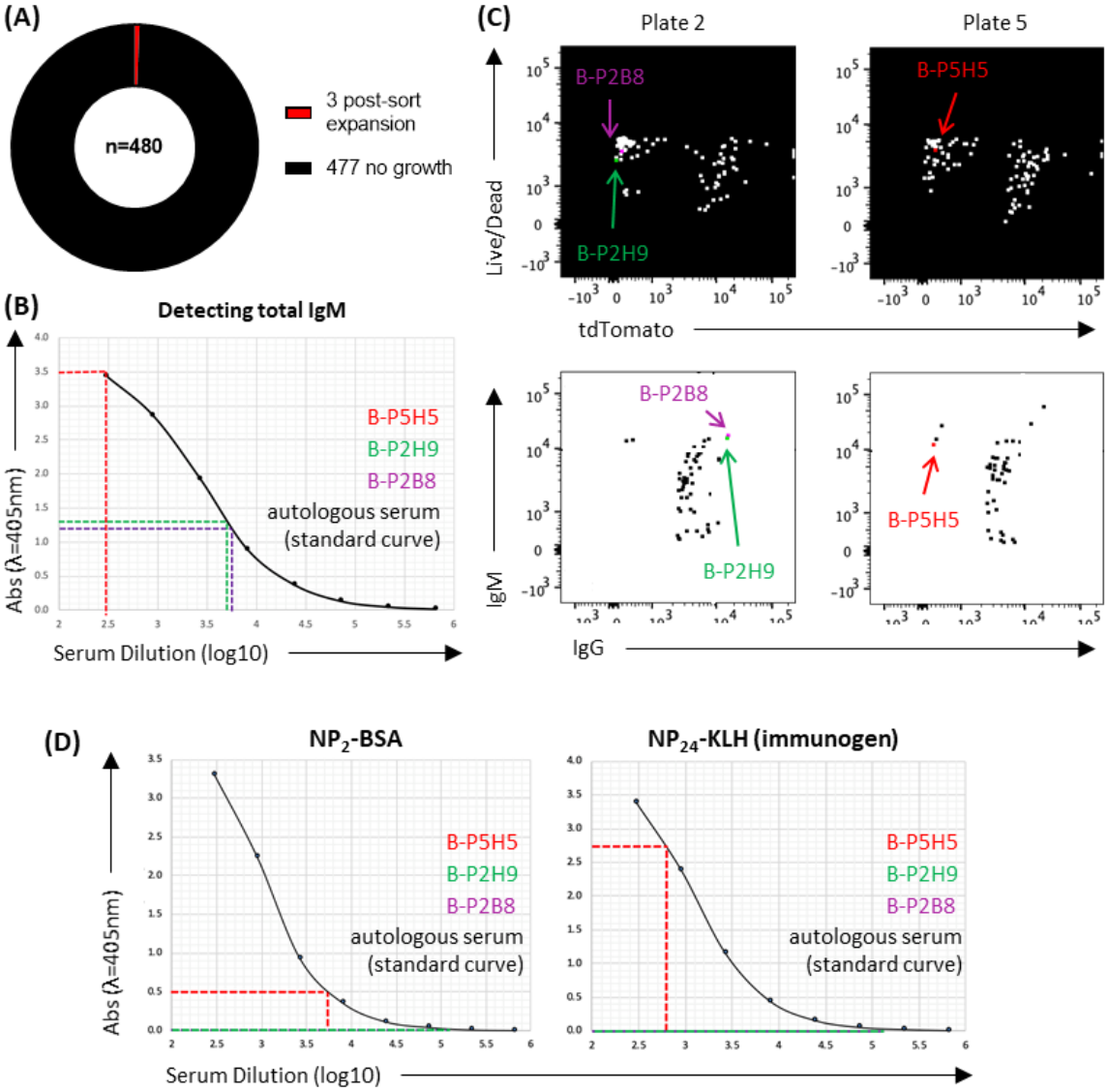

Figure 3.42 **Evaluation of hybridomas successfully re-expanded after single cell sorting**. Single cell sorted hybridomas from protocol M3 which displayed successful growth and re-expansion on 18 d post cell-sort (day before UK COVID-19 lockdown) were assessed for antibody isotype secretion and Ag-specificity. **(A)** Number of clones that expanded by day 18 after sorting. **(B)** Confirmation that expanded hybridomas secreted antibody by testing for isotype via ELISA. Shown are hybridoma supernatant IgM titres compared to autologous mouse serum from the day of hybridoma fusion (26 d post-immunisation). The same was performed for IgG and was negative (data not shown). **(C)** Correlation of re-expanded hybridoma clones with tdTomato expression and surface Ig status from index cell sorting. **(D)** Hybridomas were cell-sorted based on cell-surface BCR expression independent of information regarding Ag-specificity, therefore ELISA analysis was used to detect if clones were NP-specific or immunogen-specific. Experiment protocol outlined in Figure 3.39.

3.3 Discussion

3.3.1 The requirement for and validation of the novel HALO PC mouse.

We set out to establish a system that was able to efficiently identify affinity matured PCs, by using cell fate mapping to detect GC matured PC, and initially focussed on the time around the peak of PC output from the early GC (Zhang *et al.*, 2018). First, we tested the *Aicda*$^{ERT2Cre/+}$.*Rosa26*^{mTmG} model which has been previously used to show GC origin of GTI PBs (Zhang *et al.*, 2018). Flow cytometric analysis showed that this is an inefficient fate mapping method showing similarly low levels of mGFP expression as observed by immunofluorescence histology (Zhang *et al.*, 2018). We show that the low labelling efficiency is mainly due to the inefficient Cre induced recombination of the mTmG allele, as *Aicda*$^{ERT2Cre/+}$.*Rosa26*^{LSLtdTomato} mice show much more efficient FP induction. This is most likely due to the distance (>1600 bp) separating the LoxP sites in the mTmG allele (Vooijs, Jonkers and Berns, 2001; Muzumdar *et al.*, 2007). A more important caveat of the *Aicda*$^{ERT2Cre/+}$ reporter is that *Aicda* expression is also induced during extrafollicular Ig class switch recombination which precedes GC entry (Toellner *et al.*, 1996; Marshall *et al.*, 2011; Roco *et al.*, 2019). This renders the *Aicda*$^{ERT2Cre/+}$.*Rosa26*^{mTmG} model unsuitable.

The *S1pr2*^{ERT2Cre} mouse expresses Cre recombinase specifically within B-cells of GC B-cell phenotype (Green *et al.*, 2011; Shinnakasu *et al.*, 2016) and a kinetic assessment of various inducible Cre models highlighted its suitability for our purposes. We hypothesised that by designing the HALO PC model to combine the *S1pr2*^{ERT2Cre}, *Rosa26*^{LSLtdTomato} and *Prdm1*$^{GFP/+}$ alleles we would produce a mouse that could distinguish EF and GCmat PCs within the same immune response, with potential to timestamp GCmat output and enable *in vivo* tracking and *ex vivo* isolation of GCmat PCs without antibody manipulation.

For initial testing of the HALO PC model, we assessed the kinetics of the PC response to primary SRBC immunisation. As expected, we detected resolution of the EF PC response after day 5. The magnitude and the kinetics of GCmat P1 PBs, antibody secreting cells which are still differentiating and likely represent those which have recently left the GC, peaked at day 5 with subsequent decline, which is consistent with previous data from our lab (Zhang *et al.*, 2018). Furthermore, the overall frequency of GCmat PB-PCs in the spleen did not change, which suggests an accumulation and retention of more mature GCmat PB-PCs within the 48 h labelling windows tested, also consistent with our previous data which studied GCmat PC output only in one location (the GTI) and at one snapshot in time (Zhang *et al.*, 2018). To gain further insight into early GC PC output, the tamoxifen labelling window should be limited to between 10-24 h, supported by our kinetic assessment of tamoxifen inducible Cre activity in *S1pr2*^{ERT2Cre}.*Rosa26*^{LSLtdTomato} mice with 45-73% of total GC B-cells expressing tdTomato during this window. Experiments with NP-carrier immunisation and testing for affinity maturation through acquisition of W33L and K59R mutations in V186.2 V_H region (Allen *et al.*, 1988; Furukawa *et al.*, 1999) from single cell sorted NP-specific EF and GCmat PCs from the early GC response in draining lymphoid tissues and BM derived GCmat PCs fate mapped at a mature GC timepoint, were planned to complete the molecular validation of PC populations distinguished by the HALO PC model. However, this definitive experiment has not yet been completed due to COVID-19 restrictions. We did not detect a change in the frequency of GCmat PCs within the BM either compared to naïve tamoxifen treated mice nor at the latest time-point after immunisation. Lack of increase during the acute phase of initial splenic GCmat PC output was not entirely unexpected as the spleen can buffer the initial generation of PCs with up to 5000 PCs/mm^2 in the short term, with stable support of up to 100 PCs/mm^2 section

area (Sze *et al.*, 2000) and Ag-specific splenic PCs can be detected 1-year post-immunisation (Bohannon *et al.*, 2016). Moreover, these data suggest an initial retention of GCmat PCs in the spleen; consistent with the half-life of splenic PCs ~21 days demonstrated in a recent study, which investigated tissue-specific PC homeostatic turnover (Xu, Barbosa and Calado, 2020). To test whether there are differences in the relative contribution to the BM PC compartment of GCmat PCs migrated from immunised secondary lymphoid tissues compared to that of GCmat PCs from barrier mucosal sites with permanent GC responses (e.g., Peyer's Patches), ELISpot analysis of FACS enriched GCmat BM PCs after NP-carrier immunisation would be helpful, as well as analysing later phases of the response.

We used the HALO PC model to further investigate a population of CD138^{int} TACI^{int} cells labelled transitioning (Tr) PCs, that displayed high levels of activation markers. These cells were first noted when analysing time courses to SRBC immunisation in *S1pr2*^{ERT2Cre}.*Rosa26*^{LSLtdTomato} mice. The majority of GCmat Tr cells expressed Blimp1^{GFP}, but ~ 20% did not. Phenotypic analysis suggests that these CD138^{int} TACI^{int} GCmat tdT^{Hi} Blimp1^{GFP} negative Tr cells are an intermediate stage between Blimp1^{GFP} expressing GC B-cells and CD138^{int} TACI^{int} GCmat tdT^{+} Blimp1^{GFP} expressing Tr cells. The timing and sequence of CD138 and Blimp1^{GFP} upregulation on PC is heterogenous and can depend upon the type of signal inducing B cell differentiation; *Prdm1*$^{GFP/+}$ B-cells stimulated *in vitro* with CD40L alone show upregulation of CD138 with subsequent Blimp1^{GFP} expression, whereas LPS stimulation alone favours induces a greater proportion to first become Blimp1^{GFP} expressing prior to CD138 expression (Kallies *et al.*, 2004). Strikingly, GCmat CD138^{int} TACI^{int} Tr PCs displayed significant levels of transient cell-surface CD38 which declined as the cells progress towards a typical PC phenotype. A potential role for transient CD38 re-

expression could be augmenting strong BCR signalling in GC B-cells positively selected into the PC lineage as discussed in Section 3.3.3. To help clarify the nature and differentiation trajectory of GCmat CD138^{int} TACI^{int} tdT^{Hi} Blimp1^{GFP} negative Tr PCs, gene expression analysis for genes important for B-cell identity (*Pax5*), GC B-cell phenotype (*Aicda*, *Bcl6*, *S1pr2*), GCmat MBC precursors (*Bach2, Ccr6, Hhex*), or PCs (*Xbp1*, *Irf4*, *Igj* (*J-chain*), *Tnfrsf13b* (TACI)) should be made between cell-sorted populations of: (i) GCmat CD138^{int} TACI^{int} tdT^{Hi} Blimp1^{GFP} negative Tr PCs, (ii) GCmat CD138^{int} TACI^{int} tdT^{+} Blimp1^{GFP} expressing Tr PCs, (iii) Blimp1^{GFP} expressing GC B-cells, (iv) GCmat CD138^{Hi} TACI^{Hi} tdT^{+} Blimp1^{GFP} expressing PB-PCs, and (v) GCmat MBCs.

The HALO PC model should be a useful tool to study signals which regulate the induction, differentiation, and migration of GCmat PCs. Reduced GCmat PC output from the early GC by TACI signalling blockade previously has only been possible using histology in order to correlate microanatomical location in relation to GCs with PC differentiation stage (Zhang *et al.*, 2018). Our flow cytometric data from *S1pr2*^{ERT2Cre}.*Rosa26*^{LSLtdTomato} mice presented here are broadly consistent with the quantification of the decline in GCmat PC output by immunohistology from our group (Zhang *et al.*, 2018). Flow cytometric analysis shows that 48 h TACI signal blockade results in a 2-fold decline in the GC output efficiency of GCmat CD138^{Hi} TACI^{Hi} PCs but no change was observed after only 24 h of signal blockade. In-line with earlier findings, no changes to GC size or GCmat MBC output were found after TACI signalling blockade, confirming the effects of TACI are specific to GCmat PC differentiation. Other signals, for example inhibition of GC B-cell Tfh contacts by ICAM-1 blockade can disrupt both the GC reaction and production of Bcl6^{Lo} CD69^{Hi} LZ precursors of PCs (Ise *et al.*, 2018), and presumably GCmat MBC production, although this could not be tested in the Bcl6-

YFP system used (Ise *et al.*, 2018). HALO PC mice would be ideally suited to testing signals which transiently inhibit differentiation or exit of affinity matured PC precursors from the GC and assessing whether retention of these high-affinity clones within the GC impacts the quality of long-term humoral responses.

3.3.2 Is there a role for transient CD38 re-expression on precursors of GCmat PCs?

For over two decades it has been accepted that murine GC B-cells and terminally differentiated PCs do not express CD38 (Oliver, Martin and Kearney, 1997). We describe here that CD38 re-expression is first observed in Blimp1^{GFP} expressing GC B-cells, spikes in GCmat CD138^{int} TACI^{int} tdTomato expressing Tr PC populations and then decays as these Tr cells continue PC differentiation and express higher levels of canonical PC markers.

What functional role could transient CD38 re-expression have in Blimp1^{GFP} expressing murine GC B-cells and the early differentiation stages of GCmat PBs? CD38 is multi-functional; having both receptor signalling and ectoenzyme functions which can act independently (Lund *et al.*, 1996; Vences-Catalán and Santos-Argumedo, 2011). Study of CD38 in the murine A20 B-cell line demonstrated that co-ligation of CD38 and BCR can augment BCR signalling (Lund *et al.*, 1996) and that CD38 signalling can induce c-Rel and RelA (p65) expression in purified splenic B-cells via the NF-κB pathway (Kaku *et al.*, 2002). RelA is of known importance for PC differentiation (Heise *et al.*, 2014; Roy *et al.*, 2019). In human B-cell chronic lymphocytic leukaemia (CLL) signal induction by CD38 activates spleen tyrosine kinase (Syk) with subsequent downstream activation of Akt by serine 473 (S473) phosphorylation and upregulation of anti-apoptotic factor Mcl-1 (Benkisser-Petersen *et al.*, 2016). In mice, Mcl-1 expression has been shown to be critical for PC survival and its actions precede the repressive

functions exerted by Blimp1 (Peperzak *et al.*, 2013), and strong Syk activation in GC B-cells promotes PC formation (Davidzohn *et al.*, 2020). EZH2 is a methyltransferase expressed in GC B-cells which trimethylates histone 3 lysine 27 (H3K27me3), which can then bind to and repress the transcriptional start sites of PC determinant genes, *Irf4* and *Prdm1* (Caganova *et al.*, 2013). Regulation of EZH2 is complicated and mediated by a variety of post-translation modifications (Wan *et al.*, 2015), but interestingly, in human cell lines at least, Akt driven phosphorylation of EZH2 at serine 21 inhibits methyltransferase activity resulting in alleviation of suppressed genes (Cha *et al.*, 2005). Luo and colleagues have published a series of studies which revealed that strong BCR and CD40 signalling co-operatively overcame re-wired GC B-cell Akt signalling (Luo, Weisel and Shlomchik, 2018; Luo *et al.*, 2019). It was highlighted that in GC B-cells, phosphatase and tensin homolog (PTEN) mediated depletion of phosphatidylinositol-(3,4,5)-trisphosphate (PIP3) resulted in dampened Akt S473 phosphorylation and a change in Akt substrate specificity; with Akt phosphorylated at threonine 308 preferentially phosphorylating and activating phosphatases which negatively regulate BCR and Syk signalling (Luo *et al.*, 2019).

Taken together, one potential theory could be that transient re-expression of CD38 may play a role in augmenting strong BCR induced Syk activation in high-affinity GC B-cells to overcome the altered re-wiring of Akt in murine GC B-cells. Consequently, alleviation of PTEN mediated inhibition would result in increased levels of S473 phosphorylated Akt by mTORC2, which can in turn inactivate DZ phenotype dependent nuclear Foxo1 (Luo, Weisel and Shlomchik, 2018) and could potentially mediate de-repression of *Prdm1* gene silencing via EZH2 inactivation (Cha *et al.*, 2005; Caganova *et al.*, 2013) and/or Syk could promote upregulation of anti-apoptotic factor Mcl-1 (Peperzak *et al.*, 2013; Benkisser-Petersen *et al.*, 2016). Whether any

of these pathways are induced by re-expressed CD38 remains to be determined, as does an explanation as to why CD38 re-expression appears dispensable in murine GCmat PCs as terminal differentiation progresses. The CD38 targeted mouse ESC line (MGI:4950992) could be used to test these questions. After treatment with FLP recombinase this ESC line is a Cre conditional CD38 knock-out allele. Combination with the HALO PC mouse and tamoxifen treatment could be used to assess whether CD38 re-expression is required for the earliest stages of GCmat PC differentiation. Moreover, can this proposed function of CD38 also be applied to human B-cell biology, or is this a phenomenon limited to mice? The expression profile of CD38 in human B-cells is inverse to that of mice, with naïve Fo B-cells downregulating CD38 but displaying an increase in expression levels from GC B-cells to PBs and with the highest expression on mature PCs (Vences-Catalán and Santos-Argumedo, 2011; Sanz *et al.*, 2019). If CD38 functions in human GC B-cells to augment BCR induced Syk activation as proposed in murine GC B-cells, why then does CD38 expression increase concomitant with the loss of surface BCR expression during terminal differentiation to PCs? With the implication that human long-lived PCs could last a lifetime (Hammarlund *et al.*, 2017) and CD38 mediated anti-apoptotic factor upregulation in human B-cell malignancies (Benkisser-Petersen *et al.*, 2016), CD38 could possess species specific intrinsic requirements for maintenance of terminal B-cell differentiation and/or PC longevity.

3.3.3 Does CD11b expression represent a PC niche marker?

Flow cytometric detection of CD11b was included to aid positive identification of Blimp1^{GFP} expressing PCs by exclusion of various T-cell, NK cell, B-1 B-cell and DC populations (Martins *et al.*, 2006; Kallies *et al.*, 2009, 2011; Rutishauser *et al.*, 2009; Kim *et al.*, 2011; Baumgarth, 2016). However, bimodal separation of lymphocytes as either CD11b^{+} or CD11b^{-} falsely

excluded a significant proportion of PCs from downstream analysis. We present here that within splenic and BM CD138^{Hi} TACI^{Hi} PCs, cell-surface CD11b expression is commensurate with increased Blimp1^{GFP} expression and is inversely related to B220 expression. Although unexpected, there are a handful of reports of CD11b expression on BM and splenic PCs, as well as iLP PCs (Kunisawa *et al.*, 2013; Wilmore, Jones and Allman, 2017), as well as our unpublished histology observations of CD11b co-expression with IRF4 in a minority of splenic PCs. This raises the question; is increased CD11b expression functionally important for PCs? CD11b (α_M) is part of the integrin family and associates with CD18 (β2) to form a heterodimeric receptor $\alpha_M\beta$2 (Mac-1) (Arnaout, 2016). CD11b has > 40 reported ligands including but not limited to: iC3b of the complement system and numerous cell adhesion molecules (e.g., ICAM-1) (Arnaout, 2016). Kunisawa and colleagues found no evidence that CD11b$^+$ IgA$^+$ iLP PCs were involved in uptake of iC3b opsonised bacteria, nor were they derived from CD11b$^+$ B-1 cells migrating to the intestine (Kunisawa *et al.*, 2013). Another CD11b ligand is fibronectin (Yakubenko *et al.*, 2001). Fibronectin has recently reported to be an important mesenchymal stromal cell secreted factor for *in vitro* culture of human PCs (Nguyen *et al.*, 2018). Upregulation of receptors that can bind PC survival factors is consistent with a terminally differentiated PC phenotype, reflective of our observed Blimp1^{GFP} expression pattern. Therefore, does increased CD11b expression distinguish mature PCs resident in PC niches? Immunofluorescence histology of spleen sections from immunised HALO PC mice could address the question of spatial context. Laidlaw and colleagues have reported that almost 20% of recent GC emigrant cells (IgD^{Lo} GL7$^+$ FAS$^+$ *Efnb1*$^+$ *S1pr2*^{Lo}) express cell-surface CD11b (Laidlaw *et al.*, 2017). Taken in the context of our observations, there could be a role for CD11b expression required for a subset of cells to exit the GC and/or aid migration to local niches to gain access to survival factors. To test whether CD11b expression is required for GC exit and

migration of GCmat PBs, the GC-specific *S1pr2*^{ERT2Cre} model could be combined with the 77His transgenic mouse which contains a Cre conditional *Itgam* (CD11b) knockout allele (Avery *et al.*, 2019).

3.3.4 Initial experiments of GCmat enrichment strategies for mAb production.

Shown here are the insights from an initial attempt to enrich hybridoma fusions using mice with fluorescent reporters of GC-experience. This builds upon methods which require fluorochrome-labelled Ag for positive identification of hybridomas expressing cell surface Ag-specific BCRs (H. Liu *et al.*, 2015; Dippong *et al.*, 2017), but has the potential to enrich for hybridomas without the requirement of fluorochrome conjugated Ag, thus broadening the applicability of the protocol. COVID-19 restrictions severely hampered development and optimisation of GC-experienced enrichment protocols, but the initial data presented here highlight the potential for single cell hybridoma enrichment.

Work from the Nussenzweig group has established a protocol for single cell cloning of light- and heavy-chain cDNA from Ag-specific cells into expression vectors for mAb characterisation, which has been used to analyse affinity of MBCs (Von Boehmer *et al.*, 2016; Viant *et al.*, 2020). After molecular validation that tdTomato^{+} GFP^{+} GCmat PCs are affinity matured, incorporation of GCmat PCs from immunised HALO PC mice into this protocol without requirement of fluorochrome-labelled Ag for identification, should simplify high affinity mAb production. Parallel hybridoma enrichment and single cell sorting strategies are the next steps in this workstream.

Chapter 4. Generation of novel HAPi670 mice (High-Affinity Plasma cell near infra-red FP670)

4.1 Introduction

4.1.1 The potential of iRFPs to produce a more optimal fluorescent reporter for *in vivo* study of GCmat PCs.

Our experience with the HALO PC model has shown that extrafollicular and GCmat PCs could be distinguished by tamoxifen induced permanent fate mapping. The HALO PC model can identify up to 95% of GCmat cells accrued in the time after tamoxifen induction, meaning that dependent on the selected end-point for tissue analysis the labelled population of GCmat PCs can be heterogenous i.e., GCmat PCs labelled within a 12 h tamoxifen induction window would be recent GC emigrants whereas those labelled within 48 h induction window would be a mixture of recent and mature GCmat PCs. Moreover, the spectral characteristics of the fluorescent reporters in the HALO PC mouse are useful for *in vitro* and *ex vivo* analyses but are sub-optimal for deep tissue intravital imaging. EGFP and tdTomato have Ex_{max} 488 nm: Em_{max} 507 nm and Ex_{max} 554 nm: Em_{max} 581 nm, respectively, and do not lie within the NIR optical window which contains wavelengths which are optimal for deep tissue imaging applications with high signal:noise ratios (Weissleder, 2001). Further, autofluorescence caused by riboflavin, NADPH, mitochondria and other compounds/organelles typically excite and emit with the FITC/GFP channel. As the numbers of GCmat plasmablasts is low, and they initially express low levels of *Prdm1* controlled EGFP, autofluorescence in the EGFP detection channel is a concern. We therefore looked to see whether red-shifted or NIR fluorescent proteins could

be suitable candidates upon which to design a more optimal *in vivo* transgenic fluorescent reporter system to specifically label only GCmat PCs.

The family of iRFPs include dimeric and monomeric iRFPs that can be multiplexed and distinguished within the same cells/and or whole animal (Filonov *et al.*, 2011; Shcherbakova and Verkhusha, 2013; Shcherbakova *et al.*, 2016; Matlashov *et al.*, 2020), as well as split reporter derivatives (Filonov and Verkhusha, 2013; Shcherbakova *et al.*, 2016). To-date, diRFP713 is the only iRFP that has been used and validated as a reporter in transgenic animal models. Tran and colleagues used PNI to develop a transgenic mouse with constitutive CAG promoter driven whole body diRFP713 expression which revealed no toxicity to the mouse (M. T. N. Tran *et al.*, 2014). Further, PNI was used to generate transgenic rats with Cre inducible neuronal diRFP713 expression to study dopaminergic neurons in brain sections (Richie *et al.*, 2017). Moreover, Hock and colleagues found that targeted insertion of a single copy of Cre inducible diRFP713 under the control of the promoter of the endogenous housekeeping gene *Hprt* provided good fluorescent signal in targeted mouse ESCs upon induction (Hock *et al.*, 2017). Subsequent breeding of the *Hprt*$^{tm1(CAG-LSL-iRFP)}$ transgenic mouse with the *Rosa26* controlled inducible Cre mouse Gt(ROSA)26$^{Sortm2(cre/ERT2)Brn}$ revealed successful detection of diRFP713 expression by flow cytometry and whole animal *in vivo* imaging (Hock *et al.*, 2017). These initial successes using iRFP in transgenic animals demonstrate the potential of harnessing the expanded iRFP repertoire to create powerful reporter systems *in vivo*.

4.1.2 Analysis of existing knock-in transgenic mice with targeted insertions to either the *Prdm1* or *S1pr2* locus.

The *Prdm1*$^{GFP/+}$ transgenic developed by Kallies and colleagues has been the only targeted knock-in *Prdm1* transgenic used to study PC biology to date (Kallies *et al.*, 2004) as the *Prdm1*^{YFP} model was generated by random integration using PNI of a modified BAC transgene (Rutishauser *et al.*, 2009). The *Prdm1*$^{GFP/+}$ transgenic was generated by targeted insertion of the EGFP coding sequence into intron6-7 of the *Prdm1* locus (Kallies *et al.*, 2004). Homozygous animals are not viable due to the transgene insertion resulting in a truncated non-functional Blimp1 protein (Kallies *et al.*, 2004). Blimp1 is essential for embryo development (Mould *et al.*, 2012; Yamashiro *et al.*, 2016), hence *Prdm1*$^{GFP/GFP}$ is pre-natal embryonic lethal (Kallies *et al.*, 2004), and mouse colonies must be maintained by interbreeding heterozygous stock.

Mould and colleagues have generated the targeted knock-in allele *Prdm1*^{BEG} (Mould *et al.*, 2015). Blimp1-EGFP cDNA was fused in-frame to the ATG in exon 3 and they found that viable homozygous mice were born, but critically were sterile (Mould *et al.*, 2015). Clearly care must be taking with targeted insertion to the *Prdm1* locus.

More recently, the *Prdm1*^{Bio} transgenic was developed by targeted insertion of a sequence tag to the very C-terminus of Blimp1 immediately prior to STOP codon of *Prdm1* exon 8. Precise targeting by homologous recombination was achieved using HAs comprised of the 3'UTR of *Prdm1* exon 8 and the majority of *Prdm1* intron7-8 (Minnich *et al.*, 2016). However, the resulting transgenic produced a C-terminal tagged Blimp1 protein and did not express a reporter directly.

In B-cells, *S1pr2* expression is highly specific to GC B-cells (Green *et al.*, 2011). This expression profile was exploited to create the *S1pr2*^{ERT2Cre} mouse through random integration of a modified BAC (Shinnakasu *et al.*, 2016) and we have successfully used it to develop the HALO PC mouse (see Chapter 3). Most targeted knock-in insertions at the *S1pr2* locus create non-functional alleles, which when bred homozygous, display mild to severe neurological impairments as well as seizures and high rates of premature death (MacLennan *et al.*, 2001; Du *et al.*, 2010; Moriyama *et al.*, 2014). Interestingly, the *S1pr2*$^{(tm1Rlp)}$ strain does not report these neurological defects when the targeted allele is homozygous, but as expected, this transgenic mouse has abnormal immune responses and secondary lymphoid tissue morphology (Kono *et al.*, 2004). Clearly, to achieve homozygous stock for targeted knock-in insertion to the *S1pr2* locus care must be taken to retain functional S1PR2.

4.1.3 Objective and Aims.

The objective of this Chapter was to develop and validate a split iRFP reporter with the optimal compromise of excitation efficiency with standard 633nm lasers, brightness and photostability to be genetically targeted into mouse ESCs for conversion into a novel transgenic split fluorescent reporter system that only specifically labels GCmat PB precursors and recently emigrant GCmat PBs.

The aims were as follows:

1. Design, generate and validate novel split-diRFP670 FP suitable for incorporation into a split iRFP transgenic mouse model.
2. Characterize the biochemical and biological properties of the new split-diRFP670 FP.

3. Compare CRISPR/Cas9 enhanced to standard ESC targeting to obtain two separate mouse ESC clones each with a validated integration of one of the necessary parts of the split-diRFP670 reporter placed under the control of the endogenous promotors of either *S1pr2* or *Prdm1*.
4. Achieve germline transmission for both split-diRFP670 targeted ESC clones and interbreed to generate the final *in vivo* split reporter transgenic mouse.
5. Rigorously characterise the novel *in vivo* split reporter transgenic and validate that it can specifically label GC precursors of GCmat PBs and recently emigrant GCmat PBs by *ex vivo* and *in vivo* methods.

Please note that aims 1-3 were accomplished and germline transmission was achieved for one targeted ESC clone (aim 4), but COVID-19 restrictions meant that aims 4 and 5 could not be completed.

4.2 Results part A – split iRFP reporter

4.2.1 Design of diSplit670, a novel split iRFP reporter derived from diRFP670, and its use to generate a split iRFP reporter mouse model.

The goal of this work was to generate a novel split iRFP *in vivo* reporter system with improved characteristics that would facilitate the study of GCmat PCs both *in vivo* and *ex vivo*. This system should incorporate features that would enhance multi-parameter flow cytometry, immunofluorescence histology of *ex vivo* tissues, and intravital microscopy in live mice. Therefore, the brightness, photostability and compatibility of the excitation/emission spectra of the selected iRFP with existing standard laboratory analytic equipment were important factors to consider when selecting which iRFP to use. A comparative assessment was made between a range of existing published dimeric iRFPs; diRFP670, diRFP682, diRFP713, diRFP720; iSplit713, the split reporter of diRFP713; monomeric iRFP670 (miRFP670); and miSplit670, the split reporter of miRFP670 (Table 4.1 and Figure 4.1).

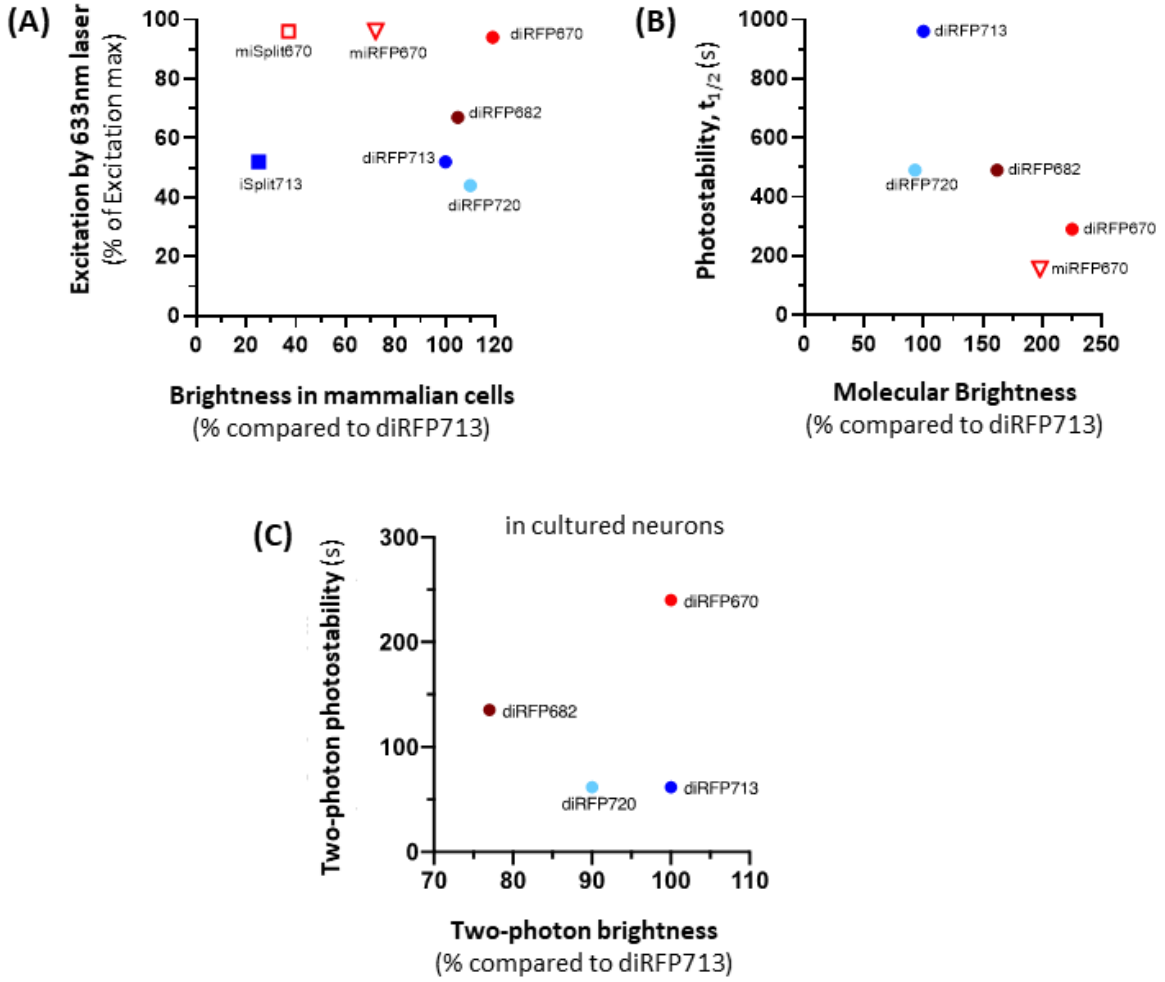

Figure 4.1 **The properties of diRFP670 and other candidates for the generation of a split iRFP variant. (A)** The brightness in mammalian cells of various existing dimeric, monomeric, split dimeric or split monomeric iRFP variants against their excitation efficiency after irradiation by a standard 633 nm laser. Excitation efficiency of miSplit670 assumes that the excitation and emission spectra of parental miRFP670 is retained by the split derivative, analogous to iSplit713 and parental diRFP713 (Filonov and Verkhusha, 2013). **(B)** Molecular brightness against photostability in mammalian cells. **(C)** Performance of iRFP variants by two-photon microscopy in cultured neurons (Piatkevich *et al.*, 2017). Open symbols represent monomeric, filled symbols dimeric, and squares represent split iRFP variants. Brightness of miSplit670 compared to diRFP713 is calculated from published data (Shcherbakova *et al.*, 2016). Two-photon brightness and two-photon photostability are calculated from reported data (Piatkevich *et al.*, 2017). See Table 4.1 for further details and full references.

NIR FP	Derived from	Ex (nm)	Em (nm)	Ex efficiency by 633nm laser[a] (%)	$t_{1/2}$ in mammalian cells[b] (s)	Molecular brightness vs diRFP713[c] (%)	Brightness vs diRFP713[d] (%)	Two-photon microscopy: Brightness vs diRFP713[e] (%)	Two-photon microscopy: $t_{1/2}$ [f] (s)	Ref
dimers										
diRFP713	*Rp*BphP2	690	713	52	960	100	100	100	~61.5	1, 2
diRFP670	*Rp*BphP6	643	670	94	290	225	119	100	240	1, 2, 3
diRFP682	*Rp*BphP2	663	682	67	490	162	105	77	~136	1, 2, 3
diRFP720	*Rp*BphP2	702	720	44	490	93	110	90	~61.5	1, 2, 3
split dimer										
iSplit713	*Rp*BphP2	690	713	52	Similar to diRFP713	86	25	n.d.	n.d.	4
monomer										
miRFP670	*Rp*BphP1	642	670	96	155	198	72	n.d.	n.d.	5
split monomer										
miSplit670	*Rp*BphP1	642*	670*	96*	n.d.	n.d.	37[g]	n.d.	n.d.	5

Table 4.1 **Comparative analysis of the properties of several iRFP variants.** [a] Excitation (Ex) efficiency of each iRFP by 633 nm laser was calculated from spectra obtained from FPbase (URL: www.fpbase.org accessed 03-Dec-2020; (Lambert, 2019)). [b] Photostability $t_{1/2}$ determined by transient expression in HeLa cells, imaged at determined time periods and raw data normalized to the absorbance spectra and extinction coefficients of each iRFP, the spectrum of 200 W Me-Ha arc lamp and the transmission of 665/45 nm photobleaching filter. [c] Molecular brightness calculated as the product of quantum yield and molar extinction coefficient of purified iRFP. [d] Brightness calculated by normalising the NIR fluorescence in HeLa cells, without exogenous BV, by the co-transfected EGFP fluorescence in the same population. [e] Brightness of diRFPs by two-photon microscopy excited at 880 nm where brightness of diRFP713 set to 100%. Fold-changes reported by Piatkevich and colleagues were converted to % (Piatkevich *et al.*, 2017). [f] Photostability of diRFPs by two-photon microscopy when excited at 880 nm. Piatkevich and colleagues reported diRFP670 $t_{1/2}$ of 240 s and $t_{1/2}$ for diRFP682 and diRFP720 as fold-changes compared to diRFP713. These fold-changes were calculated into seconds (Piatkevich *et al.*, 2017). [g] Brightness of miSplit670 vs diRFP713 is calculated as the mean of two reported brightness measures: (i) as the product of miRFP670 brightness compared to diRFP713 (72%) and the reported brightness of miSplit670 to parental miRFP670 (45%) and (ii) miSplit670 reported as 170% as bright as iSplit713. * the Ex and emission (Em) spectra and Ex efficiency of miSplit670 are assumed to match parental miRFP670, as was the case for iSplit713 and diRFP713 (Filonov and Verkhusha, 2013). References: 1 (Filonov *et al.*, 2011); 2 (Piatkevich *et al.*, 2017); 3 (Shcherbakova and Verkhusha, 2013); 4 (Filonov and Verkhusha, 2013); 5 (Shcherbakova *et al.*, 2016).

This showed that diRFP670 possessed the highest brightness in mammalian cells (119% that of diRFP713) and very high excitation efficiency 633 nm laser, commonly used for flow cytometry (Table 4.1 and Figure 4.1A). diRFP670 also displayed the highest molecular brightness and an almost 2-fold increased photostability in mammalian cells than miRFP670, the iRFP variant with the closest molecular brightness (Table 4.1 and Figure 4.1B). Further, diRFP670 exhibited the best photostability and brightness characteristics under two-photon excitation in cultured neurons, where diRFP670 was similar in brightness to diRFP713 but almost 4-fold more photostable (Table 4.1 and Figure 4.1C). Combined, this data highlighted diRFP670 as a consistent high performer across multiple key parameters and demonstrated its compatibility with standard experimental equipment. This supported the decision to choose diRFP670 as the iRFP to incorporate into the design of the novel *in vivo* reporter system.

Similar to the HALO PC transgenic, the novel iRFP based transgenic model was to identify GCmat PCs by exploitation of the inverse but overlapping expression profiles of the GC-specific promoter, *S1pr2*, and the promoter for the master transcription factor of PC phenotype, *Prdm1*. At the concept stage, there were two options available. Option 1 involved targeted knock-in of diRFP670 and another spectrally distinct diRFP to the separate *S1pr2* and *Prdm1* loci (top panel, Figure 4.2), whereas Option 2 involved targeted knock-in to the *S1pr2* and *Prdm1* loci of the two necessary components of a split iRFP reporter system; sequences encoding the PAS and GAF domains (bottom panel, Figure 4.2). When compared to HALO PC mice, both Option 1 and Option 2 would be simpler systems since they would not require the administration of exogenous tamoxifen to induce Cre recombinase mediated gene expression. Option 1 would utilise two different iRFPs (“diRFPY” and “diRFPX”) with the brightest spectral properties for *in vivo* imaging, but its design would transiently label all GC

B-cells. This is not significantly different from the HALO PC mouse as it would fate map total PCs (GCmat and EF) but would only transiently label all GC B-cells. Further, GC precursors of PCs and recently differentiated GCmat PBs could only be transiently diRFPY^{+} diRFPX^{+} double positive, meaning it could be challenging to identify theses rare desired cell populations as: a) the window would be short and b) there would be significant risk that they would be contaminated by the background of bright single diRFP^{+} positive EF PCs or GC B-cells (top panel, Figure 4.2). Option 2 however, would generate a fluorescent reporter system which transiently identifies only GC precursors of PCs and recently differentiated GCmat PBs; the cells which should be of highest affinity (bottom panel, Figure 4.2). Those cells would be suitable to study factors determining their differentiation. Further, transient fluorescence could mean the ability to study their migration without signal from cells that have been around for a long time.

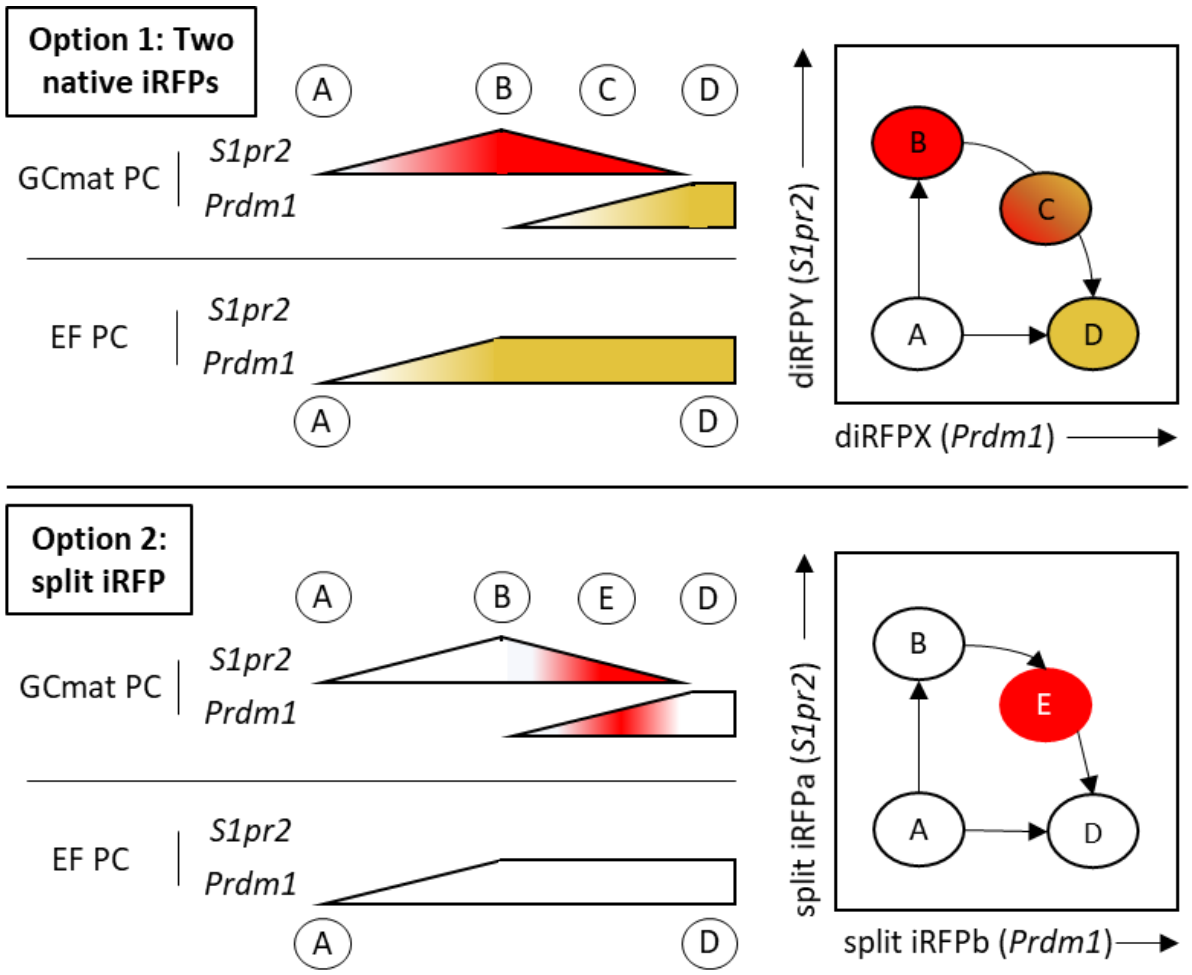

Figure 4.2 **Novel transgenic mice will use a split-iRFP fluorescent reporter to transiently identify nascent GCmat PC and their precursors**. **Left**, schematics detailing gene expression level (shape height) and native diRFP or split reporter diRFP fluorescence intensity (gradient of shape fill). **Right**, schematic to demonstrate reporter fluorescence in B-cell phenotypes. Ag activated B-cell (A) acquires GC B-cell phenotype or EF PC terminal differentiation. GC B-cell initiates terminal differentiation into GCmat PC (B). PC generated by affinity matured or EF pathways (D). **Upper panel**, total PC population permanently labelled diRFPX^{+}, total GC population labelled diRFPY^{+} and only GC B-cells differentiating into PC are transiently diRFPX^{+} and diRFPY^{+} (C). **Lower panel**, transient fluorescence reconstitution of split iRFP reporter comprised of two parts (split iRFPa and split iRFPb) only in GC B-cells undergoing differentiation to GCmat PB (E).

Split iRFP reporters of diRFP713 and miRFP670 have been published (Filonov and Verkhusha, 2013; Shcherbakova *et al.*, 2016). miSplit670, the split reporter of monomeric iRFP670, has an Em_{max} of 670 nm, however, this split reporter was not designed for maximal brightness or photostability for cell labelling but primarily for investigation of protein-protein interactions where the dimeric nature of iSplit713, the split reporter of diRFP713, could interfere with native target protein interactions by steric hinderance (Filonov and Verkhusha, 2013; Shcherbakova *et al.*, 2016). Moreover, diRFP670 is 65% brighter than miRFP670 and almost 2-fold more photostable in mammalian cells; with diRFP670 $t_{1/2}$ of 290 s compared to a $t_{1/2}$ of 155 s for miRFP670 (Table 4.1 and Figure 4.1B). Compared to diRFP713, diRFP670 is brighter in mammalian cells, is more efficiently excited by standard lasers and performs better under two-photon excitation (Table 4.1 and Figure 4.1C). Taken together, diRFP670 was hypothesised to serve as a good template for the derivation of a split reporter that could possess the characteristics required for an improved split iRFP reporter system for use *in vivo*.

In order to identify where to separate the PAS and GAF domains of the parental diRFP670 template and rationally select a suitable split position, multiple sequence alignments of diRFP670 were made against the non-split sequences of the two iRFP templates that have been validated as split iRFP reporters (Figure 4.3). diRFP670 was compared to diRFP713 alone, miRFP670 alone or simultaneously against both (the latter is shown with or without residue similarity scores in Figure 4.3). This revealed that the diRFP670 PAS fold (residues 10-117, GenBank entry AGN32863.1) ends within the areas where the PAS and GAF domains of both diRFP713 and miRFP670 had been separated (Figure 4.3A).

Figure 4.3 **Alignment of diRFP670 to iRFP sequences from which split iRFP reporters have previously been generated. (A)** The sequence of dimeric iRFP670 (d670) was aligned to diRFP713 (d713) and miRFP670 (m670). The red line indicates where the PAS fold of diRFP670 ends. The blue box indicates the four residue overlaps at the position where diRFP713 and miRFP670 were partitioned to generate their split reporters (i.e., the same four residues at the C-terminus of the PAS and N-terminus of the GAF partitions) (Filonov and Verkhusha, 2013; Shcherbakova *et al.*, 2016). **(B)** Aligned sequences are scored for overall residue identity or electrophysical similarity. Dark grey (*) are identical residues whereas residues highlighted intermediate grey (:) are more similar than those light grey (.) or no similarity (non-highlighted). Sequences were aligned using the CLUSTALO program before similarity scores attributed (bioinformatics tools accessed on UniProt. URL: https://www.uniprot.org/align/).

By comparison to the solved crystal structure of the bacterial homologue *Rp*BphP3 (Yang *et al.*, 2007), the site selected for partition of diRFP713 after the arginine residue of "PPQR" was determined to be within the linker loop between the PAS and GAF domains (Filonov and Verkhusha, 2013). Further, the more recently solved crystal structure of miRFP670 (PDB ID code 5VIV), demonstrated that the miSplit670 "RAGP" partition site is surface exposed within the linker region (Figure 4.4A-B). As both existing, validated split iRFP reporters are partitioned close to the C-terminus of the PAS fold, there was precedent to split diRFP670 in an analogous position.

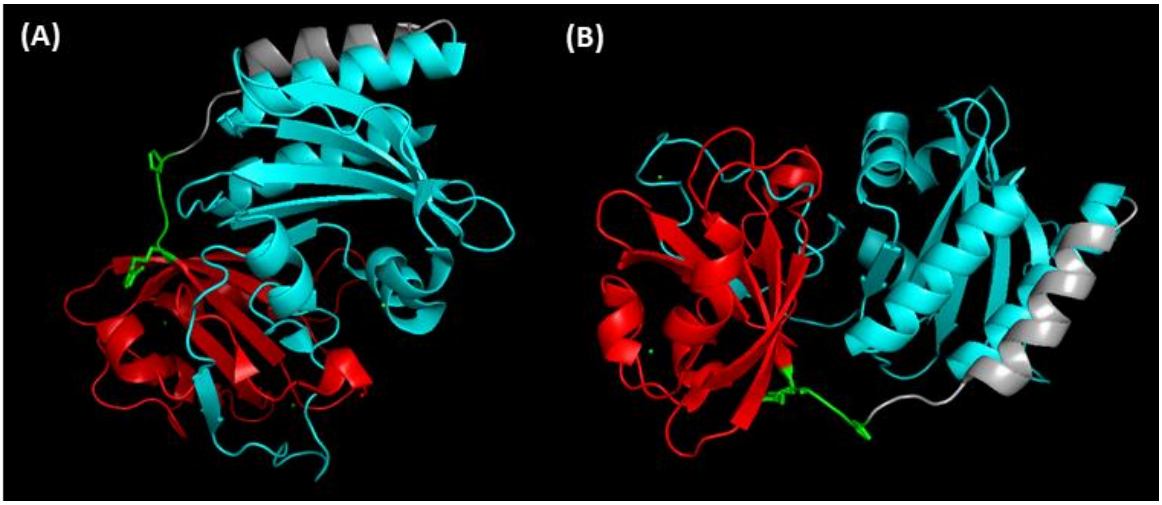

Figure 4.4 **Crystal structure of miRFP670.** Two orientations of miRFP670 are displayed to show the protein domains and surface exposed linker regions. **(A, B).** The PAS fold (red), GAF domain (cyan) and linker region (grey) were annotated and coloured according to diRFP670 features (GenBank entry AGN32863) and the sequence alignment of miRFP670 with diRFP670 in Figure 4.3. miRFP670 was split after the proline residue of "RAGP", highlighted in green, to generate miSplit670. miRFP670 crystal structure; PDB ID code 5VIV.

Therefore, diRFP670 was split between residue 119-120, "PAAA|E" generating two parts: split-diRFP670 PAS and split-diRFP670 GAF (Figure 4.5). A four residue overlap of "PAAA" between the sequence of split-diRFP670 PAS and split-diRFP670 GAF was included, similar to the four residue overlaps retained at the split sites of iSplit713 and miSplit670 (Filonov and Verkhusha, 2013; Shcherbakova *et al.*, 2016).

```
diRFP670     1          11         21         31         41         51
PAS          MARKVDLTSC DREPIHIPGS IQPCGCLLAC DAQAVRITRI TENAGAFFGR ETPRVGELLA
GAF          MARKVDLTSC DREPIHIPGS IQPCGCLLAC DAQAVRITRI TENAGAFFGR ETPRVGELLA
             ---------- ---------- ---------- ---------- ---------- ----------

            61         71         81         91        101        111     119
diRFP670     DYFGETEAHA LRNALAQSSD PKRPALIFGW RDGLTGRTFD ISLHRHDGTS IIEFEPAAAE
PAS          DYFGETEAHA LRNALAQSSD PKRPALIFGW RDGLTGRTFD ISLHRHDGTS IIEFEPAAA-
GAF          ---------- ---------- ---------- ---------- ---------- -----PAAAE

           121        131       141        151        161        171
diRFP670     QADNPLRLTR QIIARTKELK SLEEMAARVP RYLQAMLGYH RVMLYRFADD GSGMVIGEAK
PAS          ---------- ---------- ---------- ---------- ---------- ----------
GAF          QADNPLRLTR QIIARTKELK SLEEMAARVP RYLQAMLGYH RVMLYRFADD GSGMVIGEAK

           181        191        201        211        221        231
diRFP670     RSDLESFLGQ HFPASLVPQQ ARLLYLKNAI RVVSDSRGIS SRIVPEHDAS GAALDLSFAH
PAS          ---------- ---------- ---------- ---------- ---------- ----------
GAF          RSDLESFLGQ HFPASLVPQQ ARLLYLKNAI RVVSDSRGIS SRIVPEHDAS GAALDLSFAH

           241        251        261        271        281        291
diRFP670     LRSISPCHLE FLRNMGVSAS MSLSIIIDGT LWGLIICHHY EPRAVPMAQR VAAEMFADFL
PAS          ---------- ---------- ---------- ---------- ---------- ----------
GAF          LRSISPCHLE FLRNMGVSAS MSLSIIIDGT LWGLIICHHY EPRAVPMAQR VAAEMFADFL

           301        311
diRFP670     SLHFTAAHHQ R
PAS          ---------- -
GAF          SLHFTAAHHQ R
```

Figure 4.5 **Alignment of novel split-diRFP670 PAS and GAF parts with parental diRFP670**. Parental diRFP670 sequence (black font), derived from *Rp*BphP6 (Shcherbakova *et al.*, 2016), is annotated for the PAS fold (yellow highlight, residues 10-117) and the GAF domain (grey highlight, residues 141-302) as per GenBank entry AGN32863. To produce split-diRFP670 PAS and GAF domains (red and blue font, respectively), the full-length parental sequence was split between residues 116-119, with each domain retaining these 4 residues as an overlap.

Previous work with split iRFP reporters had shown that the inclusion of high affinity dimerization domains could augment the reconstitution of the split iRFP complex (Filonov and Verkhusha, 2013). One such reported dimerization system was small complementary E and K coils (Figure 4.6A-B) comprised of a pentameric repeat of a seven-residue sequence with reported 63 pM affinity (De Crescenzo *et al.*, 2003). The E and K coils with flexible glycine-glycine-serine (GGS) spacers were included at the C- and N- termini of the split-diRFP670 PAS and split-diRFP670 GAF parts respectively, generating split-diRFP670 PAS-E and K-split-diRFP670 GAF (Figure 4.6A-B). Inclusion of the E/K coils and GGS spacers was not predicted to significantly impact chromophore incorporation by the PAS and GAF domains. This was based on analysis of the crystal structure of miRFP670 (Figure 4.4) which highlighted that the interaction of the E/K coils should be situated at the surface in-between the reconstituted parts of split-diRFP670.

Cryosection, fixation of tissue (especially with acetone) and the associated wash steps required for immunohistology can result in the loss of non-membrane associated/anchored fluorescent proteins, resulting in poor signal detection. Therefore, the 20-mer plasma membrane inner leaflet trafficking palmitoylation signal from mouse Growth Associated Protein 43 (GAP-43) was included at the N-terminus of the split-diRFP670 PAS-E, creating mem-split-diRFP670 PAS-E (Figure 4.6A-B). This 20-mer had been reported to properly localise diRFP713 to the plasma membrane of cultured neurons (Richie *et al.*, 2017). iRFP-specific antibodies are lacking so separate epitope tags were added to each part to enable detection of individuals split-diRFP670 parts. A FLAG epitope tag was inserted immediately 3' to the plasma membrane signal of mem-split-diRFP670 PAS-E (generating mem-FLAG-diSplit670 PAS-E), whilst a V5 epitope tag was inserted at the C-terminus of K-split-diRFP670 GAF (generating K-diSplit670

GAF-V5) (Figure 4.6A-B). The reconstituted complex containing only the plasma membrane localisation signal is referred to as mem-split-diRFP670, whereas the version containing both the plasma membrane signal and the epitope tags has been termed diSplit670 (Figure 4.6A).

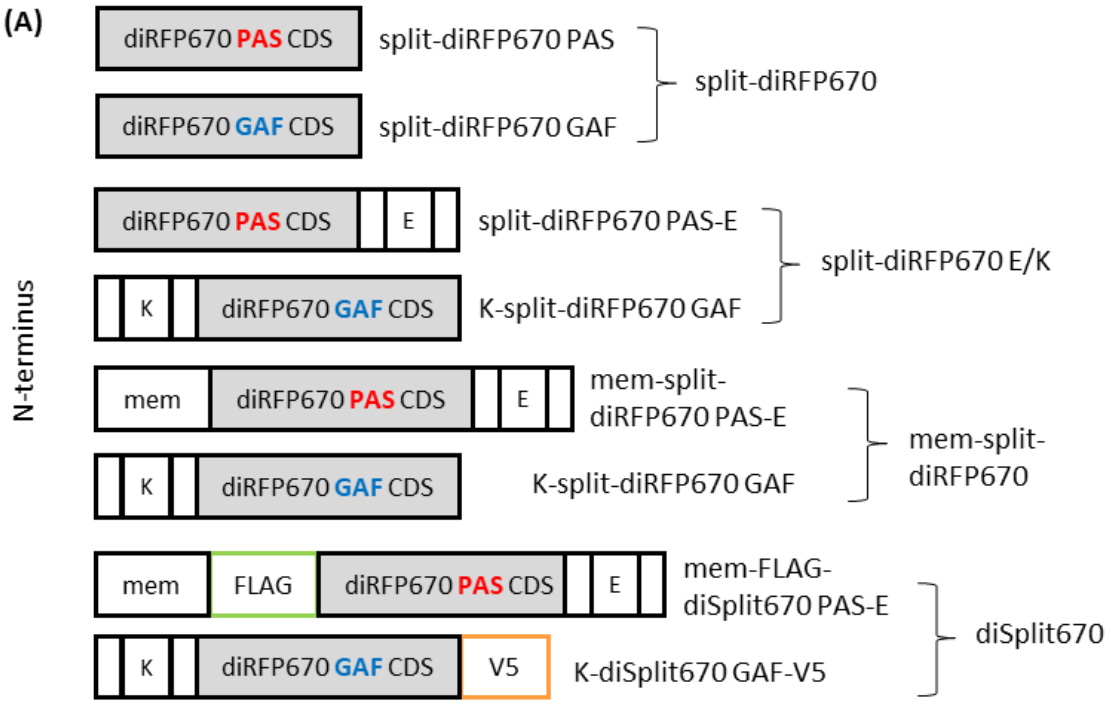

(B)

	1 11 21 31	
E5 coil (E)	EVSALEKEVS ALEKEVSALE KEVSALEKEV SALEK	
	1 11 21 31	
K5 coil (K)	KVSALKEKVS ALKEKVSALK EKVSALKEKV SALKE	
	1	
GGS linker (GGS)	GGS	
	1 11	
GAP-43 plasma membrane signal (mem)	MLCCMRRTKQ VEKNDEDQKI	
	1	
FLAG epitope tag (FLAG)	DYKDDDDK	
	1 11	
V5 epitope tag (V5)	GKPIPNPLLG LDST	

Figure 4.6 **Further modifications to split-diRFP670 PAS and split-diRFP670 GAF. (A)** Schematic representations of the coding sequences of split-diRFP670 constructs. CDS, coding sequence; E and K, complementary E5 and K5 coils (De Crescenzo *et al.*, 2003); mem, GAP-43 plasma membrane localisation signal (Richie *et al.*, 2017); empty black rectangle, GGS linker; FLAG and V5, epitope tags. **(B)** Amino acid sequences for the features included in modified split-diRFP670 constructs.

4.2.2 Validation of novel diSplit670.

First, an assessment was made as to whether co-transfection with both domains of the split-diRFP670 (under the control of strong constitutive promoters) was required for fluorescence reconstitution and whether this occurred in the absence of the high affinity complementary coils. Similar to iSplit713 (Filonov and Verkhusha, 2013), minimal fluorescence reconstitution was observed in transiently co-transfected HEK293T cells without the incorporation of the E and K coils (Figure 4.7A-B), and that co-transfection of HEK293T cells with split-diRFP670 PAS-E and K-split-diRFP670 GAF resulted in fluorescence reconstitution (Figure 4.7A-B). Fluorescence was not detected in HEK293T cells transfected with either split-diRFP670 PAS-E or K-split-diRFP670 GAF alone (Figure 4.7A). Unexpectedly, the brightness of plasma membrane localised mem-split-diRFP670 was significantly greater than split-diRFP670, presumed to be distributed within the cytoplasm (Figure 4.7C). This could be explained by localised distribution caused by plasma membrane anchoring of the mem-split-diRFP670 PAS-E domain enhancing the likelihood of interaction with the split-diRFP670 PAS and GAF domains compared to both being randomly distributed within the cytoplasm or that the plasma membrane provides a more stable environment for homodimers of diSplit670 to be maintained.

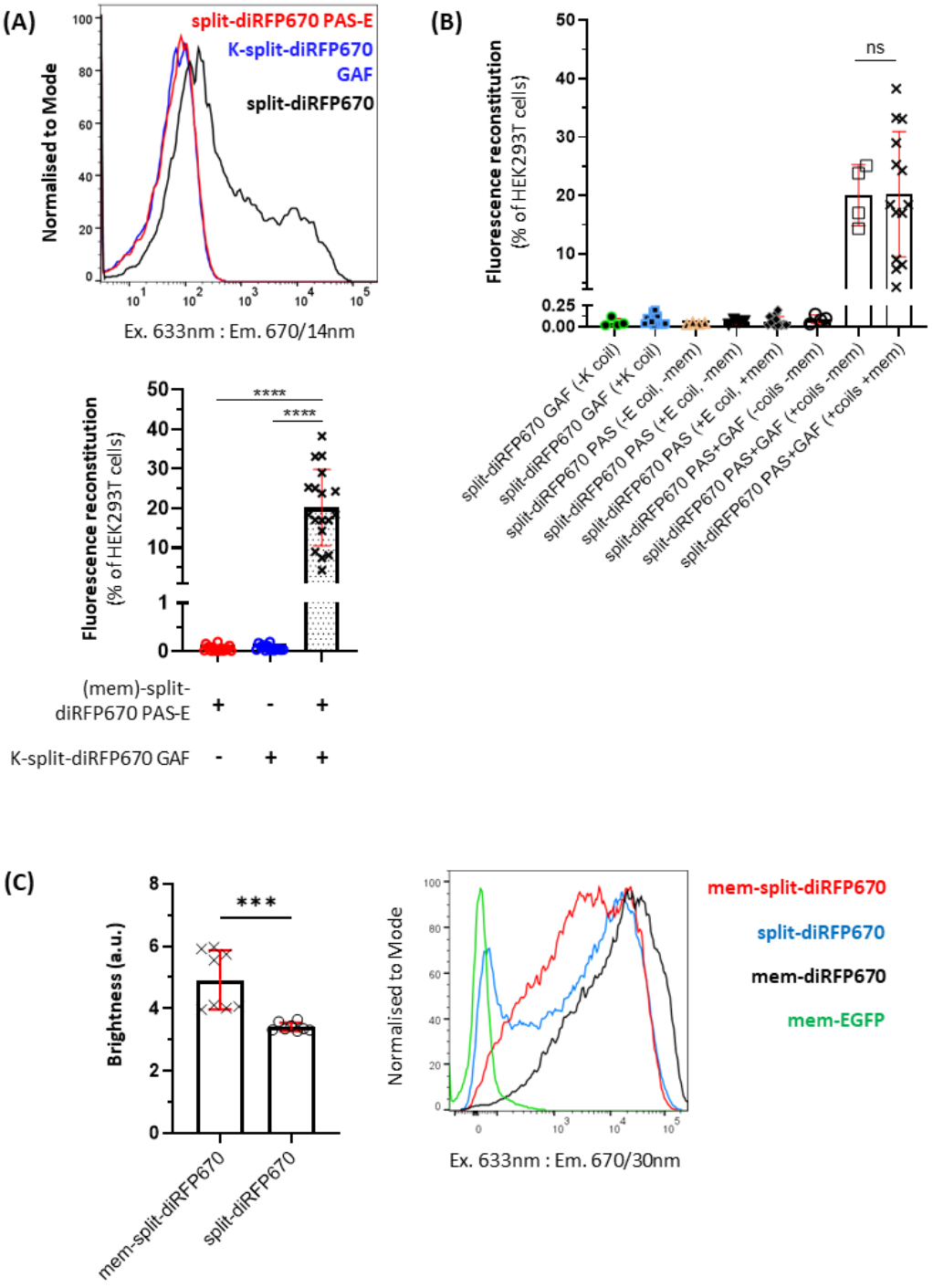

Figure 4.7 **Co-expression of split-diRFP670 PAS and GAF domains with complementary E/K coils is necessary and sufficient for split-diRFP670fluorescence reconstitution. (A)** Fluorescence reconstitution. Flow cytometry histogram (top) with corresponding fluorescence reconstitution (bottom), from 48 h transiently transfected HEK293T cells with either mem-split-diRFP670 PAS-E, split-diRFP670 PAS-E or K-split-diRFP670 GAF domains alone or in combination. Kruskal-Wallis non-parametric multiple comparisons test. (mem)-split-diRFP670 PAS-E, collated data from transfections that used split-diRFP670 PAS-E construct ± plasma membrane localisation signal. **(B)** Fluorescence reconstitution data from (A) but

separated into split-diRFP670 construct variants ± the indicated modifications. **(A, B)** n=5 independent transfections, error bars are mean ± SD. **(C)** Brightness of plasma membrane localised mem-split-diRFP670, and cytoplasmic split-diRFP670 (left) and flow cytometry histogram overlay (right). n=2 independent transfections with 4 technical repeats per transfection. Mann Whitney test (C), error bars are median with 95% CI.

As iRFP-specific antibodies are lacking, FLAG and V5 epitope tags were incorporated into mem-split-diRFP670 PAS-E and K-split-diRFP670 GAF, respectively, to enable the detection of each domain. Flow cytometric analysis revealed that the epitope tags did not affect diSplit670 fluorescence reconstitution (Figure 4.8A-B). Multiple techniques were tested to detect expression of the epitope tagged diSplit670. First, expression of the epitope tags was detected in the lysates of transfected cells after denaturing immunoblot analysis (Figure 4.8C). While this showed presence of the epitope tag, it was also able to confirm that the molecular weights (MW) of individual mem-FLAG-diSplit670 PAS-E and K-diSplit670 GAF-V5 domains were in-line with their predicted MW's of 20.6 kDa and 27.5 kDa, respectively (Figure 4.8C). Second, epitope tags were detected by intracellular flow cytometric staining (Figure 4.8D). Detection of the FLAG epitope tag in mem-FLAG-diSplit670 PAS-E transfected HEK293T cells was specific, with no non-specific labelling of sham transfected cells (bottom histogram, Figure 4.8D). However, detection of the V5 epitope tag with polyclonal rabbit α-V5 primary antibody revealed non-specific binding to HEK293T cells by the V5-specific primary antibody (Figure 4.8D, top panel, right). Despite this, ~22% of the K-diSplit670 GAF-V5 transfected cells showed a signal on average 7.5-fold higher which presumably corresponds to the true positive V5 epitope tag expressing cells.

To test whether the two-step α-epitope tag detection by flow cytometry is suitable for downstream validation of the expression of epitope tagged diSplit670 by flow cytometry, B-cell populations from non-immunised spleen and BM were stained and assessed for non-specific signal (Figure 4.9). Splenic PCs, non-GC B-cells, GC B-cells (Figure 4.9A) and BM PCs (Figure 4.9B) all displayed minimal background signal when stained with the α-epitope tag two-step stain compared to when the rabbit α-epitope tag primary antibody was replaced with a rabbit isotype primary control. This suggested that the non-specific background from α-V5 detection observed in HEK293T cells (Figure 4.8D) was either a species or cell line specific artefact. Transgenic mice which express FLAG or V5 tagged proteins would have served as useful positive controls for this assay but we did not have access to any relevant models, however, the absence of non-specific background signal in PC populations suggest that this two-step α-epitope tag flow cytometry assay is suitable for epitope tag detection in transgenic mouse cells expressing either K-diSplit670 GAF-V5 alone or diSplit670.

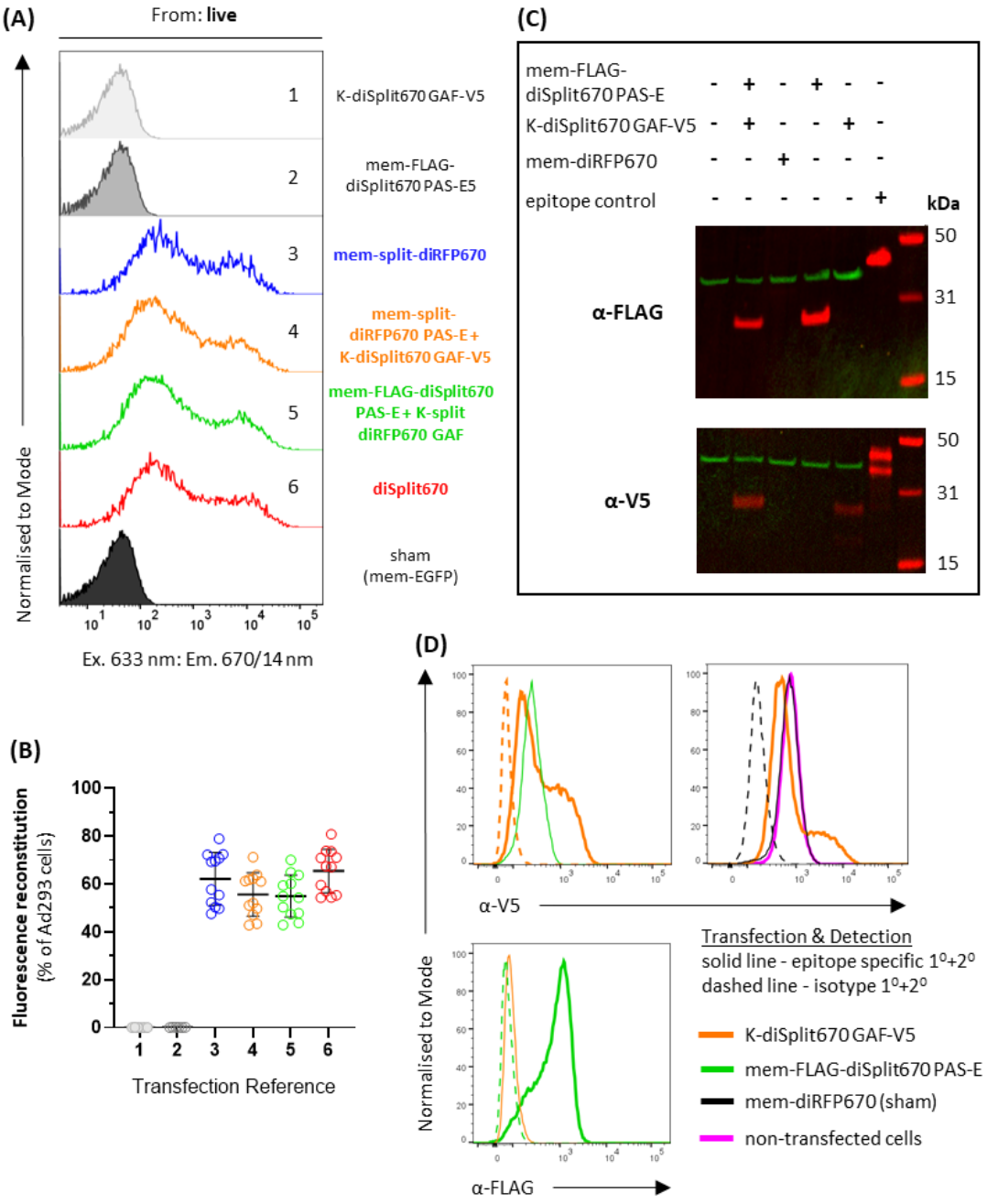

Figure 4.8 **Characterisation and detection of the epitope tags present in diSplit670. (A, B)** Assessment of whether epitope tags affected fluorescence reconstitution by flow cytometry. Fluorescence histograms (A), and corresponding diSplit670 fluorescence reconstitution rates (B) in Ad293 cells transfected with the indicated split-diRFP670 and diSplit670 constructs (as per schematics, Figure 4.6A). n=2 independent transfections, with 6 technical repeats per transfection. Error bars represent mean ± SD. Unpaired t-tests indicated no difference between groups 3-6. **(C)** SDS-PAGE immunoblot for epitope tags in HEK293T cell lysates 40 h post-transfection. Epitope tag and size standards in red, GAPDH control in green. **(D)** Detection of separate epitope tags by flow cytometry. HEK293T cells were transiently transfected (or not) with the indicated construct for at least 24 h before two-step detection for epitope tags.

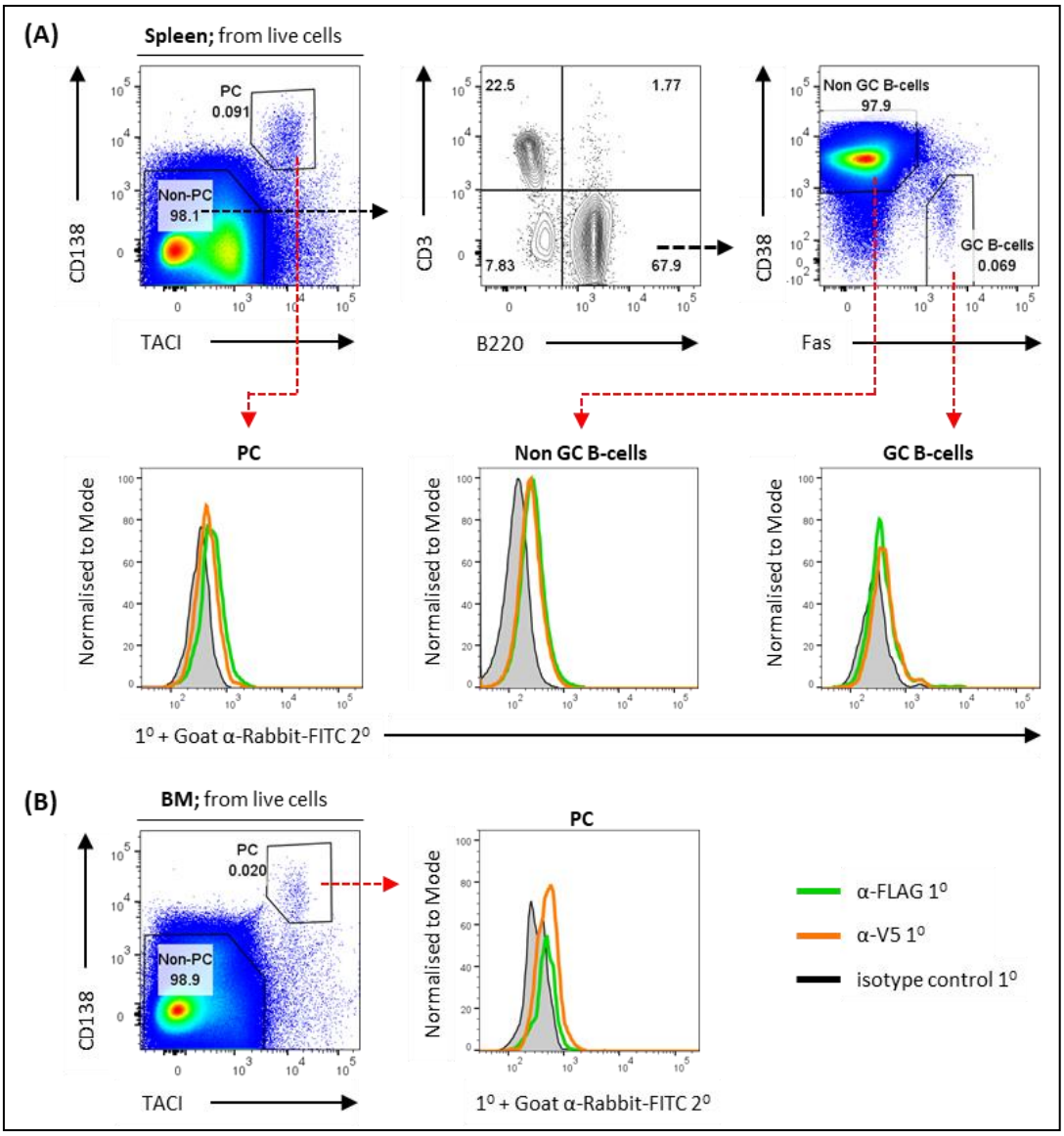

Figure 4.9 **Assessment of non-specific background for epitope tag staining protocol in mouse B-cell populations from different tissues.** Non-GC B-cells, GC B-cells, and PCs from splenocytes **(A)** and bone marrow (BM) PCs **(B)** from a naïve C57BL/6N background transgenic mouse were assessed for non-specific background binding of the two-step stain protocol for FLAG and V5 epitope tags by flow cytometry.

Confocal microscopy was used to confirm that the plasma membrane signal sequence from GAP-43 led to correct insertion of diSplit670 into the plasma cell membrane (Figure 4.10A). To do this, HEK293T cells were transiently co-transfected with diSplit670 and a plasmid which expresses EGFP that is trafficked to the plasma membrane (mem-EGFP) using the signal sequence derived from the MARCKS protein (Muzumdar *et al.*, 2007), before fixation and DAPI counterstain (Figure 4.10A). Intensity profile analysis highlighted that diSplit670 and mem-EGFP were co-localised (Figure 4.10B).

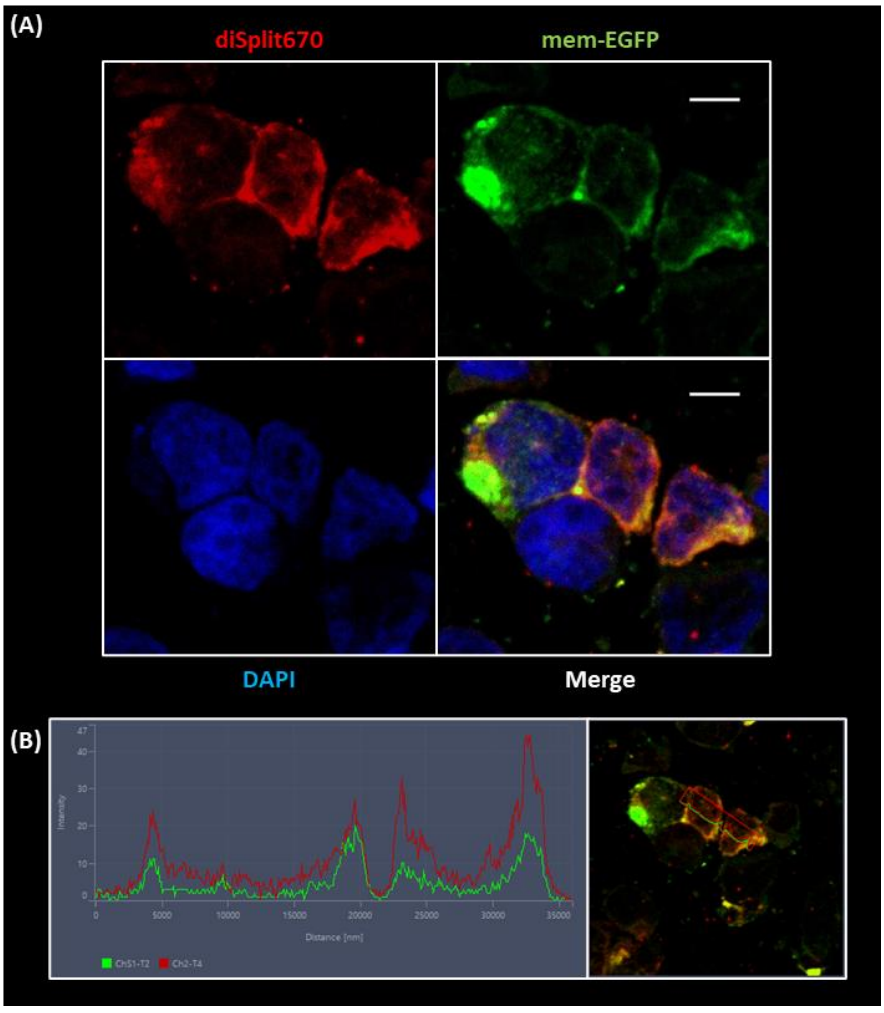

Figure 4.10 **Reconstituted diSplit670 is correctly trafficked to the plasma membrane**. **(A)** Confocal microscopy of fixed HEK293T cells 24 h after co-transfection with diSplit670 and mem-EGFP. **(B)** Profile intensity plot analysis to demonstrate co-localisation of diSplit670 and mem-EGFP at plasma membrane. Scale bar, 10 µm.

The brightness of diRFP670 in mammalian cells (Table 4.1) was a key factor for choosing this as the starting point for making the split reporter diSplit670. Thus, it was important to determine any impact on brightness from making the split version. To test this, flow cytometric analysis of transiently transfected HEK293T cells revealed that diSplit670 was 27.6% ± 3.3 (mean ± SD) the brightness of parental diRFP670 (Figure 4.11A). Moreover, it was 125.7% ± 9.4 (mean ± SD) as bright as iSplit713 when compared directly in mammalian cells (Figure 4.11B).

In vitro analyses of iSplit713 and miSplit670 determined that they are 25% and ~45% as bright as there parental iRFPs, respectively (Filonov and Verkhusha, 2013; Shcherbakova *et al.*, 2016). Further validation of these split reporters revealed their suitability, and for miSplit670, their capability to report on molecular interactions or cellular processes, by microscopy and whole animal imaging methods (Filonov and Verkhusha, 2013; Shcherbakova *et al.*, 2016). Therefore, the effect on brightness by splitting diRFP670 to generate diSplit670 was in-line with published data and not expected to impact performance in the *in vivo* split reporter system.

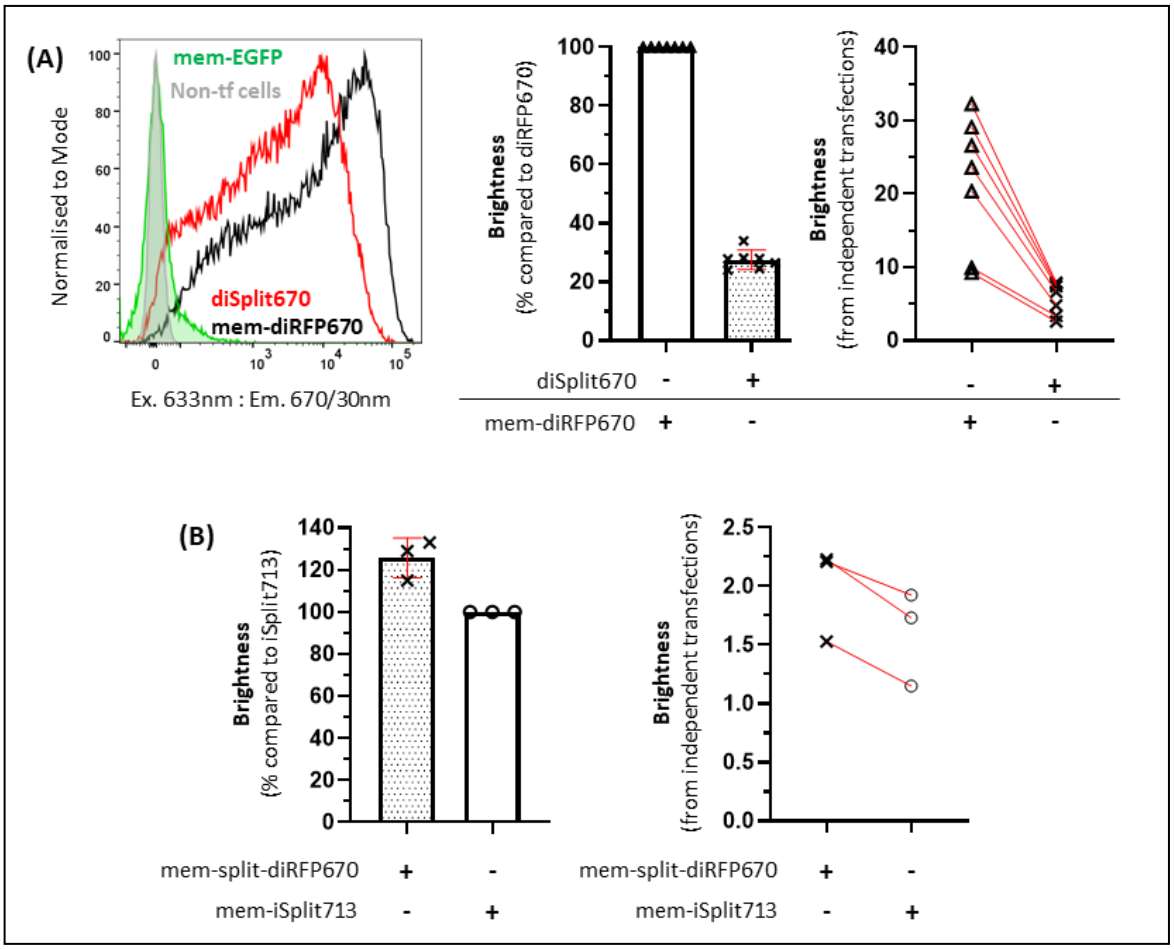

Figure 4.11 **Comparative brightness of diSplit670 in mammalian cells. (A)** Brightness of diSplit670 compared to parental mem-diRFP670 by flow cytometry. Histogram overlay (left) and brightness where the diRFP670 fluorescence from each independent transfection is normalised to 100% (middle) or displayed as the paired measurements from each transfection (right). HEK293T cells assessed 30-48 h after transfection. n=7 independent transfections. **(B)** Brightness comparison against iSplit713 by flow cytometry. Brightness displayed where iSplit713 signal from each independent transfection is normalised to 100% (left) or displayed as paired measurements from each transfection (right). Brightness of HEK293T cells 48 h after transfection. n=3 independent transfections. Error bars are mean ± SD. Excitation with 633 nm laser, with 670/14 nm and 730/45 nm emission filter sets for split-diRFP670 and iSplit713, respectively.

The dimerization of diRFPs is postulated to be via interaction of the α-helical bundles in the GAF domains (Auldridge *et al.*, 2012; Shcherbakova *et al.*, 2016). iSplit713 is thought to have retained the dimerization capability of diRFP713 (Filonov and Verkhusha, 2013). Despite retention of >25% of the brightness of parental diRFP670 (Figure 4.11A), the ability of reconstituted mem-FLAG-diSplit670 PAS-E / K-diSplit670 GAF-V5 hybrid monomers to interact and form homodimers, could have been affected by the engineering steps.

NativePAGE immunoblot was used to test whether dimers of reconstituted mem-FLAG-diSplit670 PAS-E / K-diSplit670 GAF-V5 hybrid monomers were correctly forming in living cells. Native dimerized diSplit670 complex was detected by α-FLAG and α-V5 immunoblot at the expected MW of 96.2 kDa, consistent with the predicted size for dimerization of reconstituted hybrid monomers (Table 4.2 and Figure 4.12). Lysate from cells transfected with mem-FLAG-diSplit670 PAS-E only and probed with α-FLAG revealed the predicted band at ~20 kDa, but unexpectedly, also highlighted additional bands of ~40 kDa and ~60 kDa. These larger bands could be explained by aggregation of constitutively overexpressed protein in the plasma membrane which is not disrupted by the gentle detergent/lysis buffer used for lysate preparation and non-denaturing PAGE conditions (left blot, Figure 4.12). Although, diSplit670 complex was detected by α-V5 immunoblot at the expected MW of 96.2 kDa, unexpectedly, there were no bands detected in the lysate from cells transfected with K-diSplit670 GAF-V5 only (right blot, Figure 4.12). With more time, we would repeat this native immunoblot for K-diSplit670 GAF-V5 only, but this result is not expected to impact the split reporter as transfection with K-diSplit670 GAF-V5 only can detect V5 tag by flow cytometry (Figure 4.8), the diSplit670 complex can be detected by α-V5 probe in native immunoblot (Figure 4.12), and diSplit670 complex is functional (Figure 4.11).

Splitting of diRFP670 PAS and GAF domains had not disrupted the ability of reconstituted mem-FLAG-diSplit670 PAS-E / K-diSplit670 GAF-V5 hybrid monomers (diSplit670) to interact and form homodimers (Figure 4.12). Therefore, the observed decline in fluorescence intensity of diSplit670 (Figure 4.11A) is likely to be complex intrinsic.

Protein/complex	Type	Predicted MW by amino acid composition (kDa)	Predicted MW in cell (kDa)
mem-FLAG-diSplit670 PAS-E	Hybrid monomer	20.6	20.6
K-diSplit670 GAF-V5	Hybrid monomer	27.5	55.0
diSplit670	Reconstituted diSplit670	48.1	96.2
diRFP670	Non-split, unmodified parental sequence	34.0	68.0

Table 4.2 **Predicted size of parental diRFP670, diSplit670 and its constituent parts**. Predicted MW's by amino acid composition were calculated using ExPASY ProtParam tool (Artimo *et al.*, 2012). Predicted MW for each protein/complex in the cell indicates whether each protein or reconstituted complex can dimerize when expressed in a cell.

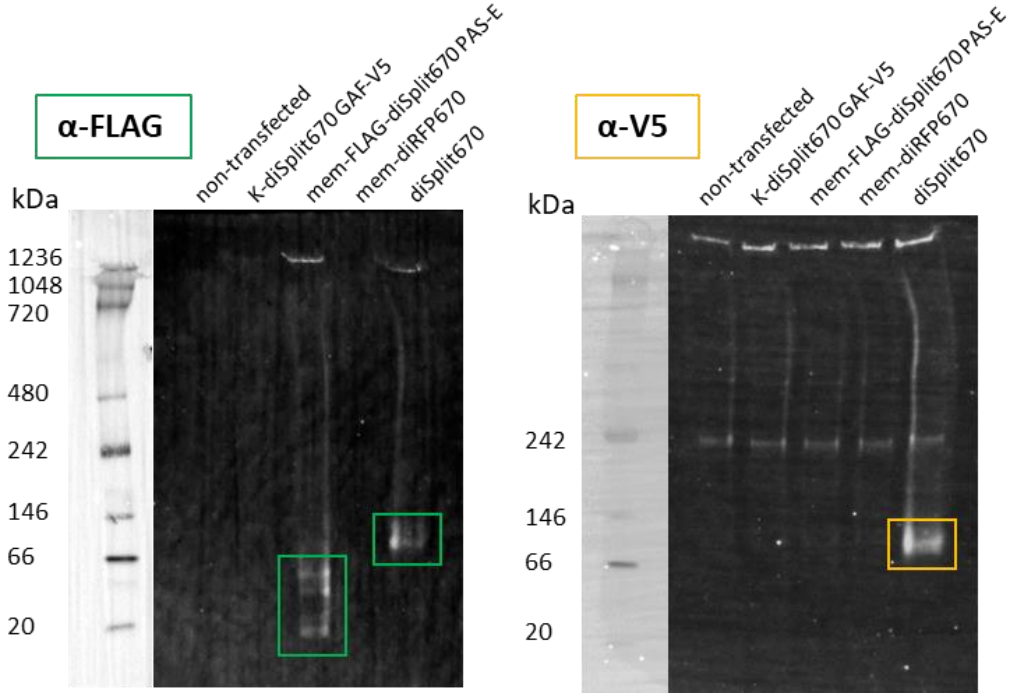

Figure 4.12 **Assessment of the oligomeric state of diSplit670 in mammalian cells.** Cell lysates from HEK293T cells either non-transfected or transiently transfected for 48 h with plasmid(s) that express: mem-diRFP670, each hybrid monomer alone (mem-FLAG-diSplit670 PAS-E or K-diSplit670 GAF-V5) or co-transfected (diSplit670). Assessment for oligomeric state by non-denaturing NativePAGE immunoblot detection of FLAG (left) or V5 (right) epitope tags. Molecular size ladder run on the same blot is shown stained with Ponceau S.

4.2.3 Rational mutagenesis failed to improve the brightness of diSplit670.

iSplit713 was developed by the introduction of three amino acid mutations by random mutagenesis into the split-diRFP713 GAF domain which improved brightness by 50% in mammalian cells (Filonov and Verkhusha, 2013). Sequence alignment of the bacterial *Rp*BphP2 and *Rp*BphP6 templates with their diRFP derivatives (Figure 4.13) and diRFP670 against diRFP713 and miRFP670 (Figure 4.3) highlighted that the F165Y substitution in iSplit713 GAF_m existed in both the native split-diRFP670 GAF and native miRFP670 sequences, whereas the W309R substitution at the C-terminus of iSplit713 had no equivalent in split-diRFP670. However, the D232Y substitution of iSplit713 GAF_m had an equivalent aligned position in split-diRFP670 GAF at E226.

Site-directed mutagenesis was performed to introduce the E226Y substitution into the K-diSplit670 GAF-V5 construct. The impact on brightness by this mutation in the E226Y mutant K-diSplit670 GAF-V5 domain was assessed by flow cytometry (Figure 4.14A). Two independent transfections showed decreased frequency of fluorescence reconstitution in cells transfected with diSplit670 containing the K-diSplit670 GAF-V5 E226Y mutant compared to diSplit670 containing non-mutated K-diSplit670 GAF-V5 (Figure 4.14B). Critically, the brightness of diSplit670 containing the K-diSplit670 GAF-V5 E226Y mutant was significantly lower compared to non-mutated diSplit670 at only 25.6% (Figure 4.14C). Introducing the E226Y substitution into K-diSplit670 GAF-V5 had a clear negative impact on the diSplit670 complex and so was not taken forward.

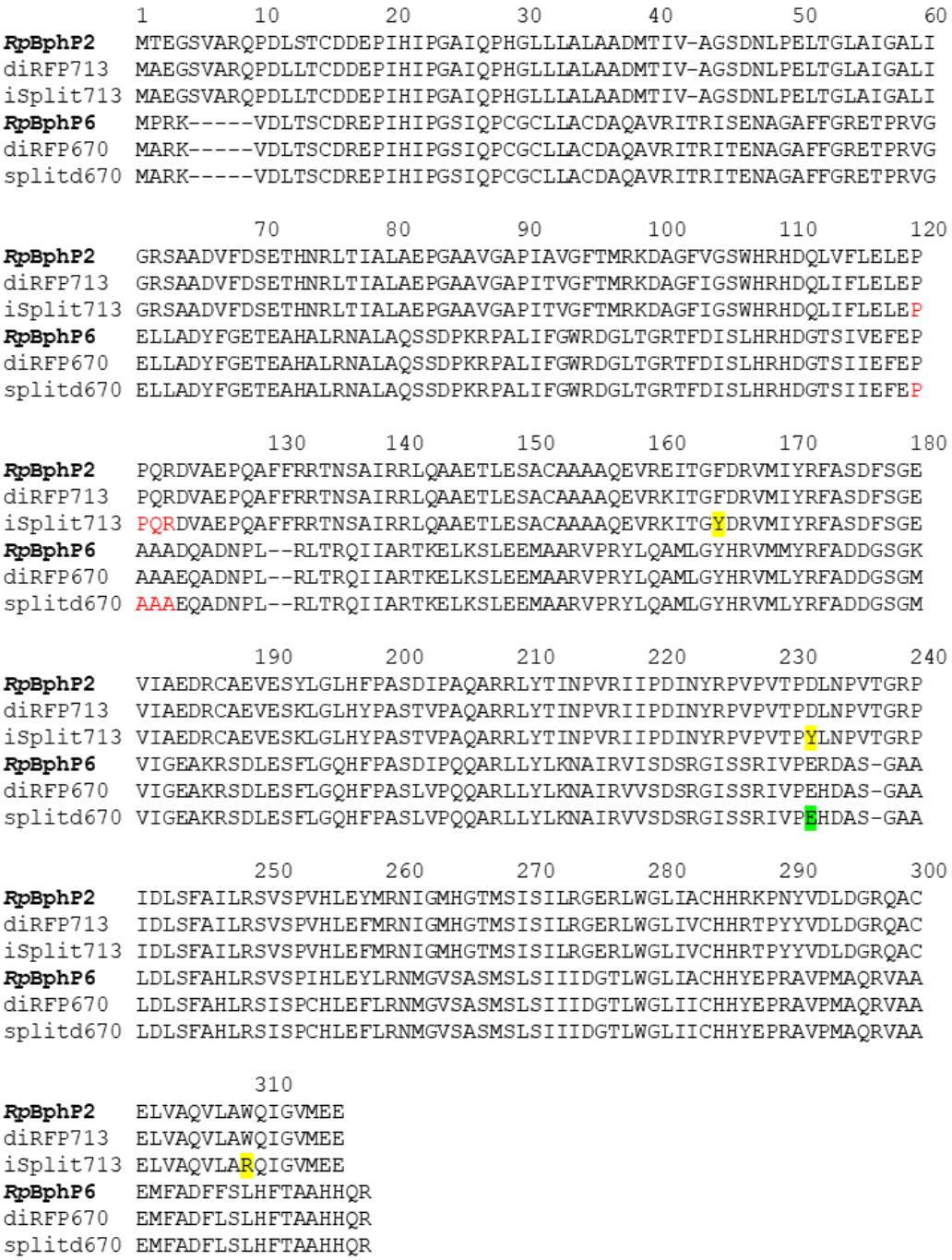

Figure 4.13 **Amino acid sequence alignment of non-split dimeric iRFPs, iSplit713 and novel split-diRFP670 against parental *Rp*BphP2 and *Rp*BphP6 templates guided rational mutagenesis.** Mutations highlighted in yellow were introduced by random mutagenesis into the GAF domain of split diRFP713 to produce the original iSplit713 GAF_m domain (Filonov and Verkhusha, 2013). The glutamate at position 232 (highlighted green), located within the GAF domain of native split-diRFP670 (splitd70) could be substituted for tyrosine, similar to iSplit713 GAF_m. Residues are numbered according to *Rp*BphP2 and residues highlighted red are present in both the PAS and GAF domains of the split iRFP reporters.

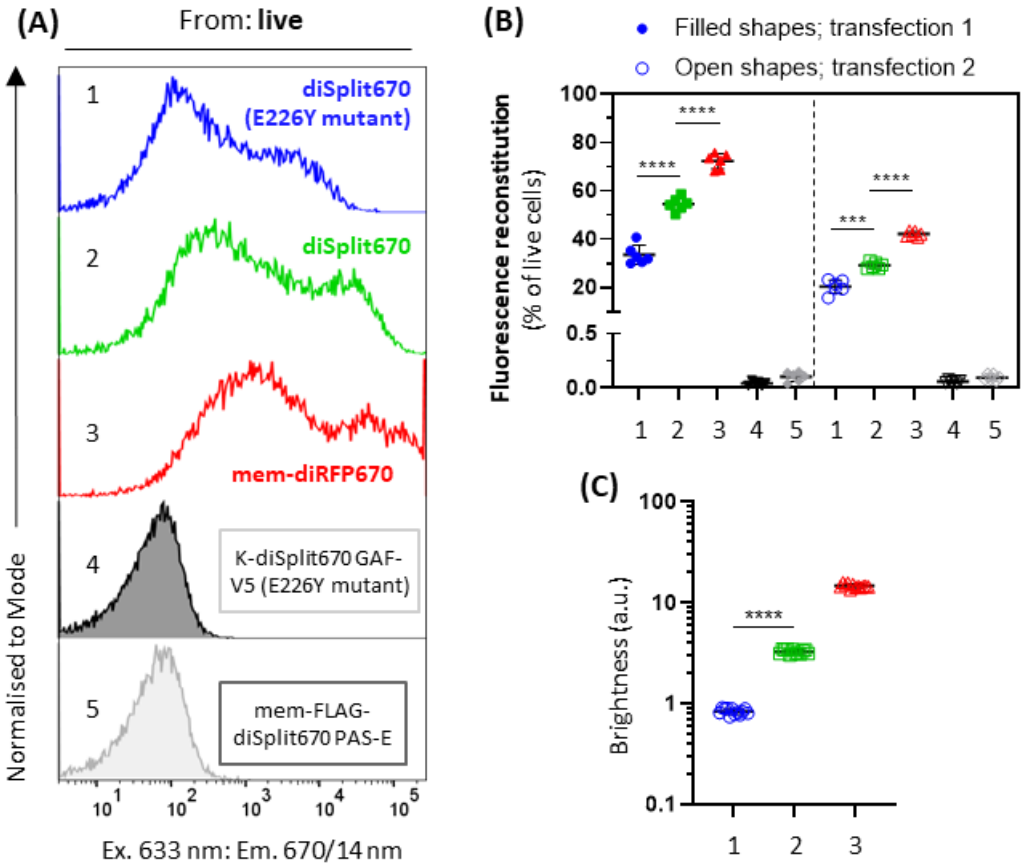

Figure 4.14 **Rational mutagenesis failed to increase the brightness of diSplit670**. HEK293T cells were transfected with the indicated constructs for 48 h before flow cytometric analysis. **(A)** Representative fluorescence histograms of transfected cells. **(B)** Fluorescence reconstitution of transfected cells are displayed as the two independent transfections. diSplit670 containing K-diSplit670 GAF-V5 E226Y mutant (blue) or non-mutated K-diSplit670 GAF-V5 (green), parental mem-diRFP670 (red) or K-diSplit670 GAF-V5 (E226Y) mutant only (black) and mem-FLAG-diSplit670 PAS-E only (grey). **(C)** Transfection normalised NIR FP gMFI for the NIR FP$^+$ cells from (B). In (B) and (C) the conditions are numbered as depicted on the left-hand side of the histogram in (A). n=2 independent transfection with 5 technical repeats per transfection. Error bars are mean ± SD. Unpaired Welch's t-test (B and C).

4.2.4 *In vitro* characterisation of diSplit670.

The resilience of FPs to routine fixatives, such as formaldehyde, is an important characteristic for downstream assays such as histology and intracellular flow cytometry. The sensitivity and longitudinal stability of diSplit670 to formaldehyde fixation were assessed by flow cytometry. First, sensitivity to fixation was assessed in transiently transfected HEK293T cells with paired data samples acquired before and immediately after fixation (Figure 4.15A). Fluorescence of both diSplit670 and parental mem-diRFP670 were minimally impacted (-6.9% vs -6.6%, respectively), and is similar to the loss of fluorescence of co-transfected mem-EGFP (Figure 4.15A, right). Once fixed, the fluorescence intensity of diSplit670 showed minimal decline at 24 h post fixation (Figure 4.15B). For the *in vivo* split reporter system, the stability of diSplit670 to routine fixation means preservation of the cell type specific diSplit670 signal whilst enabling intra-cellular staining for other targets; a useful characteristic.

We are planning to use the combination of the parts of diSplit670 to study GC-derived B-cell differentiation into PCs, where expression of the *S1pr2* controlled part of the split reporter diSplit670 will cease whilst expression of the complementary part by *Prdm1* will initiate. This means that the intracellular stability of the reconstituted diSplit670 complex in living cells is an important consideration, as the half-life of the complex would determine for how long nascent GCmat PBs would be labelled diSplit670^{+}. To test this, transfected HEK293T cells were treated with cycloheximide (CHX) to inhibit protein synthesis or DMSO as a control (Figure 4.16A). This revealed that diSplit670 complex is relatively stable as after 8 h of CHX treatment the cells retained 79.0% fluorescence intensity compared to control (mean at 4 h was 97.7 % and was 79.0 % at 8 h). The choice as to which part of the split reporter should be placed under the control of the *S1pr2* vs the *Prdm1* promoter was to be guided by the stability of the separate

mem-FLAG-diSplit670 PAS-E and K-diSplit670 GAF-V5 domains. It was thought that the better configuration would be to have the one with the longer half-life to be expressed first, under the control of the GC B-cell specific *S1pr2* promoter, in the diSplit670 reporter system. When mem-FLAG-diSplit670 PAS-E was transfected alone, FLAG epitope tag fluorescence detection in cells treated with CHX for 8 h remained at 94.1% compared to control (Figure 4.16B).

Although the stability of K-diSplit670 GAF-V5 alone was not determined, the intracellular turnover of mem-FLAG-diSplit670 PAS-E part was determined and demonstrated retention of a high proportion of protein following 8 h CHX treatment, and so was selected to be placed under control of the *S1pr2* promoter.

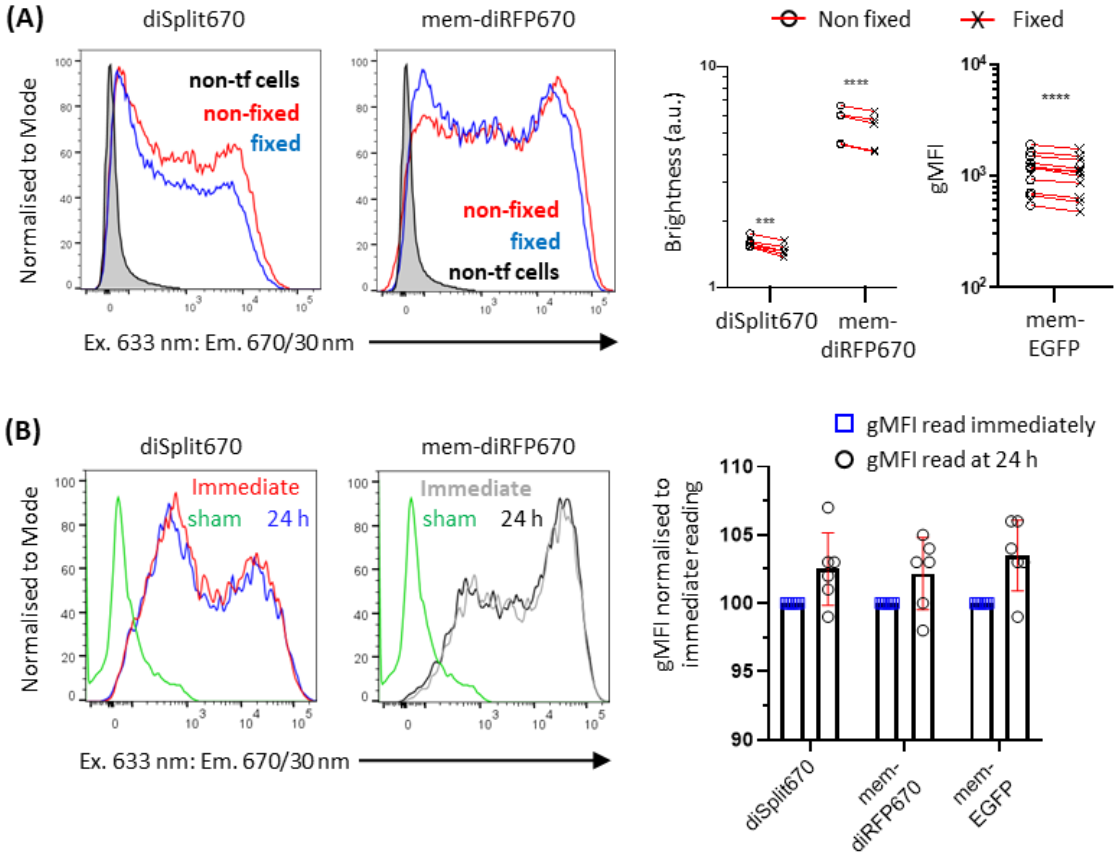

Figure 4.15 **Fixation by formaldehyde has minimal impact on the fluorescence intensity of diSplit670. (A)** Sensitivity to formaldehyde fixation. Paired fluorescence measurements of transiently transfected HEK293T cells determined by flow cytometry immediately before and after fixation. Fluorescence histogram overlays (left), brightness (middle), and geometric MFI (gMFI) for co-transfected mem-EGFP (right). Two-tailed paired t-test. Non-tf, non-transfected cells. **(B)** Fluorescence stability after formaldehyde fixation. HEK293T cells transfected with the indicated NIR FP or mem-EGFP (sham) were measured by flow cytometry either immediately or 24 h after fixation. Fluorescence histogram overlays (left), normalised gMFI where fluorescent signal acquired immediately is set to 100% (right). Two-tailed paired t-test indicated no significant decline in brightness for any FP.

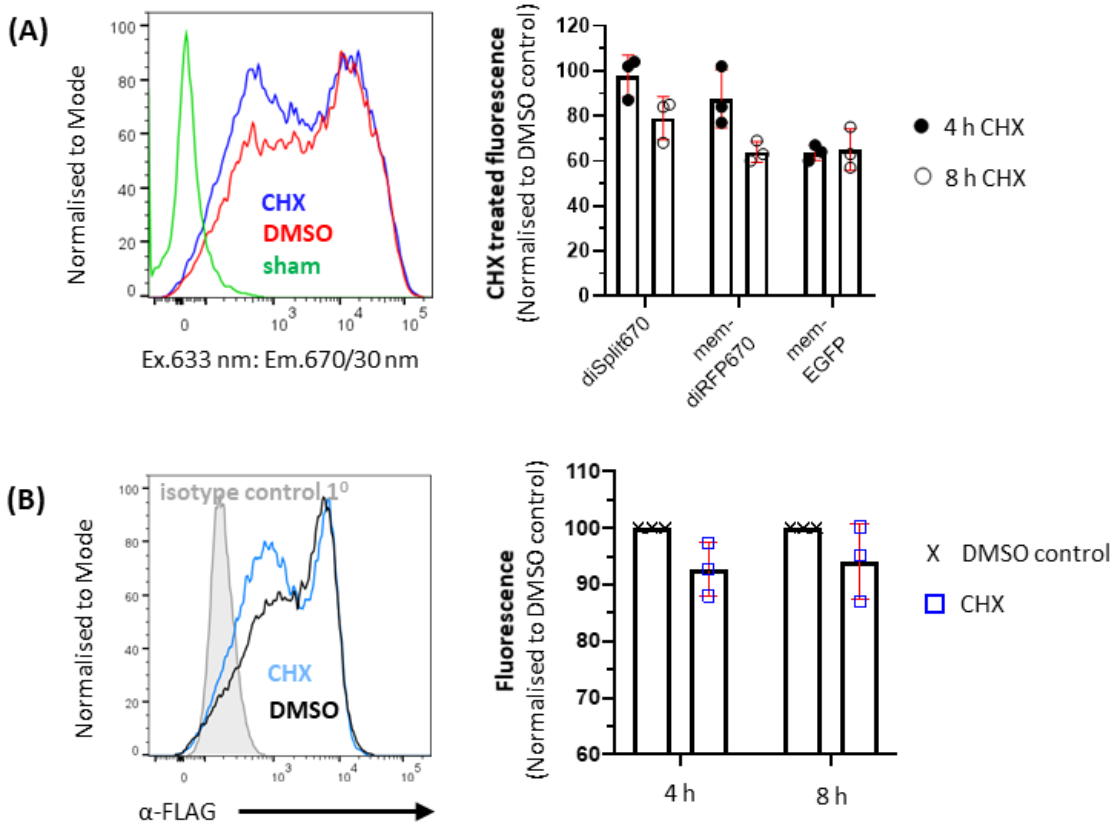

Figure 4.16 **diSplit670 complex has a comparable intracellular stability to parental mem-diRFP670.** **(A)** Intracellular stability of reconstituted diSplit670. Transiently transfected HEK293T were treated for either 4 h or 8 h with cycloheximide (CHX) at 20 µg/mL or DMSO control at 0.02% v/v. Flow cytometric overlay of diSplit670 expressing cells treated with CHX, blue, or DMSO control, red, or sham mem-EGFP expressing cells, green (left). Fluorescence of CHX treated samples normalised to DMSO treated controls at the indicated time (right). **(B)** Intracellular stability of mem-FLAG-diSplit670 PAS-E domain only. HEK293T transiently transfected with just the mem-FLAG-diSplit670 PAS-E construct was treated with CHX or DMSO as in (A). Flow cytometric overlay (left) with transfected cells stained with primary antibody isotype control, grey, fully stained transfected cells treated with CHX, blue, or DMSO control, black. Fluorescence of CHX treated samples normalised to DMSO treated controls (right). For each assay, n=3 independent transfections with 2 technical repeats per transfection. Error bars represent mean and SD. No significant differences between conditions at the same time-point or between the same condition at different time-points (unpaired t-tests with Welch's corrections).

The original diRFP670 not only possesses enhanced brightness in mammalian cells compared to miRFP670, but the reported $t_{1/2}$ of diRFP670 in mammalian cells is almost 2-fold greater than that of miRFP670 (Table 4.1 and Figure 4.1A-B). As we plan to analyse diSplit670 expression using immunofluorescence microscopy, photostability of the reconstituted diSplit670 is an important issue. The $t_{1/2}$ of the original iSplit713 is equivalent to the parental diRFP713 (Filonov and Verkhusha, 2013). We therefore compared the photostability of diSplit670 to that of parental diRFP670 by measuring photobleaching of HEK293T cells expressing either FP (Figure 4.17). Analysis of the fluorescence decay demonstrated that diSplit670 was between 17-19% more photostable than parental diRFP670 (Figure 4.17A-D), highlighted by significantly brighter fluorescence of diSplit670 at the $t_{1/2}$ of diRFP670 (Figure 4.17D). However, the precise $t_{1/2}$ of both diSplit670 and mem-diRFP670 varies slightly depending how it is calculated. Non-linear regression analysis revealed that a two-phase exponential decay model fit the data of both diSplit670 (R^2=0.9755) and mem-diRFP670 (R^2=0.9742) significantly better ($p<0.0001$) than a one-phase exponential decay model with an R^2=0.9321 for diSplit670 and R^2=0.9537 for diRFP670 (Figure 4.17B-C). Fluorescent proteins, including red fluorescent protein (RFP) derivatives and GFP, can display both mono- and multi-exponential fluorescence decay (Dean *et al.*, 2011; Bakker and Swain, 2019). Furthermore, photobleaching in RFP variants can be characterised by an initial rapid decay in fluorescence intensity within the first 5 ms (Dean *et al.*, 2011). The two-phase exponential decay models for diSplit670 and mem-diRFP670 calculated the "slow" half-life for diSplit670 $t_{1/2}$ (slow) as 357.1 s (95% CI; 350.5 to 364.0 s) and the $t_{1/2}$ (slow) for mem-diRFP670 as 299.1 s (95% CI; 293.3 to 305.1 s). However, when $t_{1/2}$ was calculated as the time when fluorescence intensity had decayed to 50% of initial value, this gave $t_{1/2}$ values of 405 s for diSplit670 and 345 s for mem-diRFP670 (Figure 4.17D). There was a low degree of variation observed for the fluorescence

decay of both NIR FPs, as the standard deviation was <5.0% of the mean fluorescence value at the $t_{1/2}$ for diSplit670 and diRFP670 and was still low at the final time-point, at <20.0% of the mean fluorescence values (represented graphically for diSplit670 in Figure 4.17E).

Both diSplit670 and mem-diRFP670 exhibit: (i) an initial rapid decrease between the initial and second intensity readings, which is consistent with rapid photobleaching observed in RFP derivatives (Dean *et al.*, 2011), and (ii) bi-exponential fluorescent decay, which is not uncommon (Diaspro *et al.*, 2006; Bakker and Swain, 2019). Factors which can contribute to multi-exponential fluorescence decay include molecular rotation (Taneja and Rutenberg, 2017), interactions between fluorophores in their excited states (Song *et al.*, 1995) and the intracellular microenvironments occupied by the fluorophore (Song *et al.*, 1997). The rapid initial fluorescence decay is not predicted to have a negative impact on the application of diSplit670 for imaging studies as it is followed by a much slower second-phase of decay. Moreover, the $t_{1/2}$ for mem-diRFP670 calculated from this photobleach assay is consistent with the reported value of 290 s (Shcherbakova and Verkhusha, 2013) and $t_{1/2}$ analysis demonstrated that diSplit670 was significantly more photostable than mem-diRFP670. Taken together, this fluorescence decay data suggests that diSplit670 is more photostability than parental FP and will be suitable for planned imaging studies in cells and tissues isolated from the proposed split iRFP reporter transgenic mouse.

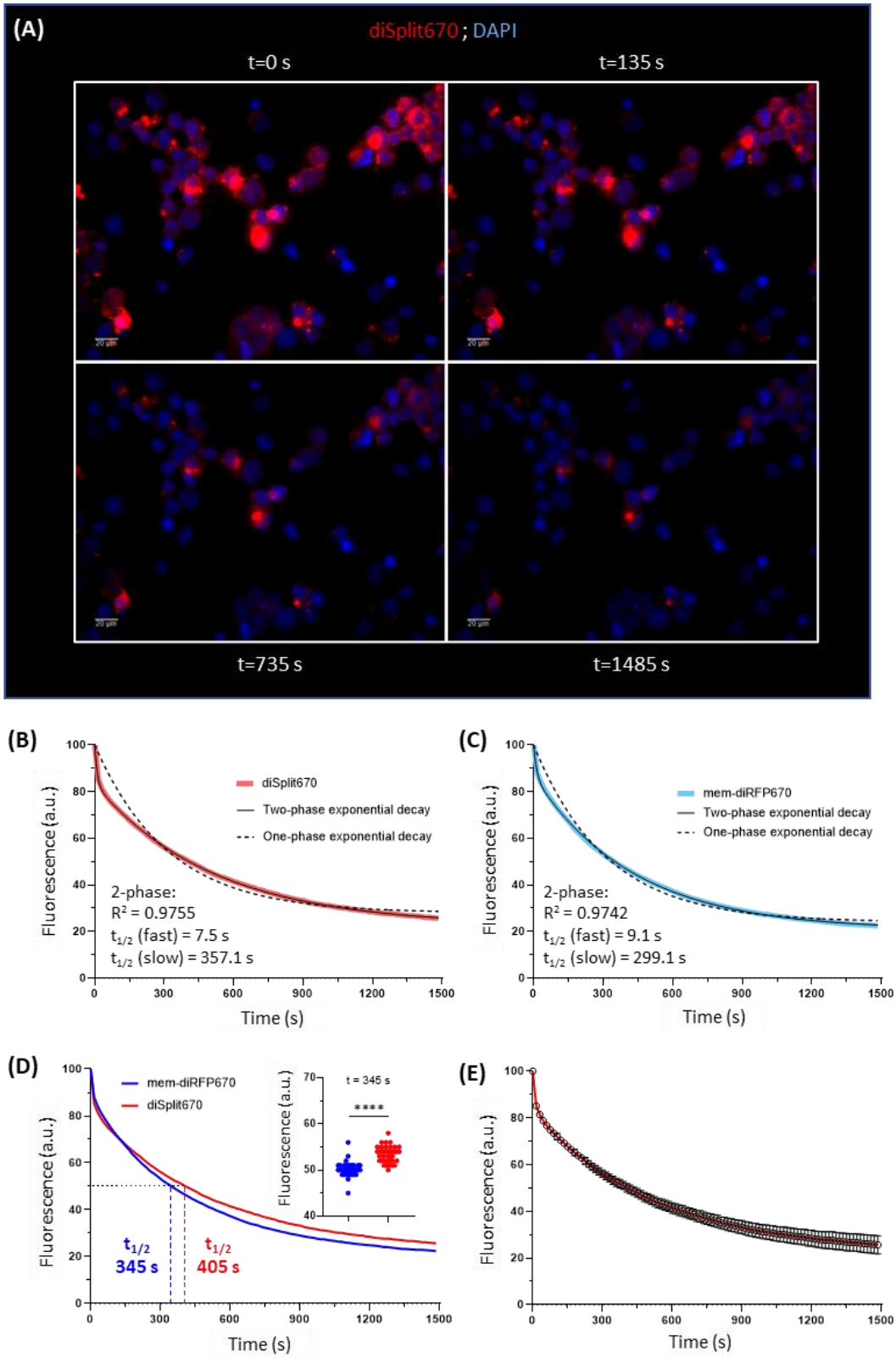

Figure 4.17 **diSplit670 shows an improved photostability profile compared to parental mem-diRFP670**. HEK293T cells were transiently co-transfected with mem-EGFP and either diSplit670 or mem-diRFP670 for 48 h. Formaldehyde fixed cells were DAPI counterstained and mounted in Prolong Diamond antifade mountant. Photo-bleach under continuous

illumination with image capture every 15 s. **(A)** diSplit670 transfected cells at cycle 1 (t=0 s), cycle 10 (t=135 s), cycle 50 (t=735 s), cycle 100 (t=1485 s). Scale bar, 20µm. **(B, C)** Non-linear regression analysis and calculated half-times ($t_{1/2}$) of fluorescence decay for diSplit670 **(B)** and mem-diRFP670 **(C)** by GraphPad Prism 9 where Y_0 was constrained to 100 in single- and two-phase exponential decay models. **(D)** Manual calculation of $t_{1/2}$ when diSplit670, red, and mem-diRFP670, blue, fluorescence intensity decayed to 50%. Inset shows fluorescence of both NIR FPs at the $t_{1/2}$ of mem-diRFP670, two-tailed Mann Whitney test. **(E)** Low amount of biological variation in fluorescent decay for diSplit670. Error bars are mean ± SD for each time-point.

The kinetics of protein folding and fluorescence emergence are important for understanding the temporal nature of GCmat PC labelling in the proposed transgenic split iRFP reporter strain. To test the kinetics of the appearance of fluorescence, a comparative time-course between diSplit670, mem-diRFP670 and mem-EGFP was performed to measure the emergence of fluorescence by flow cytometry during the first 24 h post transfection with the assumption that the plasmid transfection efficiency and transcription kinetics of the different proteins are equal (Figure 4.18A). The transcription kinetics are assumed to be equal as each FP sequence is under the control of the strong constitutive CMV promoter from the pcDNA3.1 mammalian expression plasmid. Emergence of fluorescence was detected 3-4 h earlier for HEK293T cells transfected with the single polypeptide FPs, mem-diRFP670 and mem-EGFP, than for cells co-transfected with the two plasmids which express the necessary parts of diSplit670 (Figure 4.18B). It is not clear whether this difference is due to differences in translation efficiency or slower protein folding and dimerization. A further factor that may lead to delayed detection of fluorescence may be the lower brightness of the fully folded diSplit670, which is indicated by the continued lower brightness 24 h after transfection (Figure 4.18B).

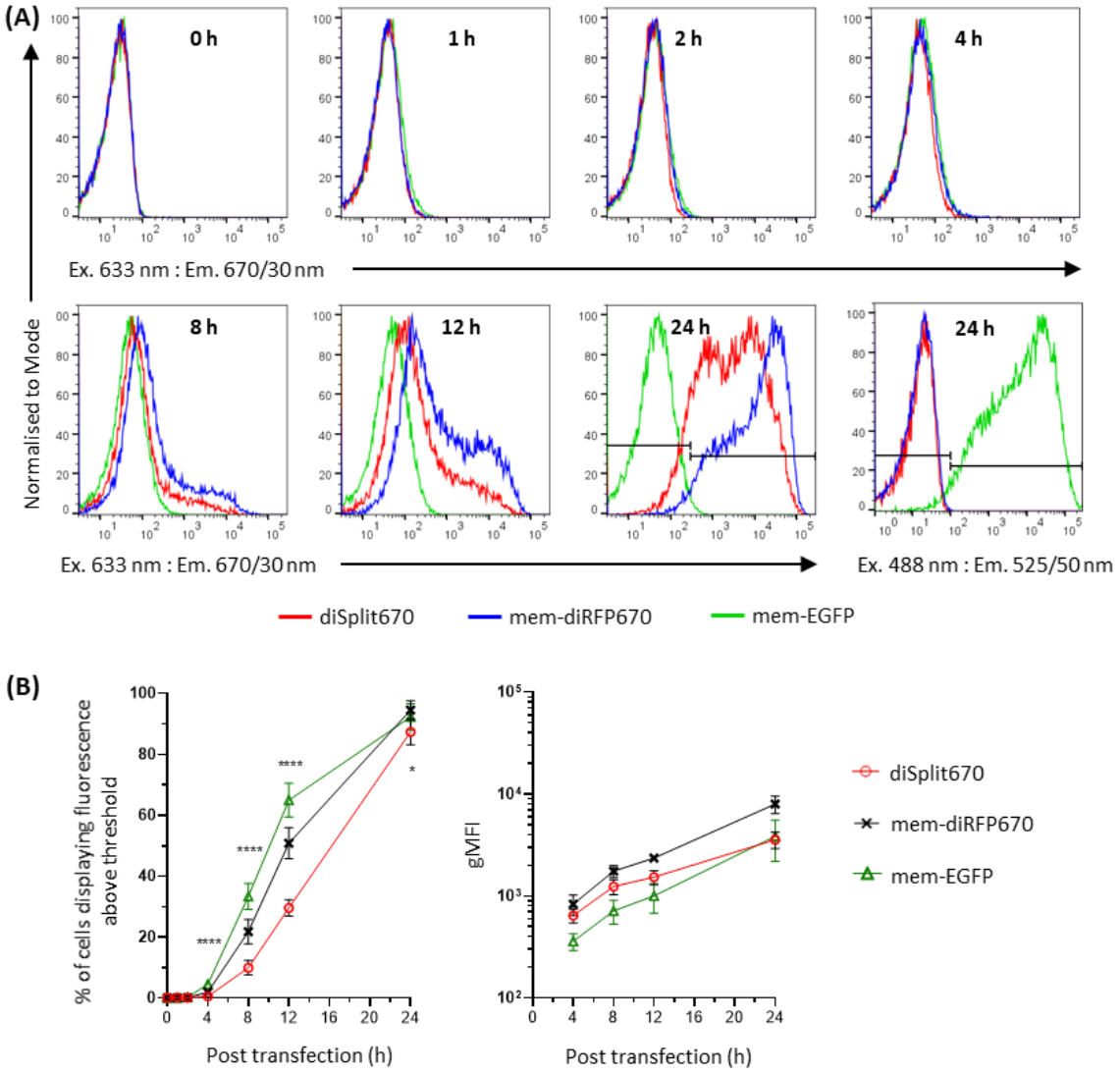

Figure 4.18 **Kinetic assessment of intrinsic protein folding and fluorescence reconstitution of diSplit670.** HEK293T cells were transfected with the indicated FP and assessed by flow cytometry during the first 24 h after transfection. **(A)** Flow cytometry histogram overlays for NIR FP fluorescence over the time-course, except bottom panel far right which is 24 h time-point in the EGFP detection channel. Gating thresholds for NIR and EGFP detection channels are shown in the histograms for the 24 h time-point. **(B)** Left, fluorescence reconstitution in all live cells. Right, fluorescence intensity of cells displaying fluorescence above threshold between 4-24 h (0-2 h not included as <0.5% of cells displayed fluorescence above threshold). Detectable fluorescence reconstitution for diSplit670 was compared to mem-diRFP670 and mem-EGFP (Browne-Forsythe and Welch's ANOVA). Error bars represent mean ± SD, n=3 independent transfections with 2 technical repeats per transfection.

4.2.5 Whole animal imaging confirmed the performance of diSplit670.

In vitro analyses had demonstrated that diSplit670 was functional and was similar in activity and stability to the parental non-split version mem-diRFP670. The next stage was to determine how it performed in an *in vivo* setting. As we planned to use diSplit670 for intravital imaging, it is important to test the brightness of diSplit670 when imaged in animals. The Spectrum In Vivo Imaging System (IVIS) has previously been used to assess the performance of iRFPs in whole animal imaging applications, including for iSplit713 (Filonov *et al.*, 2011; Filonov and Verkhusha, 2013; Shcherbakova and Verkhusha, 2013; Shcherbakova *et al.*, 2016). To compare the performance of diSplit670 to full-length mem-diRFP670 in IVIS imaging, BALB/c mice were injected subcutaneously with a high ($3.0x10^6$), intermediate ($1.0x10^6$) or low ($0.3x10^6$) number of HEK293T cells which had been transiently transfected with either diSplit670 and mem-EGFP, or mem-diRFP670 and mem-EGFP (the mem-EGFP was a control for transfection efficiency) (Figure 4.19A). diSplit670 produced a lower signal than the mem-diRFP670 at each cell "dose" (Figure 4.19A), but the magnitude of this reduction was in-line with the *in vitro* data on relative brightness determined by flow cytometry (Figure 4.11A), as diSplit670 was 28.1% ± 7.9% (mean ± SD) the brightness of mem-diRFP670 (Figure 4.19B).

IVIS data demonstrates that the excitation and emission radiation of diSplit670 can penetrate tissue, highlighting the potential for diSplit670 to be useful for intravital multiphoton applications.

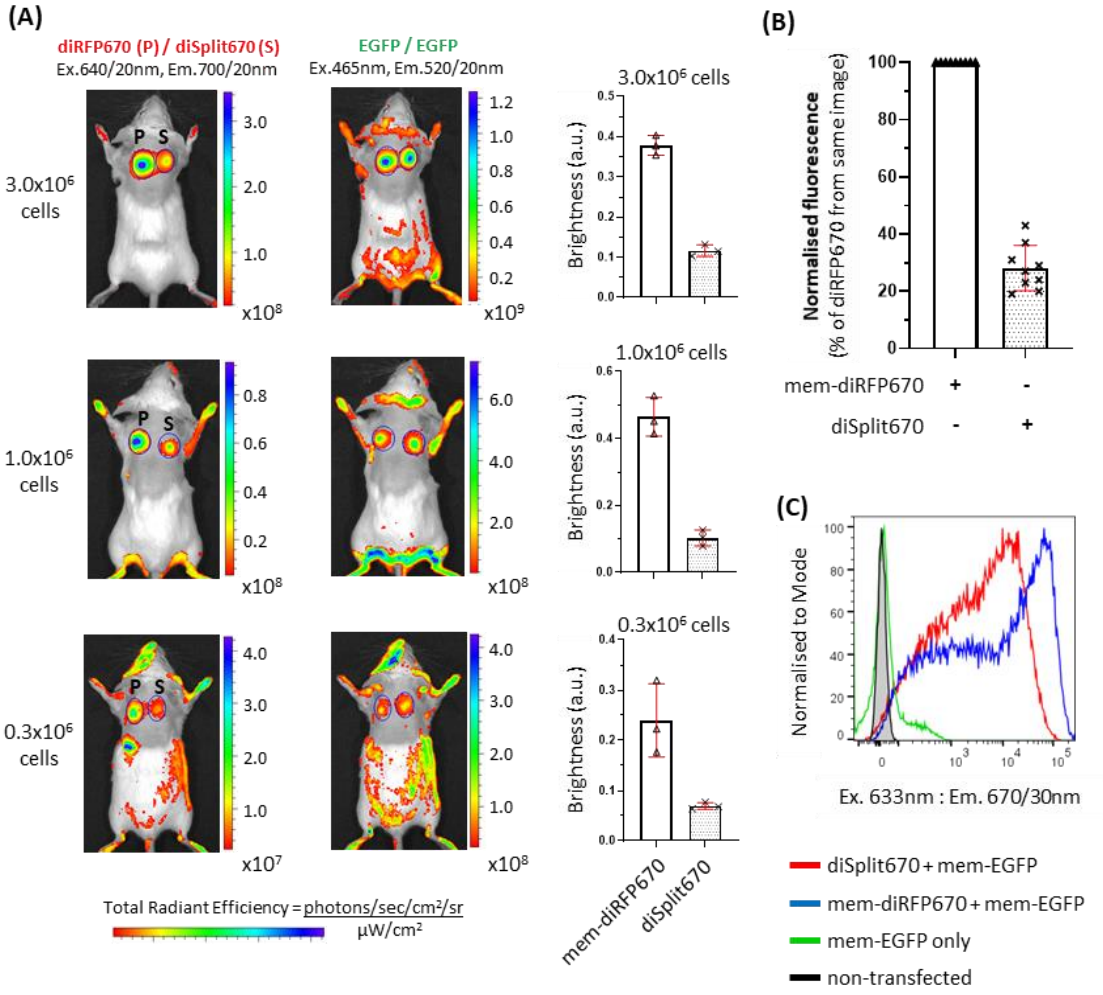

Figure 4.19 **Whole animal imaging of diSplit670. (A)** Imaging of diSplit670 using the Spectrum IVIS system. Transiently transfected HEK293T cells co-expressing mem-EGFP and either diSplit670 or mem-diRFP670 were injected s.c. into the same BALB/c cadaver for side-by-side comparison by Spectrum IVIS. mem-diRFP670+mem-EGFP co-transfected cells injected on the left (P) and diSplit670+mem-EGFP co-transfected cells on the right (S). Shown are background corrected NIR fluorescence (images, left column), EGFP fluorescence (images, middle column) and calculated brightness for each cell dose of the NIR FP (graphs, right column). **(B)** Overall brightness comparison of diSplit670 to parental mem-diRFP670 from all cell doses collated from (A). **(C)** Flow cytometric transfection efficiency and fluorescence intensity assessment of transfected HEK293T cells used for Spectrum IVIS analysis. n=2 independent transfections and acquisition sessions, total of three BALB/c mice per condition. Error bars represent mean with SD.

4.3 Results part B – gene targeting of diSplit670 to produce the HAPi670 (High-Affinity Plasma cell near infrared FP670) mouse.

4.3.1 Gene targeting strategy involving simplified targeting vectors, transient antibiotic enrichment with or without CRISPR/Cas9 enhancement.

The above *in vitro* assessments of diSplit670 had demonstrated correct plasma membrane localisation, functional FLAG and V5 epitope tags, similar intracellular stability and equivalent tolerance to formaldehyde fixation as parental diRFP670. Further, diSplit670 had retained ~28% the brightness of parental diRFP670 when measured in mammalian cells by flow cytometry or in whole animal imaging by IVIS. The next step was to generate two transgenic mouse lines each containing one part of the new diSplit670 *in vivo* reporter system which when bred together would allow the reporter to be reconstituted in just those cells where both parts were expressed. In B-cell lineages, *S1pr2* is GC B-cell specific (Green *et al.*, 2011) and its expression profile has been used to generate a transgenic mouse capable of labelling GC progeny (Shinnakasu *et al.*, 2016). *Prdm1* encodes Blimp1 and is critical for PC differentiation (Shapiro-Shelef *et al.*, 2003; Kallies *et al.*, 2004). The decision was taken to use gene targeting in mouse ESCs to make the two mouse lines by targeting one part (mem-FLAG-diSplit670 PAS-E) to the *S1pr2* locus and the second part (K-diSplit670 GAF-V5) to the *Prdm1* locus. As GCmat PCs are predicted to be the only population specifically identified as diSplit670^{+} in the split reporter transgenic, the model was designated the HAPi670 mouse (High-Affinity Plasma cell near infrared FP670).

The efficiency of gene targeting in mouse ESCs is generally low and quite variable meaning that a large number of clones have to be screened to identify those that have undergone the rare

desired homologous recombination event. Factors impacting on the efficiency include but are not limited to: length of HAs, isogenicity, locus being targeted, ESC line etc. At its simplest a Knock-Out targeting vector is made up of 5' and 3' HAs and a positive selection marker in between. The latter is often flanked by recombinase target sites to allow for later removal (Figure 4.20A). Knock-In vectors have all the elements of the Knock-Out vector but in addition also have a "cargo" which gets inserted at the desired locus upon homologous recombination (Figure 4.20B). For Knock-In projects where the cargo is a transgene, it is usually critical to remove the selectable marker cassette so that it does not interfere with expression of the incoming transgene.

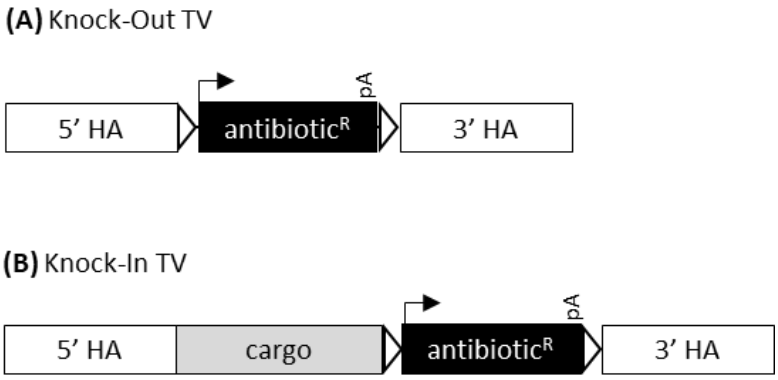

Figure 4.20 **Simplest types of gene targeting vectors**. Minimum requirements to generate a Knock-Out targeting vector **(A)** or Knock-In targeting vector **(B)**. TV, targeting vector; HA, homology arm; antibiotic^R, positive antibiotic resistance selection cassette; pA, polyadenylation sequence; black arrow, translation from initial methionine; triangles, recombinase target site; cargo, desired sequence.

Gene targeting is a relatively laborious and slow route for generating transgenic mice so anything that can simplify or speed up the process is very desirable. It has been known for some time that DSB in DNA at the site being targeted can dramatically enhance the efficiency of homologous recombination (Rouet, Smih and Jasin, 1994; Choulika *et al.*, 1995). Designer

nuclease systems such as meganucleases (Smith *et al.*, 2006), then zinc fingers (Miller *et al.*, 2007) and TALENs (Boch *et al.*, 2009; Moscou and Bogdanove, 2009; Christian *et al.*, 2010; Miller *et al.*, 2011) further demonstrated this. These approaches have since been superceded by CRISPR/Cas9 (Cong *et al.*, 2013; Mali *et al.*, 2013).

For this gene targeting project it was decided to use CRISPR/Cas9 enhanced gene targeting since this should give a much higher targeting efficiency and also mean that the homology lengths in the TVs could be reduced to simplify construction. In addition, we opted to perform selection in trans i.e., with the positive antibiotic selection cassette on a separate vector to the TV to avoid the need to perform a subsequent removal step of the selectable marker from the targeted ESC clones or after conversion to mice (Figure 4.21A). The gene targeting experiment would have two conditions: (i) TV + transient puromycin selection (TV + puro) and (ii) TV + transient puromycin selection + CRISPR/Cas9 enhancement (TV + Puro + CRISPR) (Figure 4.21B).

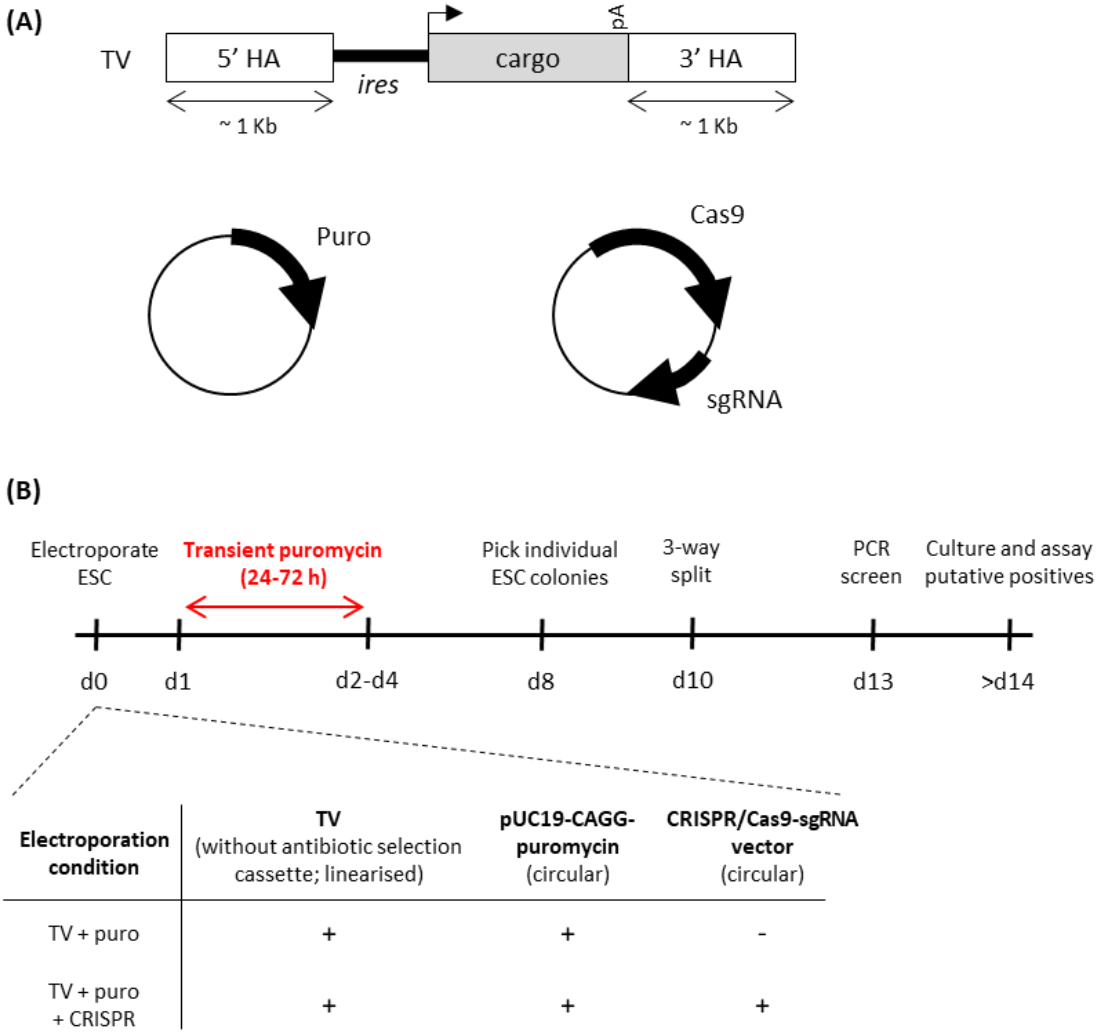

Electroporation condition	TV (without antibiotic selection cassette; linearised)	pUC19-CAGG-puromycin (circular)	CRISPR/Cas9-sgRNA vector (circular)
TV + puro	+	+	-
TV + puro + CRISPR	+	+	+

Figure 4.21 **Gene targeting strategy using targeting vectors with short homologies, transient antibiotic enrichment and with or without CRISPR/Cas9 enhancement. (A)** Targeting vector (TV) with short homology arms (HA) and lacking antibiotic resistance cassette. Separate plasmids which express either puromycin (Puro) or sgRNA and Cas9 which form the Cas9-sgRNA ribonucleoprotein complex. Black arrow depicts translation from initial methionine; pA, polyadenylation sequence; *ires*, internal ribosome entry site (thick black line). **(B)** Schematic of planned workflow using combinations of the plasmids shown in (A). Transient antibiotic selection to enrich for ESC that take up TV and selectable marker plasmid DNA ± a CRISPR/Cas9-sgRNA plasmid designed to induce DSB at, and recruit homology directed repair machinery to, the sgRNA target site. CRISPR/Cas9-sgRNA vector; pD1301-AD-CRISPR-Cas9-GFP-sgRNA.

The mouse ESC line selected for targeting, C57BL/6 JM8 A3.N1, has a repaired agouti allele to enable easy determination of the ESC contribution in chimaeras as judged by coat colour. This cell line has been reported to give rise to a very high germline transmission rate (Pettitt *et al.*, 2009). Prior to any gene targeting experiments, the first thing to do was to determine the sensitivity of the C57BL/6 JM8 A3.N1 cells to puromycin to determine the optimal concentration and selection period required to kill non-resistant ESCs. As expected, JM8 A3.N1 ESCs thrived without antibiotic present (top row, Figure 4.22). Detachment from the feeder layer and low levels of cell death were observed in ESC colonies after only 24 h of selection with 1.0 µg/mL puromycin and this progressed to significant cell death by 72 h (middle row, Figure 4.22). These effects were more pronounced as expected at 2.0 µg/mL puromycin (bottom row, Figure 4.22) and so it was decided to adopt a selection strategy of using 1.0 µg/mL puromycin for 72 h in the hope that this would result in a good enrichment for cells taking up the exogenous DNA constructs.

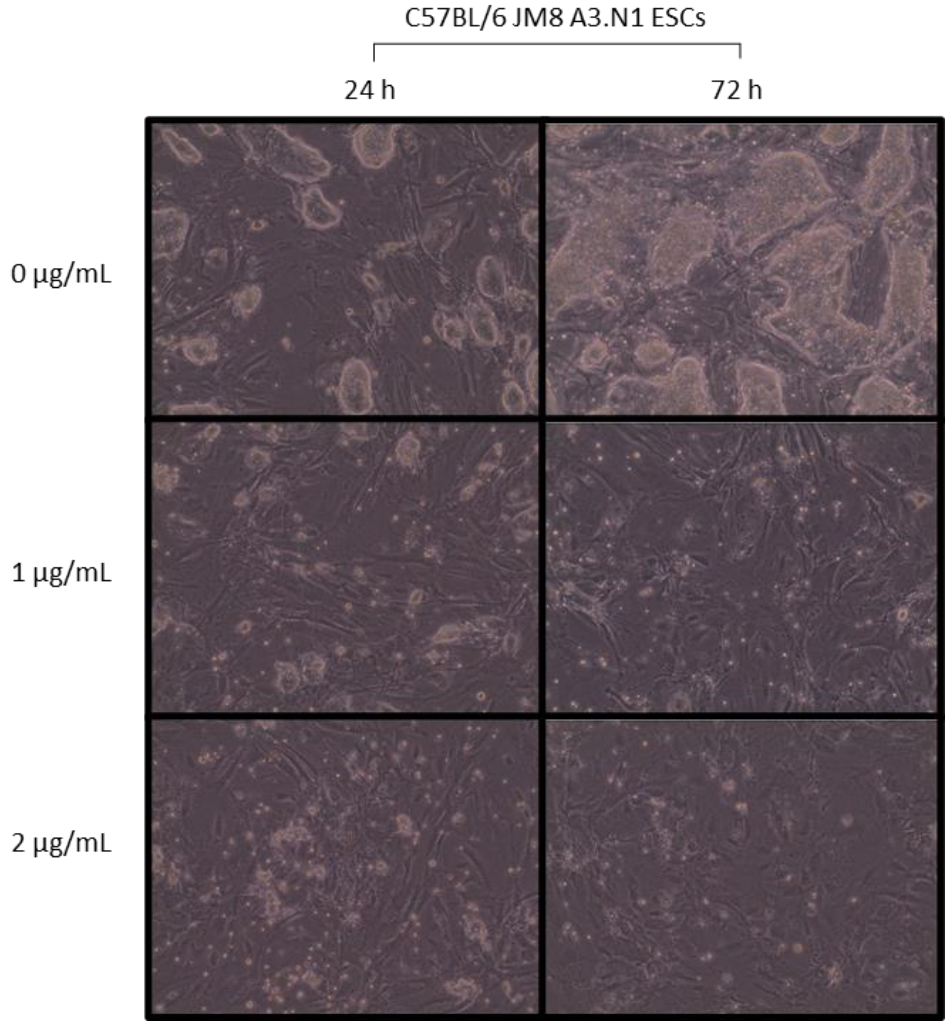

Figure 4.22 **Sensitivity of C57BL/6 JM8 A3.N1 ESC to puromycin selection.** The viability of JM8 A3.N1 ES cells growing on a feeder layer of MEFs after 24 h and 72 h under puromycin selection at the indicated concentrations. Images are at x100 magnification, captured on Leica DN IL LED microscope.

4.3.2 Pre-validation of sgRNAs for CRISPR/Cas9 enhanced targeting informed targeting vector construction.

There are several reported knock-in transgenics at the *Prdm1* locus (Kallies *et al.*, 2004; Mould *et al.*, 2015; Minnich *et al.*, 2016). Combined targeting site and phenotype analysis of these *Prdm1* locus knock-ins highlighted successful precedent for heterozygous insertion at *Prdm1* intron6-7 (Kallies *et al.*, 2004) and the potential for homozygous targeted insertion using a TV with homology sequences from the genomic region which includes the final coding exon (exon 8) (Minnich *et al.*, 2016). We therefore decided to pursue two targeting strategies: (i) to *Prdm1* intron6-7 and (ii) to the 3' UTR of *Prdm1* exon 8. There are no existing knock-in transgenics to the 3' UTR of *Prdm1* exon 8, however, this targeting strategy was hypothesised to retain functional Blimp1 protein and after germline transmission could mean that the targeted allele be maintained as homozygous stock. Similar review of transgenic mice with targeted knock-ins at the *S1pr2* locus revealed that the lack of functional S1PR2 protein, in most cases, led to neurological impairments and seizures, and in all cases, to abnormal immune responses (MacLennan *et al.*, 2001; Kono *et al.*, 2004; Du *et al.*, 2010; Moriyama *et al.*, 2014). We hypothesised that targeted insertion to the 3' UTR of the only coding exon for *S1pr2* (exon 2) could retain functional S1PR2 and we therefore developed an appropriate targeting strategy to achieve this. Although advantageous for leaving endogenous protein coding regions intact, targeted insertions into UTRs must be treated with caution as microRNA mediated gene regulation, typically mRNA destabilisation and translational repression, could be disrupted (O'Brien *et al.*, 2018). Analysis using miRDP (an online database where functional microRNA targets can be searched (Chen and Wang, 2020)) revealed there are >80 microRNA binding sites predicted with high confidence for the 3' UTR of *Prdm1* exon 8 and 12 microRNA sites for the 3' UTR of *S1pr2* exon 2. Therefore, downstream germline transmitted targeted alleles

must be subject to thorough phenotypic characterisation to ensure that the 3' UTR targeted transgenic alleles could be maintained homozygous.

For CRISPR/Cas9 enhanced targeting, appropriate sequences from *Prdm1* intron6-7 and the 3'UTR regions of both *S1pr2* exon 2 and *Prdm1* exon 8 were used to look for potential sgRNA sites. Multiple online algorithms (see Section 2.8) were used to select consistently high scoring sgRNAs for each of the three target regions. Off-target analysis by Cas-OFFinder (Bae, Park and Kim, 2014) confirmed suitability of the candidate sgRNA sequences taken forward for validation (Table 4.3). To pre-validate the sgRNA sequences, they were cloned into pD1301-AD-CRISPR-Cas9-GFP-sgRNA (ATUM), which expresses Cas9 and GFP from a bicistronic mRNA, to test whether they could correctly induce Cas9 mediated DSB in the mouse fibroblast cell line NIH-3T3. Transiently transfected NIH-3T3 cells were enriched for GFP-expressing (and therefore Cas9-expressing) cells by bulk FACS, ready for preparation of gDNA for assessment by the T7E1 assay (Figure 4.23A).

Target locus	sgRNA #	sgRNA sequence
S1pr2 exon 2 3'UTR	1	GAGAGGCCCTAAAAAGGAGG
	2	CTAGAATGTCAATACGCACA
	3	TAAGGGTCTAGGGTGACCGC
Prdm1 intron6-7	1	CTGTGGGCAGAAACCCGCGG
	2	GCAAACCAGCACGGGTCTGT
	3	GACCCGTGCTGGTTTGCCCT
Prdm1 exon 8 3'UTR	4	GCTCAACACTCTCATGTAAG
	5	CAAGCACCAAAGTCATAGCG

Table 4.3 **CRISPR/Cas9-sgRNA sequences selected for *in vitro* assessment of Cas9 targeting efficiency in mouse cells**. The most efficient sgRNA sequence for targeting CRISPR/Cas9 cutting at each genomic target site is highlighted in red text. Cutting efficiency determined by T7E1 assay in NIH-3T3 cells (Figure 4.23). The most efficient sgRNA sequences were taken forward for subsequent experiments.

The gDNA from the GFP^+ sorted NIH-3T3 cells revealed that *S1pr2* sgRNA 2 and sgRNA 3 were not suitable, as sgRNA 2 displayed multiple cleavage products where only two products were expected, and sgRNA 3 did not induce any Cas9 mediated activity (Figure 4.23C-D). However, *S1pr2* sgRNA 1 did display the expected T7E1 cleavage pattern confirming that sgRNA 1 could correctly target the Cas9/sgRNA 1 ribonucleoprotein complex (Figure 4.23B). All three sgRNAs for *Prdm1* intron6-7 induced site-specific activity, but *Prdm1* intron6-7 sgRNA 3 displayed a modest increase in efficiency over the other two (Figure 4.23E). For *Prdm1* exon 8 3'UTR, sgRNA 5 (17.2%) was twice as efficient as sgRNA 4 (8.6%) (Figure 4.23F-G).

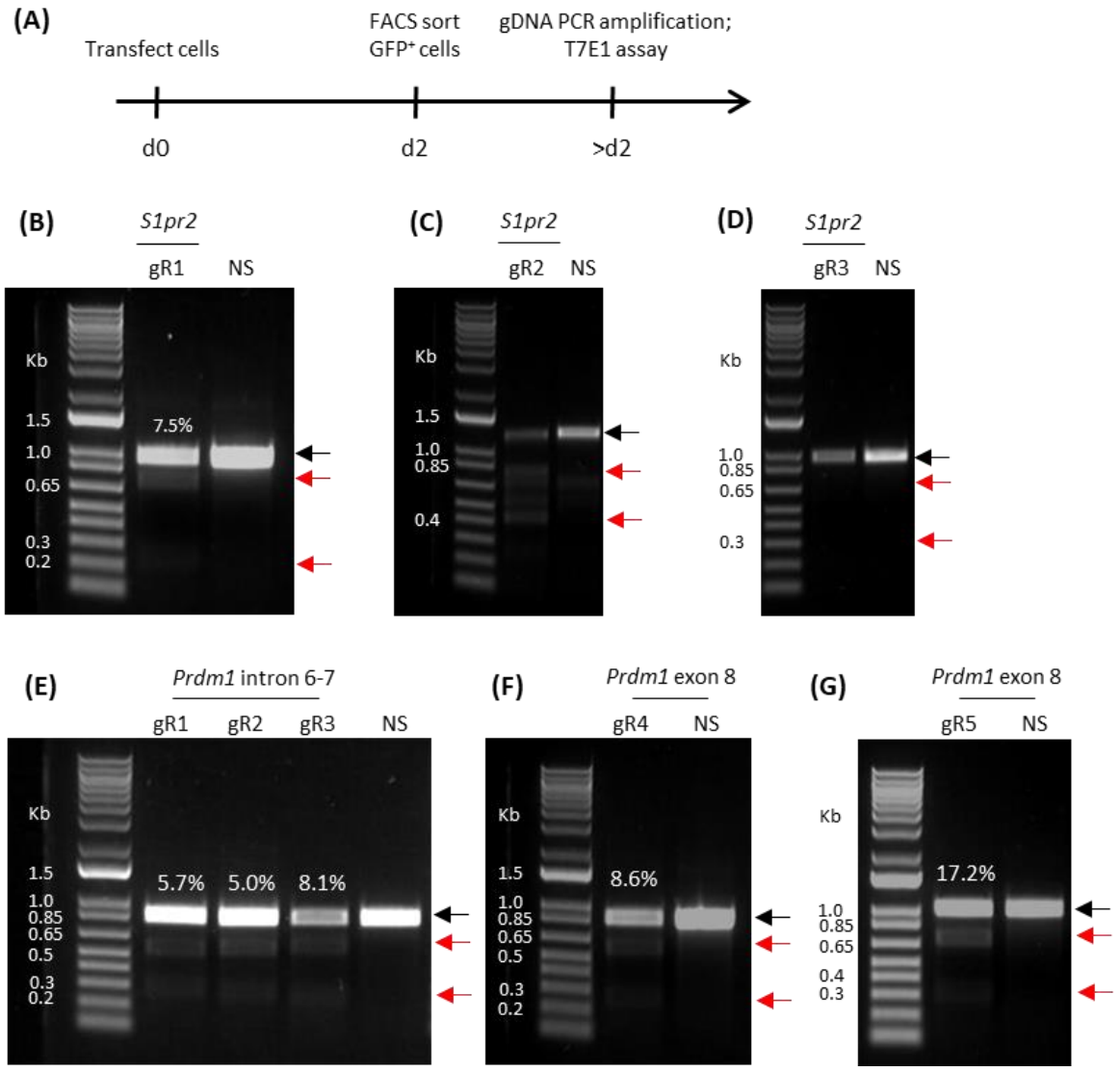

Figure 4.23 **Preliminary assessment of *S1pr2*- or *Prdm1*-specific sgRNAs in NIH-3T3 cells. (A)** Experiment schematic. NIH-3T3 cells transfected with pD1301-AD-CRISPR-Cas9-GFP-sgRNA plasmid containing CMV-Cas9-2A-GFP and relevant sgRNA. **(B-D)** T7E1 assay performed from gDNA of bulk FACS sorted GFP$^+$ NIH-3T3 specific to regions containing sgRNA targets sites for *S1pr2* exon 2 3'UTR sgRNA 1 **(B)**, sgRNA 2 **(C)** and sgRNA 3 **(D)**. T7E1 assay for *Prdm1* intron6-7 sgRNAs 1-3 **(E)** and *Prdm1* exon 8 3' UTR sgRNA 4 **(F)** and sgRNA 5 **(G)**. Black arrows indicate the size of PCR amplicon without T7E1 cleavage. Red arrows indicate expected sizes of PCR amplicon cleavage products generated by T7E1 cleavage. All three sets of cleavage products for sgRNAs to Prdm1 intron6-7 were expected to be ~540 bp and 260 bp and so are represented by a single pair of red arrows (E). Semi-quantitative assessment of sgRNA/Cas9 activity shown as percentage above lane (calculated as described in Section 2.10). NIH-3T3 gDNA prepared from cells transfected with pD1301-AD-CRISPR-Cas9-GFP-sgRNA which contained a non-specific (NS) sgRNA for human *Gusb* was amplified using the *S1pr2* or *Prdm1* sgRNA specific primers and used as a negative control for the assay.

Three targeting vectors, one for each of *S1pr2* exon 2 3'UTR, *Prdm1* intron6-7 and *Prdm1* exon 8 3'UTR, were designed with short 5' and 3' HAs (~1 Kb) that flanked the sgRNA site. It was important to use HAs that did not contain the sequence recognized by the relevant sgRNA so that after targeting the modified locus would not be a substrate for further Cas9 activity (Figure 4.24). This markedly constrained the design of the targeting vectors for *S1pr2* and *Prdm1* exon 8 3'UTR. Whereas, for *Prdm1* intron6-7 the three sgRNA sequences and their PAM sites overlapped within a 45 bp region of the 271 bp intron, which meant that HAs could be designed for a replacement targeting vector which would enable use of any of the three sgRNAs (Figure 4.24). TV construction can use IRES or 2A peptides to place the expression of the inserted DNA under the control of endogenous promoter elements. Although 2A peptides result in 1:1 stoichiometric expression of multiple genes from the same mRNA, their self-cleavage leaves a "scar" of at least 17 amino acids at the C-terminus of the upstream translated peptide and a single proline residue at the N-terminus of the downstream peptide. Although it has been reported that expression of the sequence downstream of the IRES is variable and can be lower than the upstream sequence (Ibrahimi *et al.*, 2009), IRES are "scarless" and enable co-expression of two proteins from one mRNA transcript by providing an additional binding site for the ribosome independent of the 5' cap. Efficient fluorescence reconstitution of diSplit670 relies on the high-affinity interaction between the E coil located on the C-terminus of mem-FLAG-diSplit670PAS-E and the K-coil at the N-terminus of K-diSplit670GAF-V5 (Figure 4.7A-B). The "scar" left by 2A peptide self-cleavage could have disrupted this critical interaction, and so IRES were selected for TV construction. With additional time and resource, variants of mem-FLAG-diSplit670PAS-E and K-diSplit670GAF-V5 with sequences which mimicked 2A peptide self-cleavage could have been generated and tested *in vitro* to assess whether the 2A peptide "scar" disrupted fluorescence reconstitution.

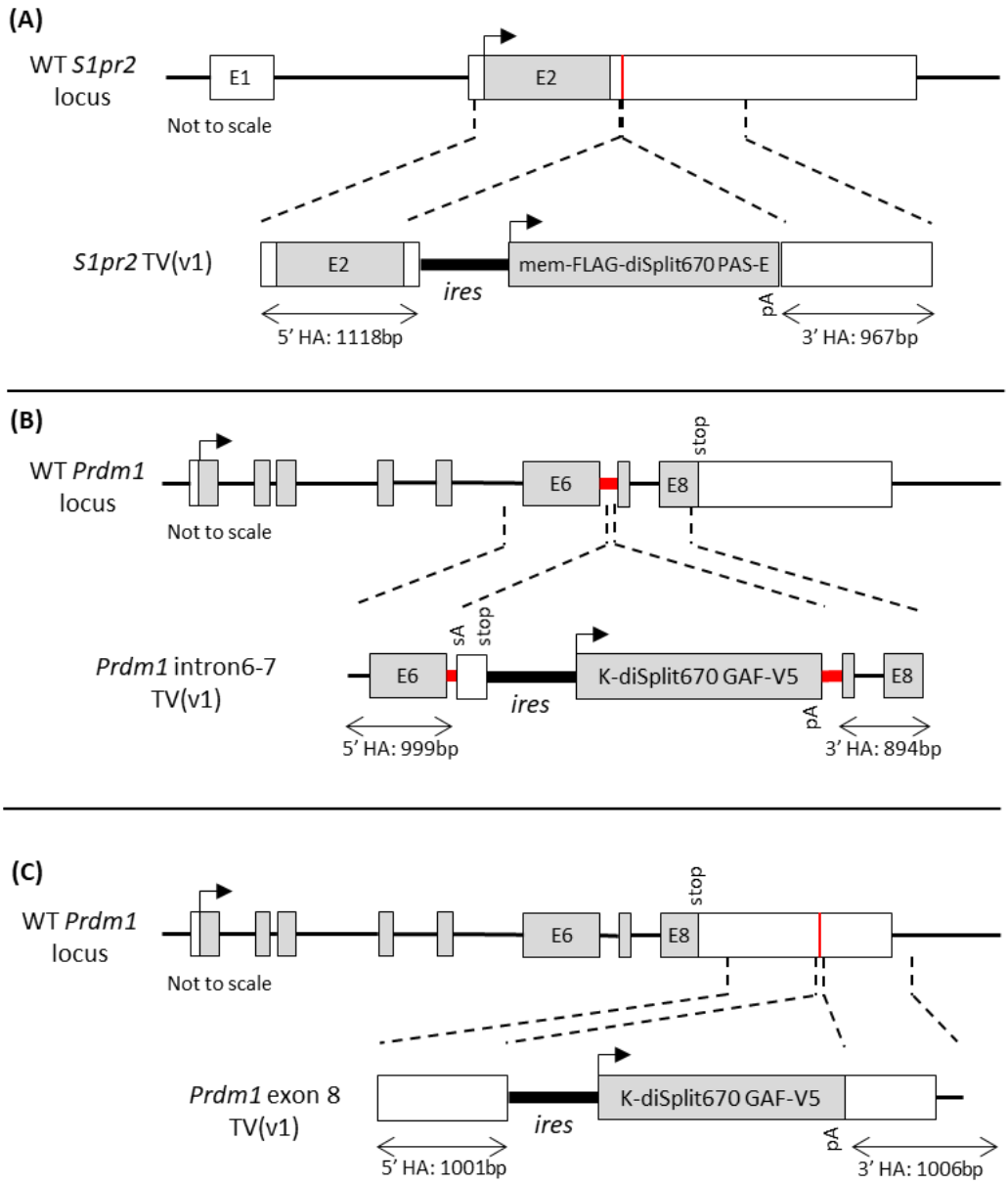

Figure 4.24 **Initial design of *S1pr2* and *Prdm1* targeting vectors with short homology arms and without positive antibiotic selection cassette.** Introns are thin black lines and exons are boxes (open for untranslated regions (UTRs), grey shaded boxes for protein coding regions). Black arrow depicts translation from initial methionine and stop indicates STOP codon. Targeted insertion points/regions are shown in red. Dashed lines represent homology sequences. **(A)** *S1pr2* exon 2 3'UTR targeting. Top, wild-type (WT) *S1pr2* locus. Bottom, initial design of *S1pr2* exon 2 3'UTR targeting vector with short 5' and 3' homology arms (HA), internal ribosome entry site (*ires*, thick black line), bovine growth hormone polyadenylation site (pA), cDNA for mem-FLAG-diSplit670 PAS-E domain. **(B)** *Prdm1* intron6-7 targeting. Top, wild-type (WT) *Prdm1* locus (transcript *Prdm1*-201 ENSMUST00000039174.10). Bottom, targeting vector. Adenoviral major late transcript splice acceptor (sA), cDNA for K-diSplit670 GAF-V5 domain. **(C)** *Prdm1* exon 8 3' UTR targeting. Top, WT *Prdm1* locus as in (B). Bottom, targeting vector.

4.3.3 Adjusted experimental plan for CRISPR/Cas9 enhanced ESC targeting; transient antibiotic selection from bicistronic Cas9/puromycin vector.

Concurrent with sgRNA cutting efficiency evaluation, preliminary experiments to ensure that the pD1301-AD-CRISPR-Cas9-GFP-sgRNA plasmid expressed GFP and Cas9 in mouse JM8 A3.N1 ESCs were undertaken to ensure the activity of CRISPR/Cas9 during gene targeting experiments. Unexpectedly, qualitative analysis of GFP expression by epifluorescence microscopy 30 h after transfection of JM8 A3.N1 ESCs by lipofection demonstrated minimal GFP fluorescence when compared to pmaxGFP transfection control (representative results for lipofectamine 2000 and 3000 are shown in Figure 4.25). The transfection used 1000 ng of each plasmid, which meant that the pmaxGFP plasmid was present at 2.3-fold higher molar ratio (415 fmol of the 3900 bp pmaxGFP control and 179 fmol of 9042 bp pD1301-AD-CRISPR-Cas9-GFP-sgRNA plasmid). Despite this, the lack of GFP expression in the pD1301-AD-CRISPR-Cas9-GFP-sgRNA transfected ESCs was disproportionate (Figure 4.25). This can be explained by reports of transient CMV expression subject to higher degrees of transgene silencing in mouse ESCs when compared to phosphoglycerate kinase (PGK) and human elongation factor-1alpha (EF-1α) promoters (Wang *et al.*, 2008). Similar results had been reported in human ESCs with CMV driven transgenes (J *et al.*, 2009) and that CMV had performed poorly in a comparative studied which tested undifferentiated ESCs of mouse, monkey, and human origin (Kim *et al.*, 2007).

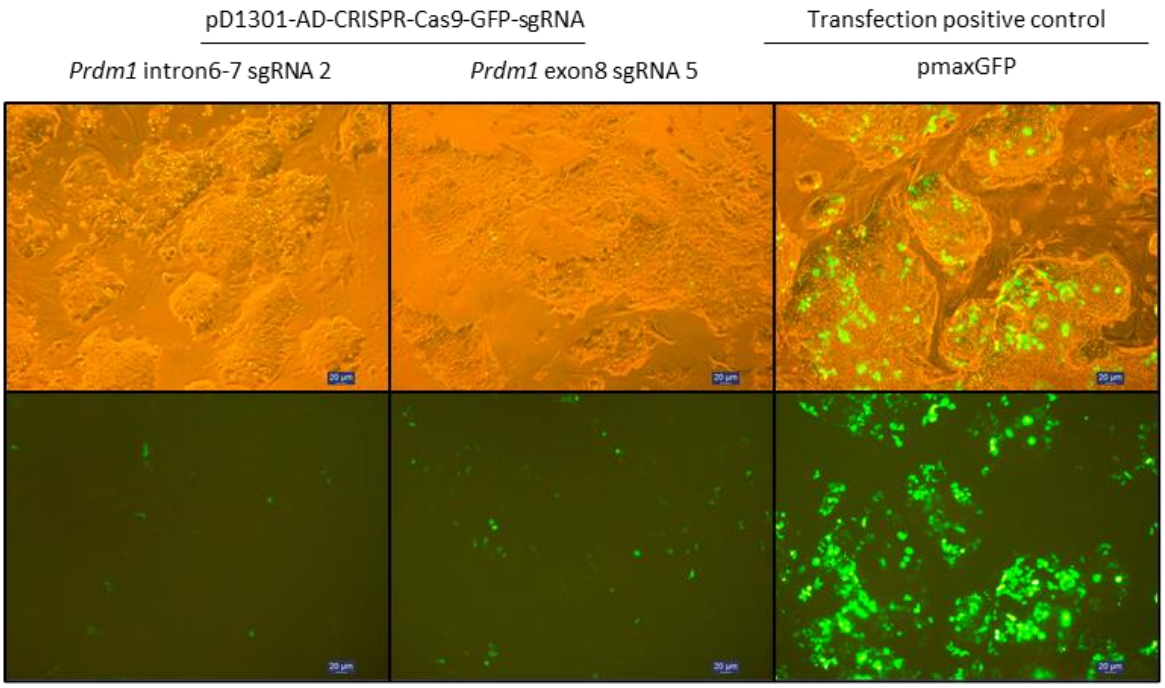

Figure 4.25 **pD1301-AD-CRISPR-Cas9-GFP-sgRNA does not express efficiently in JM8 A3.N1 ESCs.** JM8 A3.N1 ESCs on gelatin-coated plates, were transiently transfected by lipofection (lipofectamine 2000) and qualitative analysis of GFP expression by epifluorescence microscopy made after 30 h. Scale bar, 20 µm.

Therefore, a different CRISPR/Cas9-sgRNA plasmid, called all-in-one CRISPR/Cas9(Puro) was used. As well as encoding Cas9 protein and sgRNA-scaffold, it also included a puromycin selection cassette which would provide enrichment for transfected ESCs which expressed this plasmid when ESCs were subject to transient puromycin selective pressure. With consolidation of the puromycin selection cassette onto the CRISPR vector, the experimental design now only included two plasmids for co-transfection to assess the level of CRISPR/Cas9 enhanced targeting (Figure 4.26).

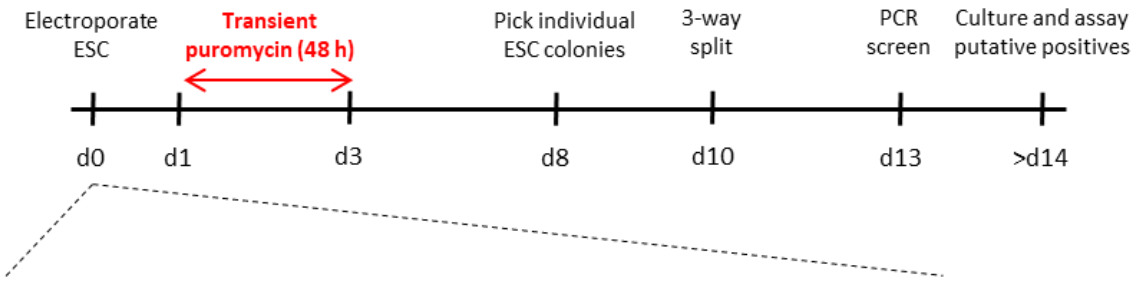

Electroporation condition	TV (without antibiotic selection cassette; linearised)	all-in-one CRISPR/Cas9(Puro) (circular)	Transient puromycin (48 h)
TV	+	-	X
TV + Puro + CRISPR	+	+	✓

Figure 4.26 **Adjusted experimental plan for gene targeting with and without CRISPR/Cas9 enhancement.** Schematic of planned workflow. TV, targeting vector; Puro, puromycin.

4.3.4 Genome editing activity of pre-validated sgRNA sequences in mouse JM8 A3.N1 ESCs.

Before undertaking the gene targeting experiments we wanted to ensure that the sgRNA sequences, that were pre-validated in NIH-3T3 cells (Figure 4.23, and highlighted in red in Table 4.3), demonstrated cutting in mouse JM8 A3.N1 ESCs when expressed by the all-in-one CRISPR/Cas9(Puro) plasmid. To do this we used a 7-day puromycin selection regimen to generate puromycin resistant ESC clones that had integrated, and were stably expressing, the all-in-one CRISPR/Cas9(Puro) plasmid (Figure 4.27A). Stable selection removes the variability of DNA transfection. Puromycin resistant ESCs should also constitutively express the Cas9 and sgRNA, and therefore could be used to test the efficiency of the pre-validated sgRNAs in ESCs. Efficacy was to be assessed by two measures: (i) T7E1 assay from individual puromycin resistant ESC colonies for sgRNA/Cas9 activity at genomic locus, and (ii) α-Cas9 western blot from expanded individual puromycin resistant ESC colonies. JM8 A3.N1 ESCs were electroporated with either: (i) all-in-one CRISPR/Cas9(Puro) plasmid containing the pre-validated *S1pr2*- or *Prdm1*-specific sgRNAs, (ii) pUC19-CAGG-Puro (positive selection control), or (iii) PBS only (negative selection control) and subjected to puromycin selection at several concentrations (see Section 2.13). Individual puromycin resistant ESC colonies were picked after 7-days and expanded for further characterisation (Figure 4.27A). In total, seven defined ESC colonies survived puromycin selection: two ESC colonies for each of the *Prdm1* sgRNAs and three colonies for the *S1pr2* sgRNA (Table 4.4). Yield of only seven puromycin resistant colonies from the three electroporations using all-in-one CRISPR/Cas9(Puro) was unexpected and low when compared to the positive selection control (Table 4.4).

Condition	Electroporated with (µg DNA)	Puromycin concentration (µg/mL)	ESC colonies (#)
S1pr2 exon 2 3' UTR targeting	all-in-one CRISPR/Cas9(Puro) (10 µg)	1.0	3
Prdm1 intron6-7 targeting	all-in-one CRISPR/Cas9(Puro) (10 µg)	1.0	2
Prdm1 exon 8 3'UTR targeting	all-in-one CRISPR/Cas9(Puro) (10 µg)	1.0 1.5	1 1
Selection positive control	pUC19-CAGG-Puro (10 µg)	1.75	140
Selection negative control	PBS only (0 µg)	1.75	0

Table 4.4 **Validation of sgRNAs in JM8 A3.N1 ESCs**. Numbers of clearly defined ESC colonies present after electroporation and 7-day puromycin selection at the indicated concentration.

A negative readout in the T7E1 assay is likely due to (i) an inefficient sgRNA unable to direct Cas9 to gDNA site, (ii) poor expression of either or both sgRNA or Cas9 from the vector, or (iii) insufficient sensitivity of T7E1 assay. An unlikely further explanation for a negative readout could be that homozygous indels could have been generated at the repaired loci that had been cut by CRISPR/Cas9. To control for the latter (unlikely) scenario, an additional T7E1 assay was performed with PCR amplicon prepared from gDNA of the ESC colony of interest (i.e., sgRNA of interest) mixed at a 3:1 mass ratio with PCR amplicon prepared from gDNA of an ESC colony targeted with a different sgRNA, this colony would have a WT locus of interest and enable mismatch annealing to be detected by the T7 endonuclease (Figure 4.27B).

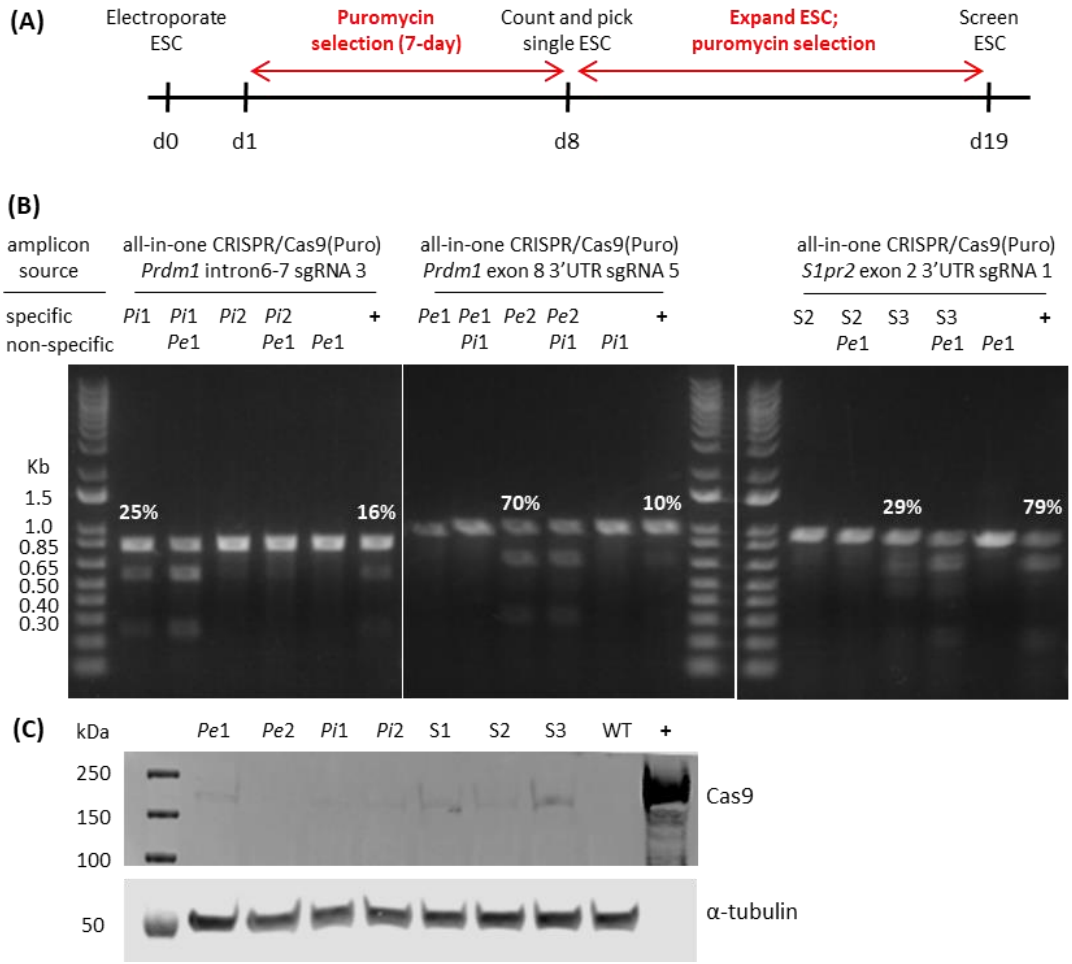

Figure 4.27 **Assessment of pre-validated *S1pr2*- or *Prdm1*-specific CRISPR/Cas9-sgRNA activity in C57BL/6 JM8 A3.N1 ESCs at the single cell level. (A)** Experiment schematic. **(B)** T7E1 assay. *Pe*, *Pi* and S represent amplicons from ESC clones electroporated with all-in-one CRISPR/Cas9(Puro) plasmid with *Prdm1* exon 8 sgRNA 5, *Prdm1* intron6-7 sgRNA 3 or *S1pr2* exon 2 sgRNA 1, respectively. Positive control (+) used a PCR amplicon from gDNA which exhibited CRISPR/Cas9 activity at the region of interest obtained from prior sgRNA validation experiment (Figure 4.23). Genomic regions which contained the *S1pr2* or *Prdm1* sgRNA target sites were amplified from ESC gDNA targeted with the corresponding all-in-one CRISPR/Cas9(Puro) ("specific") or from a non-specific sgRNA ("non-specific"). Specific amplicons were subjected to the T7E1 assay either alone or in a 3:1 mass ratio with a non-specific amplicon. For example, clone *Pi*1 was targeted at *Prdm1* intron6-7 and the PCR amplicon for this region from clone *Pi*1 was assayed alone (*Pi*1) or mixed with the amplicon of the *Prdm1* intron6-7 region from clone *Pe*1 which would have a WT *Prdm1* intron6-7 sequence as it had instead been targeted at *Prdm1* exon 8 3'UTR (a "non-specific" site). % represents the intensity of the non-cleaved amplicon compared to the larger band of the cleaved amplicons in that lane (measured using ImageJ). **(C)** αCas9 Western blot with 20 µg cell lysate from each of the expanded CRISPR/Cas9 targeted ESC clones or WT ESC. Purified recombinant *S.pyogenes* Cas9 protein (200 ng, MW 163 kDa) was used as a positive control (+). α-tubulin, control.

Six of the seven puromycin resistant ESC colonies were assayed by T7E1 and 50% (3/6) demonstrated expected CRISPR/Cas9 activity (Figure 4.27B). Immunoblot analysis detected Cas9 protein in all clones except *Pe*2 at low and variable levels (Figure 4.27C and Table 4.5). Cas9 protein expression and positive T7E1 assay results did not correlate in all clones, i.e., despite low levels of detected Cas9 protein in clones *Pi*2 and *Pe*1 their respective T7E1 assays were negative, but a strong positive T7E1 assay was observed for *Pe*2 despite no detectable Cas9 protein (Figure 4.27C and Table 4.5).

ESC Clone	**Cas9/sgRNA target region**	**Cas9 protein expression (%, normalised to clone S3)**
*Pe*1	sgRNA 5 ; *Prdm1* exon 8 3'UTR	34%
*Pe*2	sgRNA 5 ; *Prdm1* exon 8 3'UTR	0%
*Pi*1	sgRNA 3 ; *Prdm1* intron6-7	11%
*Pi*2	sgRNA 3 ; *Prdm1* intron6-7	13%
S1	sgRNA 1 ; *S1pr2* exon 2 3'UTR	50% *
S2	sgRNA 1 ; *S1pr2* exon 2 3'UTR	19%
S3	sgRNA 1 ; *S1pr2* exon 2 3'UTR	100%
WT	N/A	0%

Table 4.5 **Cas9 protein expression in expanded puromycin resistant ESC colonies to validate sgRNA-Cas9/Puro plasmids in JM8 A3.N1 ESCs.** Band intensity from α-Cas9 immunoblot, where 0% represents no detected Cas9 protein normalised to the Cas9 signal detected in clone S3. * artificially high as there appears to be background noise on the immunoblot at the same position as the expected Cas9 band. Related to Figure 4.27.

The sgRNA validation assay in ESCs showed very few puromycin resistant ESC clones after stable selection which suggested poor levels of resistance being expressed from the puro^{R} cassette on the all-in-one CRISPR/Cas9(Puro) plasmid. The decision was taken to switch a gene targeting strategy that utilised a standard positive selectable maker on the TV and stable selection to maximise likelihood of generating targeted ESC clones. If there was additional time, we would have sought to optimise gene targeting using transient puromycin selection.

4.3.5 Modified gene targeting strategy; standard positive selection for the targeting vector alone, with CRISPR/Cas9 enhancement and no additional selection, or with both CRISPR/Cas9 enhancement and dual selection.

The final targeting strategy deployed a TV with a floxed neomycin resistance (neo^R) cassette to allow direct positive selection for ESCs having taken up and stably integrated the TV DNA. This standard targeting arm was then combined with arms in which CRISPR/Cas9 enhancement was included, either with transient additional selection for the all-in-one CRISPR/Cas9(Puro) or with no additional selection (Figure 4.28). Transient additional selection for the CRISPR vector was hoped to enrich for ESCs undergoing CRISPR-enhanced gene targeting.

The new design of the final TVs required a floxed neo^R positive selection cassette to be cloned into the existing TVs for *S1pr2*, *Prdm1* intron6-7 and *Prdm1* exon 8 3'UTR (Figure 4.29 and Figure 4.30). Further, the neo^R cassette with mammalian SV40 early promoter native to the backbone of unmodified pcDNA3.1 vector was removed from the final TVs to avoid the risk of any undesired homologous recombination events between this cassette and the positive selection neo^R cassette in the cargo region.

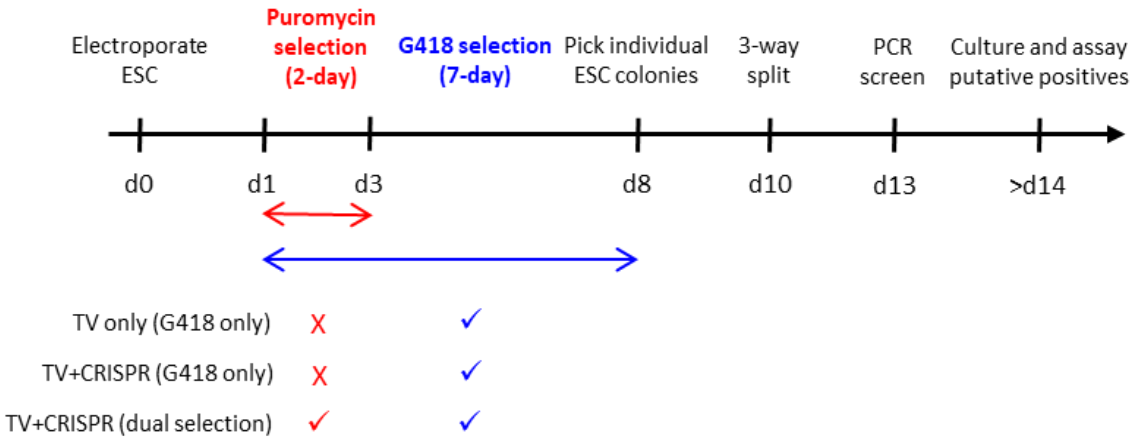

Figure 4.28 **Final experimental plan for CRISPR/Cas9-enhanced ESC gene targeting.** Schematic for planned workflow. TV; targeting vector with selectable neo^R cassette to enable positive G418 selection. CRISPR; all-in-one CRISPR/Cas9(Puro) plasmid with appropriate *S1pr2* or *Prdm1* specific sgRNA.

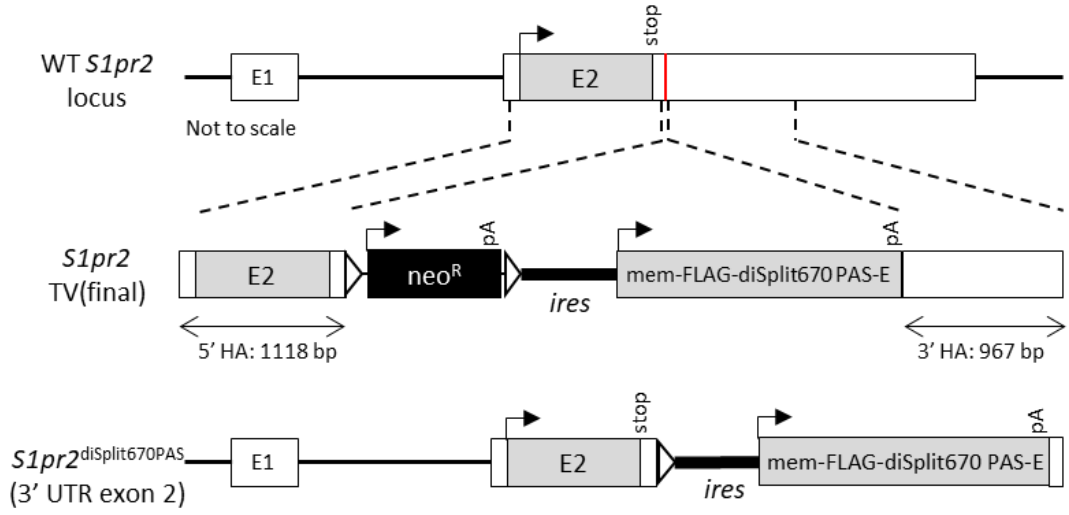

Figure 4.29 **Modified targeting vector for targeted insertion of the mem-FLAG-diSplit670 PAS-E domain to the *S1pr2* locus.** Top, wild-type (WT) *S1pr2* locus where introns are thin black lines and exons are boxes (open for untranslated regions (UTRs), grey shaded for protein coding regions). Black arrow depicts translation from initial methionine and stop indicates STOP codon. Targeted insertion site in the 3' UTR shown by red line. Dashed lines represent homology sequences. Middle, *S1pr2* TV(final); targeting vector including short 5' and 3' homology arms (HA), LoxP sequences (black triangles), G418 selection cassette (neo^R), internal ribosome entry site (*ires*, thick black line), polyadenylation site (pA) and cDNA for mem-FLAG-diSplit670 PAS-E domain. Bottom, transgenic *S1pr2* locus after Cre recombinase collapse.

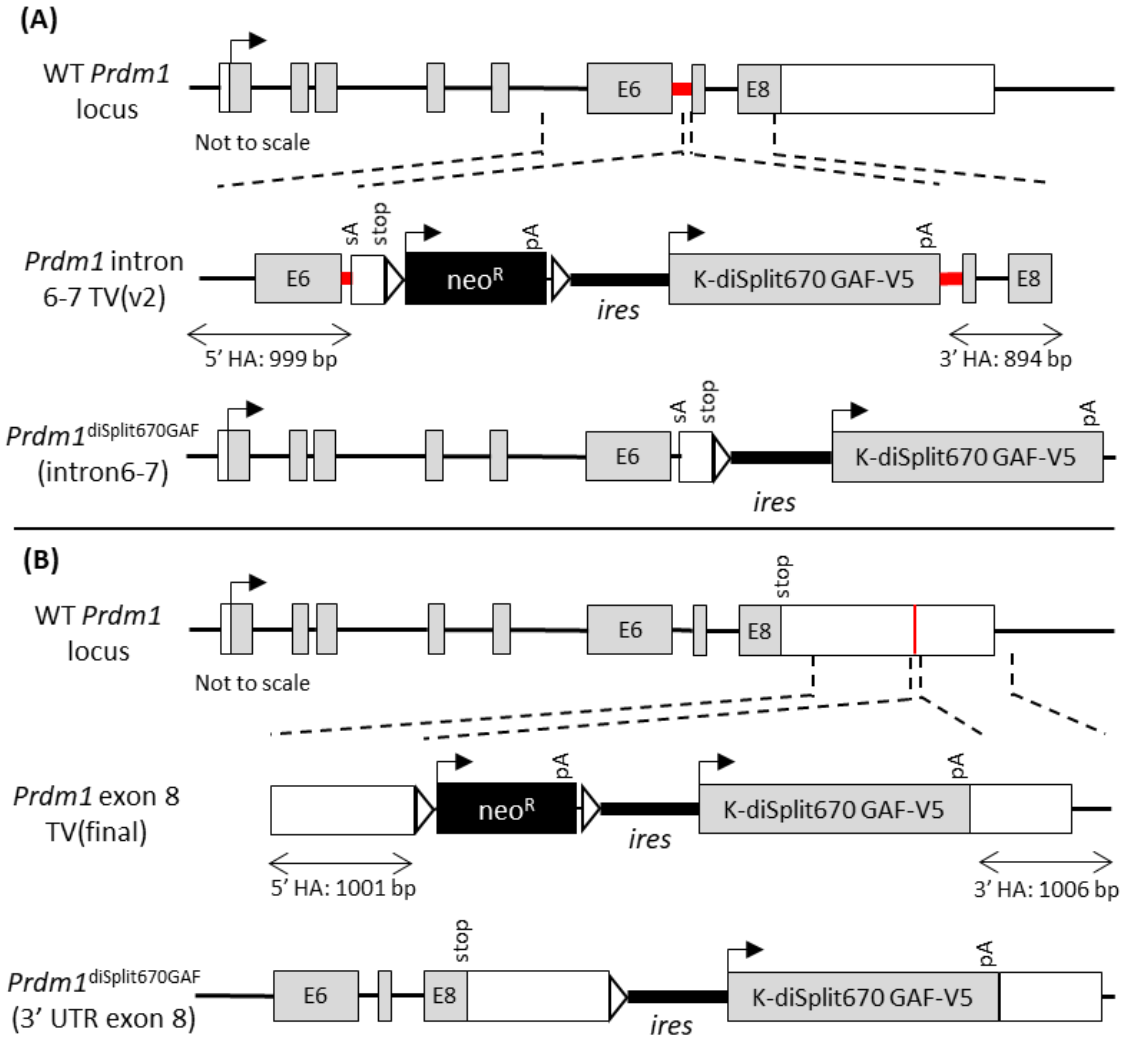

Figure 4.30 **Modified targeting vectors for two separate knock-in sites for targeted insertion of K-diSplit670 GAF-V5 domain to the *Prdm1* locus.** Targeted insertion region/point shown in red. **(A)** *Prdm1* intron6-7 targeting. Top, wild-type (WT) *Prdm1* locus (transcript *Prdm1*-201 ENSMUST00000039174.10) where introns are thin black lines, and exons as boxes (open for untranslated regions (UTRs), grey shaded for protein coding regions). Black arrow depicts translation from initial methionine and stop indicates STOP codon. Dashed lines represent homology sequences. Middle, *Prdm1* intron6-7 TV(v2); targeting vector to intron6-7 region, adenoviral major late transcript splice acceptor (sA), LoxP sequences (black triangles), G418 selection cassette (neo^R), internal ribosome entry site (*ires*, thick black line), polyadenylation site (pA), cDNA for K-diSplit670 GAF-V5 domain. Bottom, transgenic *Prdm1* locus after targeted insertion and Cre recombinase collapse. **(B)** *Prdm1* exon 8 3' untranslated region (UTR) targeting. Top, WT *Prdm1* locus as in (A). Middle, *Prdm1* exon 8 TV(final). Bottom, transgenic *Prdm1* locus after targeted insertion and Cre recombinase collapse.

4.3.6 Targeting vector validation; Cre collapse assay for functional LoxP sequences.

Since the neo^R cassettes used in these vectors had both prokaryotic (gb2) and eukaryotic PGK promoters, it meant that removal of the cassette by Cre activity could be followed by sensitivity to kanamycin. For this, SW106 *E. coli* (Warming *et al.*, 2005), which express Cre recombinase, were transformed with *S1pr2* TV(final), and plated on both ampicillin and kanamycin selection plates. The hypothesis was that if the LoxP sequences were correctly orientated in the same direction then the Cre recombinase would excise the neo^R cassette, and the transformed SW106 would be sensitive to kanamycin selection and bacterial growth would only be observed on the ampicillin selection plates conferred by the amp^R cassette on the pcDNA3.1 backbone. Correct Cre-mediated excision could then be confirmed by PCR and restriction digest assays. As expected for functional LoxP sequences, transformed bacterial isolate counts were extremely low for kanamycin selection but much greater for ampicillin selection (Table 4.6). Colony PCR screening and loss of the unique EcoRI restriction site confirmed excision of the PGK-gb2-neo^R cassette from isolates derived from the ampicillin selection plate and indicated that the minimal number of isolates from the kanamycin selection plates were escapees where incomplete Cre recombinase activity had occurred (Figure 4.31A-B). When conducting this assay to detect functional LoxP sequences, *S1pr2* TV(final) was the only TV which was complete and contained the floxed PGK-gb2-neo^R cassette. Once constructed, the LoxP sequences of *Prdm1* exon 8 TV(final) and *Prdm1* intron6-7 TV(v2) were validated by sequencing.

Antibiotic selection plate	**Volume of transformed SW106 *E. coli* plated**	
	1/50th	**1/5th**
Ampicillin	51	>250
Kanamycin	1	14

Table 4.6 **Antibiotic selection analysis and bacterial isolate counts for SW106 *E. coli* transformed with *S1pr2* TV(v1) that contained the floxed PGK-gb2-neo^R cassette**.

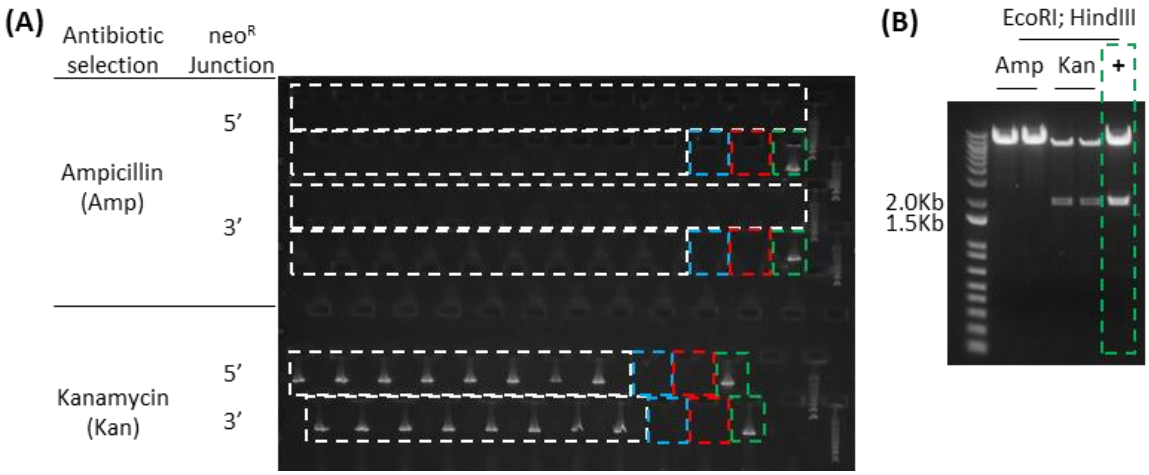

Figure 4.31 ***In vitro* Cre collapse assay to validate functional LoxP sequences flanking the PGK-gb2-neo^{R} cassette present in the *S1pr2* targeting vector.** Transformation of electrocompetent SW106 *E. coli* which express Cre recombinase with 1 ng of *S1pr2* TV(final). Transformed SW106 were grown overnight on either ampicillin or kanamycin selection plates. **(A)** Colony PCR screen for LoxP flanked PGK-gb2-neo^{R} cassette junctions. PCR templates: transformed SW106 isolates from the indicated antibiotic selection (white dashed boxes), no template control (blue dashed box), *S1pr2* TV(v1) which lacks the PGK-gb2-neo^{R} cassette (red dashed box) and *S1pr2* TV(final) that contained the floxed neo^{R} cassette and was used to transform (green dashed boxes). **(B)** EcoRI; HindIII double restriction digest of plasmid purified from transformed SW106 *E. coli* isolates picked from the indicated antibiotic selection or *S1pr2* TV(final) used for transformation (+).

4.3.7 Preliminary, qualitative gene targeting assessment of TV with or without CRISPR/Cas9 enhancement.

It was decided to conduct a preliminary gene targeting experiment without colony picking to get a quick qualitative assessment of the targeting efficiency associated with the TVs with and without CRISPR/Cas9 enhancement. Construction and sequencing of *S1pr2* TV(final) and *Prdm1* exon 8 TV(final) were complete, and these two TVs were available to be used for this qualitative assessment. Linearised targeting vectors ± the respective non-linearised (circular) all-in-one CRISPR/Cas9(Puro) plasmid were electroporated into ESCs and subjected to 6-day stable G418 selection (Figure 4.32A).

Total ESC colony counts were comparable for both vectors (Table 4.7). gDNA was pooled per condition and PCR junction screen analysis with optimised primers (Figure 2.4). The results were promising for *S1pr2* TV(final) in that gene targeting was detectable for both the TV alone and with CRISPR/Cas9 enhancement. However, for *Prdm1* exon 8 TV(final), no evidence of gene targeting could be detected when analysing the pooled gDNA samples with or without CRISPR enhancement (Figure 4.32B). This result was disappointing, but it was possible that targeting may still have been occurring at a low level but under the threshold of detection due to the dilution effect of screening pooled colonies rather than individual ones.

Electroporation Condition (µg DNA)	DNA Molar Ratio	ESC colony count after 6-day G418 selection (#)
Negative selection control; PBS only (0)	N/A	0
Positive selection control; pMS94 (1 µg)	N/A	180
Prdm1 exon 8 TV(final) (2 µg)	N/A	460
Prdm1 exon 8 TV(final) (2 µg) *Prdm1* exon 8 CRISPR (8 µg)	1:4	404
S1pr2 TV(final) (2 µg)	N/A	324
S1pr2 TV(final) (2 µg) *S1pr2* exon 2 CRISPR (8 µg)	1:4	356

Table 4.7 **Assessment of G418 selection efficiency using final *S1pr2* exon 2 3'UTR or *Prdm1* exon 8 3'UTR targeting vectors ± respective all-in-one CRISPR/Cas9(Puro) plasmids**. The positive selection control pMS94 contains a neo^R selection cassette. TV, targeting vector; CRISPR, all-in-one CRISPR/Cas9(Puro). For each condition the ESC colony number reported is the total from two 10 cm plates.

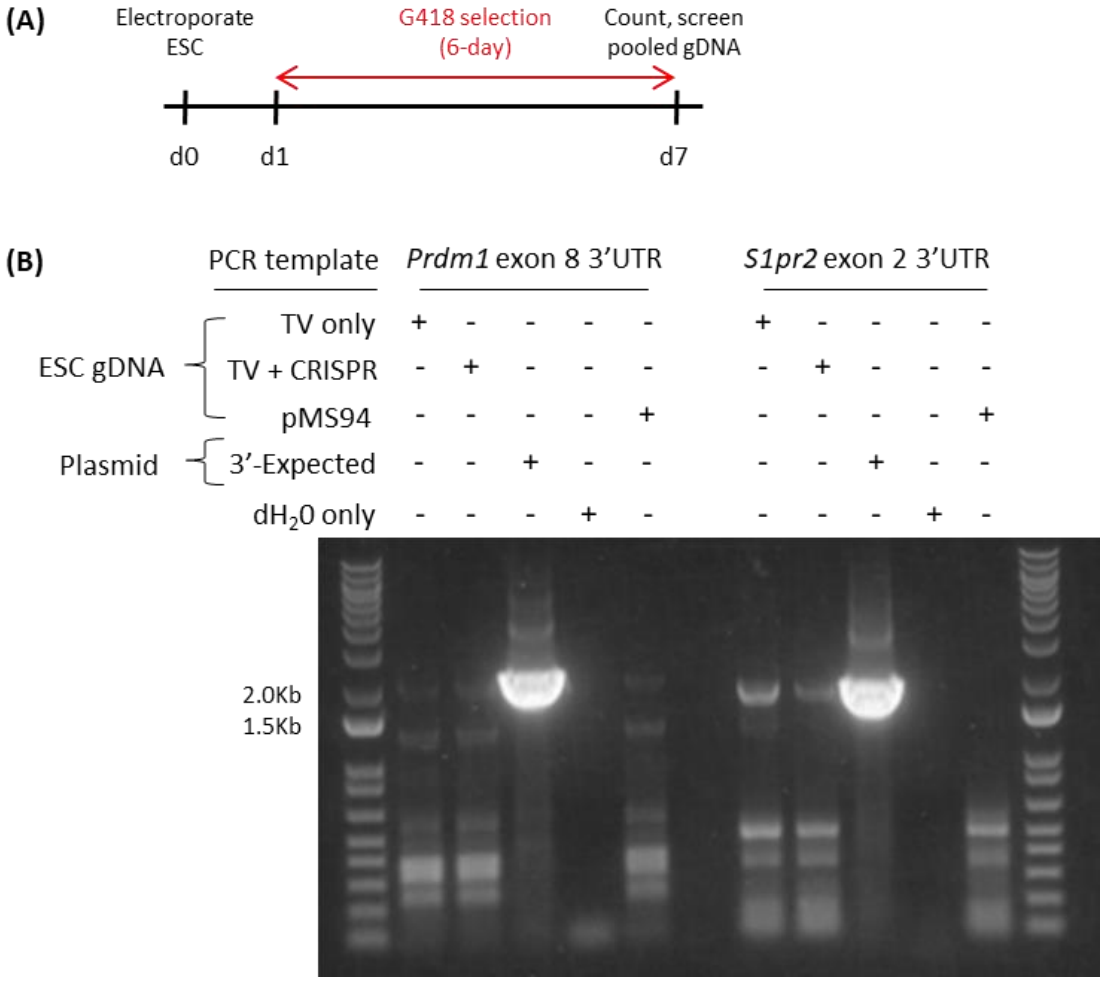

Figure 4.32 **Preliminary assessment of targeting vector efficiency using pooled ESC genomic DNA after G418 positive selection and enrichment. (A)** Schematic of experimental protocol for targeted knock-in selection and screening of pooled ESC gDNA. For each condition, $10x10^6$ electroporated ESCs were split between two 10 cm MEFs coated plates on day 0. **(B)** JM8 A3.N1 ESCs were electroporated with 2 µg of linearised *Prdm1* exon 8 TV(final) or *S1pr2* TV(final) alone (TV only) or with circular all-in-one CRISPR/Cas9(Puro) plasmid at a 1:4 molar ratio of TV:CRISPR/Cas9 vector (TV + CRISPR). Electroporation of ESCs with pMS94 served both as a positive G418 selection control and as a non-specific control for the PCR junction screen. Expected amplicon size for 3' junction of targeting to *Prdm1* exon 8 was 2172 bp and was 1887 bp for the 3' junction of targeted *S1pr2*. Further PCR controls: 3'-Expected, is a plasmid which contained additional 3' homology which is not present in the TV 3' HA and acts as the positive control for a correct targeted knock-in event (see Section 2.14); dH_20, no template control.

4.3.8 Gene targeting experiment to insert mem-FLAG-diSplit670 PAS-E into the *S1pr2* locus with or without CRISPR/Cas9 enhancement.

To achieve targeted insertion of the mem-FLAG-diSplit670 PAS-E part to the *S1pr2* locus, mouse JM8 A3.N1 ESCs were electroporated with linearised *S1pr2* TV(final) alone or with non-linearised (circular) all-in-one CRISPR/Cas9(Puro) containing *S1pr2* sgRNA 1 (at a 1:4 molar ratio of TV : all-in-one CRISPR/Cas9(Puro)) and either selected by stable G418 alone or in combination with transient puromycin selection (Figure 4.33A). For all the electroporations, one quarter of the electroporated cells were plated per recipient MEF feeder plate. For the experimental arms four plates were generated and for the positive and negative control arms just one plate was produced. As expected, the negative control displayed no colonies whereas colonies were obtained on both the positive control plate and experimental plates (Table 4.8). The G418 selection control, linearised pMS94 plasmid (kind gift of Mike Snaith), possessed a comparable ESC colony count to *S1pr2* TV(final) alone or with all-in-one CRISPR/Cas9(Puro) selected with only G418 (Table 4.8). Unexpectedly, no ESCs survived the dual antibiotic selection regimen (Table 4.8). The junctions of expected integration events were screened for by optimised PCR assays (Figure 2.4). Individual G418-resistant ESC colonies were initially screened for the 3' junction (Figure 4.33B-C), which revealed 9 putative positive clones for *S1pr2* TV(final) only and 10 putative positive clones for TV with all-in-one CRISPR/Cas9(Puro). Putative positive clones were screened for the 5' junction as well as re-screened for the 3' junction which confirmed that 8/9 and 9/10 ESC clones (89% overall) possessed correctly targeted insertion (Figure 4.34 and Table 4.8).

PCR genotyping analysis demonstrated a modest 1.5-fold increase in targeting efficiency in the CRISPR/Cas9 enhanced arm with single antibiotic selection (TV+CRISPR (G418 only) (Table

4.8). The importance of including the CRISPR/Cas9 enhanced arm with G418 selection only was demonstrated by the dual antibiotic selection CRISPR/Cas9 arm yielding zero ESC colonies (Table 4.8). Dual puromycin and G418 selection, even transiently for only 48 h, was too harsh for the ESCs. This could be linked to the poor levels of puromycin resistance from the all-in-one CRISPR/Cas9(Puro) plasmid observed previously (Table 4.4).

Condition (µg DNA)	**Antibiotic Selection**	**Mean # of ESCs colonies per plate* (total #)**	**Putative positive ESC clones**	**Number and (%) of correctly targeted clones**
Negative selection control (0 µg)	G418 (7-day)	0 (0)	N/A	N/A
pMS94 positive selection (1 µg)	G418 (7-day)	56 (56)	N/A	N/A
S1pr2 TV only (1.85 µg)	G418 (7-day)	47 (188)	9	8 (4.3%)
S1pr2 TV (1.85 µg) + CRISPR (8.15 µg)	G418 (7-day)	35 (140)	10	9 (6.4%)
S1pr2 TV (1.85 µg) + CRISPR (8.15 µg)	G418 (7-day) Puromycin (48 h)	0 (0)	N/A	N/A

Table 4.8 **CRISPR/Cas9 improved the gene targeting efficiency to the 3'UTR of *S1pr2* exon 2.** A standard positive selection targeting vector only approach (TV only) or TV in combination with *S1pr2*-specific all-in-one CRISPR/Cas9(Puro) (TV + CRISPR), with or without transient puromycin selection was tested. * four plates per experimental condition, one plate per control condition and counted on day 8 after electroporation (Figure 4.33A); TV, linearised *S1pr2* TV(final). pMS94 was linearised whereas all-in-one CRISPR/Cas9(Puro) was circular.

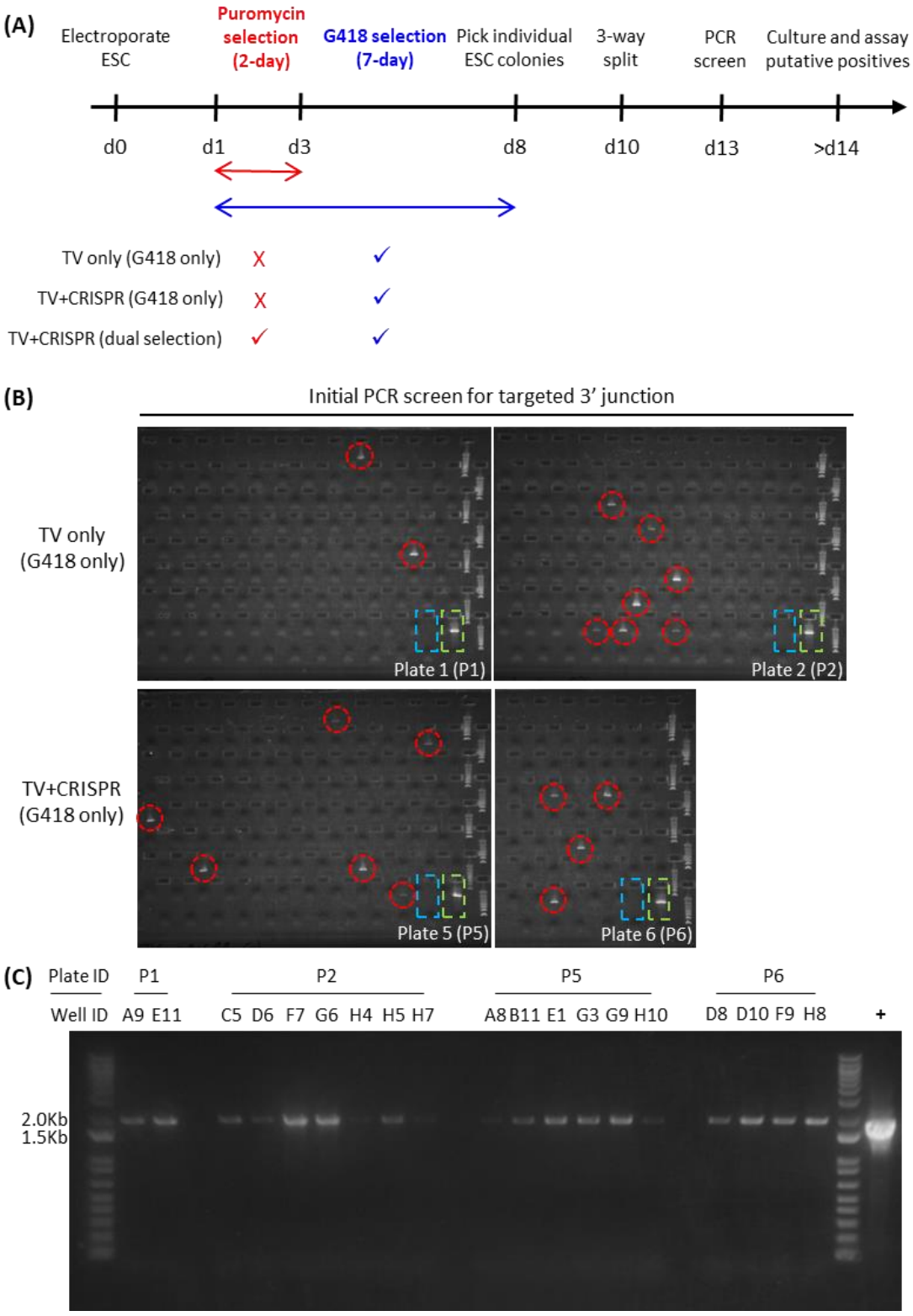

Figure 4.33 **Standard and CRISPR/Cas9 enhanced targeted knock-in at *S1pr2* exon 2 3'UTR in C57BL/6 JM8 A3.N1 ESCs**. **(A)** Schematic of experimental conditions and screening of ESC clones. **(B)** Low-resolution gel of high-throughput PCR assay for presence of 3' junction of targeted knock-in *S1pr2* alleles. In each gel, putative positive clones are highlighted (dashed red circles), well H11 (blue dashed box) is no template control and well

H12 (green dashed box) is a PCR positive control for an expected 3' junction amplicon from a targeted insertion event using 1 ng of plasmid 3'-Expected (see Section 2.16). **(C)** Higher resolution gel of the ESC clones with putative positive 3' (right) junction and PCR positive control (+) well H12 as described in (B). Well ID relates to position in 96-well plate represented in low-resolution gel shown in (B).

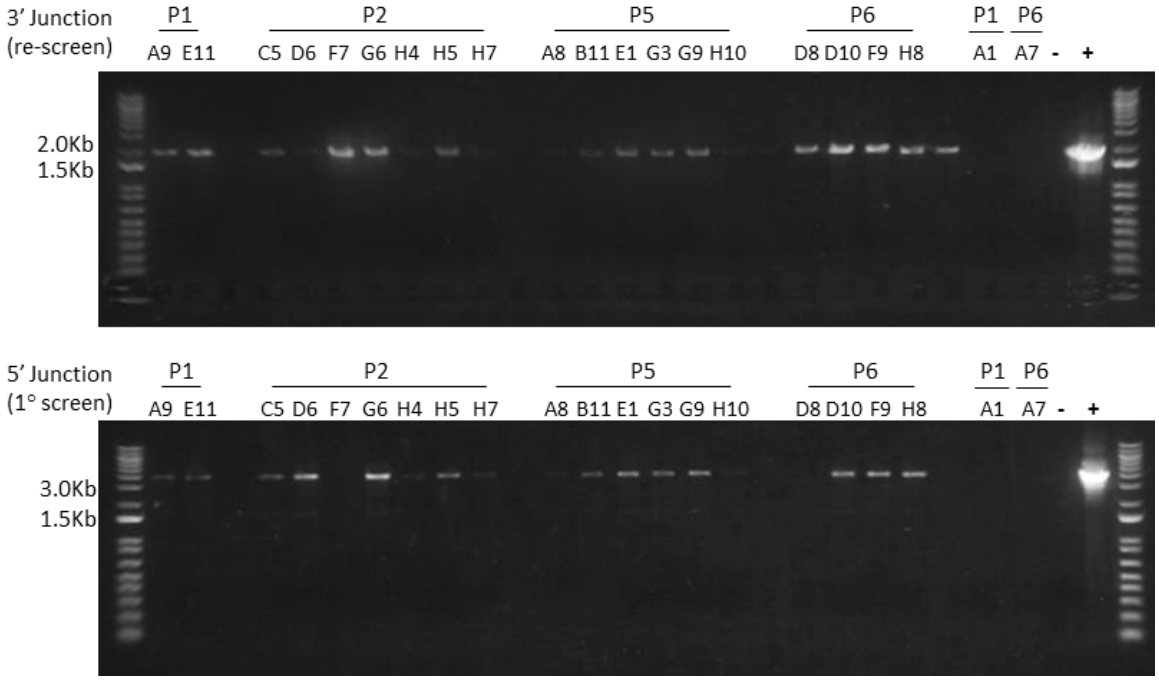

Figure 4.34 **Complete PCR junction genotyping revealed that 89% of candidate *S1pr2* knock-in clones possessed both correct junctions**. Putative positive targeted ESC clones from Figure 4.33C were screened for the presence of the 5' junction of the targeted insertion as well as re-screened for the 3' junction. Plate IDs as described in Figure 4.33. Plate ID and Well ID combined give Clone ID e.g., clone P1A9. (+), PCR positive controls for correctly targeted 3' junction as described in Figure 4.33, and a plasmid for correctly targeted 5' junction designed in an analogous manner the 3' control; (-), no template control.

4.3.9 Further characterisation of the putative targeted *S1pr2*^{diSplit670PAS} ESC clones.

Six *S1pr2* targeted ESC clones were chosen from the TV only arm and a further six from the CRISPR/Cas9 enhanced arm (12/17 total ESC clones) for further characterisation based on the intensity of the 5' and 3' junction PCR amplicons (Figure 4.34). These clones were expanded for a further six days in G418 selection media and were re-screened by PCR using 5' and 3' junction screens (Figure 4.35). This re-screening confirmed that all twelve selected ESC clones gave amplicons of the expected size.

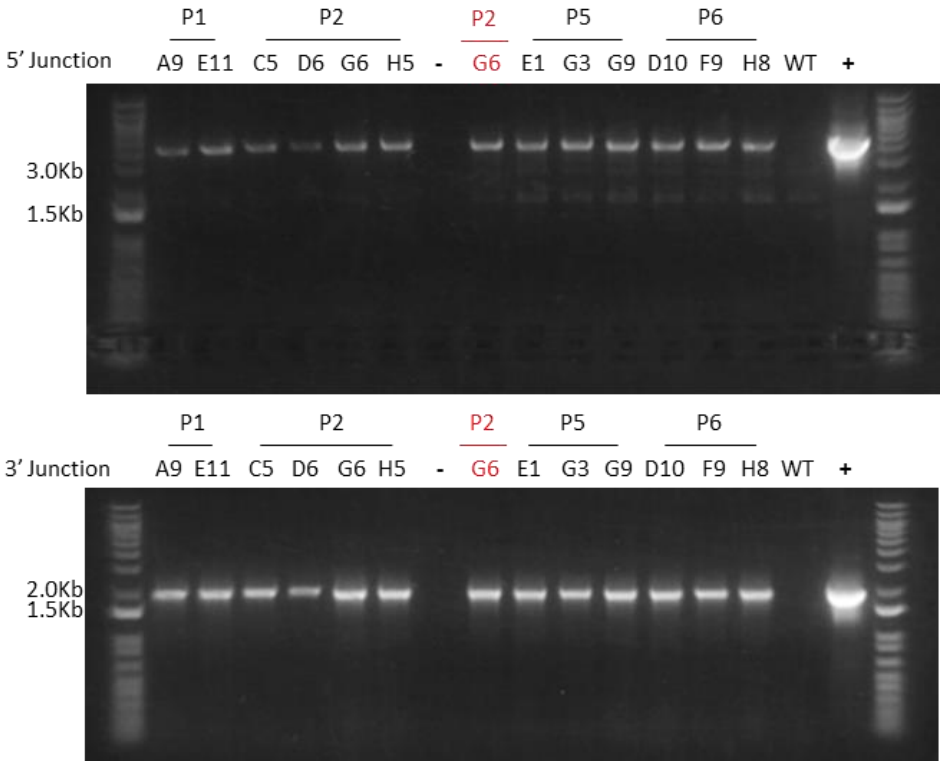

Figure 4.35 **The twelve selected *S1pr2*^{diSplit670PAS} ESC clones were expanded and re-screened for correct 5' and 3' junctions prior to further characterisation**. The putative positive *S1pr2* targeted ESC clones were re-screened for both the 5' and 3' junctions. PCR amplicons were run on 1% w/v agarose. PCR controls; (+), for both 3' and 5' junctions as described in Figure 4.33 except that a 100-fold lower mass of each plasmid was used; P2G6 highlighted red, gDNA from clone P2G6 from the initial PCR junction screen before clonal expansion; WT, 50 ng wild-type JM8 A3.N1 ESC gDNA as a non-specific control; (-), no template control.

The CRISPR/Cas9 enhanced arm used circular (non-linearised) all-in-one CRISPR/Cas9(Puro) plasmid to minimise the frequency of unwanted genomic integrations. However, it was important to determine if any of the six selected clones from this arm had indeed integrated the all-in-one CRISPR/Cas9(Puro) plasmid. For this purpose, a further PCR screen was optimised that was designed to a region including the puro^{R} and pUC origin of replication from the all-in-one CRISPR/Cas9(Puro) plasmid (Figure 4.36A). All six clones from the CRISPR/Cas9 arm were negative, as were the clones from the TV only arm which were included as PCR negative controls (Figure 4.36B). The non-specific amplicons detected when *S1pr2* targeting vector only was used as template were not detected in any of the targeted ESC clones, which suggested non-specific primer binding on the TV backbone (Figure 4.36B).

All twelve clones were next analysed to determine if they were heterozygous or homozygous for the desired genetic modification. Two assays were performed. The first was a simple PCR screen designed to detect the wild-type *S1pr2* exon 2 3'UTR allele (Figure 4.37A) which would have been replaced by a correct targeting event. The second was a qPCR assay to determine the copy number of the neo^{R} cassette (Figure 4.37B). The data obtained confirmed that all twelve ESC clones were heterozygous for the targeted *S1pr2*^{diSplit670} knock-in.

Additional molecular screening for unwanted integrations could have included design and optimisation of qPCR assays specific for each of the HAs included in the *S1pr2* TV. If only correct homologous recombination mediated events had occurred, then the expected copy number from these HA specific qPCR assays would be n=2 for detection of the two endogenous *S1pr2* alleles. However, if random TV integration had occurred, then n>2 and those ESC clones

could have been discarded. Further, a simple PCR screen for the amp^{R} cassette from the TV backbone could have been employed.

Southern blot analysis using carefully selected restriction enzyme digests and optimised hybridisation probes, can simultaneously identify correctly targeted ESC clones, analyse the structure of structure of the targeted knock-in allele and confirm insertion copy number and is considered gold standard for detection of homologous recombination events. However, the hybridisation probes are typically radioisotope labelled and the labs at AstraZeneca were not set up for radiation assays. As an alternative, "cold" non-radioactive digoxigenin-labelled probes combined with chemiluminescent detection could have been tested (Solanas and Escrich, 1997; Codner *et al.*, 2020). Despite not performing Southern blot analysis, sufficient confidence to proceed at this stage was provided by the combination of: (i) the expected long-range PCR screening results, (ii) the complementary results from the wild-type allele and neo^{R} copy number assays and (iii) that ESC clones pre-selected for chimera generation would have their targeted *S1pr2* allele sequenced.

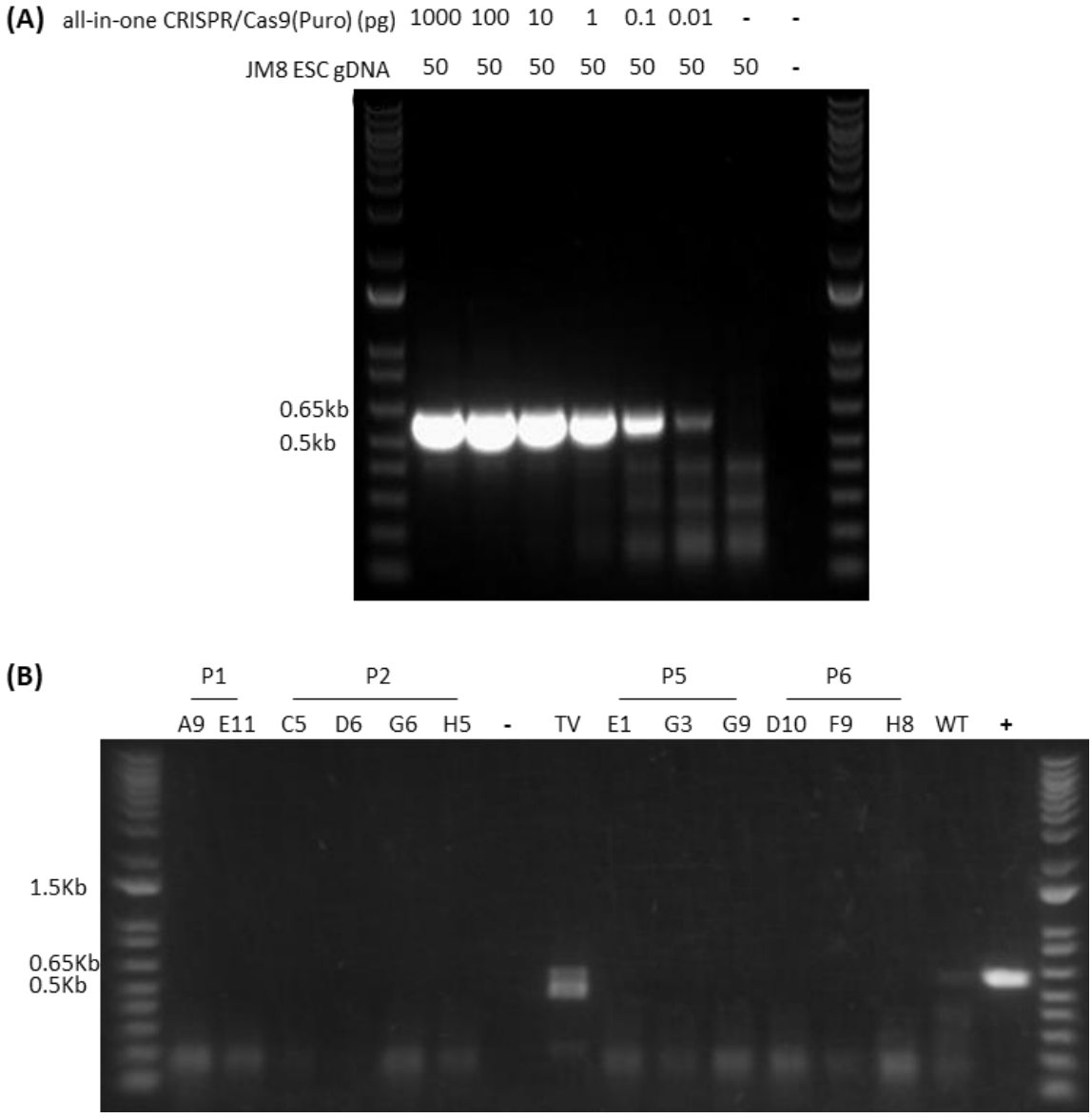

Figure 4.36 **No unwanted integration events of the all-in-one CRISPR/Cas9(Puro) plasmid were detected in expanded *S1pr2*$^{\text{diSplit670PAS}}$ targeted ESC clones**. **(A)** Detection limit of PCR assay specific for all-in-one CRISPR/Cas9(Puro) plasmid in the presence of 50 ng ESC gDNA to mimic genomic template from ESC clones. Where no DNA template was added dH_20 was added instead (-). **(B)** PCR screen of expanded *S1pr2*$^{\text{diSplit670PAS}}$ targeted ESC clones from the TV only arm (Plate IDs P1 and P2) or TV + CRISPR arm (Plate IDs P5 and P6) for unwanted genomic integration of all-in-one CRISPR/Cas9(Puro). PCR controls; TV, linearised *S1pr2* TV(final); WT, wild-type JM8 A3.N1 ESC gDNA; (-), no template control; (+) 50 ng WT JM8 ESC gDNA spiked with 0.01 ng all-in-one CRISPR/Cas9(Puro) plasmid.

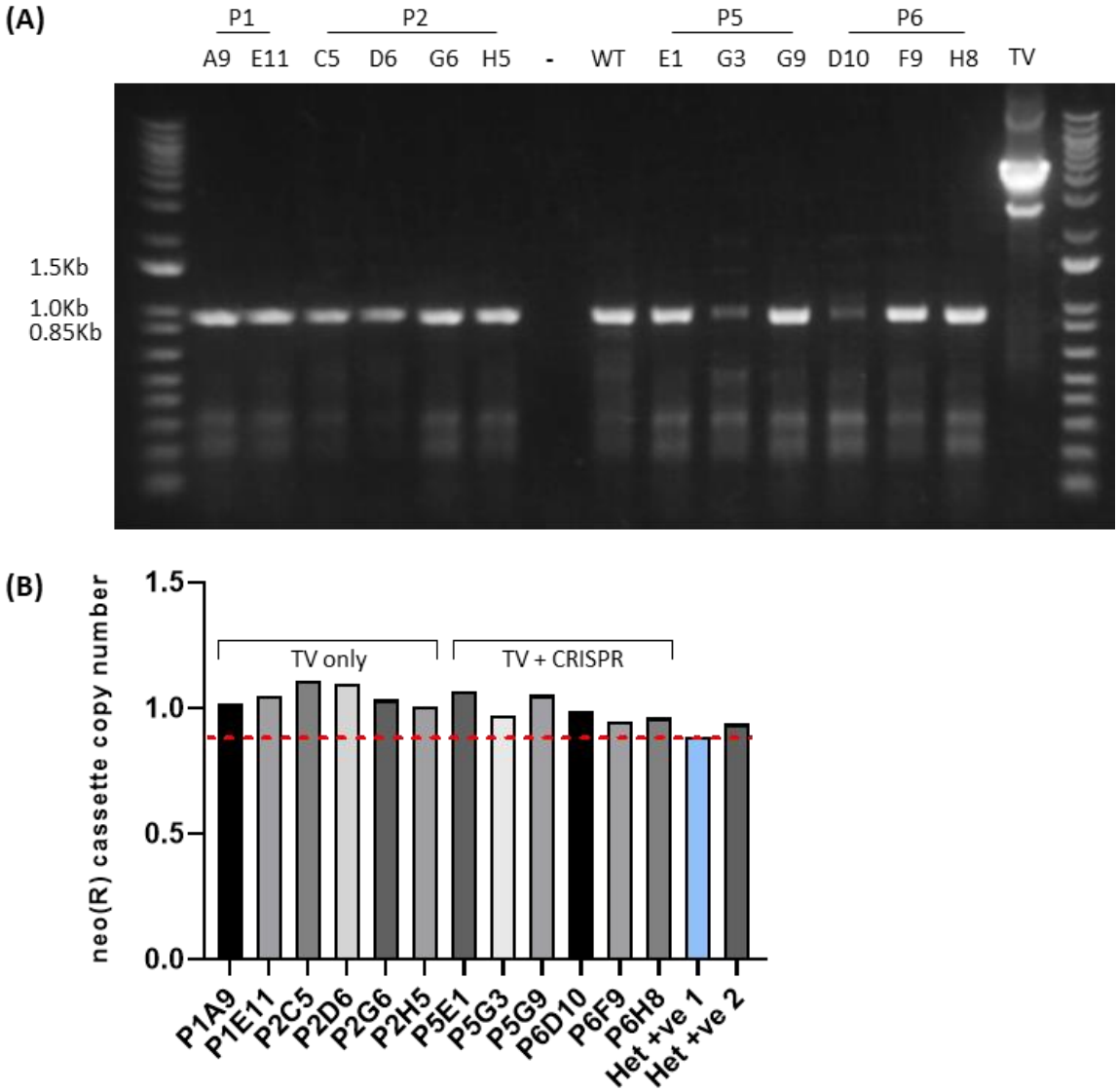

Figure 4.37 **PCR and qPCR assays confirmed that all twelve targeted ESC clones were heterozygous for *S1pr2*$^{\text{diSplit670PAS}}$.** **(A)** *S1pr2* wild-type allele PCR assay to assess whether targeted ESC clones are heterozygous or homozygous for transgene knock-in. PCR controls; WT, wild-type JM8 A3.N1 gDNA; TV, linearised *S1pr2* TV(final) as a non-specific background control; (-), no template control. **(B)** Copy number assay for neo^{R} positive selection cassette in the genome of each targeted ESC clone. Copy number positive controls; Het +ve 1 and Het +ve 2, gDNA derived from mouse ESCs each which contain a single copy of the neo^{R} cassette (kind gifts from AstraZeneca). Het +ve 1 was set as the comparator for copy number analysis by manual ΔCt. Manual analysis was in agreement with the results when analysed using Applied Biosystems Copy Caller v2.1 software (data not shown). Red dashed line used to show the signal from the Het +ve 1 single copy comparator.

Preliminary gene expression experiments had demonstrated that *S1pr2* was expressed in wild-type JM8 A3.N1 ESCs, albeit ~300-fold lower than the well characterised ESC specific gene *Pou5f1* which encodes Oct3/4 (Figure 2.5). This finding meant that the targeted clones could be analysed both for the expression of the inserted transgene (mem-FLAG-diSplit670 PAS-E) and for any impact on the targeted gene *S1pr2*. Good quality total RNA was prepared from all *S1pr2*$^{\text{diSplit670PAS}}$ clones, however, the concentration for clones P2C5 and P2D6 was lower compared to that obtained for the other ESC clones which had been expanded for an identical time (Figure 4.38A). Prior to cDNA preparation, the total RNA was treated extensively with DNaseI to remove any gDNA contamination which would provide a false positive signal for expression of mem-FLAG-diSplit670 PAS-E. Dilution series were then made using one cDNA sample to assess the efficiency and sensitivity of each qPCR assay. This was done to ensure an appropriate amount of cDNA template could be used that was within the dynamic range of the assays (Figure 4.38B).

Gene expression target	**Slope**	**Efficiency**	**R^2**	**cDNA template mass where SD ≤ 0.167 (ng)**
Actb (β-actin)	-3.80	85%	0.997	0.001
S1pr2	-3.48	95%	0.997	10
mem-FLAG-diSplit670 PAS-E	-3.96	80%	0.960	10

Table 4.9 **Performance evaluation of primers to be used to detect gene expression of *S1pr2* and mem-FLAG-diSplit670 PAS-E domain in *S1pr2*$^{\text{diSplit670PAS}}$ targeted ESC clones**. A slope of ~ –3.3 reflects primer efficiency of ~100%. A standard deviation (SD) of ≤ 0.167 indicates that in > 99.7% of instances a 2-fold dilution can be quantified and distinguished. R^2 represents the ability to predict one value from another where a score of 1 translates to the most accurate prediction.

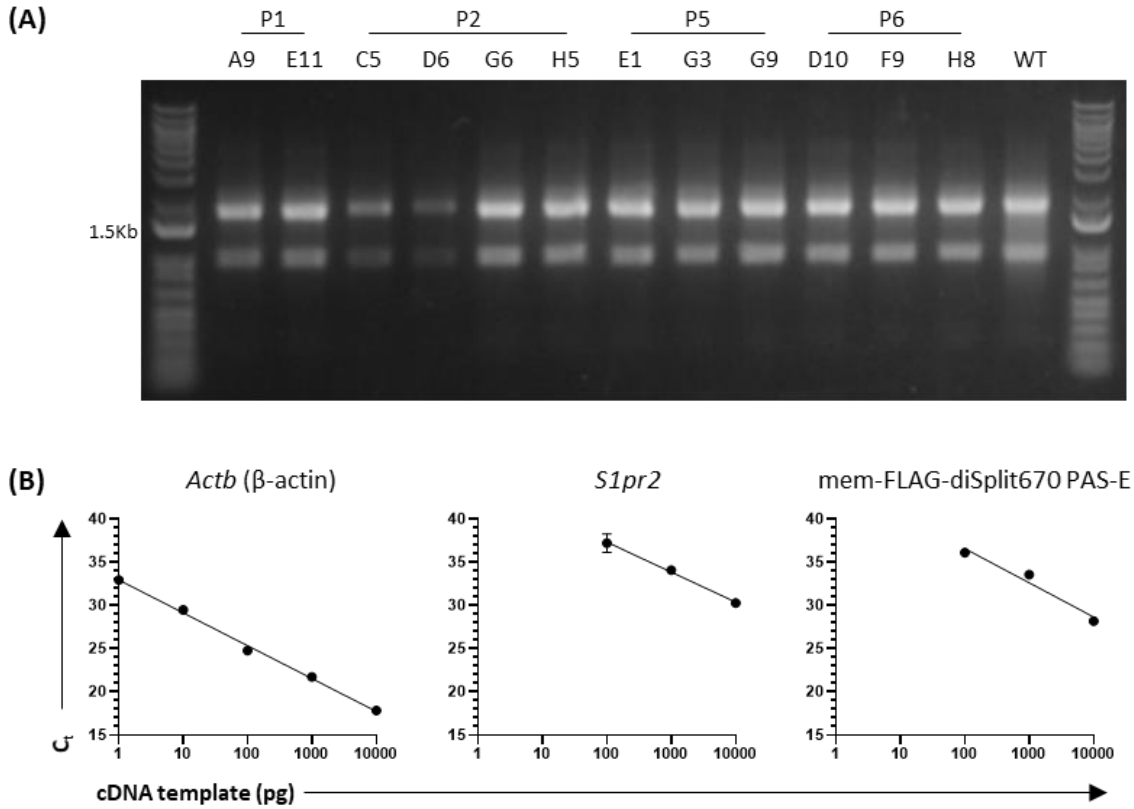

Figure 4.38 **Optimisation of qPCR assay for gene expression analysis of *S1pr2* and targeted knock-in mem-FLAG-diSplit670 PAS-E cDNA. (A)**. DNaseI treated total RNA from targeted *S1pr2*^{diSplit670PAS} ESC clones and wild-type (WT) JM8 A3.N1 ESCs (2 µL/sample) were run on a 2% w/v native agarose gel. **(B)** cDNA prepared from clone P1A9 was used to determine qPCR primer efficiency and sensitivity assessed over 5-fold (log_{10}) range. If not shown, threshold cycle (C_t) values were undetermined. Error bars are mean ± SD of 4 technical replicates (note: for almost all cDNA template masses, the SD error bars are too small to be visualised). Please see Table 4.9 for the calculated primer efficiency and precision.

Gene expression analysis revealed that: mem-FLAG-diSplit670 PAS-E domain was expressed/transcribed in all twelve *S1pr2*^{diSplit670PAS} targeted ESC clones, and as expected, absent from WT JM8 A3.N1 ESC cDNA (Figure 4.39A), that there was no detectable impact on endogenous *S1pr2* expression (Figure 4.39A), and that the expression levels of mem-FLAG-diSplit670 PAS-E were comparable to those of endogenous *S1pr2* (Figure 4.39B). Analysis of the minus reverse transcriptase (-RT) control for the mem-FLAG-diSplit670 PAS qPCR assay from *S1pr2*^{diSplit670PAS} clone P1A9 confirmed that there was no contamination from residual gDNA and that the observed signal was from true gene expression (Figure 4.39C-D). PCR amplicons from the mem-FLAG-diSplit670 PAS-E gene expression qPCR assay were sequenced and confirmed the expected product (data not shown).

Twelve *S1pr2*^{diSplit670PAS} targeted ESC clones had successfully made it through the molecular validation process. Therefore, it was possible/necessary to exclude some of the ESC clones from being taken forward to the final validation stages, which included karyotype analysis. Clones derived from the standard gene targeting arm (TV only) did not carry any of the risks associated with use of CRISPR/Cas9 and these six *S1pr2*^{diSplit670PAS} targeted ESC clones were taken forward.

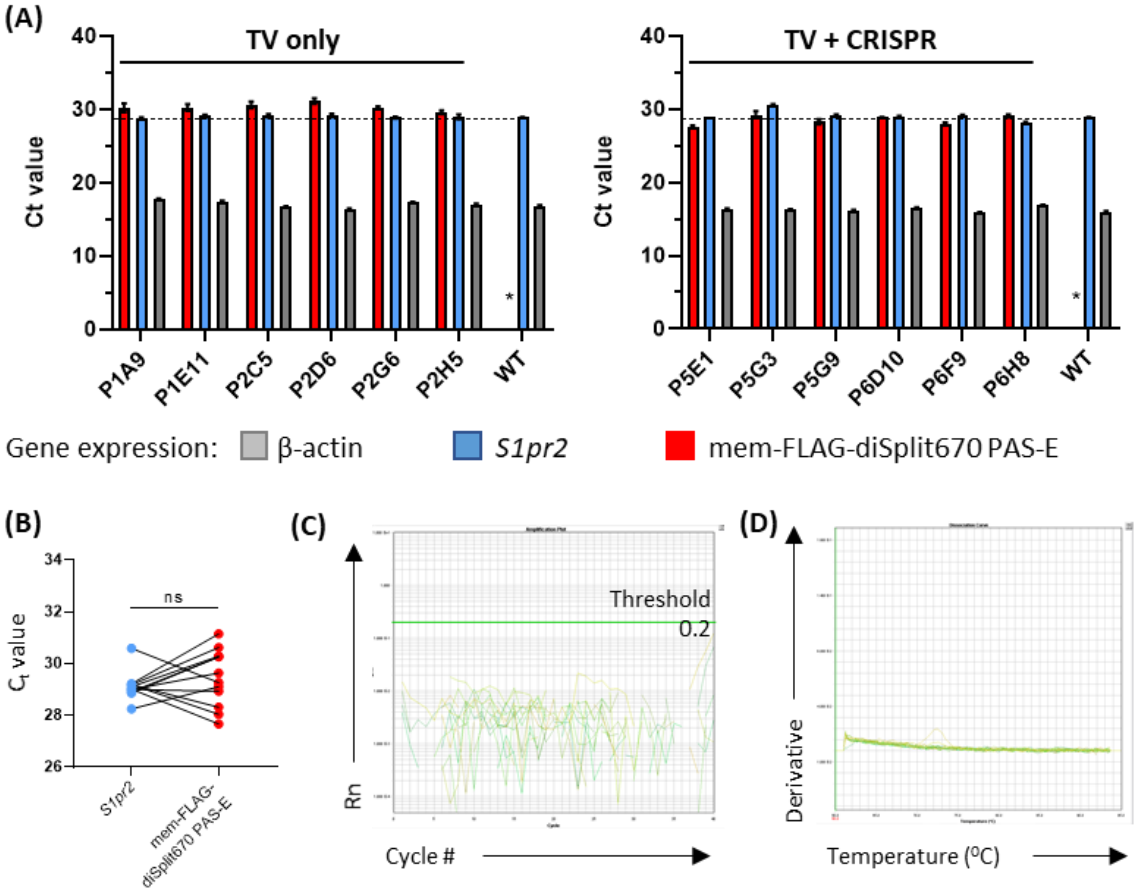

Figure 4.39 **Gene expression studies of mem-FLAG-diSplit670 PAS-E and endogenous *S1pr2*. (A)** qPCR assay to detect indicated cDNA of interest from *S1pr2*^{diSplit670PAS} clones from the targeting vector only (TV only) arm, left, and CRISPR/Cas9 enhanced arm (TV+CRISPR), right. For each sample 20 ng of cDNA template was used and the assay included no template and minus reverse transcriptase controls for each set of primers (not shown). * indicates an undetectable fluorescent qPCR signal for the in cDNA prepared from WT C57BL/6 JM8 A3.N1 ESCs. Dashed line set to *S1pr2* expression in WT ESCs. No statistical significance in endogenous *S1pr2* gene expression between targeted *S1pr2*^{diSplit670PAS} ESC clones and WT ESCs (Mann-Whitney test). **(B)** No significant difference between Ct values for gene expression of endogenous *S1pr2* and mem-FLAG-diSplit670 PAS-E for the twelve *S1pr2*^{diSplit670PAS} clones (Wilcoxon matched pairs, p=0.3394). **(C-D)** A minus reverse transcriptase (-RT) control for each qPCR primer set was included. For the mem-FLAG-diSplit670 PAS-E qPCR primers, the overlaid traces for the –RT control technical repeats of normalised fluorescent signal (Rn) against cycle number **(C)**; and dissociation curves **(D)** are shown. Detection threshold (Rn) is set at 0.2 in (C).

4.3.10 Selection of lead and backup *S1pr2*^{diSplit670PAS} targeted ESC clones.

Electroporation and continued culture of mouse ESCs can lead to chromosome instability (Gaztelumendi and Nogués, 2014) and chromosome abnormalities can interfere with ESC clone conversion into mice (Liu *et al.*, 1997; Longo *et al.*, 1997). There are 40 chromosomes in the diploid mouse genome and chromosome counting can be used to assess the karyotype of mouse ESCs. Targeted ESC clones which have a higher percentage of cells that display a normal karyotype can markedly enhance the germline contribution of ESCs in generated chimeras (Liu *et al.*, 1997; Longo *et al.*, 1997). To select the *S1pr2* targeted ESC clones with a higher chance of germline contribution to take forward for chimera generation, we performed chromosome counting (Figure 4.40A). We used the stringent criteria of ESC clones with ≥80% of cells displaying normal karyotype as strong candidates to take forward. Analysis revealed that *S1pr2*^{diSplit670PAS} clones P2H5 and P2D6 (9/15 correct counts) and P2C5 (10/15 correct counts) should not be taken forward (Figure 4.40A and Table 4.10). However, *S1pr2*^{diSplit670PAS} clones P1A9 and P2G6 were suitable lead candidates (12/15 and 13/15 correct counts, respectively) and that P1E11 (11/15 correct counts) could be suitable as a backup (Figure 4.40A and Table 4.10).

Clone	**Chromosome spreads with the indicated # of chromosomes**					**Spreads with correct 40 (%)**
	38	**39**	**40***	**41**	**42**	
P1A9	0	2	12	1	0	80
P1E11	2	1	11	1	0	73
P2C5	1	4	10	0	0	67
P2D6	2	4	9	0	0	60
P2G6	0	1	13	1	0	87
P2H5	0	6	9	0	0	60

Table 4.10 **Chromosome counts for targeted *S1pr2*^{diSplit670PAS} JM8 A3.N1 ESC clones**. * denotes the correct number of chromosomes in a diploid mouse genome.

Gene expression analysis by qPCR had detected mem-FLAG-diSplit670 PAS-E expression in all twelve targeted ESC clones, albeit at low levels compared to endogenous expression of the control gene β-actin (Figure 4.39A). Therefore, there was the possibility that mem-FLAG-diSplit670 PAS-E could be detected at the protein level in the targeted ESC clones. Denaturing immunoblot analysis did not detect the FLAG epitope tag in either of the lead clones P1A9 or P2G6 nor the backup candidate P1E11 (Figure 4.40B), however, it was possible that this was due to the low levels of transgene expression driven by the *S1pr2* promoter in the mouse ESCs.

As final quality control steps, the lead and backup candidate *S1pr2*$^{\text{diSplit670PAS}}$ clones P1A9, P2G6 and P1E11 were sequenced across the targeted knock-in alleles and the cultured ESCs were tested for the absence of mycoplasma. Sequencing confirmed the expected targeted knock-in alleles (data not shown) and all candidate clones tested negative for mycoplasma contamination (Figure 4.40C) and were ready to proceed to blastocyst injection and chimera generation.

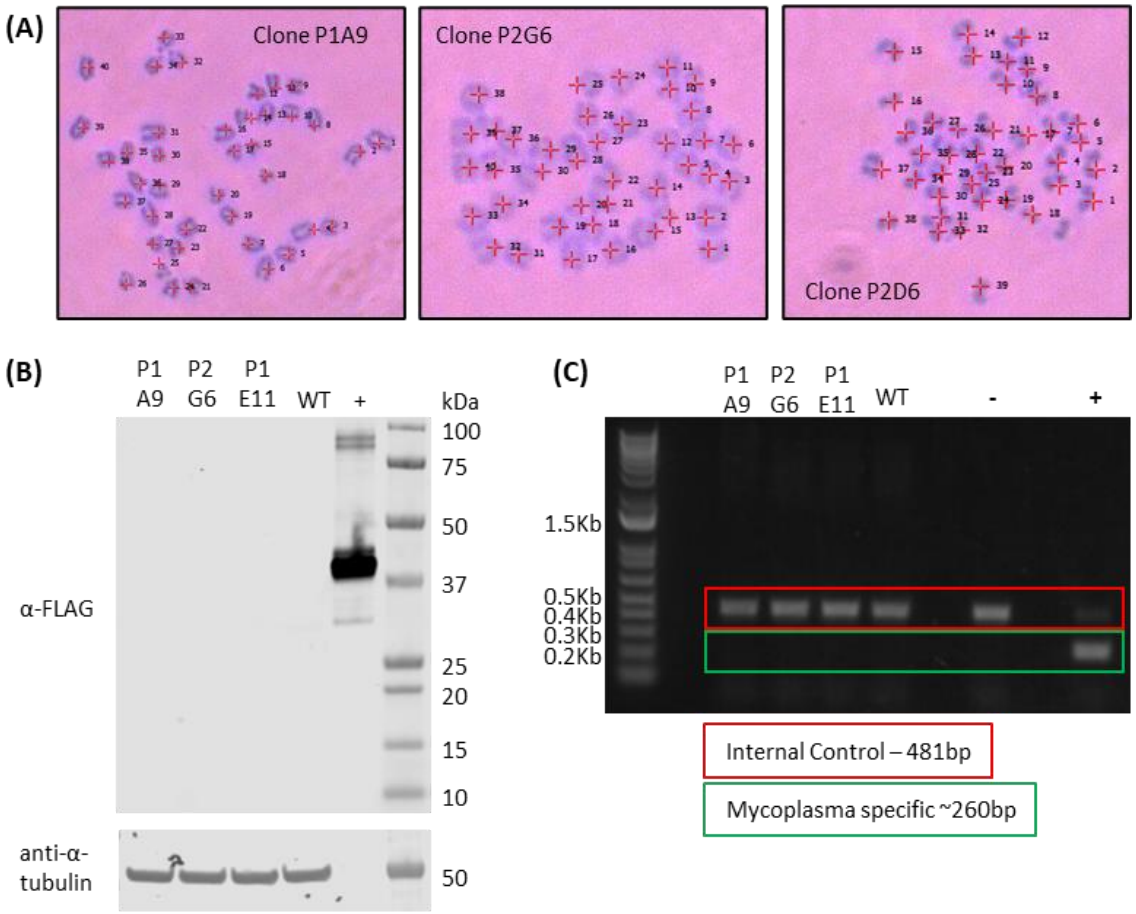

Figure 4.40 **Assessment of *S1pr2*$^{\text{diSplit670PAS}}$ ESC genetic stability and further characterisation of lead candidate ESC clones for quality and transgene protein expression.** **(A)** Example chromosome spreads of correct diploid chromosome counts (40 chromosomes) for *S1pr2* targeted clones P1A9 (left) and P2G6 (middle). An example of chromosome aneuploidy (39 chromosomes) in clone P2D6 (right). Chromosomes enumerated using Leica software Application Suite. **(B)** Transgene protein expression assessment in lead (P1A9, P2G6) and backup (P1E11) candidate clones by α-FLAG epitope tag Western blot of ESC lysate. Wild-type (WT) JM8 A3.N1 ESC lysate used as negative control and a 41 kDa recombinant protein which contained the FLAG epitope tag as positive control (+). Each well loaded with 20 µg cell lysate. α-tubulin used as control. **(C)** Heat inactivated ESC culture media was tested for mycoplasma. Each pre-prepared PCR tube contained an internal control DNA template and primers specific for mycoplasma and the internal control. Mycoplasma PCR negative control (-) has no external template added, whereas the mycoplasma PCR positive control (+) contains both the internal control DNA as well as mycoplasma DNA.

4.3.11 Chimera generation and efforts towards germline transmission from *S1pr2*^{diSplit670PAS} ESCs clones.

S1pr2^{diSplit670PAS} targeted ESC clones are derived from C57BL/6 JM8 A3.N1 ESCs which contain a repaired agouti allele (Pettitt *et al.*, 2009). Coat colour chimerism and gender can be used as surrogate markers for ESC contribution to chimeras. This meant that injection of *S1pr2*^{diSplit670PAS} ESCs into donor C57BL/6J blastocysts for implantation into pseudo-pregnant foster mice would enable pup chimerism assessment by agouti coat colour contribution (ESC-derived) to the host black coat colour (blastocyst derived). CD1 mice are reported to be "good" surrogate mothers, as females accept pups from another mother and new-born pups are attentively nursed to weaning (Plück and Klasen, 2009; Bouabe and Okkenhaug, 2013). Ten rounds of blastocyst injections were performed at the University of Birmingham (UoB), of which 50% produced litters, and 10/12 (83%) of the pups were weaned successfully (Table 4.11). Three chimeric pups were identified: two male and one female (Table 4.11). Chimerism was scored by agouti coat colour contribution (Figure 4.41) and by gender. As C57BL/6 JM8 A3.N1 ESCs have a male karyotype, an indicator of the injected ESC's contribution to pup chimerism can be made by the pup gender, as high levels of contribution should result in sex conversion of most female donor blastocysts (Pettitt *et al.*, 2009). All three chimaeras had relatively low contributions from the injected ESCs as judged by the surrogate measure of coat colour, so the probability of germline transmission was also low. This was especially the case for the female chimera since the contribution had not resulted in sex conversion of the female host C57BL/6J blastocyst.

	Blastocyst injections		Litter Analysis		
***S1pr2*^{diSplit670PAS} targeted clone**	**# performed**	**# that littered (%)**	**# of weaned pups (# born)**	**# male chimeras (%)**	**# female chimeras (%)**
P1A9	6	4 (67%)	7 (9)	1 (11%)	0 (0%)
P2G6	2	0 (0%)	0 (0)	0 (N/A)	0 (N/A)
P1E11	2	1 (50%)	3 (3)	1 (33%)	1 (33%)

Table 4.11 **Chimera generation from *S1pr2*^{diSplit670PAS} targeted JM8 A3.N1 ESC clones**. Percentage of chimeras calculated as the percentage of weaned pups.

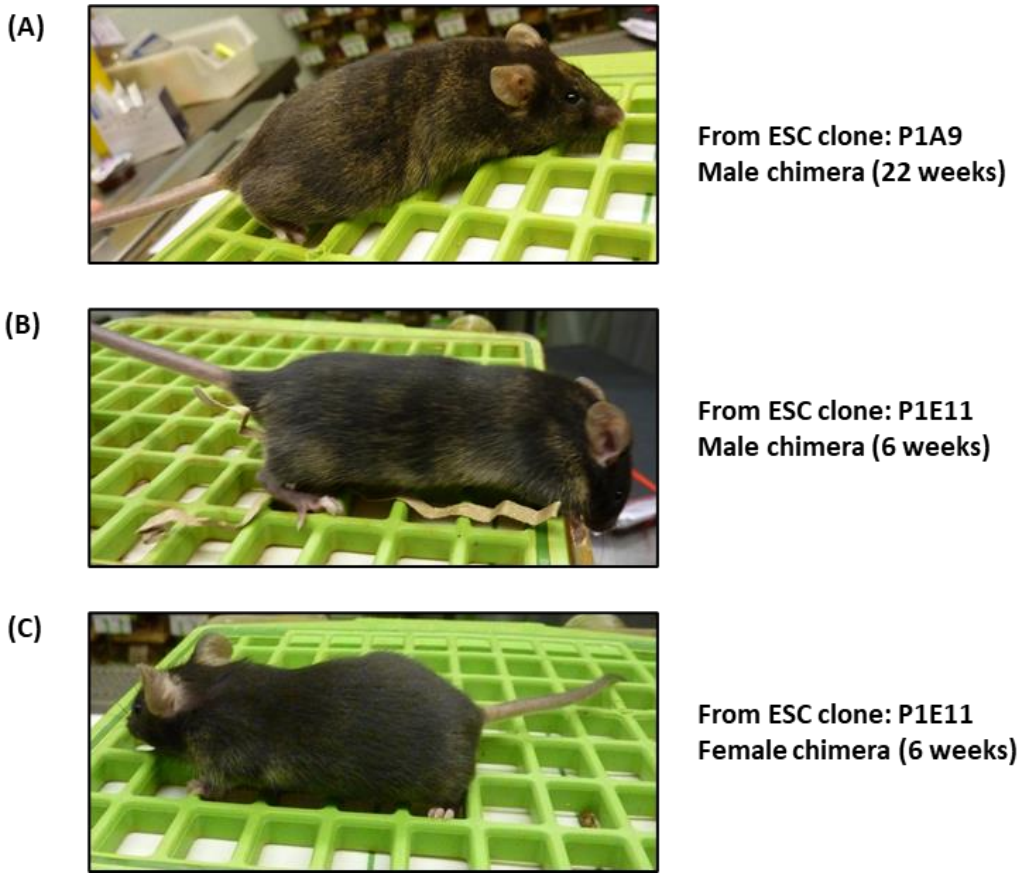

Figure 4.41 **Chimeric *S1pr2*^{diSplit670PAS} mice.** *S1pr2*^{diSplit670PAS} targeted C57BL/6N JM8 A3.N1 ESC clones (with repaired agouti allele) were injected into donor blastocysts from super ovulated C57BL/6J females (black coat) and implanted *in utero* of pseudo-pregnant CD1 surrogate mothers. Coat colour assessment of litters could be made from day 8 after birth. **(A)** 22-week old male chimera. **(B)** 6-week old male chimera. **(C)** 6-week old female chimera.

Chimeras were mated with wild-type C57BL/6N mice to test for germline transmission. Both of the male chimeras produced five litters and weaned pups came from 6 of these. None of the pups from the single litter born to the female chimera were successfully weaned (Table 4.12). Coat colour assessment revealed that 0/61 weaned pups were agouti (Table 4.12).

		Breeding for germline transmission			
Chimera (clone)	**Chimera assessment**	**# litters born**	**# pups born**	**# pups weaned (%)**	**# agouti pup (%)**
Male (P1A9)	Intermediate/Low	5	46	27 (59%)	0 (0%)
Male (P1E11)	Low	5	46	34 (74%)	0 (0%)
Female (P1E11)	Very Low	1	8	0 (0%)	0 (0%)

Table 4.12 **Germline transmission not achieved by mating**. Breeding of *S1pr2*^{diSplit670PAS} chimeras with C57BL/6N mates.

Retrospective analysis of the germline transmission strategy revealed that, like the *S1pr2*^{diSplit670PAS} allele on chromosome 9, C57BL/6 JM8 A3.N1 ESCs are heterozygous for the repaired agouti allele on chromosome 2 (Pettitt *et al.*, 2009), and that if targeted ESC clones had contributed to chimera gamete production, then the chromosomes which contain the repaired agouti and targeted *S1pr2* alleles could be segregated during meiosis. This meant that litters sired or birthed to *S1pr2*^{diSplit670PAS} chimeras could contain black coat colour pups derived from the targeted ESC clones and these black pups could carry the *S1pr2*^{diSplit670PAS} allele. The decision was made to genotype all new litters for the *S1pr2*^{diSplit670PAS} allele by PCR screen for the presence of both the targeted knock-in 3' junction and the neo^{R} cassette. Multiplex PCR genotyping assays were optimised for this purpose (Figure 4.42). Unfortunately, no further litters were born before the two chimeras from ESC clone P1E11 died. The sperm from the last male chimera was harvested, used for *in vitro fertilisation,* and was also genotyped for the

presence of the *S1pr2*^{diSplit670PAS} allele. Unfortunately, PCR genotyping yielded a negative result for the targeted *S1pr2*^{diSplit670PAS} allele in the chimera's sperm (Figure 4.43A-B).

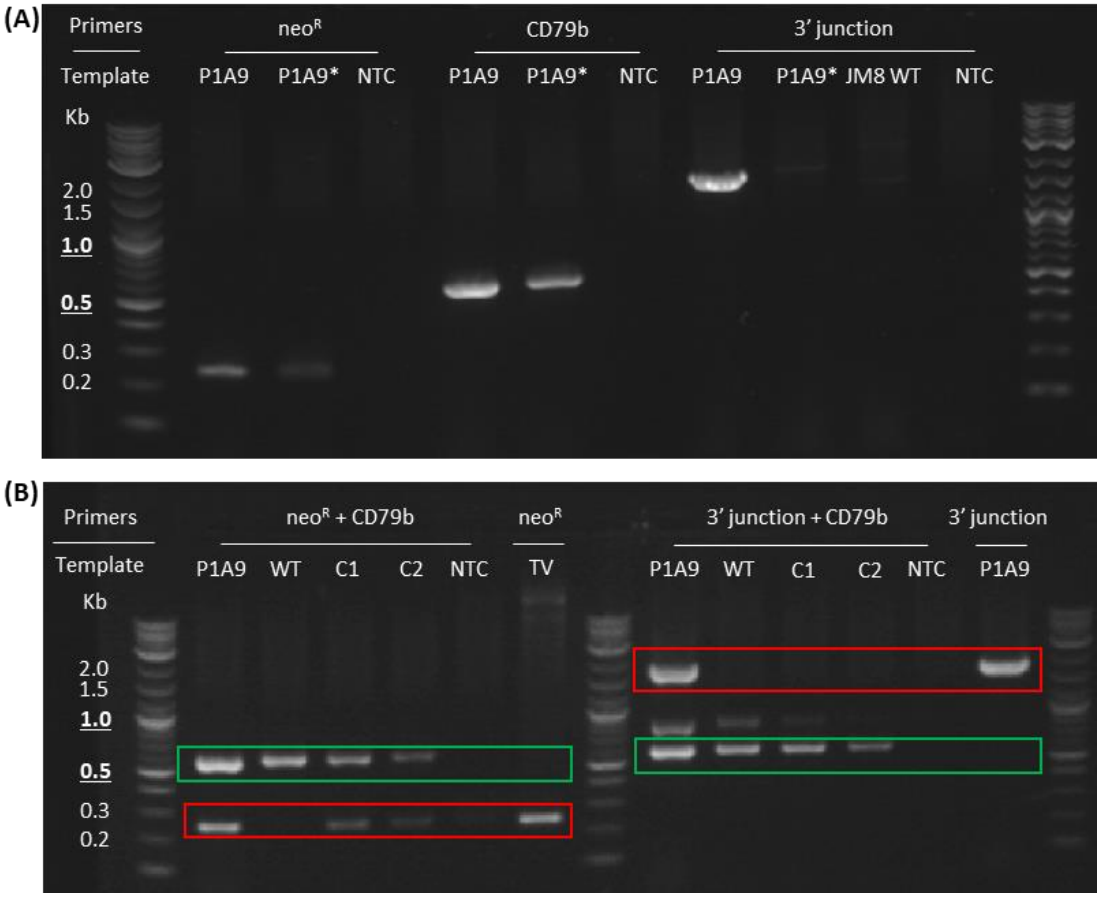

Figure 4.42 **Optimisation of a multiplex PCR genotype assay for targeted *S1pr2*^{diSplit670PAS} allele. (A)** Initially, *S1pr2* targeted ESC clone P1A9 or WT JM8 gDNA were used as templates to optimise singleplex PCR conditions. * indicates PCR reaction using the manufacturer's GC enhancer buffer. Primers: neo^R and 3' junction to detect *S1pr2*^{diSplit670PAS} allele, CD79b for mouse CD79b. PCR templates: P1A9, gDNA from *S1pr2*^{diSplit670PAS} targeted JM8 A3.N1 ESC clone P1A9; NTC, dH_20 only; JM8 WT, gDNA from wild-type JM8 A3.N1 ESC. **(B)** Multiplex genotype PCR assay for CD79b internal control and either the neo^R cassette (left) or 3' junction of the *S1pr2*^{diSplit670PAS} targeted allele (right). Multiplex PCR performed with gDNA template from cauda epididymis tissue of two Cγ1Cre.k$^{-/-}$ transgenic mice (C1 and C2) which contains the neo^R cassette but not the *S1pr2*^{diSplit670PAS} allele, WT C57BL/6 WT gDNA (WT) which contains neither neo^R nor 3' junction and *S1pr2*^{diSplit670PAS} targeted ESC clone P1A9 which contains both neo^R and 3' junction. CD79b is a PCR internal control to demonstrate mouse gDNA was present. *S1pr2* TV(final) plasmid was used as the PCR positive control for neo^R and negative control for CD79b. Red boxes, size of the expected target amplicon from the *S1pr2*^{diSplit670PAS} allele if present. Green boxes, CD79b PCR internal control.

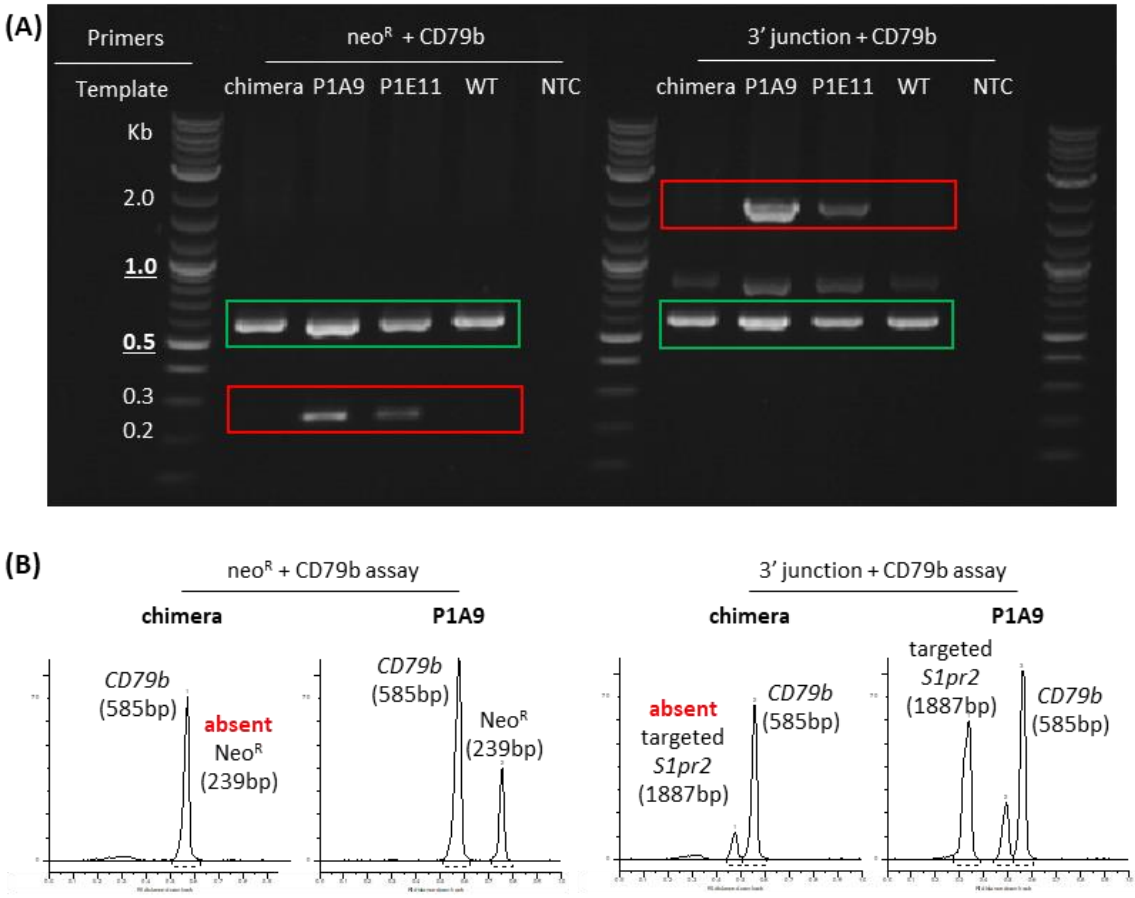

Figure 4.43 **PCR genotype assay of the sperm from the last remaining *S1pr2*^{diSplit670PAS} chimera. (A)** Multiplex PCR genotype assays to detect the neo^R cassette (neo^R, left) or targeted 3' junction of the *S1pr2*^{diSplit670PAS} allele (3' junction, right) in the sperm of male chimera derived from ESC clone P1A9. Red boxes, size of the expected target amplicon from the *S1pr2*^{diSplit670PAS} allele if present. Green boxes, CD79b PCR internal control to show gDNA was present. **(B)** Agarose gel lane analysis for the presence/absence of the expected PCR amplicons from each of the multiplex PCR assays. Common PCR templates; P1A9 and P1E11, gDNA from *S1pr2*^{diSplit670PAS} targeted JM8 A3.N1 ESC clones P1A9 and P1E11; WT, C57BL/6 WT gDNA from splenocytes; NTC, no template control.

4.3.12 Generation of transgenic mice with targeted knock-in of K-diSplit670 GAF-V5 at *Prdm1* intron6-7.

AstraZeneca were kind enough to support the production of *Prdm1*^{diSplit670GAF} transgenic mice by commercial service. The design of the experiment was a collaboration between myself, AstraZeneca scientists and Taconic Biosciences. Fortunately, Taconic agreed to include three arms for the gene targeting phase of the project to test for CRISPR/Cas9 targeting enhancement. As the budget available would only stretch to a single *Prdm1* targeting strategy, targeted insertion to *Prdm1* intron6-7 was chosen due to precedent (Kallies *et al.*, 2004). Further, it was deemed prudent to use a TV which had longer homologies that would hopefully bestow a higher baseline targeting efficiency on the TV. All work after generation of the modified *Prdm1* intron6-7 TV with longer homology arms (Figure 4.44) was carried out at Taconic Biosciences.

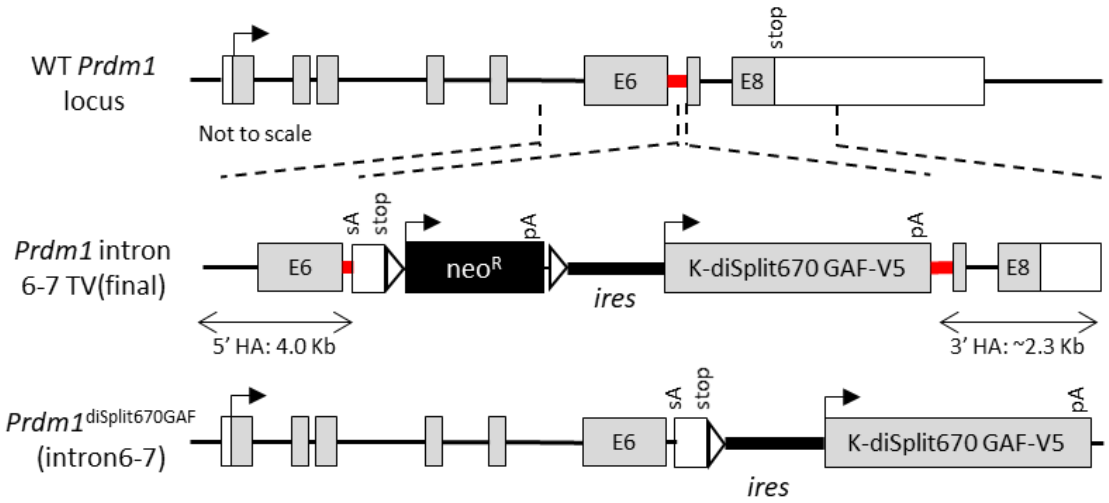

Figure 4.44 **Extension of homology arms for targeted insertion of K-diSplit670 GAF-V5 to *Prdm1* intron6-7**. *Prdm1* intron6-7 targeting. Top, wild-type (WT) *Prdm1* locus (transcript *Prdm1*-201 ENSMUST00000039174.10) where introns are thin black lines, and exons as boxes (open for untranslated regions (UTRs), grey shaded for protein coding regions). Black arrow depicts translation from initial methionine and stop indicates STOP codon. Dashed lines represent homology sequences. Middle, *Prdm1* intron6-7 TV(final); targeting vector to intron6-7 region, including extended longer 5' and 3' homology arms (HA) when compared to *Prdm1* intron6-7 TV(v2), adenoviral major late transcript splice acceptor (sA), LoxP sequences (black triangles), G418 selection cassette (neo^{R}), internal ribosome entry site (*ires*, thick black

line), polyadenylation site (pA), cDNA for K-diSplit670 GAF-V5 domain. Bottom, transgenic *Prdm1* locus after targeted insertion and Cre recombinase collapse.

A Taconic in-house validated C57BL/6NTac ESC line was used to perform a three-arm ESC targeting experiment which differed slightly from the *S1pr2* targeted insertion protocol used. The three arms were: (i) standard positive selection for TV (neo^R / G418), (ii) CRISPR/Cas9 enhanced targeting with selection just for a CRISPR/Cas9 all-in-one vector (puromycin), and (iii) CRISPR/Cas9 enhanced targeting with selection for both the CRISPR/Cas9 all-in-one vector and the TV (neo^R / G418 and puromycin) (Figure 4.45).

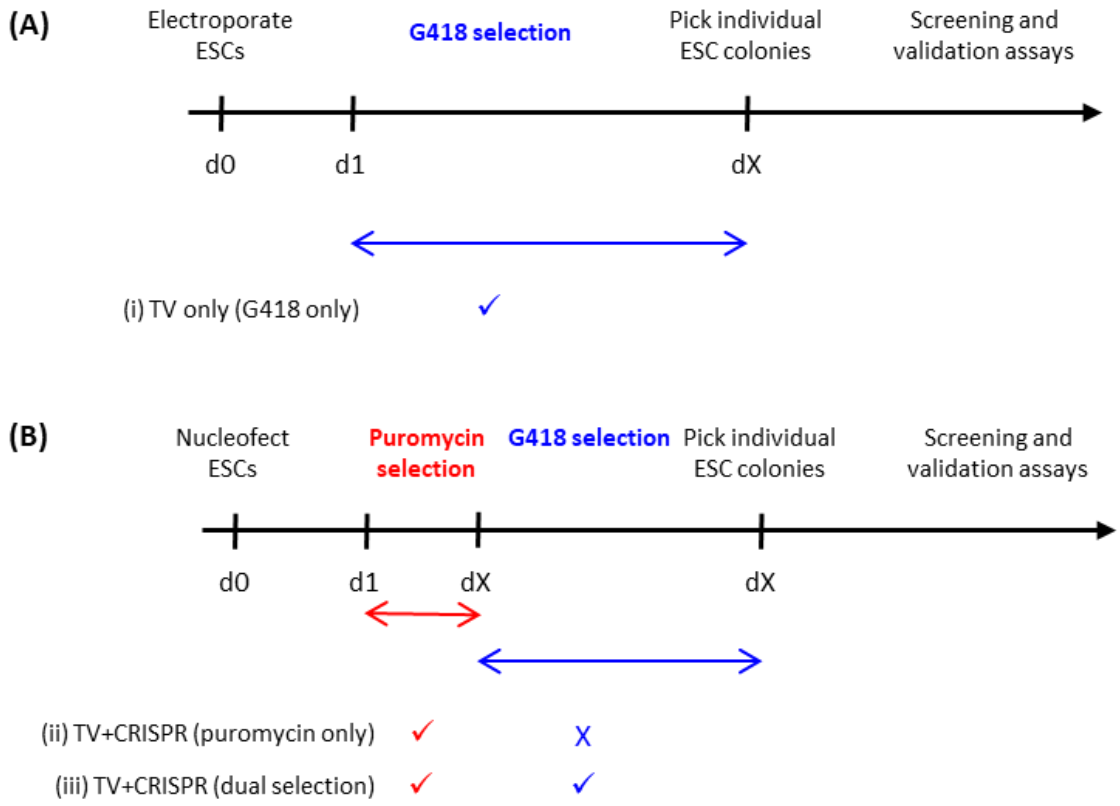

Figure 4.45 **Gene targeting experiment to insert K-diSplit670 GAF-V5 to the *Prdm1* locus at intron6-7.** Performed at Taconic. Schematic for the gene targeting experiment performed in a standard manner **(A)** or enhanced by CRISPR/Cas9 **(B)**. TV, *Prdm1* intron6-7 TV(final); CRISPR, CRISPR/Cas9 all-in-one vector that contained validated *Prdm1* intron6-7 sgRNA 3 (Table 4.3), puro^R and Cas9; (i), (ii), (iii) refer to experimental arms described in the text.

Arm (iii) resulted in growth of just 13 resistant clones, but primary PCR junction screening revealed a high efficiency of targeted knock-ins with 11/13 (85%) clones putative positive (Table 4.13). Arm (i) produced the most clones of which 192 were screened but none of these clones turned out to be positive for the desired targeted insertion suggesting that the intrinsic targeting efficiency of the TV (despite its longer homology arms) was low. Transient puromycin enrichment only, arm (ii), generated an intermediate number of resistant clones (104), and this method displayed a good targeting enrichment with 17/96 (18%) of clones screened putative positive (Table 4.13). These clones were further pre-validated by two PCR assays; first, a negative selection screen to exclude clones with unwanted integration events of the transfected plasmids i.e., clones positive for the plasmid backbone amp^R cassette, and second, to positively select for clones with heterozygous knock-in i.e., where the *Prdm1* wild-type allele was successfully detected. Heterozygous targeted knock-in was desired due to homozygous pre-natal lethal nature of both alleles harbouring targeted knock-in at *Prdm1* intron6-7 (Kallies *et al.*, 2004). The targeted integration events of the six heterozygous pre-validated clones were then analysed extensively by Southern Blot (data not shown), which excluded an additional clone and meant there were five fully validated *Prdm1*^{diSplit670GAF} targeted ESC clones in total, three from experimental arm (ii) and two from arm (iii) (Table 4.13).

One heterozygous *Prdm1*^{diSplit670GAF} ESC clone from each experimental arm was taken forward for blastocyst injections to generate chimeras; clone A-B01 from experimental arm (iii) and clone B-B10 from experimental arm (ii). Three blastocyst transfers of each clone were performed. Zero pups were obtained from clone A-B01 but 3/8 (37.5%) of pups from clone B-B10 were chimeric, with a single male chimera scored >50% chimeric by coat colour

assessment (Table 4.14). This high percentage chimera was sacrificed, and its sperm used for two rounds of IVF. In total, 7/11 (64%) of pups born from IVF were genotyped as heterozygous for the targeted *Prdm1*$^{\text{diSplit670GAF}}$ allele. These mice were generated in the week that national UK COVID-19 restrictions were enacted in March 2020 and unfortunately live mice could not be transferred to UoB to establish a founder colony nor to perform initial validation experiments. Male *Prdm1*$^{\text{diSplit670GAF}}$ mice were sacrificed and cryopreserved as sperm. The sperm aliquots of have subsequently been shipped to UoB ready for the transgenic mice to be re-derived for assessment of faithful transgene expression under the control of the endogenous *Prdm1* promoter.

Experimental Arm	Antibiotic resistant clones	Clones PCR screened	Targeted clones (%)	Clones amp^{R} negative + WT *Prdm1* allele detected	Clones validated by Southern Blot
(i) TV only (G418 only)	214	192	0/192 (0%)	N/A	N/A
(ii) TV+CRISPR (puromycin only)	104	96	17/96 (18%)	4	B-B10, B-E03, B-F11
(iii) TV+CRISPR (dual selection)	13	13	11/13 (85%)	2	A-A02, A-B01

Table 4.13 **Summary of standard vs CRISPR/Cas9 enhanced targeted insertion of K-diSplit670 GAF-V5 to *Prdm1* intron6-7.** All assays used to screen and validate clones were PCR based. All work conducted by Taconic Biosciences using *Prdm1* intron6-7 TV(final) and *Prdm1* intron6-7 sgRNA 3 (Table 4.3).

Prdm1^{diSplit670GAF} ESC Clone (from experimental arm #)	Transfers	Litters	Pups born	Weaned chimeras	Male chimeras >50% (% of total chimeras)	Male chimeras ≤ 50% (% of total chimeras)
A-B01 (iii)	3	3	0	N/A	N/A	N/A
B-B10 (ii)	3	2	8	3	1 (33%)	2/3 (66%)

Table 4.14 **Summary of blastocyst injections to generate chimeras from *Prdm1*^{diSplit670GAF} ESC clones.** Chimeric percentage assessed by coat colour assessment of black C57BL/6NTac ESC contribution to BALB/c host. Performed by Taconic Biosciences.

4.4 Discussion

4.4.1 diSplit670, a new split diRFP reporter.

We set out to design a more optimal transgenic *in vivo* fluorescent reporter system that could specifically label only GCmat PCs. To do this we developed a gene targeting strategy that would utilise a split NIR fluorescent reporter. Using published work as a guide (Filonov and Verkhusha, 2013; Shcherbakova *et al.*, 2016), we present here the development, characterisation, and validation of a split dimeric NIR fluorescent protein, diSplit670, derived from the dimeric fluorescent protein diRFP670.

diSplit670 demonstrates a number of properties that make it a desirable fluorescent reporter including: (1) high brightness in mammalian cells, (2) resistance to routine formaldehyde fixative, and (3) validated protein detection by epitope tags and plasma membrane localisation. diSplit670 was ~28% as bright as the parental diRFP670 in mammalian cells, whether assayed *in vitro* (flow cytometry) or by whole animal imaging (IVIS), in-line with existing split NIR FP reporters iSplit713 and miSplit670 which are 25% and ~45% as bright as parental diRFP713 and miRFP670, respectively (Filonov and Verkhusha, 2013; Shcherbakova *et al.*, 2016). Despite the similar names, diRFP670 and miRFP670 are derived from different bacterial phytochrome templates, and in mammalian cells non-split diRFP670 is 65% brighter than non-split miRFP670 (Table 4.1). This implies that the split derivatives, diSplit670 and miSplit670, have equivalent brightness in mammalian cells. Plasma membrane localisation of diSplit670 enhances suitability for immunofluorescence histology from frozen tissue sections, as this will prevent FP loss when tissues are stained with water-based antibody preparations. Functional epitope tags provide an intrinsic quality control for protein expression of the separate parts of

diSplit670 during validation of transgenic *in vivo* reporter systems; useful if diSplit670 mRNA but not fluorescence reconstitution can be detected.

Similarly to iSplit713 (Filonov and Verkhusha, 2013), it was necessary to add a pair of high affinity complementary binding coils to promote reconstitution of the two parts of diSplit670. Furthermore, like iSplit713 and its parental diRFP713 (Filonov and Verkhusha, 2013), diSplit670 has displayed an improved photostability compared to parental diRFP670, which exceeded expectations. Although the photostability of miSplit670 has not been determined (Shcherbakova *et al.*, 2016), the fact that the photostability of parental diRFP670 is ~2-fold larger than miRFP670, suggests that diSplit670 may be better suited than miSplit670 for microscopy applications such as time-lapse intravital imaging.

Further evaluation of diSplit670 showed that it has retained the *in situ* dimerised oligomeric state and short-term intracellular stability of the parental dimer diRFP670. When expression of the two parts of diSplit670 are controlled by phenotype specific promoters with inverse but overlapping expression profiles, the intrinsic diSpit670 intracellular decay could be used as a molecular clock to timestamp how recently the fluorescent cell changed gene expression patterns. In the case of the HAPi670 transgenic model, this could be used to analyse tissues by immunohistology to identify the most recent GC emigrant plasmablasts and understand their migration pathways.

These results demonstrate that diSplit670 is perfectly suited to be incorporated into a transgenic animal reporter.

4.4.2 Steps towards the generation of the novel HAPi670 transgenic.

Using the validated diSplit670 fluorescent reporter, we wanted to create an *in vivo* system to label cells for which unique cell-surface markers are not available, such as GCmat PCs. The split nature of diSplit670 enabled us to exploit the overlapping, inverse expression profiles of GC-specific *S1pr2* and PC-specific *Prdm1* thereby specifically labelling GC B-cells as they initiate differentiation into PCs and GCmat plasmablasts which are recent GC emigrants.

Using existing knock-in transgenic mice as a guide, we developed gene targeting strategies that placed the expression of each part of diSplit670 under control of the endogenous *S1pr2* or *Prdm1* promoter, so that transgene expression would be constitutive whilst the endogenous gene was active. We did not include an exogenous induction mechanism, such as tamoxifen / ERT2, as we wanted to create a system that could detect GCmat plasmablasts and their precursors both at the earliest timepoint of production (Zhang *et al.*, 2018) and throughout the entire GC reaction. Further, no requirement for tamoxifen represents a refinement in the use of animal models in research, which is in-line with the principles set out by the National Centre for the Replacement, Refinement, and Reduction of Animals in Research (NC3Rs) (Burden *et al.*, 2015).

Standard targeting vectors used to generate knock-in transgenic mouse ESCs have long homology arms (typically multiple kilobases) to promote the frequency of rare homologous recombination events (Jasin and Berg, 1988; Hasty, Rivera-Pérez and Bradley, 1991; Deng and Capecchi, 1992). The advent of CRISPR/Cas9 technology, with the ability to readily induce site specific DSB breaks (Cong *et al.*, 2013; Mali *et al.*, 2013), has led to reported successes of CRISPR/Cas9 enhanced targeted insertion of small to medium cargo sequences into mouse

ESCs using targeting vectors with only short (<1000 bp) or very short (<100 bp) homology arms (Li *et al.*, 2014; Zhang *et al.*, 2015). The use of short homology arms simplifies targeting vector construction and we therefore decided to use CRISPR/Cas9 enhanced gene targeting.

We report here successful targeted insertion of mem-FLAG-diSplit670 PAS-E to the *S1pr2* locus of mouse C57BL/6 JM8 A3.N1 ESCs (Pettitt *et al.*, 2009) using a targeting vector with short homology arms by both standard and CRISPR/Cas9 enhanced gene targeting. This involved de novo construction of a targeting vector and the validation of a sgRNA for use in the CRISPR/Cas9 enhanced experimental arm. Initially, the gene targeting strategy involved three components: (i) a simple targeting vector with short (~1 Kb) homology arms lacking a positive selectable marker flanked by recombinase specific recognition sites, (ii) transient antibiotic enrichment provided in trans (i.e., on a separate plasmid), and (iii) ± CRISPR/Cas9 enhancement. This strategy was favourable as targeted mouse ESCs, and the transgenic mouse produced by germline transmission, would not require recombinase mediated excision of the selectable marker and thus would not possess the "scar" left by this process. However, preliminary experiments using pD1301-AD-CRISPR-Cas9-GFP-sgRNA in JM8 A3.N1 ESCs revealed poor levels of expression from this plasmid. We therefore adapted the gene targeting strategy to use a plasmid which expresses both the sgRNA and Cas9, and which also confers puromycin resistance, all-in-one. This changed the experimental design to a two-component system involving only: (i) the original targeting vector with short homology arms and no selectable marker, and (ii) the all-in-one CRISPR/Cas9(Puro). A preliminary experiment to evaluate the efficiency of the pre-validated sgRNAs in mouse ESCs used stable puromycin selection of ESCs electroporated with all-in-one CRISPR/Cas9(Puro) vector and revealed low levels of puromycin resistance. As we had planned to only perform transient puromycin (and

therefore CRISPR/Cas9) enrichment using the all-in-one CRISPR/Cas9(Puro) vector, the low numbers of stable puromycin resistance ESC clones indicated that transient selection was unlikely to provide targeting enhancement. This guided our decision to switch targeting strategy and to include a positive selectable marker (neo^R) in the targeting vector but still to use only short homology arms. We validated the LoxP sequences flanking the neo^R cassette by shuttling the modified targeting vector through Cre recombinase expressing bacteria and by sequencing. We used the *S1pr2* targeting vector with neo^R to successfully generate ESCs with targeted knock-in at the 3'UTR of *S1pr2* exon 2 by standard targeting vector alone and with CRISPR/Cas9 enhancement. Further, we show a modest improvement in targeting efficiency in the CRISPR/Cas9 arm. Targeted ESCs were characterised by a multitude of molecular biology techniques and clones with the most normal karyotype analysis were selected for conversion into mice. All three of the selected clones were heterozygous for targeted knock-in of mem-FLAG-diSplit670 PAS-E. To date, multiple rounds of ESC injections have produced three low percentage chimeras with no germline transmission. To achieve germline transmission, we are planning further rounds of ESC injections or if this is unsuccessful, could return to ESC targeting to generate additional clones.

We designed two targeting strategies for knock-in to different regions of the *Prdm1* locus, validated sgRNA sequences for each site, and constructed two separate targeting vectors which both contained short homology arms and no selectable marker cassette. The first target site was *Prdm1* intron6-7 as there is precedent for functional expression of a targeted knock-in reporter to this region (Kallies *et al.*, 2004). However, as functional Blimp1 protein is required for proper embryo development (Mould *et al.*, 2012; Yamashiro *et al.*, 2016) and targeting to *Prdm1* intron6-7 only enables heterozygous stock (Kallies *et al.*, 2004), a second strategy was

conceived for knock-in to the 3' UTR of the last exon of *Prdm1* (exon 8); hypothesised to retain functional Blimp1 protein. Similarly to *S1pr2*, the all-in-one CRISPR/Cas9(Puro) plasmids containing sgRNAs specific for *Prdm1* intron6-7 or *Prdm1* exon 8 3'UTR specific showed reduced levels of puromycin resistance. AstraZeneca generously supported collaboration with Taconic Biosciences to produce ESCs with knock-in of K-diSplit670 GAF-V5 at the *Prdm1* locus and for targeted ESC conversion into transgenic mice. As there was only a single opportunity to achieve targeted knock-in, insertion to *Prdm1* intron6-7 was selected due to precedent (Kallies *et al.*, 2004). Further, to improve the likelihood of homologous recombination, the homology arms of the targeting vector were lengthened from ~1 Kb each to multiple kilobases each. Taconic kindly agreed to perform gene targeting with comparative arms to test whether CRISPR/Cas9 enhanced gene targeting. This workflow showed that gene targeting to this region of the *Prdm1* locus (intron6-7) was critically dependent on the action of CRISPR/Cas9, as only experiment arms with CRISPR/Cas9 enhancement produced ESC clones with targeted insertion and targeting vector alone did not. The *Prdm1*$^{\text{diSplit670GAF}}$ targeted ESC clones were characterised molecularly, were heterozygous for targeted knock-in and successfully achieved germline transmission. Due to COVID-19 restrictions the animal facility at UoB could not receive the live *Prdm1*$^{\text{diSplit670GAF}}$ mice, but the transgenic line has been cryopreserved as sperm and transferred to UoB for re-derivation as soon as possible. Initial validation experiments will test the new *Prdm1*$^{\text{diSplit670GAF}}$ mouse for faithful *Prdm1* controlled expression of K-diSplit670 GAF-V5 in PCs by flow cytometry, Western blot and immunohistology in response to T-I and T-D antigens.

Chapter 5. Conclusions and Future Perspectives

5.1 Conclusions

Affinity matured PCs and the high-affinity antibodies which they constitutively secrete are critical for acquisition of sterile immunity and high-quality therapeutic or research reagents. As such, efforts to understand how GCmat PCs are formed, and the environments required for their survival are paramount. Developments in this field may be translated into advances in mAb production and intelligent vaccine design. Presented here are the concept, design and progress-to-date of two novel fluorescent reporter transgenic mice; tools which could be used to address these pertinent issues.

The HALO PC and HAPi670 transgenic mice are two linked, but distinct, strategies that could be employed to test existing concepts or new hypotheses about the biology of affinity matured PC. We have shown that the two-colour fluorescent reporter system of the HALO PC mouse enables resolution and study of both the extrafollicular and GCmat response at the earliest time after formation of mature GCs (Figure 3.26). Flow cytometric analysis of the HALO PC model revealed peak output of GCmat PBs in the spleen 5 d post-immunisation; consistent with the data of Zhang and colleagues determined by immunohistology (Zhang *et al.*, 2018) and in disagreement with a preferential output of MBCs from the early GC (Shinnakasu *et al.*, 2016; Weisel *et al.*, 2016). This initial level of higher GCmat PC output from the GC may reflect a lower stringency for LZ GC B-cell access to FDC sequestered Ag, displayed during the earliest stages of the primary GC formation as immune complex with low-affinity antibody from the EF response (Sze *et al.*, 2000) and/or the highest affinity clones from the initial heterogeneous repertoire of BCR affinities which seed the GC (Tas *et al.*, 2016). The affinity matured antibody

secreted from early GCmat PCs could increase selection stringency in the LZ by replacing low-affinity antibodies in immune complex, in the process of antibody feedback (Zhang *et al.*, 2013), and thereby raise selection thresholds and regulate GCmat PC output. Flow cytometric analysis also revealed that CD11b expression is increased commensurate with PC maturity; an interesting finding that could be linked to the promiscuous binding of CD11b and one of its ligands fibronectin; a PC survival factor (Yakubenko *et al.*, 2001; Arnaout, 2016; Nguyen *et al.*, 2018). Furthermore, unexpected re-expression of cell-surface CD38 was first detected at low level on Blimp1^{GFP} expressing GC B-cells, rose significantly and spiked in GC experienced CD138^{int} TACI^{int} tdT^{Hi} Blimp1^{GFP} negative Tr PB-PCs, and then fell but remained higher than expected in CD138^{int} TACI^{int} tdT^{+} Tr PB-PCs expressing Blimp1^{GFP} (Figure 3.25 and Figure 3.28). CD38 re-expression correlated with a highly activated phenotype. Although not entirely characterised, CD38 can augment BCR signalling and signal via NF-κB in mice (Lund *et al.*, 1996; Kaku *et al.*, 2002), and in human B lymphocyte derived malignancies can signal via Syk and PI3K to activate Akt (Benkisser-Petersen *et al.*, 2016). CD38 mediated BCR signal augmentation in GC B-cells could activate Akt by S473 phosphorylation and this way can overcome the re-wired Akt signalling in GC B-cells (Luo *et al.*, 2019). We speculate that there may be a transient role required for this process in the early stages of plasma cell differentiation. The potential functional roles of both CD38 and CD11b in differentiation and migration/maturation/survival of GCmat PCs could be explored by combining the alleles from the HALO PC mouse with the Cre conditional CD38 knockout allele (MGI:4950992) or Cre conditional CD11b knockout His77 transgenic mouse, respectively (Avery *et al.*, 2019).

In an alternative strategy, we designed, validated, and characterised a novel split NIR reporter, diSplit670, that is bright and efficiently excited using standard red 633 nm lasers. diSplit670

is resistant to short-term formaldehyde fixation, is more photostable than parental diRFP670 and is localised to the plasma membrane to increase signal preservation during immunofluorescence histology staining. By incorporating diSplit670, the aim of the HAPi670 model is to transiently identify GCmat PCs at the earliest stage of differentiation initiation. We show here how CRISPR/Cas9 technology can enhance targeted knock-in of transgenic sequences into moues ESCs by insertion of the two parts of diSplit670 into either the *S1pr2* locus, leading to GC-specific expression, or the *Prdm1* locus, which is critical and strongly expressed during PC generation. Germline transmission has been achieved for one part of the diSplit670 split reporter, generating *Prdm1*$^{\text{diSplit670GAF}}$ mice.

5.2 Future Perspectives

Generation of the HAPi670 model is near completion. Re-derivation of cryopreserved *Prdm1*$^{\text{diSplit670GAF}}$ sperm by IVF will enable the first *in vivo* expression data in the near term. Concurrently, efforts to achieve germline transmission of the second part of diSplit670 to the *S1pr2* locus from *S1pr2*$^{\text{diSplit670PAS}}$ targeted ESCs will continue. Once ready, *Prdm1*$^{\text{diSplit670GAF}}$ and *S1pr2*$^{\text{diSplit670PAS}}$ strains will be interbred to obtain the final novel HAPi670 transgenic which can then be rigorously characterised.

After completion of the HAPi670 transgenic mouse we will have achieved the generation of two novel murine tools to identify markers, signals and mechanisms which distinguish GCmat PCs and can be used to test how differentiation from GC B-cells to PCs occurs. This is an area of intense current research which are not yet well understood (Ise *et al.*, 2018; Luo, Weisel and Shlomchik, 2018; Zhang *et al.*, 2018; Radtke and Bannard, 2019; Davidzohn *et al.*, 2020; Toboso-Navasa *et al.*, 2020). For HALO PC mice, bulk cell sorting and 3’ mRNAseq will be

used to determine gene expression signatures of GCmat PCs, EF PCs, and Blimp1^{GFP} expressing DZ or LZ GC B-cells from the peak of the early GCmat PC response at 5 d post SRBC immunisation and compare these to BM derived GCmat PCs labelled during the mature stage of a GC response (i.e., 14 d post SRBC immunisation). This may lead to the identification of gene candidates that can identify affinity matured PCs. If these are encoding cell-surface expressed proteins, they could become valuable tools to identify differentiation stages of GCmat PC by flow cytometry and immunohistology. Protein markers identified could be useful in hybridoma or Ag-specific single cell screening strategies to further expedite high-quality mAb generation. Epigenetic studies should be used to complement gene expression analysis to determine if there is an epigenetic and gene signature for affinity matured PCs. Prior epigenetic studies have investigated PCs in T-I or late-stage GC responses (Barwick *et al.*, 2016, 2018; Scharer *et al.*, 2018). Isolation of EF and GCmat PCs from the HALO PC model would enable investigation as to whether there is an epigenetic and gene expression signature that is imprinted and retained during GC maturation and when terminal PC differentiation is achieved, whereas the HAPi670 model would be a useful tool to investigate the immediate epigenetic and gene expression modifications during differentiation initiation. Following a primary T-D response, GCmat PC, EF PC, LZ Blimp1^{GFP} expressing GCmat PC precursors (HALO PC model) and diSplit670^{+} GCmat PC precursors (HAPi670 model) could be cell sorted and used for separate single cell RNA-sequencing and single cell assay for transposase-accessible chromatin (ATAC) sequencing reactions (Chopp *et al.*, 2020). Alternatively, paired single cell chromatin accessibility and gene expression datasets could be generated from sorted single cells using a newer workflow; Chromium Next GEM Single Cell Multiome ATAC + Gene Expression (10x Genomics). These experiments would provide detailed mechanistic insights into how PC

differentiation is initiated in GC B-cells but also identify how epigenetic mechanisms relate to gene expression which determine EF and GCmat PC long-term fate.

The spectral characteristics and expression patterns of the fluorescent reporters in HALO PC and HAPi670 mice would enable the study of spatial aspects of GCmat PCs with secondary lymphoid tissues. Light sheet microscopy of fixed whole LNs could help to produce a comprehensive analysis of PC niches, whilst intravital multiphoton microscopy of live GCmat PCs could test directionality of migration to these niches (Mohr *et al.*, 2009; Fooksman *et al.*, 2010; Zhang *et al.*, 2018).

Long-lived high-affinity Ab production is vital for natural or induced protective responses to pathogens. Ag-specific adoptive transfer of PCs and their long-term survival and Ag-specific Ab titres have supported this (Manz *et al.*, 1998; Slifka *et al.*, 1998; Bohannon *et al.*, 2016). The GFP and tdTomato fluorescent reporter proteins of the HALO PC mouse would enable the isolation and adoptive transfer of GCmat PCs with subsequent *in vivo*/*ex vivo* tracking in the recipient. These adoptive transfer experiments would test if GCmat PCs isolated from different secondary lymphoid tissues or BM have differential tissue-specific migration patterns, longevity, and proliferative capacity.

After achievement of germline transmission, and if the two parts of the diSplit670 reporter are faithfully expressed, then the novel HAPi670 transgenic mouse would provide a complementary but distinct system to the HALO PC mouse. These new strains should become uniquely suited tools for experiments to interlink fundamental PC immunology with translational applications and antibody discovery.

Chapter 6. References

Allen, C. D. *et al.* (2004) 'Germinal center dark and light zone organization is mediated by CXCR4 and CXCR5', *Nat Immunol*. 2004/08/01, 5(9), pp. 943–952. doi: 10.1038/ni1100.

Allen, D. *et al.* (1988) 'Antibody engineering for the analysis of affinity maturation of an anti-hapten response.', *The EMBO Journal*. Wiley, 7(7), pp. 1995–2001. doi: 10.1002/j.1460-2075.1988.tb03038.x.

Allman, D. *et al.* (2001) 'Resolution of Three Nonproliferative Immature Splenic B Cell Subsets Reveals Multiple Selection Points During Peripheral B Cell Maturation', *The Journal of Immunology*. The American Association of Immunologists, 167(12), pp. 6834–6840. doi: 10.4049/jimmunol.167.12.6834.

Amanna, I. J., Carlson, N. E. and Slifka, M. K. (2007) 'Duration of Humoral Immunity to Common Viral and Vaccine Antigens', *New England Journal of Medicine*. Massachusetts Medical Society, 357(19), pp. 1903–1915. doi: 10.1056/NEJMoa066092.

Arnaout, M. A. (2016) 'Biology and structure of leukocyte β2integrins and their role in inflammation', *F1000Research*. F1000 Research Ltd, 5. doi: 10.12688/f1000research.9415.1.

Artimo, P. *et al.* (2012) 'ExPASy: SIB bioinformatics resource portal', *Nucleic Acids Research*. Nucleic Acids Res, 40(W1). doi: 10.1093/nar/gks400.

Auldridge, M. E. *et al.* (2012) 'Structure-guided engineering enhances a phytochrome-based infrared fluorescent protein', *Journal of Biological Chemistry*. American Society for Biochemistry and Molecular Biology, 287(10), pp. 7000–7009. doi: 10.1074/jbc.M111.295121.

Avery, J. T. *et al.* (2019) 'Mice expressing the variant rs1143679 allele of ITGAM (CD11b) show impaired DC-mediated T cell proliferation', *Mammalian Genome*. Springer New York LLC, 30(9–10), pp. 245–259. doi: 10.1007/s00335-019-09819-y.

Babcook, J. S. *et al.* (1996) 'A novel strategy for generating monoclonal antibodies from single, isolated lymphocytes producing antibodies of defined specificities', *Proceedings of the National Academy of Sciences of the United States of America*. Proc Natl Acad Sci U S A, 93(15), pp. 7843–7848. doi: 10.1073/pnas.93.15.7843.

Bachmann Link, M. F. *et al.* (2014) 'Producing Increased Levels of Antibodies Memory B Cells into Secondary Plasma Cells Viral Particles Drive Rapid Differentiation of'. doi: 10.4049/jimmunol.1400065.

Bae, S., Park, J. and Kim, J. S. (2014) 'Cas-OFFinder: A fast and versatile algorithm that searches for potential off-target sites of Cas9 RNA-guided endonucleases', *Bioinformatics*, 30(10), pp. 1473–1475. doi: 10.1093/bioinformatics/btu048.

Bakker, E. and Swain, P. S. (2019) 'Estimating numbers of intracellular molecules through analysing fluctuations in photobleaching', *Scientific Reports*. Nature Publishing Group, 9(1),

pp. 1–13. doi: 10.1038/s41598-019-50921-7.

Barnett, B. E. *et al.* (2012) 'Asymmetric B cell division in the germinal center reaction', *Science*. 2011/12/15, 335(6066), pp. 342–344. doi: 10.1126/science.1213495.

Barwick, B. G. *et al.* (2016) 'Plasma cell differentiation is coupled to division-dependent DNA hypomethylation and gene regulation', *Nature Immunology*. Nature Publishing Group, 17(10), pp. 1216–1225. doi: 10.1038/ni.3519.

Barwick, B. G. *et al.* (2018) 'B cell activation and plasma cell differentiation are inhibited by de novo DNA methylation', *Nature Communications*. Nature Publishing Group, 9(1), pp. 1–14. doi: 10.1038/s41467-018-04234-4.

Basso, K. *et al.* (2010) 'Integrated biochemical and computational approach identifies BCL6 direct target genes controlling multiple pathways in normal germinal center B cells', *Blood*. 2009/12/03, 115(5), pp. 975–984. doi: 10.1182/blood-2009-06-227017.

Baumgarth, N. (2016) 'B-1 cell heterogeneity and the regulation of natural and antigen-induced IgM production', *Frontiers in Immunology*. Frontiers Media S.A., p. 324. doi: 10.3389/fimmu.2016.00324.

Baumgarth, N. (2017) 'A Hard(y) Look at B-1 Cell Development and Function', *The Journal of Immunology*. The American Association of Immunologists, 199(10), pp. 3387–3394. doi: 10.4049/jimmunol.1700943.

Bellini, D. and Papiz, M. Z. (2012) 'Structure of a bacteriophytochrome and light-stimulated protomer swapping with a gene repressor', *Structure*. 2012/07/12, 20(8), pp. 1436–1446. doi: 10.1016/j.str.2012.06.002.

Bende, R. J. *et al.* (2007) 'Germinal centers in human lymph nodes contain reactivated memory B cells', *Journal of Experimental Medicine*. The Rockefeller University Press, 204(11), pp. 2655–2665. doi: 10.1084/jem.20071006.

Benkisser-Petersen, M. *et al.* (2016) 'Spleen Tyrosine Kinase Is Involved in the CD38 Signal Transduction Pathway in Chronic Lymphocytic Leukemia', *PLOS ONE*. Edited by S. Bondada. Public Library of Science, 11(12), p. e0169159. doi: 10.1371/journal.pone.0169159.

Bergstedt-Lindqvist, S. *et al.* (1984) 'Regulation of Ig Class Secretion by Soluble Products of Certain T-Cell Lines', *Immunological Reviews*. Immunol Rev, 78(1), pp. 25–50. doi: 10.1111/j.1600-065X.1984.tb00475.x.

Bibikova, M. *et al.* (2001) 'Stimulation of Homologous Recombination through Targeted Cleavage by Chimeric Nucleases', *Molecular and Cellular Biology*. American Society for Microbiology, 21(1), pp. 289–297. doi: 10.1128/mcb.21.1.289-297.2001.

Bibikova, M. *et al.* (2002) 'Targeted chromosomal cleavage and mutagenesis in Drosophila using zinc-finger nucleases', *Genetics*. Genetics Society of America, 161(3), pp. 1169–1175. Available at: /pmc/articles/PMC1462166/?report=abstract (Accessed: 5 February 2021).

Boch, J. *et al.* (2009) 'Breaking the code of DNA binding specificity of TAL-type III effectors',

Science. Science, 326(5959), pp. 1509–1512. doi: 10.1126/science.1178811.

Von Boehmer, L. *et al.* (2016) 'Sequencing and cloning of antigen-specific antibodies from mouse memory B cells', *Nature Protocols*. Nature Publishing Group, 11(10), pp. 1908–1923. doi: 10.1038/nprot.2016.102.

Bohannon, C. *et al.* (2016) 'Long-lived antigen-induced IgM plasma cells demonstrate somatic mutations and contribute to long-Term protection', *Nature Communications*. Nature Publishing Group, 7(1), pp. 1–13. doi: 10.1038/ncomms11826.

Bossen, C. and Schneider, P. (2006) 'BAFF, APRIL and their receptors: Structure, function and signaling', *Seminars in Immunology*. Academic Press, pp. 263–275. doi: 10.1016/j.smim.2006.04.006.

Bouabe, H. and Okkenhaug, K. (2013) 'Gene targeting in mice: a review', *Methods Mol Biol*, 1064, pp. 315–336. doi: 10.1007/978-1-62703-601-6_23.

Brink, R. and Phan, T. G. (2018) 'Self-Reactive B Cells in the Germinal Center Reaction', *Annual Review of Immunology*. Annual Reviews Inc., 36(1), pp. 339–357. doi: 10.1146/annurev-immunol-051116-052510.

Burden, N. *et al.* (2015) 'Pioneering better science through the 3Rs: An introduction to the National Centre for the Replacement, Refinement, and Reduction of Animals in Research (NC3Rs)', *Journal of the American Association for Laboratory Animal Science*, 54(2), pp. 198–208. Available at: https://pubmed.ncbi.nlm.nih.gov/25836967/ (Accessed: 17 February 2021).

Caganova, M. *et al.* (2013) 'Germinal center dysregulation by histone methyltransferase EZH2 promotes lymphomagenesis', *Journal of Clinical Investigation*. American Society for Clinical Investigation, 123(12), pp. 5009–5022. doi: 10.1172/JCI70626.

Campbell, R. E. *et al.* (2002) 'A monomeric red fluorescent protein', *Proc Natl Acad Sci U S A*, 99(12), pp. 7877–7882. doi: 10.1073/pnas.082243699.

Carsetti, R., Köhler, G. and Lamers, M. C. (1995) 'Transitional B cells are the target of negative selection in the B cell compartment', *Journal of Experimental Medicine*. J Exp Med, 181(6), pp. 2129–2140. doi: 10.1084/jem.181.6.2129.

Casamayor-Palleja, M., Khan, M. and MacLennan, I. C. (1995) 'A subset of CD4+ memory T cells contains preformed CD40 ligand that is rapidly but transiently expressed on their surface after activation through the T cell receptor complex', *J Exp Med*, 181(4), pp. 1293–1301. Available at: https://www.ncbi.nlm.nih.gov/pubmed/7699321.

Casini, A. *et al.* (2018) 'A highly specific SpCas9 variant is identified by in vivo screening in yeast', *Nat Biotechnol*. 2018/01/29, 36(3), pp. 265–271. doi: 10.1038/nbt.4066.

Casola, S. *et al.* (2006) 'Tracking germinal center B cells expressing germ-line immunoglobulin γ1 transcripts by conditional gene targeting', *Proceedings of the National Academy of Sciences of the United States of America*. National Academy of Sciences, 103(19), pp. 7396–7401. doi: 10.1073/pnas.0602353103.

Cassese, G. *et al.* (2001) 'Inflamed kidneys of NZB / W mice are a major site for the homeostasis of plasma cells', *European Journal of Immunology*. Wiley-VCH Verlag, 31(9), pp. 2726–2732. doi: 10.1002/1521-4141(200109)31:9<2726::AID-IMMU2726>3.0.CO;2-H.

Cassese, G. *et al.* (2003) 'Plasma Cell Survival Is Mediated by Synergistic Effects of Cytokines and Adhesion-Dependent Signals', *The Journal of Immunology*. The American Association of Immunologists, 171(4), pp. 1684–1690. doi: 10.4049/jimmunol.171.4.1684.

Cattoretti, G. *et al.* (2009) 'Targeted disruption of the S1P2 sphingosine 1-phosphate receptor gene leads to diffuse large B-cell lymphoma formation', *Cancer Res*. 2009/11/10, 69(22), pp. 8686–8692. doi: 10.1158/0008-5472.CAN-09-1110.

Cerutti, A., Cols, M. and Puga, I. (2013) 'Marginal zone B cells: Virtues of innate-like antibody-producing lymphocytes', *Nature Reviews Immunology*. NIH Public Access, pp. 118–132. doi: 10.1038/nri3383.

Cha, T. L. *et al.* (2005) 'Molecular biology: Akt-mediated phosphorylation of EZH2 suppresses methylation of lysine 27 in histone H3', *Science*. Science, 310(5746), pp. 306–310. doi: 10.1126/science.1118947.

Chen, Y. and Wang, X. (2020) 'MiRDB: An online database for prediction of functional microRNA targets', *Nucleic Acids Research*. Oxford University Press, 48(D1), pp. D127–D131. doi: 10.1093/nar/gkz757.

Chernov, K. G. *et al.* (2017) 'Near-Infrared Fluorescent Proteins, Biosensors, and Optogenetic Tools Engineered from Phytochromes', *Chem Rev*. 2017/04/12, 117(9), pp. 6423–6446. doi: 10.1021/acs.chemrev.6b00700.

Chopp, L. B. *et al.* (2020) 'An Integrated Epigenomic and Transcriptomic Map of Mouse and Human αβ T Cell Development', *Immunity*. Cell Press, 53(6), pp. 1182-1201.e8. doi: 10.1016/j.immuni.2020.10.024.

Choulika, A. *et al.* (1995) 'Induction of homologous recombination in mammalian chromosomes by using the I-SceI system of Saccharomyces cerevisiae.', *Molecular and Cellular Biology*. American Society for Microbiology, 15(4), pp. 1968–1973. doi: 10.1128/mcb.15.4.1968.

Christian, M. *et al.* (2010) 'Targeting DNA double-strand breaks with TAL effector nucleases', *Genetics*. Genetics, 186(2), pp. 756–761. doi: 10.1534/genetics.110.120717.

Chu, V. T. *et al.* (2011) 'Eosinophils are required for the maintenance of plasma cells in the bone marrow', *Nature Immunology*. Nature Publishing Group, 12(2), pp. 151–159. doi: 10.1038/ni.1981.

Chu, V. T. and Berek, C. (2012) 'Immunization induces activation of bone marrow eosinophils required for plasma cell survival', *European Journal of Immunology*. John Wiley & Sons, Ltd, 42(1), pp. 130–137. doi: 10.1002/eji.201141953.

Codner, G. F. *et al.* (2020) 'Universal Southern blot protocol with cold or radioactive probes for the validation of alleles obtained by homologous recombination', *Methods*. Academic Press

Inc., 191, pp. 59–67. doi: 10.1016/j.ymeth.2020.06.011.

Collins, A. M. (2016) 'IgG subclass co-expression brings harmony to the quartet model of murine IgG function', *Immunology and Cell Biology*. Nature Publishing Group, pp. 949–954. doi: 10.1038/icb.2016.65.

Cong, L. *et al.* (2013) 'Multiplex genome engineering using CRISPR/Cas systems', *Science*. American Association for the Advancement of Science, 339(6121), pp. 819–823. doi: 10.1126/science.1231143.

De Crescenzo, G. *et al.* (2003) 'Real-time monitoring of the interactions of two-stranded de novo designed coiled-coils: effect of chain length on the kinetic and thermodynamic constants of binding', *Biochemistry*, 42(6), pp. 1754–1763. doi: 10.1021/bi0268450.

Davidzohn, N. *et al.* (2020) 'Syk degradation restrains plasma cell formation and promotes zonal transitions in germinal centers', *Journal of Experimental Medicine*. NLM (Medline), 217(3). doi: 10.1084/jem.20191043.

Dean, K. M. *et al.* (2011) 'Analysis of Red-Fluorescent Proteins Provides Insight into Dark-State Conversion and Photodegradation', *Biophysj*, 101, pp. 961–969. doi: 10.1016/j.bpj.2011.06.055.

Deng, C. and Capecchi, M. R. (1992) 'Reexamination of gene targeting frequency as a function of the extent of homology between the targeting vector and the target locus.', *Molecular and Cellular Biology*. American Society for Microbiology, 12(8), pp. 3365–3371. doi: 10.1128/mcb.12.8.3365.

Denton, A. E. *et al.* (2019) 'Type I interferon induces CXCL13 to support ectopic germinal center formation', *Journal of Experimental Medicine*. Rockefeller University Press, 216(3), pp. 621–637. doi: 10.1084/jem.20181216.

Diaspro, A. *et al.* (2006) 'Photobleaching', in *Handbook of Biological Confocal Microscopy: Third Edition*. Springer US, pp. 690–702. doi: 10.1007/978-0-387-45524-2_39.

Dippong, M. *et al.* (2017) 'Hapten-Specific Single-Cell Selection of Hybridoma Clones by Fluorescence-Activated Cell Sorting for the Generation of Monoclonal Antibodies', *Analytical Chemistry*, 89(7), pp. 4007–4012. doi: 10.1021/acs.analchem.6b04569.

Do, D. V. *et al.* (2013) 'A genetic and developmental pathway from STAT3 to the OCT4-NANOG circuit is essential for maintenance of ICM lineages in vivo', *Genes and Development*. Genes Dev, 27(12), pp. 1378–1390. doi: 10.1101/gad.221176.113.

Doench, J. G. *et al.* (2016) 'Optimized sgRNA design to maximize activity and minimize off-target effects of CRISPR-Cas9', *Nature Biotechnology*. Nature Publishing Group, 34(2), pp. 184–191. doi: 10.1038/nbt.3437.

Dogan, I. *et al.* (2009) 'Multiple layers of B cell memory with different effector functions', *Nature Immunology*. Nature Publishing Group, 10(12), pp. 1292–1299. doi: 10.1038/ni.1814.

Dominguez-Sola, D. *et al.* (2015) 'The FOXO1 Transcription Factor Instructs the Germinal

Center Dark Zone Program', *Immunity*. Cell Press, 43(6), pp. 1064–1074. doi: 10.1016/j.immuni.2015.10.015.

Du, W. *et al.* (2010) 'S1P2, the G protein-coupled receptor for sphingosine-1- phosphate, negatively regulates tumor angiogenesis and tumor growth in vivo in mice', *Cancer Research*. Cancer Res, 70(2), pp. 772–781. doi: 10.1158/0008-5472.CAN-09-2722.

Ellyard, J. I. *et al.* (2004) 'Antigen-selected, immunoglobulin-secreting cells persist in human spleen and bone marrow', *Blood*. American Society of Hematology, 103(10), pp. 3805–3812. doi: 10.1182/blood-2003-09-3109.

Filonov, G. S. *et al.* (2011) 'Bright and stable near-infrared fluorescent protein for in vivo imaging', *Nat Biotechnol*. 2011/07/17, 29(8), pp. 757–761. doi: 10.1038/nbt.1918.

Filonov, G. S. and Verkhusha, V. V (2013) 'A near-infrared BiFC reporter for in vivo imaging of protein-protein interactions', *Chem Biol*. 2013/07/25, 20(8), pp. 1078–1086. doi: 10.1016/j.chembiol.2013.06.009.

Finkin, S. *et al.* (2019) 'Protein Amounts of the MYC Transcription Factor Determine Germinal Center B Cell Division Capacity', *Immunity*. Cell Press, 51(2), pp. 324-336.e5. doi: 10.1016/j.immuni.2019.06.013.

Fooksman, D. R. *et al.* (2010) 'Development and Migration of Plasma Cells in the Mouse Lymph Node', *Immunity*. Immunity, 33(1), pp. 118–127. doi: 10.1016/j.immuni.2010.06.015.

Friedrich, G. and Soriano, P. (1991) 'Promoter traps in embryonic stem cells: A genetic screen to identify and mutate developmental genes in mice', *Genes and Development*. Genes Dev, 5(9), pp. 1513–1523. doi: 10.1101/gad.5.9.1513.

Furukawa, K. *et al.* (1999) 'Junctional amino acids determine the maturation pathway of an antibody', *Immunity*. Cell Press, 11(3), pp. 329–338. doi: 10.1016/S1074-7613(00)80108-9.

García De Vinuesa, C. *et al.* (1999) 'T-independent type 2 antigens induce B cell proliferation in multiple splenic sites, but exponential growth is confined to extrafollicular foci', *European Journal of Immunology*. Wiley-VCH Verlag, 29(4), pp. 1314–1323. doi: 10.1002/(sici)1521-4141(199904)29:04<1314::aid-immu1314>3.0.co;2-4.

Gatto, D. *et al.* (2009) 'Guidance of B cells by the orphan G protein-coupled receptor EBI2 shapes humoral immune responses', *Immunity*. 2009/07/16, 31(2), pp. 259–269. doi: 10.1016/j.immuni.2009.06.016.

Gaztelumendi, N. and Nogués, C. (2014) 'Chromosome Instability in mouse Embryonic Stem Cells', *Scientific Reports*. Nature Publishing Groups, 4(1), pp. 1–8. doi: 10.1038/srep05324.

Gitlin, A. D., Shulman, Z. and Nussenzweig, M. C. (2014) 'Clonal selection in the germinal centre by regulated proliferation and hypermutation', *Nature*. Nature Publishing Group, 509(7502), pp. 637–640. doi: 10.1038/nature13300.

Good-Jacobson, K. L. *et al.* (2010) 'PD-1 regulates germinal center B cell survival and the formation and affinity of long-lived plasma cells', *Nature Immunology*. Nature Publishing

Group, 11(6), pp. 535–542. doi: 10.1038/ni.1877.

Gordon, J. W. *et al.* (1980) 'Genetic transformation of mouse embryos by microinjection of purified DNA', *Proc Natl Acad Sci U S A*, 77(12), pp. 7380–7384. Available at: https://www.ncbi.nlm.nih.gov/pubmed/6261253.

Gould, H. J. *et al.* (2003) 'The biology of IgE and the basis of allergic disease', *Annual Review of Immunology*. Annual Reviews 4139 El Camino Way, P.O. Box 10139, Palo Alto, CA 94303-0139, USA , pp. 579–628. doi: 10.1146/annurev.immunol.21.120601.141103.

Green, J. A. *et al.* (2011) 'The sphingosine 1-phosphate receptor S1P2 maintains the homeostasis of germinal center B cells and promotes niche confinement', *Nature Immunology*. Nature Publishing Group, 12(7), pp. 672–680. doi: 10.1038/ni.2047.

Gutzeit, C., Chen, K. and Cerutti, A. (2018) 'The enigmatic function of IgD: some answers at last', *European Journal of Immunology*. Wiley-VCH Verlag, pp. 1101–1113. doi: 10.1002/eji.201646547.

Hammarlund, E. *et al.* (2017) 'Plasma cell survival in the absence of B cell memory', *Nature Communications*. Nature Publishing Group, 8(1), pp. 1–11. doi: 10.1038/s41467-017-01901-w.

Han, S. *et al.* (1995) 'Cellular interaction in germinal centers. Roles of CD40 ligand and B7-2 in established germinal centers', *J Immunol*, 155(2), pp. 556–567. Available at: https://www.ncbi.nlm.nih.gov/pubmed/7541819.

Hasty, P., Rivera-Pérez, J. and Bradley, A. (1991) 'The length of homology required for gene targeting in embryonic stem cells.', *Molecular and Cellular Biology*. American Society for Microbiology, 11(11), pp. 5586–5591. doi: 10.1128/mcb.11.11.5586.

Hauser, A. E. *et al.* (2002) 'Chemotactic Responsiveness Toward Ligands for CXCR3 and CXCR4 Is Regulated on Plasma Blasts During the Time Course of a Memory Immune Response', *The Journal of Immunology*. The American Association of Immunologists, 169(3), pp. 1277–1282. doi: 10.4049/jimmunol.169.3.1277.

Haynes, N. M. *et al.* (2007) 'Role of CXCR5 and CCR7 in follicular Th cell positioning and appearance of a programmed cell death gene-1high germinal center-associated subpopulation', *J Immunol*, 179(8), pp. 5099–5108. Available at: https://www.ncbi.nlm.nih.gov/pubmed/17911595.

Heise, N. *et al.* (2014) 'Germinal center B cell maintenance and differentiation are controlled by distinct NF-κB transcription factor subunits', *Journal of Experimental Medicine*. Rockefeller University Press, 211(10), pp. 2103–2118. doi: 10.1084/jem.20132613.

Heng, T. S. P. *et al.* (2008) 'The immunological genome project: Networks of gene expression in immune cells', *Nature Immunology*. Nat Immunol, pp. 1091–1094. doi: 10.1038/ni1008-1091.

Hermiston, M. L., Xu, Z. and Weiss, A. (2003) 'CD45: A Critical Regulator of Signaling Thresholds in Immune Cells', *Annual Review of Immunology*. Annual Reviews 4139 El

Camino Way, P.O. Box 10139, Palo Alto, CA 94303-0139, USA , 21(1), pp. 107–137. doi: 10.1146/annurev.immunol.21.120601.140946.

Hey, Y. Y. and O'Neill, H. C. (2012) 'Murine spleen contains a diversity of myeloid and dendritic cells distinct in antigen presenting function', *Journal of Cellular and Molecular Medicine*. John Wiley & Sons, Ltd, 16(11), pp. 2611–2619. doi: 10.1111/j.1582-4934.2012.01608.x.

Hibi, T. and Dosch, H. -M (1986) 'Limiting dilution analysis of the B cell compartment in human bone marrow', *European Journal of Immunology*. Eur J Immunol, 16(2), pp. 139–145. doi: 10.1002/eji.1830160206.

Ho, F. *et al.* (1986) 'Distinct short-lived and long-lived antibody-producing cell populations', *European Journal of Immunology*. John Wiley & Sons, Ltd, 16(10), pp. 1297–1301. doi: 10.1002/eji.1830161018.

Hock, A. K. *et al.* (2017) 'Development of an inducible mouse model of iRFP713 to track recombinase activity and tumour development in vivo', *Scientific Reports*. Nature Publishing Group, 7(1), pp. 1–9. doi: 10.1038/s41598-017-01741-0.

Hsu, P. D., Lander, E. S. and Zhang, F. (2014) 'Development and applications of CRISPR-Cas9 for genome engineering', *Cell*. Cell Press, pp. 1262–1278. doi: 10.1016/j.cell.2014.05.010.

Hu, J. H. *et al.* (2018) 'Evolved Cas9 variants with broad PAM compatibility and high DNA specificity', *Nature*. 2018/02/28, 556(7699), pp. 57–63. doi: 10.1038/nature26155.

Huang, C. *et al.* (2014) 'The BCL6 RD2 domain governs commitment of activated B cells to form germinal centers', *Cell Rep*. 2014/08/28, 8(5), pp. 1497–1508. doi: 10.1016/j.celrep.2014.07.059.

Ibrahimi, A. *et al.* (2009) 'Highly efficient multicistronic lentiviral vectors with peptide 2A sequences', *Human Gene Therapy*. Hum Gene Ther, 20(8), pp. 845–860. doi: 10.1089/hum.2008.188.

Iizuka, R., Yamagishi-Shirasaki, M. and Funatsu, T. (2011) 'Kinetic study of de novo chromophore maturation of fluorescent proteins', *Analytical Biochemistry*. Academic Press Inc., 414(2), pp. 173–178. doi: 10.1016/j.ab.2011.03.036.

Ise, W. *et al.* (2018) 'T Follicular Helper Cell-Germinal Center B Cell Interaction Strength Regulates Entry into Plasma Cell or Recycling Germinal Center Cell Fate', *Immunity*. Cell Press, 48(4), pp. 702-715.e4. doi: 10.1016/j.immuni.2018.03.027.

Ise, W. and Kurosaki, T. (2019) 'Plasma cell differentiation during the germinal center reaction', *Immunological Reviews*. Blackwell Publishing Ltd, 288(1), pp. 64–74. doi: 10.1111/imr.12751.

Iwakoshi, N. N. *et al.* (2003) 'Plasma cell differentiation and the unfolded protein response intersect at the transcription factor XBP-1', *Nat Immunol*. 2003/03/03, 4(4), pp. 321–329. doi: 10.1038/ni907.

J, L. *et al.* (2009) ‘Stable transgene expression in human embryonic stem cells after simple chemical transfection’, *Molecular reproduction and development*. Mol Reprod Dev, 76(6). doi: 10.1002/MRD.20983.

Jaenisch, R. (1976) ‘Germ line integration and Mendelian transmission of the exogenous Moloney leukemia virus’, *Proc Natl Acad Sci U S A*, 73(4), pp. 1260–1264. Available at: https://www.ncbi.nlm.nih.gov/pubmed/1063407.

Jasin, M. and Berg, P. (1988) ‘Homologous integration in mammalian cells without target gene selection.’, *Genes & development*. Genes Dev, 2(11), pp. 1353–1363. doi: 10.1101/gad.2.11.1353.

Jinek, M. *et al.* (2012) ‘A programmable dual-RNA-guided DNA endonuclease in adaptive bacterial immunity’, *Science*. 2012/06/28, 337(6096), pp. 816–821. doi: 10.1126/science.1225829.

Kaku, H. *et al.* (2002) ‘NF-κB is required for CD38-mediated induction of Cγ1 germline transcripts in murine B lymphocytes’, *International Immunology*. Int Immunol, 14(9), pp. 1055–1064. doi: 10.1093/intimm/dxf072.

Kallies, A. *et al.* (2004) ‘Plasma cell ontogeny defined by quantitative changes in blimp-1 expression’, *J Exp Med*, 200(8), pp. 967–977. doi: 10.1084/jem.20040973.

Kallies, A. *et al.* (2009) ‘Blimp-1 Transcription Factor Is Required for the Differentiation of Effector CD8+ T Cells and Memory Responses’, *Immunity*. Immunity, 31(2), pp. 283–295. doi: 10.1016/j.immuni.2009.06.021.

Kallies, A. *et al.* (2011) ‘A role for Blimp1 in the transcriptional network controlling natural killer cell maturation’, *Blood*. American Society of Hematology, 117(6), pp. 1869–1879. doi: 10.1182/blood-2010-08-303123.

Kayaba, A. *et al.* (2018) ‘Bone marrow PDGFRα+Sca-1+-enriched mesenchymal stem cells support survival of and antibody production by plasma cells in vitro through IL-6’, *International Immunology*. Oxford University Press, 30(6), pp. 241–253. doi: 10.1093/intimm/dxy018.

Kelly, L. M. *et al.* (2011) ‘EBI2 guides serial movements of activated B cells and ligand activity is detectable in lymphoid and nonlymphoid tissues’, *J Immunol*. 2011/08/15, 187(6), pp. 3026–3032. doi: 10.4049/jimmunol.1101262.

Kent, W. J. *et al.* (2002) ‘The Human Genome Browser at UCSC’, *Genome Research*. Cold Spring Harbor Laboratory, 12(6), pp. 996–1006. doi: 10.1101/gr.229102.

Kerfoot, S. M. *et al.* (2011) ‘Germinal center B cell and T follicular helper cell development initiates in the interfollicular zone’, *Immunity*, 34(6), pp. 947–960. doi: 10.1016/j.immuni.2011.03.024.

Khalil, A. M., Cambier, J. C. and Shlomchik, M. J. (2012) ‘B cell receptor signal transduction in the GC is short-circuited by high phosphatase activity’, *Science*. 2012/05/03, 336(6085), pp. 1178–1181. doi: 10.1126/science.1213368.

Khodadadi, L. *et al.* (2019) 'The Maintenance of Memory Plasma Cells', *Frontiers in Immunology*. Frontiers Media SA, 10, p. 721. doi: 10.3389/fimmu.2019.00721.

Kim, S. *et al.* (2007) 'Efficiency of the elongation factor-1α promoter in mammalian embryonic stem cells using lentiviral gene delivery systems', *Stem Cells and Development*. Stem Cells Dev, 16(4), pp. 537–545. doi: 10.1089/scd.2006.0088.

Kim, S. J. *et al.* (2011) 'Tolerogenic function of Blimp-1 in dendritic cells', *Journal of Experimental Medicine*. The Rockefeller University Press, 208(11), pp. 2193–2199. doi: 10.1084/jem.20110658.

Kitano, M. *et al.* (2011) 'Bcl6 Protein Expression Shapes Pre-Germinal Center B Cell Dynamics and Follicular Helper T Cell Heterogeneity', *Immunity*. Elsevier, 34(6), pp. 961–972. doi: 10.1016/j.immuni.2011.03.025.

Köhler, G. and Milstein, C. (1975) 'Continuous cultures of fused cells secreting antibody of predefined specificity', *Nature*. American Association of Immunologists, 256(5517), pp. 495–497. doi: 10.1038/256495a0.

Kono, M. *et al.* (2004) 'The sphingosine-1-phosphate receptors S1P1, S1P2, and S1P3 function coordinately during embryonic angiogenesis', *Journal of Biological Chemistry*. J Biol Chem, 279(28), pp. 29367–29373. doi: 10.1074/jbc.M403937200.

Kõressaar, T. *et al.* (2018) 'Primer3-masker: Integrating masking of template sequence with primer design software', *Bioinformatics*. Oxford University Press, 34(11), pp. 1937–1938. doi: 10.1093/bioinformatics/bty036.

Kräutler, N. J. *et al.* (2017) 'Differentiation of germinal center B cells into plasma cells is initiated by high-affinity antigen and completed by Tfh cells', *Journal of Experimental Medicine*. Rockefeller University Press, 214(5), pp. 1259–1267. doi: 10.1084/jem.20161533.

Kunisawa, J. *et al.* (2013) 'Microbe-dependent CD11b+ IgA+ plasma cells mediate robust early-phase intestinal IgA responses in mice', *Nature Communications*. Nat Commun, 4. doi: 10.1038/ncomms2718.

Labun, K. *et al.* (2016) 'CHOPCHOP v2: a web tool for the next generation of CRISPR genome engineering.', *Nucleic acids research*, 44(W1), pp. W272-6. doi: 10.1093/nar/gkw398.

Laidlaw, B. J. *et al.* (2017) 'The Eph-related tyrosine kinase ligand Ephrin-B1 marks germinal center and memory precursor B cells', *The Journal of experimental medicine*. The Rockefeller University Press, 214(3), pp. 639–649. doi: 10.1084/jem.20161461.

Lambert, T. J. (2019) 'FPbase: a community-editable fluorescent protein database', *Nature Methods*. Nature Publishing Group, pp. 277–278. doi: 10.1038/s41592-019-0352-8.

Lambooy, S. P. H. *et al.* (2017) 'The Novel Compound Sul-121 Preserves Endothelial Function and Inhibits Progression of Kidney Damage in Type 2 Diabetes Mellitus in Mice', *Scientific Reports*. Nature Publishing Group, 7(1), pp. 1–13. doi: 10.1038/s41598-017-11582-6.

Landsverk, O. J. B. *et al.* (2017) 'Antibody-secreting plasma cells persist for decades in human

intestine', *Journal of Experimental Medicine*. Rockefeller University Press, 214(2), pp. 309–317. doi: 10.1084/jem.20161590.

Lemke, A. *et al.* (2016) 'Long-lived plasma cells are generated in mucosal immune responses and contribute to the bone marrow plasma cell pool in mice', *Mucosal Immunology*. Nature Publishing Group, 9(1), pp. 83–97. doi: 10.1038/mi.2015.38.

Li, K. *et al.* (2014) 'Optimization of genome engineering approaches with the CRISPR/Cas9 system', *PloS one*. 2014/08/28, 9(8), p. e105779. doi: 10.1371/journal.pone.0105779.

Li, X. *et al.* (2018) 'Cbl Ubiquitin Ligases Control B Cell Exit from the Germinal-Center Reaction', *Immunity*. Cell Press, 48(3), pp. 530-541.e6. doi: 10.1016/j.immuni.2018.03.006.

Lightman, S. M., Utley, A. and Lee, K. P. (2019) 'Survival of long-lived plasma cells (LLPC): Piecing together the puzzle', *Frontiers in Immunology*. Frontiers Media S.A. doi: 10.3389/fimmu.2019.00965.

Linterman, M. A. *et al.* (2010) 'IL-21 acts directly on B cells to regulate Bcl-6 expression and germinal center responses', *J Exp Med*. 2010/02/08, 207(2), pp. 353–363. doi: 10.1084/jem.20091738.

Liu, D. *et al.* (2015) 'T-B-cell entanglement and ICOSL-driven feed-forward regulation of germinal centre reaction', *Nature*. Nature, 517(7533), pp. 214–218. doi: 10.1038/nature13803.

Liu, H. *et al.* (2015) 'A Rapid Method to Characterize Mouse IgG Antibodies and Isolate Native Antigen Binding IgG B Cell Hybridomas', *PLOS ONE*. Edited by J. S. Tregoning, 10(8), p. e0136613. doi: 10.1371/journal.pone.0136613.

Liu, X. *et al.* (1997) 'Trisomy eight in ES cells is a common potential problem in gene targeting and interferes with germ line transmission', *Developmental Dynamics*. John Wiley and Sons Inc., 209(1), pp. 85–91. doi: 10.1002/(SICI)1097-0177(199705)209:1<85::AID-AJA8>3.0.CO;2-T.

Livet, J. *et al.* (2007) 'Transgenic strategies for combinatorial expression of fluorescent proteins in the nervous system', *Nature*, 450(7166), pp. 56–62. doi: 10.1038/nature06293.

Loder, F. *et al.* (1999) 'B cell development in the spleen takes place in discrete steps and is determined by the quality of B cell receptor-derived signals', *Journal of Experimental Medicine*. J Exp Med, 190(1), pp. 75–89. doi: 10.1084/jem.190.1.75.

Longo, L. *et al.* (1997) 'The chromosome make-up of mouse embryonic stem cells is predictive of somatic and germ cell chimaerism', *Transgenic Research*. Kluwer Academic Publishers, 6(5), pp. 321–328. doi: 10.1023/A:1018418914106.

Lu, P., Shih, C. and Qi, H. (2017) 'Germinal centers: Ephrin B1-mediated repulsion and signaling control germinal center T cell territoriality and function', *Science*. American Association for the Advancement of Science, 356(6339). doi: 10.1126/science.aai9264.

Lund, F. E. *et al.* (1996) 'Signaling through CD38 augments B cell antigen receptor (BCR) responses and is dependent on BCR expression.', *Journal of immunology (Baltimore, Md. :*

1950), 157(4), pp. 1455–67. Available at: https://pubmed.ncbi.nlm.nih.gov/8759726/ (Accessed: 4 March 2021).

Luo, W. *et al.* (2019) 'The AKT kinase signaling network is rewired by PTEN to control proximal BCR signaling in germinal center B cells', *Nature Immunology*. Nature Publishing Group, 20(6), pp. 736–746. doi: 10.1038/s41590-019-0376-3.

Luo, W., Weisel, F. and Shlomchik, M. J. (2018) 'B Cell Receptor and CD40 Signaling Are Rewired for Synergistic Induction of the c-Myc Transcription Factor in Germinal Center B Cells', *Immunity*. Elsevier, 48(2), pp. 313-326.e5. doi: 10.1016/J.IMMUNI.2018.01.008.

MacLennan, A. J. *et al.* (2001) 'An essential role for the H218/AGR16/Edg-5/LPB2 sphingosine 1-phosphate receptor in neuronal excitability', *European Journal of Neuroscience*. Eur J Neurosci, 14(2), pp. 203–209. doi: 10.1046/j.0953-816X.2001.01634.x.

MacLennan, I. C. *et al.* (1997) 'The changing preference of T and B cells for partners as T-dependent antibody responses develop', *Immunol Rev*, 156, pp. 53–66. Available at: https://www.ncbi.nlm.nih.gov/pubmed/9176699.

MacLennan, I. C. M. *et al.* (1990) 'The evolution of B-cell clones', *Current Topics in Microbiology and Immunology*. Curr Top Microbiol Immunol, pp. 37–63. doi: 10.1007/978-3-642-75244-5_3.

MacLennan, I. C. M. (1994) 'Germinal centers', *Annual Review of Immunology*. Annual Reviews Inc., pp. 117–139. doi: 10.1146/annurev.iy.12.040194.001001.

MacLennan, I. C. M. *et al.* (2003) 'Extrafollicular antibody responses', *Immunological Reviews*, 194(1), pp. 8–18. doi: 10.1034/j.1600-065X.2003.00058.x.

Madisen, L. *et al.* (2010) 'A robust and high-throughput Cre reporting and characterization system for the whole mouse brain', *Nat Neurosci*. 2009/12/20, 13(1), pp. 133–140. doi: 10.1038/nn.2467.

Mali, P. *et al.* (2013) 'RNA-guided human genome engineering via Cas9', *Science*. 2013/01/03, 339(6121), pp. 823–826. doi: 10.1126/science.1232033.

Mankarious, S. *et al.* (1988) 'The half-lives of IgG subclasses and specific antibodies in patients with primary immunodeficiency who are receiving intravenously administered immunoglobulin', *Journal of Laboratory and Clinical Medicine*, 112(5), pp. 634–640. Available at: https://pubmed.ncbi.nlm.nih.gov/3183495/ (Accessed: 6 February 2021).

Mansour, S. L., Thomas, K. R. and Capecchi, M. R. (1988) 'Disruption of the proto-oncogene int-2 in mouse embryo-derived stem cells: A general strategy for targeting mutations to non-selectable genes', *Nature*. Nature, 336(6197), pp. 348–352. doi: 10.1038/336348a0.

Manz, R. A. *et al.* (1998) 'Survival of long-lived plasma cells is independent of antigen', *International Immunology*. Int Immunol, 10(11), pp. 1703–1711. doi: 10.1093/intimm/10.11.1703.

Manz, R. A. and Radbruch, A. (2002) 'Plasma cells for a lifetime?', *European Journal of*

Immunology. John Wiley & Sons, Ltd, 32(4), pp. 923–927. doi: 10.1002/1521-4141(200204)32:4<923::AID-IMMU923>3.0.CO;2-1.

Manz, R. A., Thiel, A. and Radbruch, A. (1997) 'Lifetime of plasma cells in the bone marrow [3]', *Nature*. Nature Publishing Group, pp. 133–134. doi: 10.1038/40540.

Marshall, J. L. *et al.* (2011) 'Early B blasts acquire a capacity for Ig class switch recombination that is lost as they become plasmablasts', *European Journal of Immunology*, 41(12), pp. 3506–3512. doi: 10.1002/eji.201141762.

Martin, F., Oliver, A. M. and Kearney, J. F. (2001) 'Marginal zone and B1 B cells unite in the early response against T-independent blood-borne particulate antigens', *Immunity*. Cell Press, 14(5), pp. 617–629. doi: 10.1016/S1074-7613(01)00129-7.

Martins, G. A. *et al.* (2006) 'Transcriptional repressor Blimp-1 regulates T cell homeostasis and function', *Nature Immunology*. Nat Immunol, 7(5), pp. 457–465. doi: 10.1038/ni1320.

Matlashov, M. E. *et al.* (2020) 'A set of monomeric near-infrared fluorescent proteins for multicolor imaging across scales', *Nature Communications*. Nature Research, 11(1), pp. 1–12. doi: 10.1038/s41467-019-13897-6.

Mcheyzer-Williams, L. J. *et al.* (2015) 'Class-switched memory B cells remodel BCRs within secondary germinal centers', *Nature Immunology*. Nature Publishing Group, 16(3), pp. 296–305. doi: 10.1038/ni.3095.

Merrell, K. T. *et al.* (2006) 'Identification of Anergic B Cells within a Wild-Type Repertoire', *Immunity*. Immunity, 25(6), pp. 953–962. doi: 10.1016/j.immuni.2006.10.017.

Meyer-Hermann, M. *et al.* (2012) 'A theory of germinal center B cell selection, division, and exit', *Cell Rep*. 2012/06/28, 2(1), pp. 162–174. doi: 10.1016/j.celrep.2012.05.010.

Miller, J. C. *et al.* (2007) 'An improved zinc-finger nuclease architecture for highly specific genome editing', *Nature Biotechnology*. Nature Publishing Group, 25(7), pp. 778–785. doi: 10.1038/nbt1319.

Miller, J. C. *et al.* (2011) 'A TALE nuclease architecture for efficient genome editing', *Nature Biotechnology*. Nat Biotechnol, 29(2), pp. 143–150. doi: 10.1038/nbt.1755.

Minnich, M. *et al.* (2016) 'Multifunctional role of the transcription factor Blimp-1 in coordinating plasma cell differentiation', *Nature Immunology*. Nature Publishing Group, 17(3), pp. 331–343. doi: 10.1038/ni.3349.

Modzelewski, A. J. *et al.* (2018) 'Efficient mouse genome engineering by CRISPR-EZ technology', *Nat Protoc*. 2018/05/10, 13(6), pp. 1253–1274. doi: 10.1038/nprot.2018.012.

Mohr, E. *et al.* (2009) 'Dendritic Cells and Monocyte/Macrophages That Create the IL-6/APRIL-Rich Lymph Node Microenvironments Where Plasmablasts Mature', *The Journal of Immunology*. The American Association of Immunologists, 182(4), pp. 2113–2123. doi: 10.4049/jimmunol.0802771.

Moriyama, S. *et al.* (2014) 'Sphingosine-1-phosphate receptor 2 is critical for follicular helper T cell retention in germinal centers', *Journal of Experimental Medicine*. Rockefeller University Press, 211(7), pp. 1297–1305. doi: 10.1084/jem.20131666.

Morozova, K. S. *et al.* (2010) 'Far-red fluorescent protein excitable with red lasers for flow cytometry and superresolution STED nanoscopy', *Biophys J*, 99(2), pp. L13-5. doi: 10.1016/j.bpj.2010.04.025.

Moscou, M. J. and Bogdanove, A. J. (2009) 'A simple cipher governs DNA recognition by TAL effectors', *Science*. Science, 326(5959), p. 1501. doi: 10.1126/science.1178817.

Mould, A. *et al.* (2012) 'Blimp1/Prdm1 governs terminal differentiation of endovascular trophoblast giant cells and defines multipotent progenitors in the developing placenta', *Genes and Development*. Cold Spring Harbor Laboratory Press, 26(18), pp. 2063–2074. doi: 10.1101/gad.199828.112.

Mould, A. W. *et al.* (2015) 'Blimp1/Prdm1 Functions in Opposition to Irf1 to Maintain Neonatal Tolerance during Postnatal Intestinal Maturation', *PLOS Genetics*. Edited by A. Kallies. Public Library of Science, 11(7), p. e1005375. doi: 10.1371/journal.pgen.1005375.

Muramatsu, M. *et al.* (2000) 'Class switch recombination and hypermutation require activation-induced cytidine deaminase (AID), a potential RNA editing enzyme', *Cell*. Cell Press, 102(5), pp. 553–563. doi: 10.1016/S0092-8674(00)00078-7.

Murphy, K. C. (1998) 'Use of bacteriophage lambda recombination functions to promote gene replacement in Escherichia coli', *J Bacteriol*, 180(8), pp. 2063–2071. Available at: https://www.ncbi.nlm.nih.gov/pubmed/9555887.

Muyrers, J. P. *et al.* (1999) 'Rapid modification of bacterial artificial chromosomes by ET-recombination', *Nucleic Acids Res*, 27(6), pp. 1555–1557. Available at: https://www.ncbi.nlm.nih.gov/pubmed/10037821.

Muzumdar, M. D. *et al.* (2007) 'A global double-fluorescent Cre reporter mouse', *Genesis*, 45(9), pp. 593–605. doi: 10.1002/dvg.20335.

Del Nagro, C. J. *et al.* (2005) 'CD19 function in central and peripheral B-cell development', *Immunologic Research*. Humana Press Inc., pp. 119–131. doi: 10.1385/IR:31:2:119.

Nguyen, D. C. *et al.* (2018) 'Factors of the bone marrow microniche that support human plasma cell survival and immunoglobulin secretion', *Nature Communications*. Nature Publishing Group, 9(1), pp. 1–12. doi: 10.1038/s41467-018-05853-7.

Nutt, S. L. *et al.* (2015) 'The generation of antibody-secreting plasma cells', *Nat Rev Immunol*. 2015/02/20, 15(3), pp. 160–171. doi: 10.1038/nri3795.

O'Brien, J. *et al.* (2018) 'Overview of microRNA biogenesis, mechanisms of actions, and circulation', *Frontiers in Endocrinology*. Frontiers Media S.A., p. 402. doi: 10.3389/fendo.2018.00402.

Ochiai, K. *et al.* (2013) 'Transcriptional Regulation of Germinal Center B and Plasma Cell

Fates by Dynamical Control of IRF4', *Immunity*. Immunity, 38(5), pp. 918–929. doi: 10.1016/j.immuni.2013.04.009.

Ohinata, Y. *et al.* (2008) 'A comprehensive, non-invasive visualization of primordial germ cell development in mice by the Prdm1-mVenus and Dppa3-ECFP double transgenic reporter', *Reproduction*. Reproduction, 136(4), pp. 503–514. doi: 10.1530/REP-08-0053.

Oliver, A. M., Martin, F. and Kearney, J. F. (1997) 'Mouse CD38 is down-regulated on germinal center B cells and mature plasma cells.', *Journal of immunology (Baltimore, Md. : 1950)*, 158(3), pp. 1108–15. Available at: https://pubmed.ncbi.nlm.nih.gov/9013949/ (Accessed: 4 March 2021).

Park, J., Bae, S. and Kim, J. S. (2015) 'Cas-Designer: A web-based tool for choice of CRISPR-Cas9 target sites', *Bioinformatics*, 31(24), pp. 4014–4016. doi: 10.1093/bioinformatics/btv537.

Peperzak, V. *et al.* (2013) 'Mcl-1 is essential for the survival of plasma cells', *Nature Immunology*. Nature Publishing Group, 14(3), pp. 290–297. doi: 10.1038/ni.2527.

Petti, L. *et al.* (2020) 'Unveiling role of sphingosine-1-phosphate receptor 2 as a brake of epithelial stem cell proliferation and a tumor suppressor in colorectal cancer', *Journal of Experimental and Clinical Cancer Research*. BioMed Central Ltd, 39(1), pp. 1–14. doi: 10.1186/s13046-020-01740-6.

Pettitt, S. J. *et al.* (2009) 'Agouti C57BL/6N embryonic stem cells for mouse genetic resources', *Nature Methods*. Nature Publishing Group, 6(7), pp. 493–495. doi: 10.1038/nmeth.1342.

Piatkevich, K. D. *et al.* (2017) 'Near-Infrared Fluorescent Proteins Engineered from Bacterial Phytochromes in Neuroimaging', *Biophysical Journal*. Biophysical Society, 113(10), pp. 2299–2309. doi: 10.1016/j.bpj.2017.09.007.

Piatkevich, K. D. and Verkhusha, V. V. (2011) *Guide to red fluorescent proteins and biosensors for flow cytometry*, *Methods in Cell Biology*. NIH Public Access. doi: 10.1016/B978-0-12-374912-3.00017-1.

Pillai, S. and Cariappa, A. (2009) 'The follicular versus marginal zone B lymphocyte cell fate decision', *Nature Reviews Immunology*. Nat Rev Immunol, pp. 767–777. doi: 10.1038/nri2656.

Plessis, A. *et al.* (1992) 'Site-specific recombination determined by I-SceI, a mitochondrial group I intron-encoded endonuclease expressed in the yeast nucleus', *Genetics*. Genetics Society of America, 130(3), pp. 451–460. doi: 10.1093/genetics/130.3.451.

Plück, A. and Klasen, C. (2009) 'Generation of chimeras by microinjection', *Methods in Molecular Biology*. Humana Press Inc., 561, pp. 199–217. doi: 10.1007/978-1-60327-019-9_13.

Pracht, K. *et al.* (2017) 'A new staining protocol for detection of murine antibody-secreting plasma cell subsets by flow cytometry', *Eur J Immunol*. 2017/07/13, 47(8), pp. 1389–1392. doi: 10.1002/eji.201747019.

Price, S. T. *et al.* (2015) 'Sphingosine 1-Phosphate Receptor 2 Regulates the Migration,

Proliferation, and Differentiation of Mesenchymal Stem Cells.', *International journal of stem cell research and therapy*. NIH Public Access, 2(2). doi: 10.23937/2469-570x/1410014.

Radbruch, A. *et al.* (2006) 'Competence and competition: The challenge of becoming a long-lived plasma cell', *Nature Reviews Immunology*. Nature Publishing Group, pp. 741–750. doi: 10.1038/nri1886.

Radtke, D. and Bannard, O. (2019) 'Expression of the Plasma Cell Transcriptional Regulator Blimp-1 by Dark Zone Germinal Center B Cells During Periods of Proliferation', *Frontiers in Immunology*. Frontiers Media S.A., 9(JAN), p. 3106. doi: 10.3389/fimmu.2018.03106.

Reif, K. *et al.* (2002) 'Balanced responsiveness to chemoattractants from adjacent zones determines B-cell position', *Nature*, 416(6876), pp. 94–99. doi: 10.1038/416094a.

Richie, C. T. *et al.* (2017) 'Near-infrared fluorescent protein iRFP713 as a reporter protein for optogenetic vectors, a transgenic Cre-reporter rat, and other neuronal studies', *J Neurosci Methods*. 2017/04/02, 284, pp. 1–14. doi: 10.1016/j.jneumeth.2017.03.020.

Te Riele, H., Maandag, E. R. and Berns, A. (1992) 'Highly efficient gene targeting in embryonic stem cells through homologous recombination with isogenic DNA constructs', *Proceedings of the National Academy of Sciences of the United States of America*. Proc Natl Acad Sci U S A, 89(11), pp. 5128–5132. doi: 10.1073/pnas.89.11.5128.

Rockwell, N. C. and Lagarias, J. C. (2010) 'A brief history of phytochromes', *Chemphyschem*, 11(6), pp. 1172–1180. doi: 10.1002/cphc.200900894.

Roco, J. A. *et al.* (2019) 'Class-Switch Recombination Occurs Infrequently in Germinal Centers', *Immunity*. Cell Press, 51(2), pp. 337-350.e7. doi: 10.1016/j.immuni.2019.07.001.

Rolink, A. G. *et al.* (1999) 'B cell development in the mouse from early progenitors to mature B cells', in *Immunology Letters*. Immunol Lett, pp. 89–93. doi: 10.1016/S0165-2478(99)00035-8.

Rolink, A. G., Andersson, J. and Melchers, F. (1998) 'Characterization of immature B cells by a novel monoclonal antibody, by turnover and by mitogen reactivity', *European Journal of Immunology*. Eur J Immunol, 28(11), pp. 3738–3748. doi: 10.1002/(SICI)1521-4141(199811)28:11<3738::AID-IMMU3738>3.0.CO;2-Q.

Rossant, C. J. *et al.* (2014) 'Phage display and hybridoma generation of antibodies to human CXCR2 yields antibodies with distinct mechanisms and epitopes', *MAbs*, 6(6), pp. 1425–1438. doi: 10.4161/mabs.34376.

Rouet, P., Smih, F. and Jasin, M. (1994) 'Introduction of double-strand breaks into the genome of mouse cells by expression of a rare-cutting endonuclease.', *Molecular and Cellular Biology*. American Society for Microbiology, 14(12), pp. 8096–8106. doi: 10.1128/mcb.14.12.8096.

Rowland, S. L. *et al.* (2010) 'BAFF Receptor Signaling Aids the Differentiation of Immature B Cells into Transitional B Cells following Tonic BCR Signaling', *The Journal of Immunology*. The American Association of Immunologists, 185(8), pp. 4570–4581. doi: 10.4049/jimmunol.1001708.

Roy, K. *et al.* (2019) 'A Regulatory Circuit Controlling the Dynamics of NFκB cRel Transitions B Cells from Proliferation to Plasma Cell Differentiation', *Immunity*. Cell Press, 50(3), pp. 616-628.e6. doi: 10.1016/j.immuni.2019.02.004.

Rudin, N., Sugarman, E. and Haber, J. E. (1989) 'Genetic and physical analysis of double-strand break repair and recombination in Saccharomyces cerevisiae.', *Genetics*. Genetics Society of America, 122(3), pp. 519–534. doi: 10.1093/genetics/122.3.519.

Russell, D. M. *et al.* (1991) 'Peripheral deletion of self-reactive B cells', *Nature*. Nature Publishing Group, 354(6351), pp. 308–311. doi: 10.1038/354308a0.

Rutishauser, R. L. *et al.* (2009) 'Transcriptional Repressor Blimp-1 Promotes CD8+ T Cell Terminal Differentiation and Represses the Acquisition of Central Memory T Cell Properties', *Immunity*. NIH Public Access, 31(2), pp. 296–308. doi: 10.1016/j.immuni.2009.05.014.

Sander, S. *et al.* (2015) 'PI3 Kinase and FOXO1 Transcription Factor Activity Differentially Control B Cells in the Germinal Center Light and Dark Zones', *Immunity*. Cell Press, 43(6), pp. 1075–1086. doi: 10.1016/j.immuni.2015.10.021.

Sanz, I. *et al.* (2019) 'Challenges and opportunities for consistent classification of human b cell and plasma cell populations', *Frontiers in Immunology*. Frontiers Media S.A., p. 2458. doi: 10.3389/fimmu.2019.02458.

Scharer, C. D. *et al.* (2018) 'Plasma cell differentiation is controlled by multiple cell division-coupled epigenetic programs', *Nature Communications*, 9(1), p. 1698. doi: 10.1038/s41467-018-04125-8.

Schneider, C. A., Rasband, W. S. and Eliceiri, K. W. (2012) 'NIH Image to ImageJ: 25 years of image analysis', *Nature Methods*. Nat Methods, pp. 671–675. doi: 10.1038/nmeth.2089.

Schroeder, H. W. and Cavacini, L. (2010) 'Structure and function of immunoglobulins', *Journal of Allergy and Clinical Immunology*. NIH Public Access, 125(2 SUPPL. 2), p. S41. doi: 10.1016/j.jaci.2009.09.046.

Sciammas, R. *et al.* (2006) 'Graded Expression of Interferon Regulatory Factor-4 Coordinates Isotype Switching with Plasma Cell Differentiation', *Immunity*. Immunity, 25(2), pp. 225–236. doi: 10.1016/j.immuni.2006.07.009.

Shapiro-Shelef, M. *et al.* (2003) 'Blimp-1 is required for the formation of immunoglobulin secreting plasma cells and pre-plasma memory B cells', *Immunity*, 19(4), pp. 607–620. Available at: https://www.ncbi.nlm.nih.gov/pubmed/14563324.

Sharrock, R. A. (2008) 'The phytochrome red/far-red photoreceptor superfamily', *Genome Biol*. 2008/08/28, 9(8), p. 230. doi: 10.1186/gb-2008-9-8-230.

Shcherbakova, D. M. *et al.* (2016) 'Bright monomeric near-infrared fluorescent proteins as tags and biosensors for multiscale imaging', *Nat Commun*. 2016/08/19, 7, p. 12405. doi: 10.1038/ncomms12405.

Shcherbakova, D. M. and Verkhusha, V. V (2013) 'Near-infrared fluorescent proteins for

multicolor in vivo imaging', *Nat Methods*. 2013/06/16, 10(8), pp. 751–754. doi: 10.1038/nmeth.2521.

Shcherbo, D. *et al.* (2009) 'Far-red fluorescent tags for protein imaging in living tissues', *Biochem J*, 418(3), pp. 567–574. doi: 10.1042/BJ20081949.

Shcherbo, D. *et al.* (2010) 'Near-infrared fluorescent proteins', *Nat Methods*. 2010/09/05, 7(10), pp. 827–829. doi: 10.1038/nmeth.1501.

Shi, W. *et al.* (2015) 'Transcriptional profiling of mouse B cell terminal differentiation defines a signature for antibody-secreting plasma cells', *Nat Immunol*. 2015/04/20, 16(6), pp. 663–673. doi: 10.1038/ni.3154.

Shih, T. A. *et al.* (2002) 'Role of BCR affinity in T cell dependent antibody responses in vivo', *Nat Immunol*. 2002/05/20, 3(6), pp. 570–575. doi: 10.1038/ni803.

Shinnakasu, R. *et al.* (2016) 'Regulated selection of germinal-center cells into the memory B cell compartment', *Nat Immunol*. 2016/05/09, 17(7), pp. 861–869. doi: 10.1038/ni.3460.

Shu, X. *et al.* (2009) 'Mammalian expression of infrared fluorescent proteins engineered from a bacterial phytochrome', *Science*, 324(5928), pp. 804–807. doi: 10.1126/science.1168683.

Shulman, Z. *et al.* (2014) 'Germinal centers: Dynamic signaling by T follicular helper cells during germinal center B cell selection', *Science*. American Association for the Advancement of Science, 345(6200), pp. 1058–1062. doi: 10.1126/science.1257861.

Silva-Cayetano, A. and Linterman, M. A. (2020) 'Stromal cell control of conventional and ectopic germinal centre reactions', *Current Opinion in Immunology*. Elsevier Ltd, pp. 26–33. doi: 10.1016/j.coi.2020.03.007.

De Silva, N. S. and Klein, U. (2015) 'Dynamics of B cells in germinal centres', *Nature Reviews Immunology*. Nature Publishing Group, 15(3), pp. 137–148. doi: 10.1038/nri3804.

Slifka, M. K. *et al.* (1998) 'Humoral immunity due to long-lived plasma cells', *Immunity*. Cell Press, 8(3), pp. 363–372. doi: 10.1016/S1074-7613(00)80541-5.

Slifka, M. K. and Ahmed, R. (1996) 'Long-term antibody production is sustained by antibody-secreting cells in the bone marrow following acute viral infection', in *Annals of the New York Academy of Sciences*. Blackwell Publishing Inc., pp. 166–176. doi: 10.1111/j.1749-6632.1996.tb52958.x.

Smith, G. P. (1985) 'Filamentous fusion phage: novel expression vectors that display cloned antigens on the virion surface', *Science*, 228(4705), pp. 1315–1317. Available at: https://www.ncbi.nlm.nih.gov/pubmed/4001944.

Smith, J. *et al.* (2006) 'A combinatorial approach to create artificial homing endonucleases cleaving chosen sequences', *Nucleic Acids Research*. Oxford University Press, 34(22), p. e149. doi: 10.1093/nar/gkl720.

Smith, K. G. *et al.* (1997) 'The extent of affinity maturation differs between the memory and

antibody-forming cell compartments in the primary immune response', *EMBO J*, 16(11), pp. 2996–3006. doi: 10.1093/emboj/16.11.2996.

Smith, K. G. *et al.* (2000) 'bcl-2 transgene expression inhibits apoptosis in the germinal center and reveals differences in the selection of memory B cells and bone marrow antibody-forming cells', *J Exp Med*, 191(3), pp. 475–484. Available at: https://www.ncbi.nlm.nih.gov/pubmed/10662793.

Snippert, H. J. *et al.* (2010) 'Intestinal crypt homeostasis results from neutral competition between symmetrically dividing Lgr5 stem cells', *Cell*. Cell Press, 143(1), pp. 134–144. doi: 10.1016/j.cell.2010.09.016.

Solanas, M. and Escrich, E. (1997) 'An improved protocol to increase sensitivity of Southern blot using dig- labelled DNA probes', *Journal of Biochemical and Biophysical Methods*. J Biochem Biophys Methods, 35(3), pp. 153–159. doi: 10.1016/S0165-022X(97)00031-6.

Song, L. *et al.* (1995) 'Photobleaching kinetics of fluorescein in quantitative fluorescence microscopy', *Biophysical Journal*, 68(6), pp. 2588–2600. doi: 10.1016/S0006-3495(95)80442-X.

Song, L. *et al.* (1997) 'Influence of fluorochrome labeling density on the photobleaching kinetics of fluorescein in microscopy', *Cytometry*, 27(3), pp. 213–223. doi: 10.1002/(SICI)1097-0320(19970301)27:3<213::AID-CYTO2>3.0.CO;2-F.

Stavnezer, J. (1996) 'Immunoglobulin class switching', *Current Opinion in Immunology*. Elsevier Ltd, 8(2), pp. 199–205. doi: 10.1016/S0952-7915(96)80058-6.

Stevens, T. L. *et al.* (1988) 'Regulation of antibody isotype secretion by subsets of antigen-specific helper T cells', *Nature*. Nature, 334(6179), pp. 255–258. doi: 10.1038/334255a0.

Strack, R. L. *et al.* (2009) 'A rapidly maturing far-red derivative of DsRed-Express2 for whole-cell labeling', *Biochemistry*, 48(35), pp. 8279–8281. doi: 10.1021/bi900870u.

Suan, D. *et al.* (2017) 'CCR6 Defines Memory B Cell Precursors in Mouse and Human Germinal Centers, Revealing Light-Zone Location and Predominant Low Antigen Affinity', *Immunity*. Cell Press, 47(6), pp. 1142-1153.e4. doi: 10.1016/j.immuni.2017.11.022.

Sze, D. M. *et al.* (2000) 'Intrinsic constraint on plasmablast growth and extrinsic limits of plasma cell survival', *J Exp Med*, 192(6), pp. 813–821. Available at: https://www.ncbi.nlm.nih.gov/pubmed/10993912.

Tan, H. X. *et al.* (2019) 'Inducible bronchus-associated lymphoid tissues (IBALT) serve as sites of B cell selection and maturation following influenza infection in mice', *Frontiers in Immunology*. Frontiers Media S.A., 10(MAR). doi: 10.3389/fimmu.2019.00611.

Taneja, S. and Rutenberg, A. D. (2017) 'Photobleaching of randomly rotating fluorescently decorated particles', *Journal of Chemical Physics*. American Institute of Physics Inc., 147(10). doi: 10.1063/1.4989673.

Tas, J. M. *et al.* (2016) 'Visualizing antibody affinity maturation in germinal centers', *Science*.

2016/02/18, 351(6277), pp. 1048–1054. doi: 10.1126/science.aad3439.

Teague, B. N. *et al.* (2007) 'Cutting Edge: Transitional T3 B Cells Do Not Give Rise to Mature B Cells, Have Undergone Selection, and Are Reduced in Murine Lupus', *The Journal of Immunology*. The American Association of Immunologists, 178(12), pp. 7511–7515. doi: 10.4049/jimmunol.178.12.7511.

Tedder, T. F., Inaoki, M. and Sato, S. (1997) 'The CD19-CD21 complex regulates signal transduction thresholds governing humoral immunity and autoimmunity', *Immunity*. Cell Press, pp. 107–118. doi: 10.1016/S1074-7613(00)80418-5.

Thaunat, O. *et al.* (2012) 'Asymmetric segregation of polarized antigen on B cell division shapes presentation capacity', *Science*, 335(6067), pp. 475–479. doi: 10.1126/science.1214100.

Thomas, K. R., Folger, K. R. and Capecchi, M. R. (1986) 'High frequency targeting of genes to specific sites in the mammalian genome', *Cell*. Cell, 44(3), pp. 419–428. doi: 10.1016/0092-8674(86)90463-0.

Tickle, S. *et al.* (2009) 'High-Throughput Screening for High Affinity Antibodies', *Journal of the Association for Laboratory Automation*, 14, pp. 303–307. doi: 10.1016/j.jala.2009.05.004.

Toboso-Navasa, A. *et al.* (2020) 'Restriction of memory B cell differentiation at the germinal center B cell positive selection stage', *Journal of Experimental Medicine*. J Exp Med, 217(7). doi: 10.1084/jem.20191933.

Toellner, K. M. *et al.* (1996) 'Immunoglobulin switch transcript production in vivo related to the site and time of antigen-specific B cell activation', *J Exp Med*, 183(5), pp. 2303–2312. Available at: https://www.ncbi.nlm.nih.gov/pubmed/8642339.

Toellner, K. M. *et al.* (1998) 'T helper 1 (Th1) and Th2 characteristics start to develop during T cell priming and are associated with an immediate ability to induce immunoglobulin class switching', *J Exp Med*, 187(8), pp. 1193–1204. Available at: https://www.ncbi.nlm.nih.gov/pubmed/9547331.

Toellner, K. M. *et al.* (2002) 'Low-level hypermutation in T cell-independent germinal centers compared with high mutation rates associated with T cell-dependent germinal centers', *J Exp Med*, 195(3), pp. 383–389. Available at: https://www.ncbi.nlm.nih.gov/pubmed/11828014.

Tokoyoda, K. *et al.* (2004) 'Cellular niches controlling B lymphocyte behavior within bone marrow during development', *Immunity*. Elsevier, 20(6), pp. 707–718. doi: 10.1016/j.immuni.2004.05.001.

Tran, M. T. *et al.* (2014) 'In vivo image analysis using iRFP transgenic mice', *Exp Anim*, 63(3), pp. 311–319. Available at: https://www.ncbi.nlm.nih.gov/pubmed/25077761.

Tran, M. T. N. *et al.* (2014) 'In Vivo image Analysis Using iRFP Transgenic Mice', *Experimental Animals*. International Press Editing Centre Incorporation, 63(3), pp. 311–319. doi: 10.1538/expanim.63.311.

Tung, J. W. *et al.* (2004) 'Identification of B-cell subsets: an exposition of 11-color (Hi-D)

FACS methods.', *Methods in molecular biology (Clifton, N.J.)*, 271, pp. 37–58. doi: 10.1385/1-59259-796-3:037.

Turner, C. A., Mack, D. H. and Davis, M. M. (1994) 'Blimp-1, a novel zinc finger-containing protein that can drive the maturation of B lymphocytes into immunoglobulin-secreting cells', *Cell*. Cell, 77(2), pp. 297–306. doi: 10.1016/0092-8674(94)90321-2.

Urnov, F. D. *et al.* (2005) 'Highly efficient endogenous human gene correction using designed zinc-finger nucleases', *Nature*. Nature, 435(7042), pp. 646–651. doi: 10.1038/nature03556.

Vences-Catalán, F. and Santos-Argumedo, L. (2011) 'CD38 through the life of a murine B lymphocyte', *IUBMB Life*. John Wiley & Sons, Ltd, 63(10), pp. 840–846. doi: 10.1002/iub.549.

Viant, C. *et al.* (2020) 'Antibody Affinity Shapes the Choice between Memory and Germinal Center B Cell Fates', *Cell*. Elsevier BV, 0(0). doi: 10.1016/j.cell.2020.09.063.

Victora, G. D. *et al.* (2010) 'Germinal center dynamics revealed by multiphoton microscopy with a photoactivatable fluorescent reporter', *Cell*, 143(4), pp. 592–605. doi: 10.1016/j.cell.2010.10.032.

Victora, G. D. and Nussenzweig, M. C. (2012) 'Germinal Centers', *Annual Review of Immunology*. Annual Reviews, 30(1), pp. 429–457. doi: 10.1146/annurev-immunol-020711-075032.

Vidarsson, G., Dekkers, G. and Rispens, T. (2014) 'IgG subclasses and allotypes: From structure to effector functions', *Frontiers in Immunology*. Frontiers Media S.A., 5(OCT). doi: 10.3389/fimmu.2014.00520.

Vieira, P. and Rajewsky, K. (1988) 'The half-lives of serum immunoglobulins in adult mice', *European Journal of Immunology*. John Wiley & Sons, Ltd, 18(2), pp. 313–316. doi: 10.1002/eji.1830180221.

Vinuesa, C. G. *et al.* (2001) 'Tracking the response of Xid B cells in vivo: TI-2 antigen induces migration and proliferation but Btk is essential for terminal differentiation', *Eur J Immunol*, 31(5), pp. 1340–1350. doi: 10.1002/1521-4141(200105)31:5<1340::AID-IMMU1340>3.0.CO;2-H.

Vinuesa, C. G. *et al.* (2005) 'A RING-type ubiquitin ligase family member required to repress follicular helper T cells and autoimmunity', *Nature*, 435(7041), pp. 452–458. doi: 10.1038/nature03555.

Vooijs, M., Jonkers, J. and Berns, A. (2001) 'A highly efficient ligand-regulated Cre recombinase mouse line shows that LoxP recombination is position dependent', *EMBO Reports*. European Molecular Biology Organization, 2(4), pp. 292–297. doi: 10.1093/embo-reports/kve064.

Vuletic, I. *et al.* (2015) 'Establishment of an mKate2-Expressing Cell Line for Non-Invasive Real-Time Breast Cancer In Vivo Imaging', *Mol Imaging Biol*, 17(6), pp. 811–818. doi: 10.1007/s11307-015-0853-5.

Wagner, J. R. *et al.* (2005) 'A light-sensing knot revealed by the structure of the chromophore-binding domain of phytochrome', *Nature*, 438(7066), pp. 325–331. doi: 10.1038/nature04118.

Wan, J. *et al.* (2015) 'PCAF-primed EZH2 acetylation regulates its stability and promotes lung adenocarcinoma progression', *Nucleic Acids Research*. Oxford University Press, 43(7), pp. 3591–3604. doi: 10.1093/nar/gkv238.

Wang, H. *et al.* (2013) 'One-step generation of mice carrying mutations in multiple genes by CRISPR/cas-mediated genome engineering', *Cell*. Elsevier, 153(4), pp. 910–918. doi: 10.1016/j.cell.2013.04.025.

Wang, R. *et al.* (2008) 'Promoter-dependent enchanced green fluorescent protein expression during embryonic stem cell propagation and differentiation', *Stem Cells and Development*. Stem Cells Dev, 17(2), pp. 279–289. doi: 10.1089/scd.2007.0084.

Warming, S. *et al.* (2005) 'Simple and highly efficient BAC recombineering using galK selection', *Nucleic Acids Research*, 33(4), pp. 1–12. doi: 10.1093/nar/gni035.

Weisel, F. J. *et al.* (2016) 'A Temporal Switch in the Germinal Center Determines Differential Output of Memory B and Plasma Cells', *Immunity*. Cell Press, 44(1), pp. 116–130. doi: 10.1016/j.immuni.2015.12.004.

Weissleder, R. (2001) 'A clearer vision for in vivo imaging', *Nat Biotechnol*, 19(4), pp. 316–317. doi: 10.1038/86684.

Wilmore, J. R., Jones, D. D. and Allman, D. (2017) 'Protocol for improved resolution of plasma cell subpopulations by flow cytometry', *Eur J Immunol*. 2017/06/28, 47(8), pp. 1386–1388. doi: 10.1002/eji.201746944.

Winnard, P. T., Kluth, J. B. and Raman, V. (2006) 'Noninvasive optical tracking of red fluorescent protein-expressing cancer cells in a model of metastatic breast cancer', *Neoplasia*, 8(10), pp. 796–806. doi: 10.1593/neo.06304.

Wols, H. A. M. *et al.* (2002) 'The Role of Bone Marrow-Derived Stromal Cells in the Maintenance of Plasma Cell Longevity', *The Journal of Immunology*. The American Association of Immunologists, 169(8), pp. 4213–4221. doi: 10.4049/jimmunol.169.8.4213.

Woof, J. M. and Ken, M. A. (2006) 'The function of immunoglobulin A in immunity', *Journal of Pathology*. J Pathol, pp. 270–282. doi: 10.1002/path.1877.

Xu, A. Q., Barbosa, R. R. and Calado, D. P. (2020) 'Genetic timestamping of plasma cells in vivo reveals tissue-specific homeostatic population turnover', *eLife*, 9. doi: 10.7554/eLife.59850.

Yagi, T. *et al.* (1990) 'Homologous recombination at c-fyn locus of mouse embryonic stem cells with use of diphtheria toxin A-fragment gene in negative selection', *Proceedings of the National Academy of Sciences of the United States of America*. National Academy of Sciences, 87(24), pp. 9918–9922. doi: 10.1073/pnas.87.24.9918.

Yakubenko, V. P. *et al.* (2001) 'Identification of the Binding Site for Fibrinogen Recognition

Peptide γ383-395 within the αMI-Domain of Integrin α Mβ2', *Journal of Biological Chemistry*. American Society for Biochemistry and Molecular Biology Inc., 276(17), pp. 13995–14003. doi: 10.1074/jbc.M010174200.

Yamashiro, C. *et al.* (2016) 'Persistent requirement and alteration of the key targets of PRDM1 during primordial germ cell development in mice', *Biology of Reproduction*. Society for the Study of Reproduction, 94(1). doi: 10.1095/biolreprod.115.133256.

Yang, X. *et al.* (2007) 'Crystal structure of the chromophore binding domain of an unusual bacteriophytochrome, RpBphP3, reveals residues that modulate photoconversion', *Proc Natl Acad Sci U S A*. 2007/07/17, 104(30), pp. 12571–12576. doi: 10.1073/pnas.0701737104.

Yau, I. W. *et al.* (2013) 'Censoring of Self-Reactive B Cells by Follicular Dendritic Cell–Displayed Self-Antigen', *The Journal of Immunology*. The American Association of Immunologists, 191(3), pp. 1082–1090. doi: 10.4049/jimmunol.1201569.

Zehentmeier, S. *et al.* (2014) 'Static and dynamic components synergize to form a stable survival niche for bone marrow plasma cells', *European Journal of Immunology*. Wiley-VCH Verlag, 44(8), pp. 2306–2317. doi: 10.1002/eji.201344313.

Zhang, H. *et al.* (2017) 'Novel high-throughput cell-based hybridoma screening methodology using the Celigo Image Cytometer', *J Immunol Methods*. 2017/04/14, 447, pp. 23–30. doi: 10.1016/j.jim.2017.04.003.

Zhang, L. *et al.* (2015) 'Large genomic fragment deletions and insertions in mouse using CRISPR/Cas9', *PloS one*. 2015/03/24, 10(3), p. e0120396. doi: 10.1371/journal.pone.0120396.

Zhang, Y. *et al.* (1998) 'A new logic for DNA engineering using recombination in Escherichia coli', *Nat Genet*, 20(2), pp. 123–128. doi: 10.1038/2417.

Zhang, Y. *et al.* (2013) 'Germinal center B cells govern their own fate via antibody feedback', *Journal of Experimental Medicine*, 210(3), pp. 457–464. doi: 10.1084/jem.20120150.

Zhang, Y. *et al.* (2018) 'Plasma cell output from germinal centers is regulated by signals from Tfh and stromal cells', *J Exp Med*. 2018/03/16, 215(4), pp. 1227–1243. doi: 10.1084/jem.20160832.

Zhang, Y., Garcia-Ibanez, L. and Toellner, K.-M. (2016) 'Regulation of germinal center B-cell differentiation', *Immunological Reviews*. Blackwell Publishing Ltd, 270(1), pp. 8–19. doi: 10.1111/imr.12396.

Zotos, D. *et al.* (2010) 'IL-21 regulates germinal center B cell differentiation and proliferation through a B cell-intrinsic mechanism', *J Exp Med*. 2010/02/08, 207(2), pp. 365–378. doi: 10.1084/jem.20091777.